NASA Contractor Report ~~159~~154 - Volume I

FINAL REPORT

DIGITAL ADAPTIVE CONTROLLERS FOR VTOL VEHICLES

I. Concept Evaluation

G.L. Hartmann, G. Stein,
and S.G. Pratt

HONEYWELL INC.
Systems and Research Center
Minneapolis, Minnesota 55413

CONTRACT NAS1-14921
November 1979

NASA
National Aeronautics and
Space Administration

Langley Research Center
Hampton, Virginia 23665
AC 804 827-3966

1. Report No. NASA Contractor Report 159154 -- Volume I	2. Government Accession No.	3. Recipient's Catalog No.

4. Title and Subtitle DIGITAL ADAPTIVE CONTROLLERS FOR VTOL VEHICLES. Volume I - Concept Evaluation.	5. Report Date November 1979 6. Performing Organization Code
7. Author(s) Gary L. Hartmann, Gunter Stein, and Stephen G. Pratt	8. Performing Organization Report No. 2825-41592
9. Performing Organization Name and Address Honeywell Inc. Systems and Research Center 2600 Ridgway Parkway N.E. Minneapolis, Minnesota 55413	10. Work Unit No. 11. Contract or Grant No. NAS1-14921
12. Sponsoring Agency Name and Address National Aeronautics and Space Administration Langley Research Hampton, Virginia 23665	13. Type of Report and Period Covered Contractor Final Report June 1977 - June 1979 14. Sponsoring Agency Code

15. Supplementary Notes

NASA Project Monitor: Dr. David R. Downing

X 3209

16. Abstract

The VTOL Approach and Landing Technology (VALT) Program of the National Aeronautics and Space Administration is conducting research in navigation, guidance, control display, and flight management for future VTOL aircraft. As part of the research in advanced control technology, Honeywell designed a digital self-adaptive flight control system for flight test in the VALT research aircraft -- a tandem-rotor, medium-transport helicopter (a modified CH-47).

The control laws accept commands from an automatic on-board guidance system. The primary objective of the control laws is to provide good command-following with a minimum cross-axis response. Three attitudes and vertical velocity are separately commanded. Adaptation of the control laws is based on information from rate and attitude gyros and a vertical velocity measurement. The final design resulted from a comparison of two different adaptive concepts -- one based on explicit parameter estimates from a real-time Maximum- Likelihood Estimation algorithm, the other based on an implicit Model Reference adaptive system. The two designs were compared on the basis of performance and complexity.

17. Key Words (Suggested by Author(s)) Adaptive control, VTOL, CH-47, parameter identification	18. Distribution Statement Unclassified - unlimited

19. Security Classif. (of this report) Unclassified	20. Security Classif. (of this page) Unclassified	21. No. of Pages 196	22. Price*

* For sale by the National Technical Information Service, Springfield, Virginia 22151

NASA-C-168 (Rev. 6-71)

N80-16065#

CONTENTS

CONTENTS -- CONCLUDED

FIGURES

FIGURES -- CONTINUED

FIGURES -- CONTINUED

FIGURES -- CONTINUED

FIGURES -- CONTINUED

FIGURES -- CONTINUED

FIGURES -- CONCLUDED

TABLES

DIGITAL ADAPTIVE CONTROLLERS
FOR VTOL VEHICLES--VOLUME I

Gary L. Hartmann, Gunter Stein, and Stephen G. Pratt
Honeywell Inc.
Systems and Research Center
Minneapolis, Minnesota

SECTION 1
INTRODUCTION

Background

The VTOL Approach and Landing Technology (VALT) program of the National Aeronautics and Space Administration is developing a technology base for future VTOL systems. This research includes the development of a navigation, guidance, and control system to permit automatic flight along complex four-dimensional (space and time) mission profiles from takeoff to landing under all weather conditions.

One area of the overall program is developing digital control design procedures for VTOL aircraft and demonstrating these methods by application to a VALT research aircraft. This aircraft is a modified CH-47B, a tandem-rotor, medium-transport helicopter. Its size is representative of future passenger-carrying VTOL aircraft. This aircraft was previously used in the United States Army's Tactical Aircraft Guidance System (TAGS) program.[1]

A large floating-point computer is part of the present on-board digital control system. This computer's capability permits in-flight evaluation of

---

[1] Anon., "Tactical Aircraft Guidance System Advanced Development Program Flight Test Phase Report," Vols. I and II, USAAMRDL TR-73-89A, B, Ft. Eustis, Virginia, April 1974.

a variety of guidance and control algorithms by simply programming the software in FORTRAN. Control commands are transmitted from the computer to the helicopter's mechanical linkages by electrohydraulic actuators.

As part of this research activity, Honeywell initiated work in 1977 under contract NAS1-14921 to provide a system of digital adaptive control laws for flight evaluation. The control laws are self-adaptive in that they modify the control law on the basis of existing feedback signals. The use of air data sensors was specifically excluded from the control system. The control system was specified to be an attitude command system and was to interface with existing guidance algorithms.

Candidate Adaptive Concepts

Two different adaptive concepts were selected at the outset for evaluation using a design based on the CH-47's longitudinal axis. For maximum research value, one implicit method and one explicit method were selected.

Explicit parameter estimation. -The Maximum-Likelihood Estimation (MLE) algorithm recently developed for the F-8 Digital Fly-by-Wire program was selected as the explicit concept.[2]

This algorithm is superior to other explicit identification concepts in several respects. It is not subject to estimation bias in the presence of gust inputs which is a problem for designs based on weighted least-squares-output error-matching techniques. The MLE procedure differs from the output-error least-square technique by minimizing a residual sequence rather than the measurement error. By using a Kalman filter, the random inputs (gusts) are properly accounted for. The algorithm can also be tailored for real-time parameter estimation.

---

[2] Hartmann, G. L., et al., "F-8C Adaptive Flight Control Laws, NASA CR-2880, September 1977.

The MLE algorithm has been implemented in a parallel-channel configuration to eliminate the need for multiple on-line iterations and eliminates the need for convergence tests.

In an explicit identification approach, an algorithm is required for adjusting the control law on the basis of parameter estimates. For application to the VALT helicopter, the control laws were structured to provide an attitude command system. Estimates of helicopter parameters (obtained on-line from MLE) perform the gain adjustment.

Implicit model reference. -An implicit model-following design was the second approach investigated. Model-following systems, per se, have been popular for flight control, since it is often convenient to express the desired closed-loop response of the vehicle in the form of an idealized model.[3] VTOLs are no exception. As parameters in the plant vary, adjustments to the feedforward and feedback gains are made to maintain a response closely matching the model. The model used was formulated from the attitude command response specifications.

Document Organization

This report is divided into 11 sections. Section 2 contains the list of symbols used throughout. Ground rules and requirements for the adaptive designs are set forth in Section 3. The helicopter model used for design is given in Section 4. The control structure common to both adaptive concepts is described in Section 5. Sections 6 and 7 contain design details for the MLE and the Model reference concepts, respectively. Section 8 compares the concepts and presents the design recommended for flight test. Section

---

[3] Landau, I. D., "A Survey of Model Reference Adaptive Techniques--Theory and Application," Automatica, Vol. 10, p. 353, 1974.

9 covers the guidance interface. Section 10 summarizes results of the off-line processing of flight data. Conclusions and recommendations are presented in Section 11.

SECTION 2
LIST OF SYMBOLS

Operators

$\operatorname{Arg}\min_{x} f(x)$	minimizing argument of function $f(\cdot)$
$E(\cdot)$	mathematical expectation
$\exp(\cdot)$	exponential
$\ln(\cdot)$	natural logarithm
$\ln\det(\cdot)$	natural log of determinant
$p(x/y)$	conditional probability distribution of x given y
s	Laplace operator
z	delay operator
$(\cdot) = \frac{d}{dt}$	time derivative
$\Delta(\cdot)$	increment
$\nabla(\cdot)$	gradient vector with respect to parameter vector ζ
$\nabla^2(\cdot)$	second partial derivative matrix with respect to parameters ζ
$\nabla_p(\cdot)$	pth component of $\nabla(\cdot)$
Σ	summation
$\lvert x\rvert$	absolute value
$\lVert x\rVert_M^2$	quadratic form $x^T M x$

Superscripts

$(\hat{\ })$ - estimated value

$(\bar{\ })$ - one-step predicted value

$(\ )^{(i)}$ - value for parallel channel i

Upper Case Symbols

A - system dynamics matrix

b - (1) discrete system input matrix
(2) residual covariance matrix

D - measurement matrix, y due to u

E_q, E_θ, E_{VZ} - model-following errors

H - measurement matrix

I - identity matrix

J - partial likelihood function $L - 1/2\Sigma \ln \det B$

K - Kalman filter gains

K_1, K_2, K_x, K_y - control gains

P - Kalman filter covariance matrix

P_o - a priori parameter covariance matrix

S - Kalman filter design statistic

U_N - sequence of N control inputs

V - air speed

Y_N - sequence of N measurements

Lower Case Symbols

a_x, a_y, a_z - acceleration along body axes

$\underline{c}$, c_i - parameter vector with components c_i

Lower Case Symbols (cont.)

$\underline{c}_o$ - a priori estimate of c

g - gravity

h - altitude

i^* - index of the minimum-L channel

n - system order

p - roll rate

$\bar{q}$ - dynamic pressure

r - (1) yaw rate
(2) number of measurements

t - time

u - control input vectors

v - lateral velocity perturbation

v_g - lateral gust component

x - state vector

y - measurement vector

Greek Symbols

Upper Case

Γ - discrete system noise input matrix

Lower Case

α - angle of attack

α_g - gust angle of attack

β - angle of sideslip

β_g - gust angle of sideslip

Greek Symbols

Lower Case (cont.)

δ_i - aerodynamic surface positions $i = B, C, S, R$
ϵ_k, $\Delta\epsilon_k$ - generic likelihood filter states
γ_{ij} - ij element of Γ
ζ - dummy argument for values of parameter vector $\underline{\zeta}$
η - white noise process
θ - pitch attitude
μ - $\exp(-\Delta t/\tau)$
ν - Kalman filter residuals
ξ - white noise process
ρ - air density
σ, σ_x - standard deviation of variable x
τ - time constant
ϕ - roll attitude
ψ - yaw attitude
ω - natural frequency

SECTION 3
DESIGN GROUND RULES AND REQUIREMENTS

The primary application of the adaptive controller is in automatic trajectory-following. A candidate VALT flight path is shown in Figure 1. It is representative of the terminal portion of a VTOL's flight. It includes a number of heading changes and concludes with a constant-velocity descent followed by a decelerating descent to a hover condition. The adaptive controller will accept commands from an existing guidance law. An overall block diagram is shown in Figure 2. An attitude control mode was specified. The performance requirements for attitude control are given in Table 1.

The adaptive control algorithm shall fit in a reasonable allocation of the on-board ROLM-1664 digital computer. As a design goal the adaptive software will operate at 10 samples per second. Sensor outputs sampled at 40 sps are available should a faster update rate be required.

The sensors were limited to the present VALT sensor complement, excluding air data. The sensors are listed in Table 2.

The adaptive algorithm used estimates of the three Euler angles (θ, ϕ, ψ), the body angular rates (p, q, and r), and vertical velocity. These signals were supplied by existing onboard estimates that combined the various sensor outputs.

Position information about the aircraft is supplied to the guidance algorithm from a barometric altimeter and a radar/laser tracking system located on the ground.

The adaptive controller will operate with the unaugmented vehicle. Finally, the adaptive controller must not interfere with the normal mission of the aircraft by requiring large test signals.

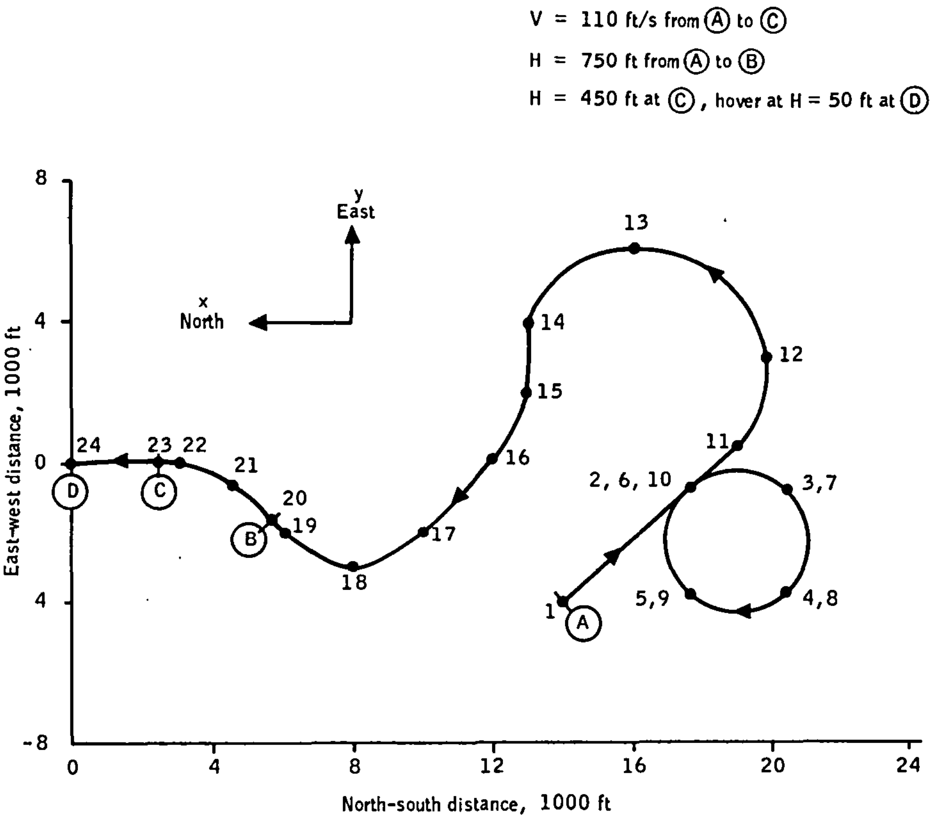

a) Horizontal profile

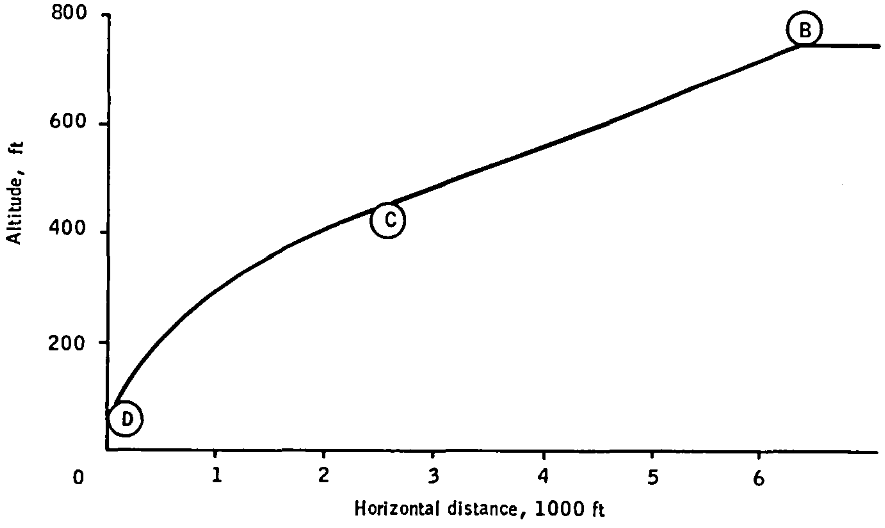

b) Altitude profile

Figure 1. -VALT trajectory (typical).

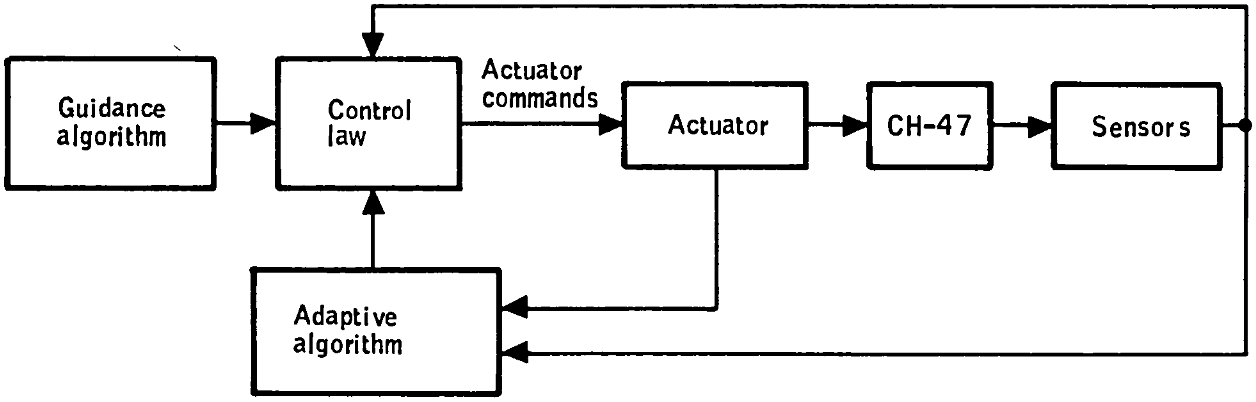

Figure 2. -System functional block diagram.

TABLE 1. -ATTITUDE COMMAND SPECIFICATIONS

Parameter	Requirement
a) Angle commands (θ, ϕ, ψ):	
Rise time criterion	Amplitude >90% of final value within 1.5 s.
Overshoot criterion	Overshoot <15% of final value.
Settling time criterion	Amplitude within 5% of final value in 5 s or less.
b) V_z command:	
Rise time criterion	Amplitude >90% of final value within 2 s.
Overshoot criterion:	Overshoot <5% of final value for $0 < V_x < 10$ kt.
	Overshoot <0.5 V_x% of final value for $10 < V_x < 40$ kt.
	Overshoot <0.5 V_x% of final value for $10 < V_x < 40$ kt.
	Overshoot <20% of final value for $V_x > 40$ kt.
c) Minimal cross-axis response	

TABLE 2. -SENSORS FOR VALT RESEARCH AIRCRAFT

Sensor	Variable measured	Dynamic model	Location with respect to c.g.			Dynamic range
			x(in.) (m)	y(in.) (m)	z(in.) (m)	
Accelerometer	a_x, a_y, a_z	$\frac{1}{1.005s + 1}$	10 (0.254)	0 (0)	-20 (-0.508)	±0.5g (±4.9 m/s^2)
Angular rate gyro (3)	p, q, r	$\frac{(100)^2}{s^2 + 2(0.65)(100)s + (100)^2}$	-110 (-2.8)	20 (0.508)	30 (0.762)	±30° (±0.52 rad)
Vertical gyro: Pitch Roll	 θ ϕ	1	-110 (2.8)	20 (0.508)	30 (0.762)	 ±30° (±0.52 rad) ±45° (±0.78 rad)
Gyromagnetic compass	ψ	$\frac{(100)^2}{s^2 + 2(0.65)(100)s + (100)^2}$	Not specified			0 to 360° (0 to 6.28 rad)
Instantaneous vertical speed indicator (IVSI)	$\dot{z}$	$\frac{1}{\tau s + 1}$	Not specified			±200 kt (±103 m/s)
Barometric altimeter	h	$\frac{1}{0.07s + 1}$	Pressure ports at			0 to 5000 ft (0 to 1524 m)
			280 (7.11)	40 (1.016)	-10 (-0.254)	
Calibrated airspeed	-	$\frac{1}{0.025s + 1}$	Aircraft nose			50 to 200 kt (25.74 m/s to 103 m/s)

SECTION 4
MODELS AND SIMULATION

CH-47 Model

The helicopter model used for analysis and design consists of linear differential equations and a corresponding set of stability derivatives.

The tables of stability derivatives are taken from Appendix E (pp. 85-93) of ref. 4.[4] They were used to define 99 flight conditions. These are numbered consecutively such that each flight condition corresponds to a column of Table E2. The state vector, x, and the control vector, δ, for the model are defined below:

State Vector	Control Vector	
u	δ_B	differential collective
v	δ_C	collective
w	δ_S	cyclic
p	δ_R	differential cyclic
q		
r		
ϕ		
θ		
ψ		

---

[4] Ostroff, A. J., Downing, D. R., and Root, W. J., "A Technique Using a Nonlinear Helicopter Model for Determining Trims and Derivatives," NASA TN D-8159.

For control design purposes, the model was decoupled into separate longitudinal and a lateral-directional models. For the pitch-axis model, the u and v velocities were rotated to earth-referenced coordinates, x and z. This was done to permit direct evaluation of guidance command responses. The variables, control inputs, and guidance commands are given in Table 3.

TABLE 3. -CH-47 VARIABLES

Parameter	Pitch model	Lateral-directional model
Variable	V_x V_z q θ	V p r ϕ
Control	δ_B δ_C	δ_S δ_R
Command	θ V_z	ϕ ψ

Each of the uncoupled models is represented by a linear model in the usual form

$$\dot{x} = Ax + B\delta$$

Thirty-three trim points (flight conditions) were selected for design and analysis purposes. These 33 flight conditions cover the range of the CH-47's operating envelope shown in Figure 3.

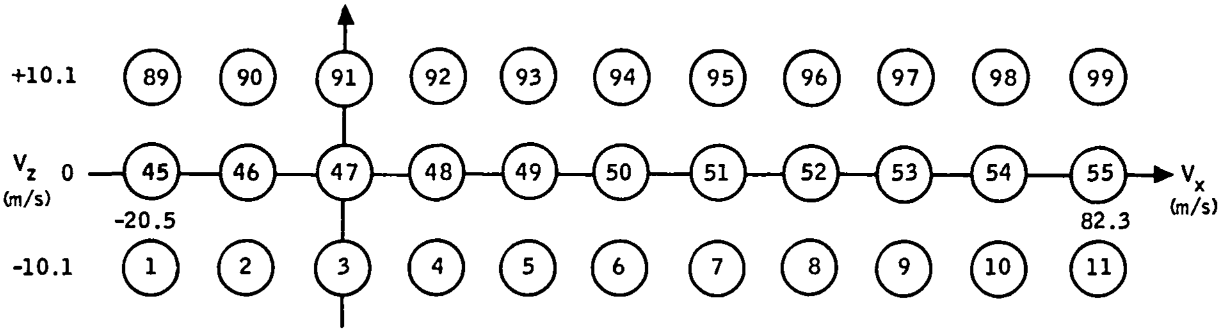

Figure 3. -CH-47 flight conditions.

Actuator and Rotor Models

The rotor and actuator model used for design is shown in Figure 4. This configuration evolved from the CH-47 TAGS systems as modified for the NASA Langley VALT program. The gain K_1 was introduced to convert any stick deflection into standard CH-47 stick inches compatible with the set of stability derivatives.

Simulations

A digital simulation of the CH-47 was developed for use at Honeywell in designing the adaptive controllers. It operates with a specified sample rate and integrates the differential equations to compute CH-47 time histories in response to commands and/or disturbances. The simulation uses constant parameters representing a fixed flight condition. The simulation has the option of representing either longitudinal, lateral-directional, or coupled longitudinal-lateral dynamics.

A random-number generator is used to represent sensor noise, and random sequences shaped by 1-second first-order lag filters are used to represent forward and vertical gusts.

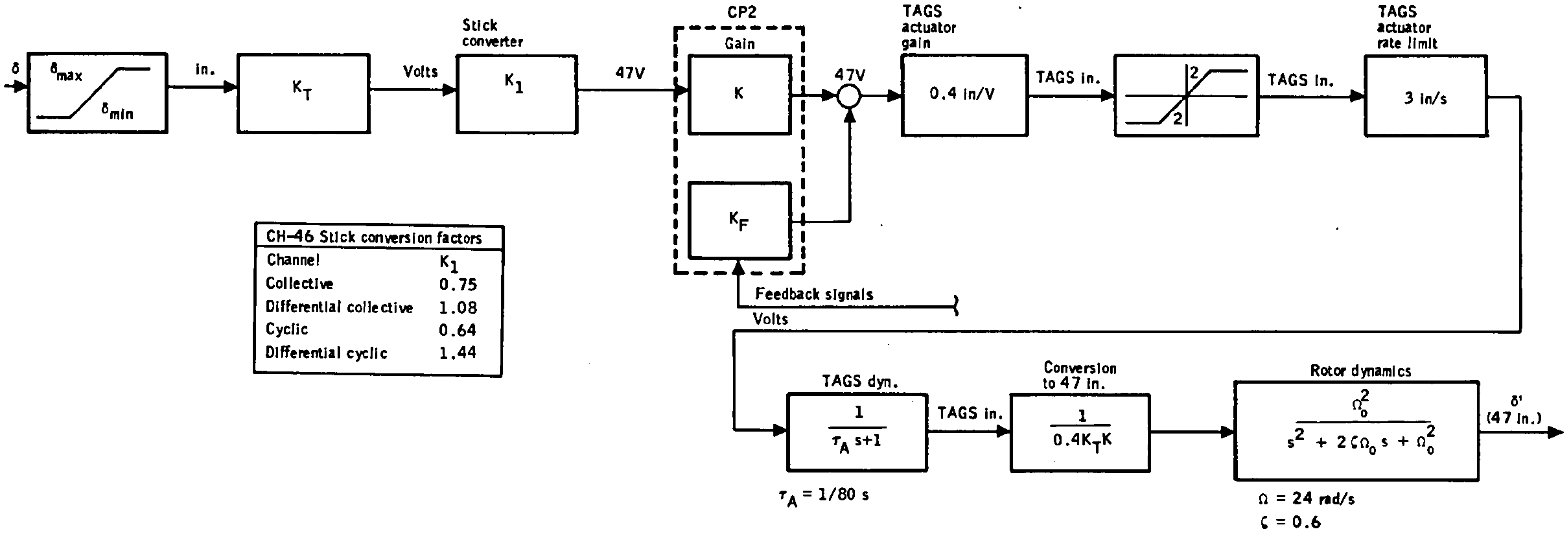

CH-46 Stick conversion factors	
Channel	K_1
Collective	0.75
Differential collective	1.08
Cyclic	0.64
Differential cyclic	1.44

Figure 4. -Model of CH-47 VALT control system for control system design.

The simulation includes the linear model for the rotor dynamics from Figure 4. Rate limiting of the actuator was included, since this nonlinearity tends to affect the stability of command responses and thus is important.

The simulation used for design verification was the nonlinear six-degree-of-freedom VALT simulation at NASA Langley Research Center. It operates in real time on a Control Data CYBER computer and has the capability of interfacing with the actual flight computer.

The control laws designed for this program are described in the next section.

SECTION 5
CONTROL LAW STRUCTURE

A design procedure based on state-variable feedback was used to design the attitude command system. The design procedure uses an algebraic model-following method and includes integral control to eliminate steady-state errors and improve decoupling. Uncoupled controllers were designed for the pitch and lateral-directional axes. Each design is discussed below.

Longitudinal Control

The specified θ attitude response is essentially a second-order response. Consideration of the desired speed of response leads to a requirement for $\omega > 1.3$ rad/s and $\zeta > 0.5$ in a second-order response. The closed-loop pole corresponding to the integral was placed at -0.8, which is sufficiently fast so that the response is dominated by the complex pair of poles. If the integrator pole is moved further left, rate-limiting problems are encountered. A feedforward gain was used to add a zero at -0.8, cancelling the closed-loop integrator pole. Thus, the desired transfer function for a θ command is:

$$\frac{\theta}{\theta_c} = \frac{6\ (s + 0.8)}{(s^2 + 3s + 6)\ (s + 0.8)}$$

Similarly, the first-order V_z response has a desired transfer function:

$$\frac{V_z}{V_{z_c}} = \frac{2\ (s + 1)}{(s + 2)\ (s + 1)}$$

where the feedforward is again used to cancel the closed-loop integrator pole.

The addition of integral control adds two additional states. Thus, the pitch-axis design involves six states and two command inputs:

$$X^T = (V_x, V_z, q, \theta, I_1, I_2)$$

where

$$\dot{I}_1 = V_{z_c} - V_z$$

$$\dot{I}_2 = \theta_c - \theta$$

and

$$U^T = (V_{z_c}, \theta_c)$$

The desired transfer functions can be put in state form:

$$\dot{x} = A_m x + B_m u$$

where x and u are as defined above. This yields:

$$A_m = \begin{bmatrix} - & - & - & - & - & - \\ 0 & -3 & 0 & 0 & 2 & 0 \\ 0 & 0 & -4 & -9 & 0 & 6 \\ 0 & 0 & 1 & 0 & 0 & 0 \\ 0 & 0 & 0 & -1 & 0 & 0 \\ 0 & -0.8 & 0 & 0 & 0 & 0 \end{bmatrix} \qquad B_m = \begin{bmatrix} 0 & 0 \\ 2 & 0 \\ 0 & 6 \\ 0 & 0 \\ 1 & 0 \\ 0 & 0.8 \end{bmatrix}$$

to realize the desired θ and V_z transfer functions. (The first row of A_m has been ignored, since V_x is not being controlled.)

The vehicle model has the form:

$$\dot{x} = Ax + B\delta$$

where the actuator commands (δ) are

$$\delta = K_x x + K_u U$$

The control design task is to specify feedback gains, K_x, and feedforward gains, K_u.

The block diagram is shown in Figure 5.

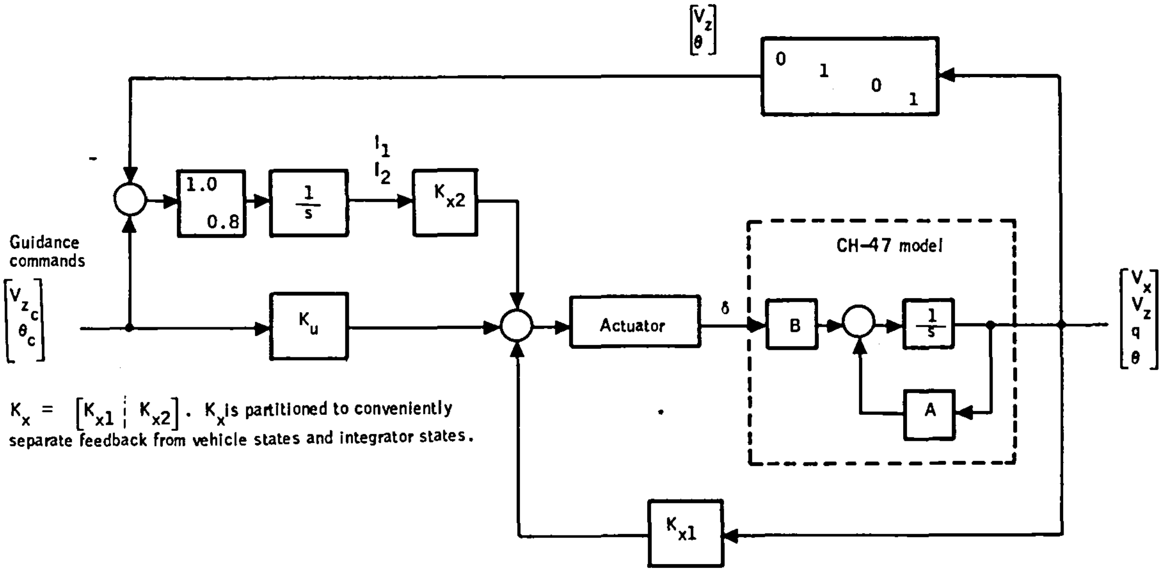

$K_x = [K_{x1} \mid K_{x2}]$. K_x is partitioned to conveniently separate feedback from vehicle states and integrator states.

Figure 5. -Pitch-axis block diagram.

The feedback gains were computed algebraically from

$$K_x = \left[\bar{B}\right]^{-1} \left[\overline{A_m - A}\right] \tag{1}$$

where $\bar{B}$ is a 2 x 2 submatrix containing rows two and three of B, and rows two and three of $A_m - A$ are used (indicated by overbar).

Similarly,

$$K_u = \left[\bar{B}\right]^{-1} B_m \tag{2}$$

The 12 elements of the gain matrix were computed at 33 flight conditions using Equations (1) and (2). The values are plotted in Appendix A. An analysis of the gains indicated they could be made simple functions of V_x. These schedules are given in Table 4 and also plotted in Appendix A. For convenience, the scheduling parameter was defined as forward velocity normalized by its maximum value ($\bar{v}$). Thus, $-0.25 \le \bar{v} \le 1.0$.

Transients responses for θ and V_z commands based on these gain schedules satisfy the specification and exhibit very little cross coupling. Figures 6 and 7 show a representative response and the specification envelope for a V_z and a θ step command, respectively.

Lateral-Directional Axes

A lateral-directional controller was designed for the CH-47 to accept ϕ and ψ guidance commands. The feedback and feedforward gains were computed to provide the desired command responses and to minimize the cross-axis response. The controller incorporates integral control for each command and uses measurements of p, r, ϕ, and ψ in the feedback. The controller outputs are δ_S (cyclic) and δ_R (differential cyclic) commands.

The lateral-directional controller also has the functional block diagram shown in Figure 8, where

$\delta^T = (\delta_S, \delta_R)$ are the actuator commands

$u^T = (\phi_c, \psi_c)$ are command inputs from guidance

$x^T = (v, p, r, \phi, \psi, I_3, I_4)$

and two command error integrators have been appended to the vehicle states:

$$\dot{I}_3 = \phi_c - \phi$$

$$\dot{I}_4 = \psi_c - \psi$$

TABLE 4. -PITCH-AXIS GAIN SCHEDULE

K_x element	Function
(1, 1)	0
(1, 2)	$-0.25\ \bar{v} \quad \bar{v} < 0.5$
	$-0.125 \quad \bar{v} \geq 0.5$
(1, 3)	$-7.6 + 1.5\ \bar{v}$
(1, 4)	$-27 + 6\ \bar{v}$
(1, 5)	$0.14\ \bar{v} \quad \bar{v} < 0.5$
	$0.07 \quad \bar{v} \geq 0.5$
(1, 6)	$17.5 \quad -5\ \bar{v}$
(2, 1)	0
(2, 2)	$0.3 \quad -0.12\ \bar{v}$
(2, 3)	$-1.0\ \bar{v} \quad \bar{v} < 0.5$
	$-0.5 \quad \bar{v} \geq 0.5$
(2, 4)	$-18\ \bar{v}$
(2, 5)	$-0.23 + 0.08\ \bar{v}$
(2, 6)	$2\ \bar{v} \quad \bar{v} < 0.4$
	$1.04 - 0.6\ \bar{v} \quad \bar{v} \geq 0.4$

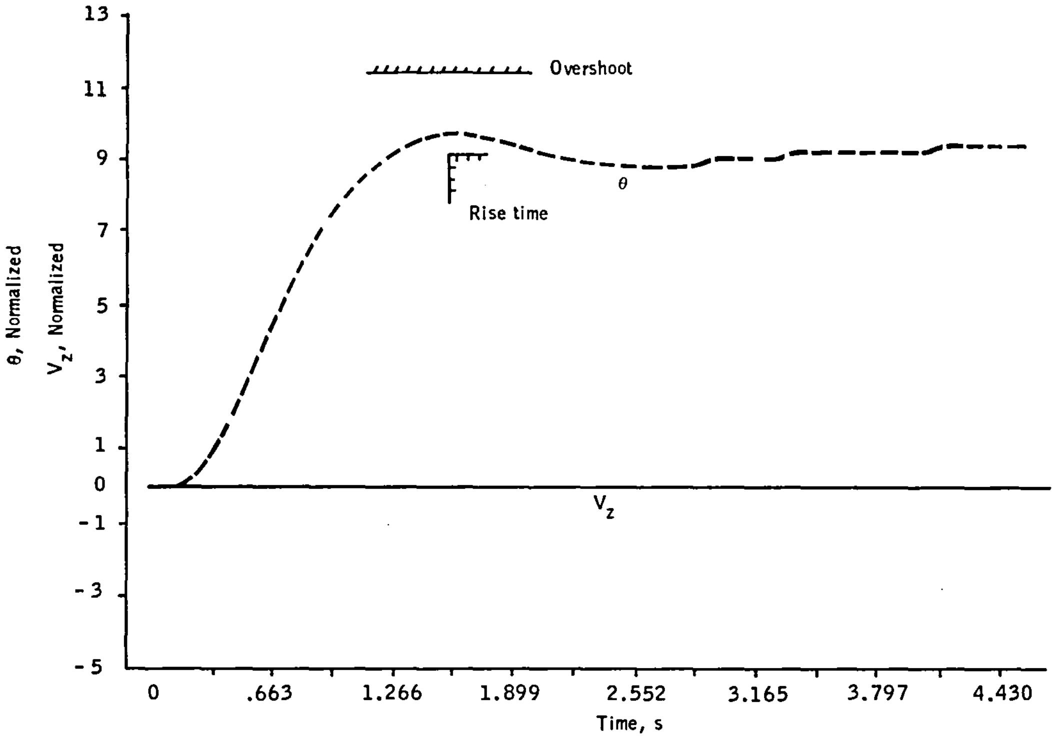

Figure 6.-Typical command response at flight condition 47 for Δθ command.

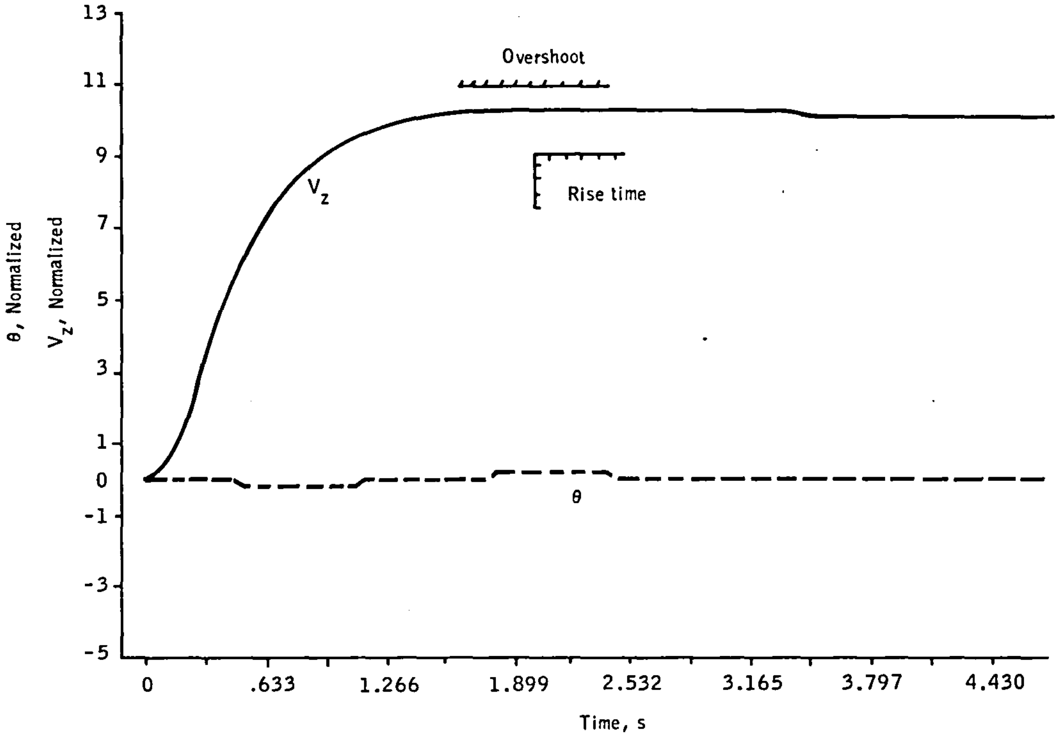

Figure 7.-Typical command response at flight condition 47 for V_z command.

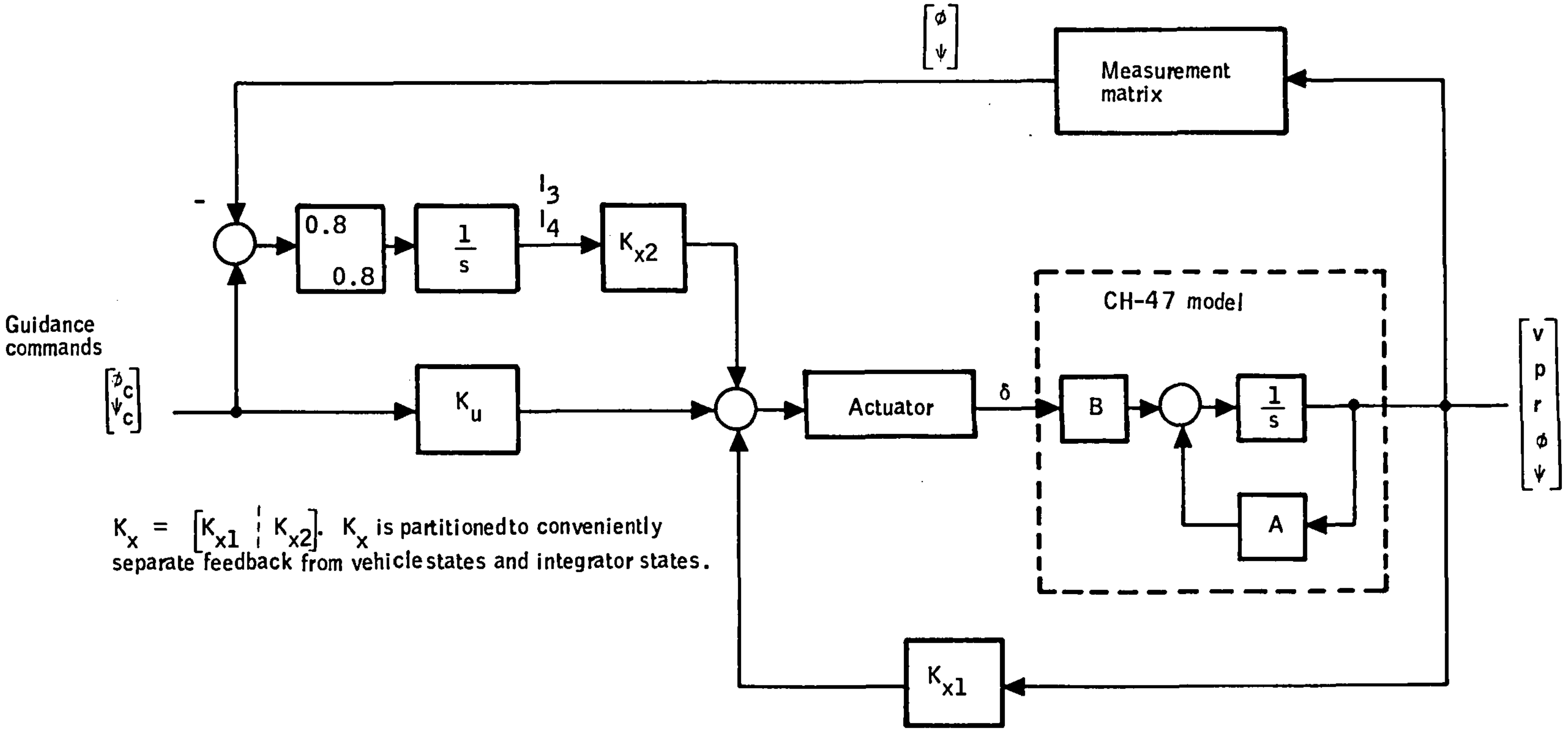

$K_x = [K_{x1} \mid K_{x2}]$. K_x is partitioned to conveniently separate feedback from vehicle states and integrator states.

Figure 8. - Lateral-directional block diagram.

The desired gain values were determined in a manner analogous to the design of the pitch axis. The desired transfer function for ϕ and ψ commands is identical to the θ transfer function. A model with system matrices A_m and B_m was defined that provides uncoupled ϕ and ψ responses that satisfy the transient response specification. The gains were determined by the relations:

$$K_x = [\bar{B}]^{-1}[\overline{A_m - A}]$$

$$K_u = [\bar{B}]^{-1}[B_m]$$

As the CH-47 parameters (A, B) change with flight condition, the desired gain will vary. Appendix B presents a plot of the desired gains for 33 flight conditions covering the CH-47's flight envelope. The gains are defined as:

$$\begin{bmatrix} \delta_S \\ \delta_R \end{bmatrix} = \begin{bmatrix} K_{11} & K_{12} & K_{13} & K_{14} & K_{15} & K_{16} & K_{17} \\ K_{21} & K_{22} & K_{23} & K_{24} & K_{25} & K_{26} & K_{27} \end{bmatrix} \begin{vmatrix} v \\ p \\ r \\ \phi \\ \psi \\ I_3 \\ I_4 \end{vmatrix}$$

where I_3 and I_4 are the command error integrators.

It is worth noting that there is no strong dependence on forward velocity as there was in the pitch axis. The variation of gains over the 33 flight conditions is also rather limited. The major trend in the data seems to be a variation of gains with vertical velocity for forward speeds greater than 41.1 m/s (135 ft/s). This is probably due to similar variations in elements of the B matrix.

As a first design, the 14 gains were held constant over the flight envelope. (Gains on sideslip were set to zero.) The responses to ϕ and ψ commands were evaluated over the flight envelope using a coupled pitch and lateral simulation. The ϕ and ψ responses meet specifications and exhibit minimal cross-axis response even at forward airspeeds greater than 41 m/s. In addition, no interaction was observed between the pitch and lateral-directional controller. Representative ϕ and ψ time histories are contained in Appendix C. A representative response is shown in Figure 9.

It is concluded that fixed lateral gains are completely satisfactory and there is no advantage to adjusting them. Thus, the system recommended for flight test consists of an adaptive pitch controller and a fixed-gain lateral-directional controller.

The next two sections describe details of each of the adaptive algorithms evaluated.

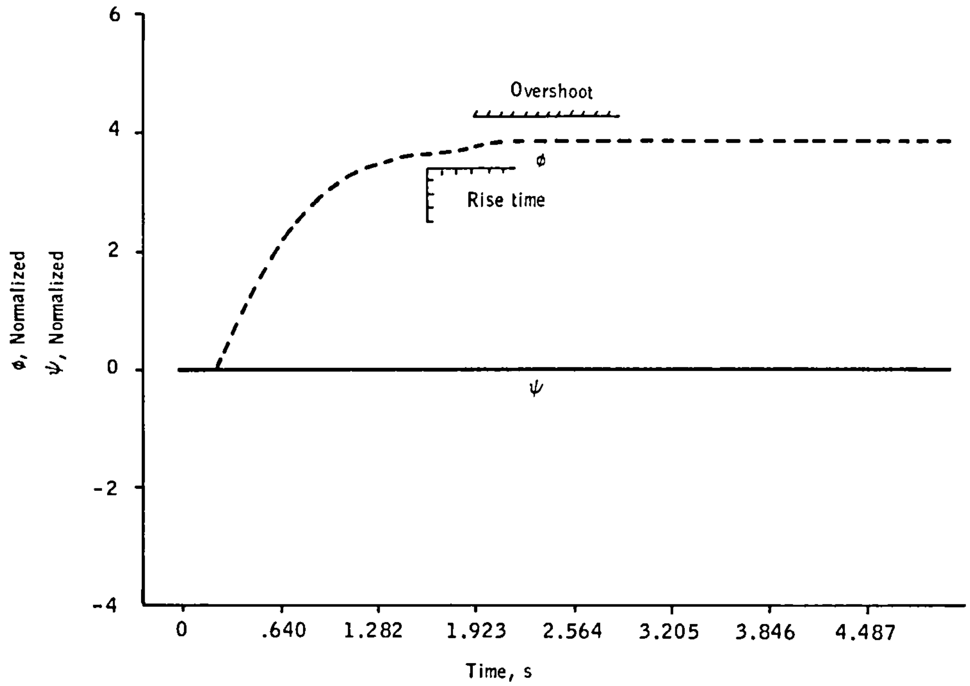

a) ϕ Command

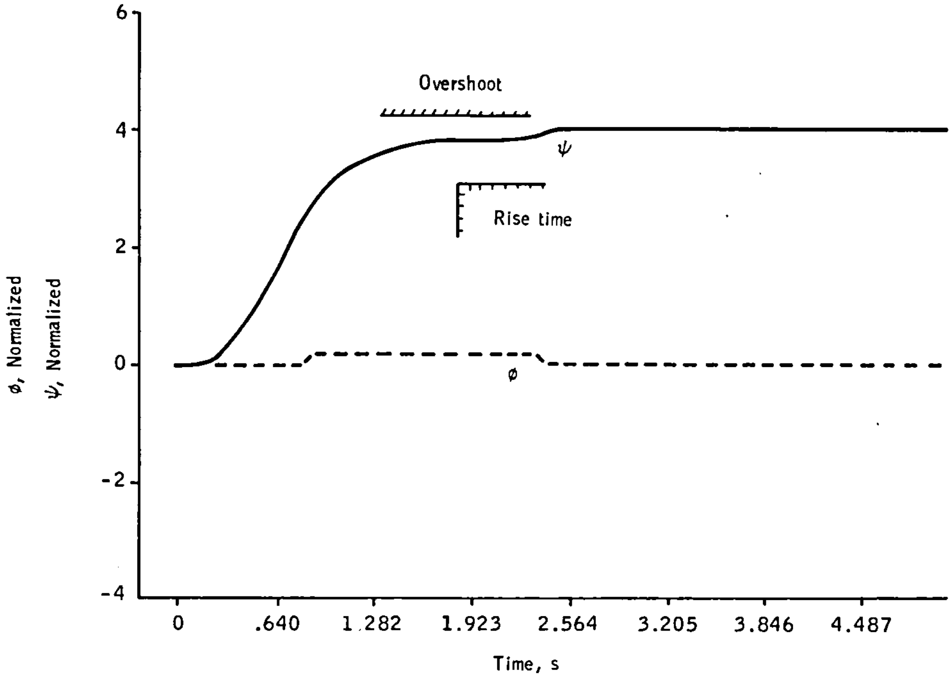

b) ψ Command

Figure 9.-ϕ and ψ Normalized versus time.

SECTION 6
THE MAXIMUM-LIKELIHOOD ALGORITHM

This section presents the design of an explicit parameter estimation algorithm. It was combined with algebraic gain computation to serve as one of the candidate adaptive concepts.

First, a review of the MLE Algorithm is presented, then the design issues are discussed. This is followed by a summary of the simulator performance of the algorithm.

Overview of Algorithm

Parameter uncertainties in aircraft generally take the form of unknown parameters in an otherwise known model structure (i. e., coefficients of linearized equations of motions). Their range of uncertainty is largely due to widely varying flight environments (dynamic pressure, velocity, angle of attack) and configuration variations (center of gravity, fuel, payload). However, the individual coefficients are strongly interrelated and only a few must be known accurately for control law design. The explicit identification problem then is:

Given a continuous plant

$$\dot{x} = A(c)x + B(c)u + \Gamma(c)\xi$$

with discrete measurements

$$Y_i = H(c)x_i + D(c)u_i + \eta_i$$

find the unknown parameter vector, c. The ξ is a white noise process driving gust states and the η_i are sensor measurement noise.

There is a variety of explicit identification methods. If the inputs and outputs of a plant are known, a least-squares equation error is appropriate. If the outputs are noisy, then an output error method will provide unbiased estimates. Finally if the plant has stochastic inputs and noisy measurements, a Kalman filter approach provides unbiased estimates.

If the parameters are modeled as states and the resulting filter is nonlinear, approximations can be implemented (see ref. 5 for an aircraft example).[5] If one is interested in the first and second moments, then a maximum likelihood procedure can be used. This approach was attractive because it provides unbiased estimates (in the limit) with random inputs and noisy measurements.

The general process of maximum-likelihood identification is to find parameter estimates which maximize the a posteriori probability distribution for the observed outputs conditioned on the unknowns and the measured inputs; i. e. :

$$\hat{\underline{c}} = \text{Arg}\,\{\max_{\zeta} p(y_1, y_2, \ldots y_n \mid \underline{c} = \zeta; u_o, u_1, \ldots u_{n-1})\}$$

When the unknowns are constant and the plant dynamics are linear, this maximization problem leads to the solution shown in Figure 10.[6] The

---

[5] Gelb, et al., <u>Applied Optical Estimation</u>, The MIT Press, Cambridge, Mass., 1977.

[6] Balakrishnan, A. V., "Identification and Adaptive Control: An Application to Flight Control Systems," J. Optimization Theory and Applications, Vol. 9, No. 3, March 1972.

solution consists of a Kalman filter designed for the true system structure but with parameters equal to an estimate, $\underline{c} = \zeta$. The filter tracks the true system outputs and generates a residual sequence $\{\nu_k = y_k - \hat{y}_k \; k = 1, 2, \ldots\}$. This sequence is accumulated into a likelihood function:

$$L(\zeta, N) \triangleq -\ell n \, (y_1, y_2, \ldots y_n \mid \underline{c} = \zeta; u_o, u_1, \ldots u_{n-1})$$

which is then minimized over the parameter estimate, ζ. At first glance, this solution appears ideal for onboard applications. The Kalman filter is relatively simple and runs recursively, processing data samples as they appear. The same is true for the likelihood accumulation operation. The difficulty, of course, is the last step of the solution: the minimization. This requires repeated or parallel processing through the data and adds significantly to computational complexity. Two algorithms were considered for the likelihood minimization operation: 1) iterative Newton-Raphson calculations, and 2) parallel noniterative calculations.

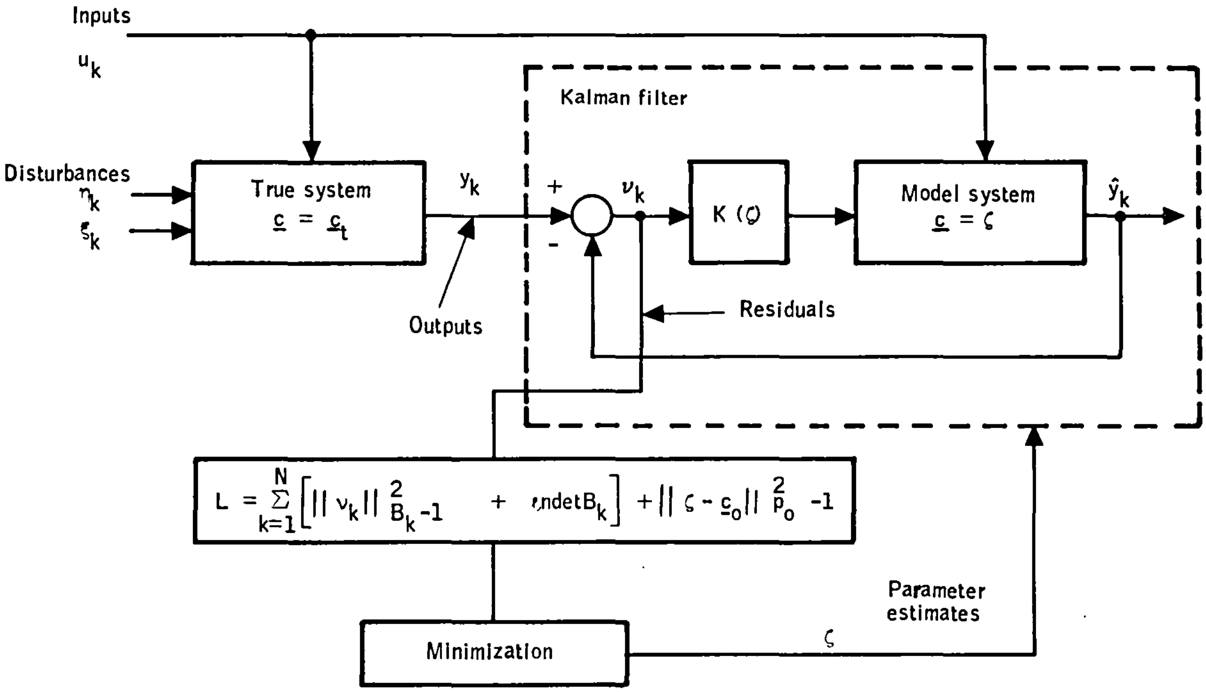

Figure 10. -Maximum-likelihood estimation.

The first algorithm begins by collecting a sequence of input/output data. The Kalman filter is then run with parameters $\underset{\sim}{c}$ equal to a priori estimates, $\underset{\sim}{c} = \zeta^o = \underset{\sim}{c}_o$. This generates the likelihood function, L. At the same time, a set of sensitivity equations is processed which permits calculation of first- and second-partial derivatives, ∇L and $\nabla^2 L$ (some form of approximation is usually used to simplify equations for the latter). These derivatives are then used to obtain a new parameter estimate using a standard Newton-Raphson formula. The filtering, accumulation, and Newton-Raphson operations are performed repeatedly for the same data set until convergence is achieved. The data set itself is usually kept current by a "sliding window" process. This algorithm has been implemented successfully for various postflight data processing applications.[6]

The second algorithm replaces iterative calculations with parallel ones. The sequence of input/output observations is sent simultaneously to M Kalman filter channels, each with its own sensitivity calculations and likelihood accumulations. The channels are distinguished by their assumed parameter values. Each one operates with a different parameter estimate, $\underset{\sim}{c} = \zeta^{(i)}$, and hence computes, $L^{(i)}$, $\nabla L^{(i)}$, and $\nabla^2 L^{(i)}$ at a different fixed point in parameter space. The likelihood functions at these points are then compared to find the approximate minimum point, and a single Newton-Raphson step is taken from there to estimate the true extremum. As in Algorithm 1, some procedure must generally be added to keep the processed data current. This is done by highpass operations which provide exponential de-weighting of past accumulated data samples. General parallel estimation structures have been suggested in several references.[7,8]

---

[7] Stein, G. and Saridis, G. N., "A Parameter Adaptive Control Technique," Automatica, Vol. 5, pp. 731-739, 1969.

[8] Lainiotis, D. G., "Optimal Adaptive Estimation: Structure and Parameter Adaptation," IEEE Trans. Auto. Control, Vol. AC-14, No. 2, April 1959.

As criteria for onboard application, the recursiveness and fixed structure of Algorithm 2 make it ideally suited for real-time operation.

Filter, Sensitivity, and Likelihood Equations

The basic data processing equations which must be resolved by each filter channel are summarized in this subsection. They are stated in terms of general symbols corresponding to the following discretized plant equations:

$$x_{k+1} + Ax_k + Bu_k + \Gamma\eta_k$$

$$y_k = Hx_k + Du_k + N\xi_k$$

The matrices A, B, Γ, H, D, and N should all be thought of as dependent functions of the parameter vector $\underset{\sim}{c}$. Then the channel equations are:

- Filter equations:

$$\bar{x}_{k+1} = A\hat{x}_k + Bu_k$$

$$\nu_{k+1} = y_{k+1} - H\bar{x}_{k+1} - D\nu_{k+1}$$

$$\hat{x}_{k+1} = \bar{x}_{k+1} + K_{k+1}\,\nu_{k+1}$$

- Sensitivity equations for each component c_p of $\underset{\sim}{c}$ (derived by differentiating with respect to c_p):

$$\nabla_p\bar{x}_{k+1} = A\nabla_p x_k + (\nabla_p A)x_k + (\nabla_p B)u_k$$

$$\nabla_p\nu_{k+1} = -H\nabla_p\bar{x}_{k+1} - (\nabla_p H)\bar{x}_{k+1} - (\nabla_p D)u_{k+1}$$

$$\nabla_p\hat{x}_{k+1} = \nabla_p\bar{x}_{k+1} + K_{k+1}\,\nabla_p\nu_{k+1} + (\nabla_p K_{k+1})\nu_{k+1}$$

- Filter gains:[2]

$$\bar{P}_{k+1} = A\, P_k\, A + \Gamma\Gamma^T$$

$$B_{k+1} = (H\, \bar{P}_{k+1}\, H^T + N\, N^T)$$

$$K_{k+1} = \bar{P}_{k+1}\, H^G\, B_{k+1}^{-1}$$

$$P_{k+1} = \bar{P}_{k+1} - K_{k+1}\, H\, \bar{P}_{k+1}$$

- Likelihood accumulation:

$$L_{k+1} = \mu L_k + 1/2\, [\,|\,|\nu_{k+1}|\,|^2\, B_{k+1}^{-1} + \ell\, n\, \det B_{k+1}]$$

$$\nabla L_{k+1} = \mu \nabla L_k + \nabla \nu_{k+1}^T\, B_{k+1}^{-1}\, \nu_{k+1}$$

$$+\, 1/2\ \mathrm{Trace}\ (\nu_{k+1}\nu_{k+1}^T - B_{k+1})\ \nabla(B_{k+1}^{-1})$$

$$\nabla^2\, L_{k+1} \doteq \mu \nabla^2 L_k + \nabla \nu_{k+1}^T\, B_{k+1}^{-1}\, \nabla \nu_{k+1}$$

with $\mu = \exp\,(-\Delta t/\tau)$ for exponential deweighting of past data. The choice of τ is discussed in this section.

These equations warrant two explanatory comments. First, there are no sensitivity equations for the filter gains. This is because the matrix ∇K was computed by numerical differentiation throughout the design program; i.e.:

$$\nabla_p K = [K(\underline{c} + \lambda_p e_p) - K(\underline{c})]\lambda_p$$

where e_p is a unit vector in the ith coordinate direction and λ_p was chosen small compared to the range of c_p.

Second, since $\nabla^2 L$ includes approximations, all second-partial derivatives and products of derivatives have been ignored. This is a common approximation for so-called modified Newton-Raphson procedures and has the important advantage of eliminating second-partial derivative sensitivity equations. It is also common practice to eliminate the last term of the ∇L equation and to replace the filter gain equations with their steady-state solutions.

Parameterization

The CH-47 model was parameterized for several reasons:

- Some "structure" must be imposed on the model if the identification is to work at all. If each of the elements of the A and B matrix are treated as independent variables, one simply cannot learn much by processing 5 to 10 seconds of data.
- Real-time computing constraints demand that only a limited number of parameters be identified. With a software structure like PCMLE, the computer time and memory required grow linearly with the number of parameters we try to estimate.
- From a control viewpoint, only a few "dominant" characteristics are important for adjusting the control law. For the CH-47, as shown in Section 5, the $\bar{v}$ parameter turns out to be the most important factor for this function.

The CH-47 pitch axis model was parameterized by expressing all the A and B elements in terms of the $\bar{v}$ parameter plus individual perturbations to this function. The initial uncertainty was estimated from the range of the parameters over the flight envelope. Identifiability then indicates how much reduction in the initial uncertainty can be expected by processing practical amounts of sensor data from a physically realistic noisy environment.

Plots of the longitudinal model coefficients are contained in Appendix D for 33 flight conditions that completely cover the CH-47's operating envelope. The parameters are plotted against forward airspeed (-20.5 to +82.3 m/s) for three values of vertical velocity (-10.0 m/s, 0, and +10.3 m/s). Each of these 18 model parameters was characterized in a manner analogous to the F-8 Adaptive Study.[2] Parameters showing a strong dependence on normalized forward airspeed ($\bar{v}$) were made a function of $\bar{v}$ plus a perturbation parameter c_i. If the parameter didn't show a $\bar{v}$ dependence it was defined as a constant (which could be zero) plus the perturbation quantity. This method of parameterization is used to reduce the initial parameter uncertainty. The parameterization being used is given in Table 5 and is also plotted in Appendix D. A model based on this parameterization was used in the following identifiability analyses.

Identifiability Analysis

The design issues are primarily resolved with an "identifiability analysis." A linear system identification problem is formulated to estimate a parameterized model from closed-loop input/output records generated by a simulation. As shown in the literature,[9] the theoretical accuracies attainable are bounded from below by the "Fisher information matrix." Thus, this matrix is computed for various operational situations and its accuracy bounds are used to structure the identifier.

The model shown in Figure 11 was used for the pitch-axis identifiability analysis. This model includes first-order gusts models for forward and vertical gusts. The bandwidth of each gust process is one rad/s.

---

[9] Tse, E., "Information Matrix and Local Identifiability of Parameters," JACC, Columbus, Ohio, 1973.

TABLE 5. -CH-47 PARAMETERIZATION

Function	RMS c_i
$a_{11} = -0.018 - 0.034\,\bar{v}^2 + c_2$	0.0045
$a_{12} = 0.048\,\bar{v}^2 + c_3$	0.009
$a_{13} = 2.8 + c_4$	0.4
$a_{14} = -32.2 + (14 + c_5)\,\bar{v}^2$	3.0
$a_{21} = (0.18 + c_6)\,\frac{(\lvert\bar{v}\rvert - 0.75)}{0.75}\ \mathrm{sgn}\,\bar{v}$	0.04
$a_{22} = -0.5 + c_7$	0.25
$a_{23} = c_8$	1.6
$a_{24} = -180\,\bar{v} + c_9$	10.0
$a_{31} = c_{10}$	0.02
$a_{32} = 0.02\,\bar{v} + c_{11}$	0.006
$a_{33} = -1.5 + c_{12}$	0.25
$a_{34} = 4\,\lvert\bar{v}\rvert + c_{13}$	0.5
$b_{11} = 0.12 + c_{14}$	0.06
$b_{12} = C_{15}$	0.3
$b_{21} = 0.70\,\bar{v} + c_{16}$	0.25
$b_{22} = -7.8 - 3\,\bar{v} + c_{17}$	0.8
$b_{31} = 0.35 + 0.12\,\bar{v} + c_{18}$	0.05
$b_{32} = 0.24\,\bar{v} + c_{19}$	0.08

$$\frac{d}{dt}\begin{bmatrix}\dot{X}_T\\ \dot{Z}_T\\ q\\ \theta\\ \dot{X}_g\\ \dot{Z}_g\end{bmatrix} = \begin{bmatrix} a_{11} & a_{12} & a_{13} & a_{14} & -1 & 0\\ a_{21} & a_{22} & a_{23} & a_{24} & 0 & -1\\ a_{31} & a_{32} & a_{33} & a_{34} & 0 & 0\\ 0 & 0 & 1 & 0 & 0 & 0\\ 0 & 0 & 0 & 0 & -1 & 0\\ 0 & 0 & 0 & 0 & 0 & -1\end{bmatrix}\begin{bmatrix}\dot{X}_T\\ \dot{Z}_T\\ q\\ \theta\\ \dot{X}_g\\ \dot{Z}_g\end{bmatrix} + \begin{bmatrix} b_{11} & b_{12}\\ b_{21} & b_{22}\\ b_{31} & b_{32}\\ 0 & 0\\ 0 & 0\\ 0 & 0\end{bmatrix}\begin{bmatrix}\delta_B\\ \delta_C\end{bmatrix} \begin{bmatrix}\sqrt{2\sigma_1} & 0\\ 0 & \sqrt{2\sigma_2}\\ 0 & 0\\ 0 & 0\\ \sqrt{2\sigma_1} & 0\\ 0 & \sqrt{2\sigma_2}\end{bmatrix}\begin{bmatrix}\eta_1\\ \eta_2\end{bmatrix}$$

$$\begin{bmatrix}Y_1\\ Y_2\\ Y_3\end{bmatrix} = \begin{bmatrix} 0 & 1 & 0 & 0 & 0 & 0\\ 0 & 0 & 0 & 0 & 1 & 0\\ 0 & 0 & 0 & 0 & 0 & 1\end{bmatrix}\begin{bmatrix}\dot{X}_T\\ \dot{Z}_T\\ q\\ \theta\\ \dot{X}_g\\ \dot{Z}_g\end{bmatrix} + \begin{bmatrix}\xi_1\\ \xi_2\\ \xi_3\end{bmatrix}$$

Figure 11. -CH-47 model for identifiability analysis.

For the majority of the analysis, the sensor rms noise magnitudes were selected as:

σ_{V_z} = 1.3 m/s

σ_q = 0.0026 rad/s

σ_θ = 0.017 rad

The CH-47 was modeled with $\bar{v}$ as a dominant parameter plus smaller perturbation parameters yielding 19 parameters. Adding two parameters for X and Z gust intensity plus the six initial conditions on the state results in a total of 27 longitudinal parameters.

The identification problem was then formulated to estimate these parameters from closed-loop input (δ_B, δ_c) and output V_z, q, θ) time histories. For the majority of runs, 5 seconds of data were used.

Qualitative characteristics of the identifiability analysis are given in Table 6. The results basically show that under most conditions about five to nine of the perturbation parameters can be identified (parameter uncertainty reduced by at least a factor of two). The quality of the identification does not vary much with flight condition. The gust levels can be estimated only when they dominate command and sensor noise effects. (This was observed on F-8 also.)

Assuming reduced sensor noise does not dramatically change the results, note that for many of the model parameters, knowledge of $\bar{v}$ yields a good estimate. The perturbation parameters with very small uncertainties are not important. Experiments with estimating a subset of seven parameters have shown little degradation in their accuracy due to the parameters not being estimated (also observed on F-8).

In our initial identifiability analyses, most of the data used both $\Delta\theta$ and ΔV_z commands and predicted accuracy results were good. However, when ΔV_z commands only are used, the predictions get substantially poorer, particularly when reduced-parameter identification is attempted. Results for this ΔV_z-only case are presented below.

Figure 12 shows the reduction in the $\bar{v}$ uncertainty using 5 seconds of data containing ΔV_z commands only. The reduction is shown as a function of the parameter set identified. Even with all the parameters estimated, the theoretical bound is $\sigma = 0.15$, which is not too good. Our baseline parameter set has $\sigma = 0.3$, and a better four-parameter set for V_z commands would give $\sigma = 0.17$, which is nearly as good as estimating all the parameters.

TABLE 6. -SUMMARY OF PITCH-AXIS IDENTIFIABILITY

Flight condition	Command	RMS gusts	Sensor noise	Number of paramested estimated	Parameters identified	Comments
55	$\Delta\theta = 10°$	0	No	All	$\bar{v}$, a_{31}, a_{33}, b_{31}, b_{32}	Command is doublet with 4-sec period.
55	$\Delta V_z = 10$ ft/s	0	No	All	$\bar{v}$, a_{22}, (a_{32}), b_{31}, b_{32}	Command is doublet with 4-sec period.
55	$\Delta\theta = 10°$ $\Delta V_z = 10$ ft/s	$u_g = 1$ ft/s $w_g = 1$ ft/s	Yes	All	$\bar{v}$, (a_{22}), a_{31}, a_{32}, a_{33}, b_{31}, b_{32}	Commands push gust estimate to lower than actual value.
55	$\Delta\theta = 10°$ $\Delta V_z = 10$ ft/s	$u_g = 1$ ft/s $w_g = 1$ ft/s	Yes	7 identified above	$\bar{v}$, a_{31}, a_{32}, a_{33}, b_{31}, b_{32}	a_{22} and a_{31} degraded when subset estimated; a_{31} still improves.
55	$\Delta\theta = 10°$ $\Delta V_z = 10$ ft/s	$u_g = 1$ft/s $w_g = 1$ ft/s	Yes	All	$\bar{v}$, (a_{33}), b_{31}, b_{32}	Only 1 s of data used. Response on $\bar{v}$, b_{31}, b_{32} is very fast.
55	$\Delta\theta = 10°$ $\Delta V_z = 10$ ft/s	$u_g = 1$ ft/s $w_g = 1$ ft/s	No	All	$\bar{v}$, (a_{22}), a_{31}, a_{32}, a_{33}, b_{31}, b_{32}	Gust estimates go even closer to zero than row 3.
55	$\Delta\theta = 1°$ $\Delta V_z = 1$ ft/s	$u_g = 1$ ft/s $w_g = 1$ ft/s	No	All	$\bar{v}$, (a_{31}), (a_{33}), b_{31}, b_{32}	$A_z = 0.06$g rms $\theta = 0.75°$ rms $V_z = 0.8$ ft/s rms
55	None	$u_g = 1$ ft/s $w_g = 1$ ft/s	Yes	All	$(\bar{v})$, a_{31}	$A_z = 0.047$ g rms $\theta = 0.025°$ rms $V_z = 0.55$ ft/s rms
55	Random $\Delta\theta$ Random ΔV_z	0	No	All	$(\bar{v})$, b_{31}, (b_{32})	$A_z = 0.05$g rms $\theta = 0.083°$ rms $V_z = 0.17$ ft/s rms Note lower bandwidth of V_z and θ loops results in less excitation with random inputs.
55	Amplitude doubled from above	0	No	All	$\bar{v}$, (a_{33}), b_{31}, b_{32}	More low-frequency test signal would be better.
5	$\Delta\theta = 10°$ $\Delta V_z = 10$ ft/s	$u_g = 1$ ft/s $w_g = 1$ ft/s	Yes	All	$\bar{v}$, (a_{22}), a_{31}, a_{32}, (a_{33}) (a_{34}), (b_{22}), b_{31}, b_{32}	Doublet commands compare with row 3 (Fc 55)
93	$\Delta\theta = 10°$ $\Delta V_z = 10$ ft/s	$u_g = 1$ ft/s $w_g = 1$ ft/s	Yes	All	$\bar{v}$, a_{22}, a_{31}, (a_{32}), a_{33} (a_{34}), (a_{22}), b_{31}, b_{32}	Doublet commands compare with row 3 (Fc 55).
47	$\Delta\theta = 10°$	No	No	All	$\bar{v}$, a_{31}, (a_{33}), (a_{34}), b_{31}	Doublet commands
47	$\Delta V_z = 10$ ft/s	No	No	All	$\bar{v}$, a_{22}, (a_{23}), a_{32}, b_{21}, b_{22}, b_{32}	Doublet commands
47	$\Delta\theta = 10°$ $\Delta V_z = 10$ ft/s	$u_g = 1$ ft/s $w_g = 1$ ft/s	Yes	All	$\bar{v}$, (a_{22}), a_{31}, a_{32}, a_{33}, (a_{34}) , (b_{22}), b_{31}, b_{32}	Doublet commands
47	$\Delta\theta = 10°$ $\Delta V_z = 10$ ft/s	$u_g = 10$ ft/s $w_g = 10$ ft/s	Yes	All	Same as above plus u and w gust intensity	Doublet commands

( ) Indicates improvement in initial uncertainty but by less than a factor of two.

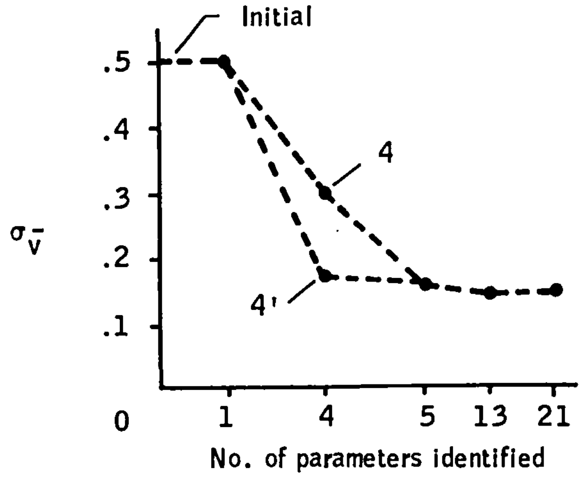

Fc 51 (80 kt)
$\Delta V_z = 10$ ft/s doublet
5 s of data
No gusts or sensor noise

Parameter sets

1 = $\bar{v}$
4 = $\bar{v}$, a_{33}, b_{31}, b_{32} (baseline set)
4' = $\bar{v}$, a_{32}, b_{31}, b_{32}
5 = $\bar{v}$, a_{32}, a_{33}, b_{31}, b_{32}
13 = $\bar{v}$, a_{12}, a_{22}, a_{31}, q_{33}, a_{34}, b_{21}, b_{22}, b_{31}, b_{32}, u_g, w_g

Figure 12. -Theoretical 1-sigma accuracy in $\bar{v}$ as function of parameter set estimated.

Subsequent analysis of the likelihood function indicated that the pitch rate residuals are heavily weighted. Much of the identification is therefore based on the pitching moment response. For ΔV_z responses, the coupling term a_{32} is important. Figure 13 shows the influence of this parameter on $\bar{v}$ accuracy for the baseline set of four parameters. (This confirms the difference between set 4 and 4' in Figure 12).

On the basis of Figure 12, several runs were made with the PCMLE algorithm modified to estimated a_{32} rather than a_{33}. There was no improvement in the estimate for the V_x = 135 ft/s flight condition, although (theoretically) the 1-sigma accuracy bound is smaller. If the A and B matrices correspond to the parameterization, then $\bar{v}$ is correctly estimated. A number of experiments with varying elements of the A and B matrices lead to the conclusion that errors in parameters not estimated shift the minimum of the likelihood function from the correct value of $\bar{v}$. Furthermore, this effect is not caused by one or two parameters but is the effect of all the parameters contributing to the uncertainty of $\bar{v}$.

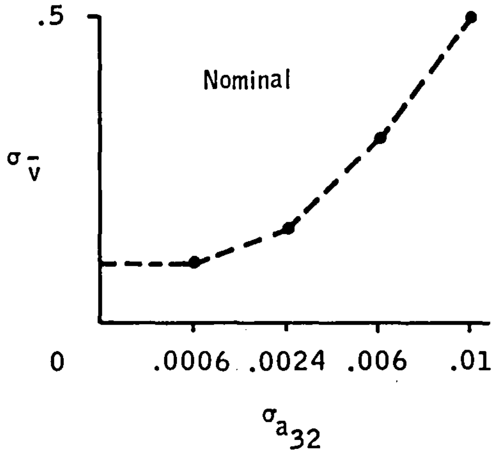

Figure 13. -Uncertainty in $\bar{v}$ as a function of uncertainty in a_{32} model coefficient (four-parameter identification, V_z commands).

For comparison, Figure 14 shows the reduction in $\bar{v}$ uncertainty with $\Delta\theta$ doublets (no gusts or sensor noise). The baseline set of four has $\sigma = 0.12$ compared with $\sigma = 0.075$ for estimating all the parameters. Set 4', which looked better with V_z commands, does not perform as well as the baseline set for $\Delta\theta$ commands.

Finally, Figure 15 shows that the theoretical accuracy level is relatively constant over the flight envelope.

Analysis of Likelihood Function Contours

An important aspect of MLE parameter estimation concerns the shape of the likelihood function away from the correct parameter values. This significantly influences the region of parameter space that can be estimated from any given channel.

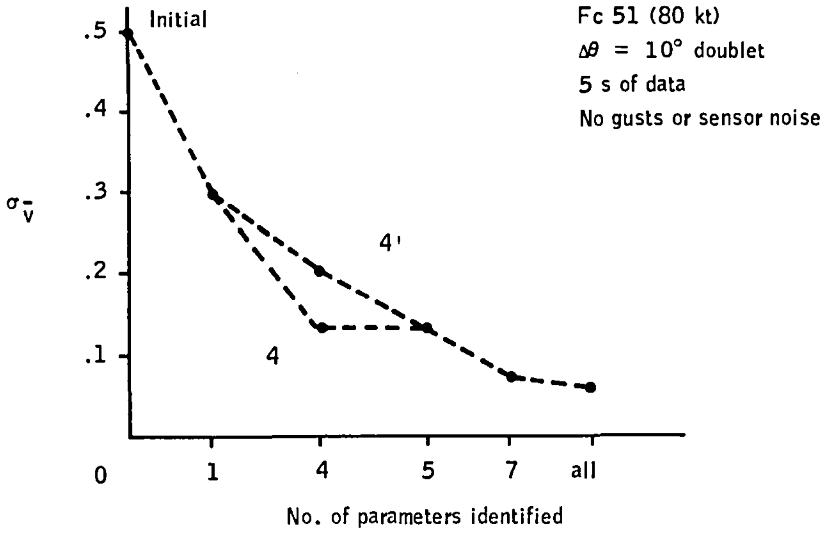

Parameter sets

1 = $\bar{v}$
4 = $\bar{v}, a_{33}, b_{31}, b_{32}$
4' = $\bar{v}, a_{32}, b_{31}, b_{32}$
5 = $\bar{v}, a_{32}, a_{33}, b_{31}, b_{32}$
7 = $\bar{v}, a_{31}, a_{32}, a_{33}, a_{34}, b_{31}, b_{32}$

Figure 14. -Theoretical 1-sigma accuracy in $\bar{v}$ as function of parameter set measured.

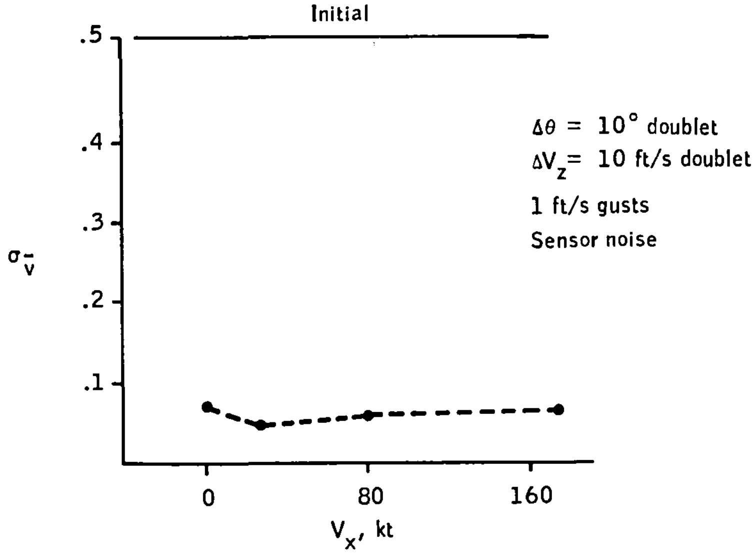

Figure 15. -Theoretical uncertainty level for estimating all parameters as a function of flight condition.

Representative contours produced by the initial filter designs are shown in Figure 16. The major problem is near hover. Here a very sharp notch results because the filter has the forward and vertical gust states decoupled from q and θ states at hover. This problem was remedied by redesigning the filter. Figure 17 shows PCMLE estimates from simulation data based on our $\bar{v}$ parameterization of the CH-47 pitch axis. Note the minimum occurs at the correct parameter value, the shapes are approximately quadratic, and the gradients computed away from the true parameter point to the correct answer (parameter value corresponding to minimum).

By plotting likelihood functions, it was determined that $\bar{v}$ could not be estimated accurately by minimizing the likelihood function with this single parameter. This effect is shown in Figure 18 which illustrates minimizing only along the $\bar{v}$ direction, assuming the perturbation parameters (c_i) are zero gives an erroneous $\bar{v}$ estimate. Thus, it was found to accurately estimate $\bar{v}$ required estimating three additional parameters. This is discussed further in the next section.

Identifier Design for CH-47

An identifier was developed for the pitch axis in view of the identifiability results and the control requirements for gain adjustment. The identifier uses the parallel minimization algorithm previously discussed. It is based on a reduced parameter set and identifies four parameters -- $\bar{v}$ plus perturbations on B(3, 1), B(3, 2), and A(3, 3) (recall state equations of vehicle). Four state, constant-gain Kalman filters are used. Three filters are used in the baseline configuration to cover the operating envelope.

The major design issues include:

- The identification model
- Channel selection

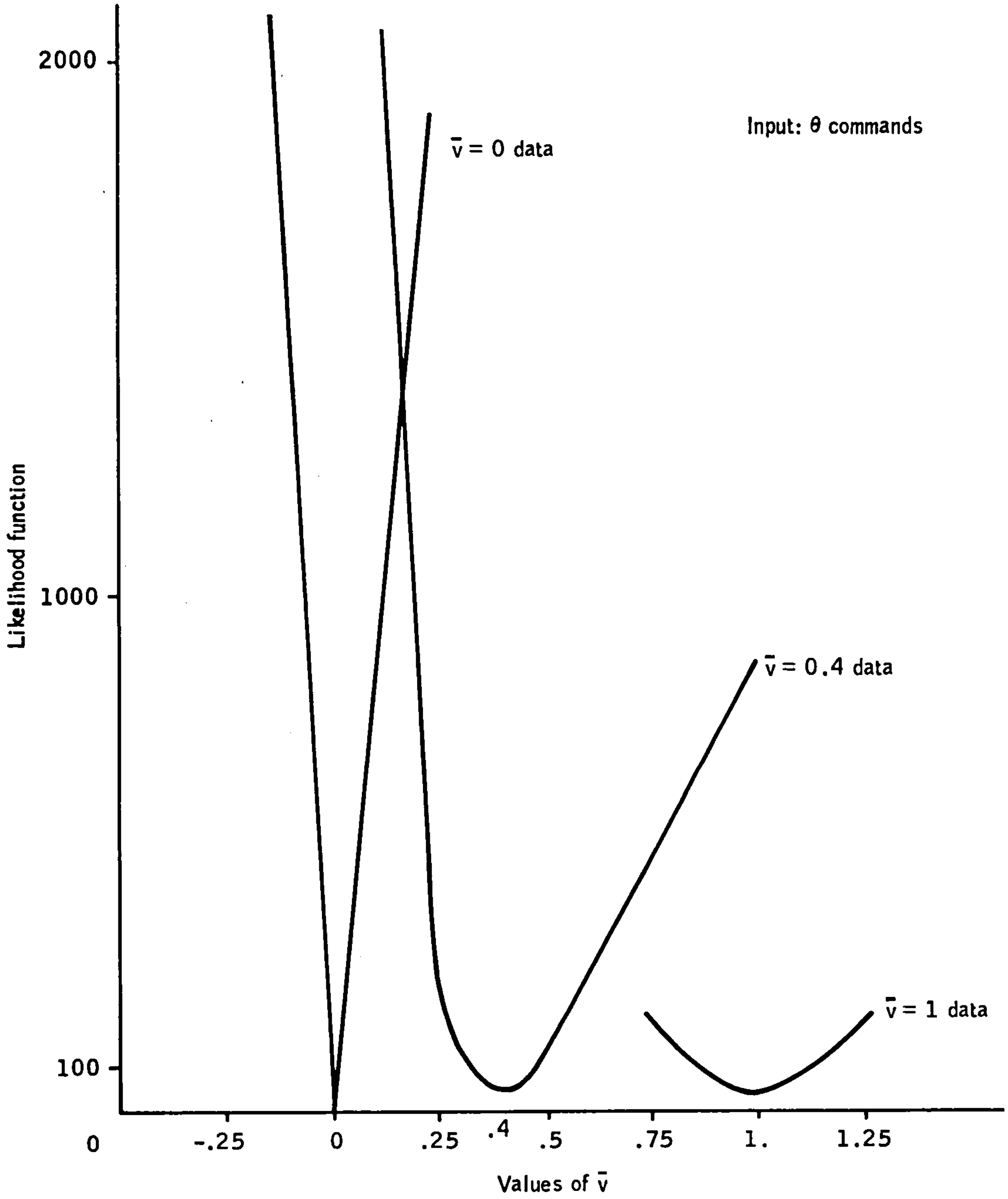

Figure 16. - Likelihood contours from simulation data.

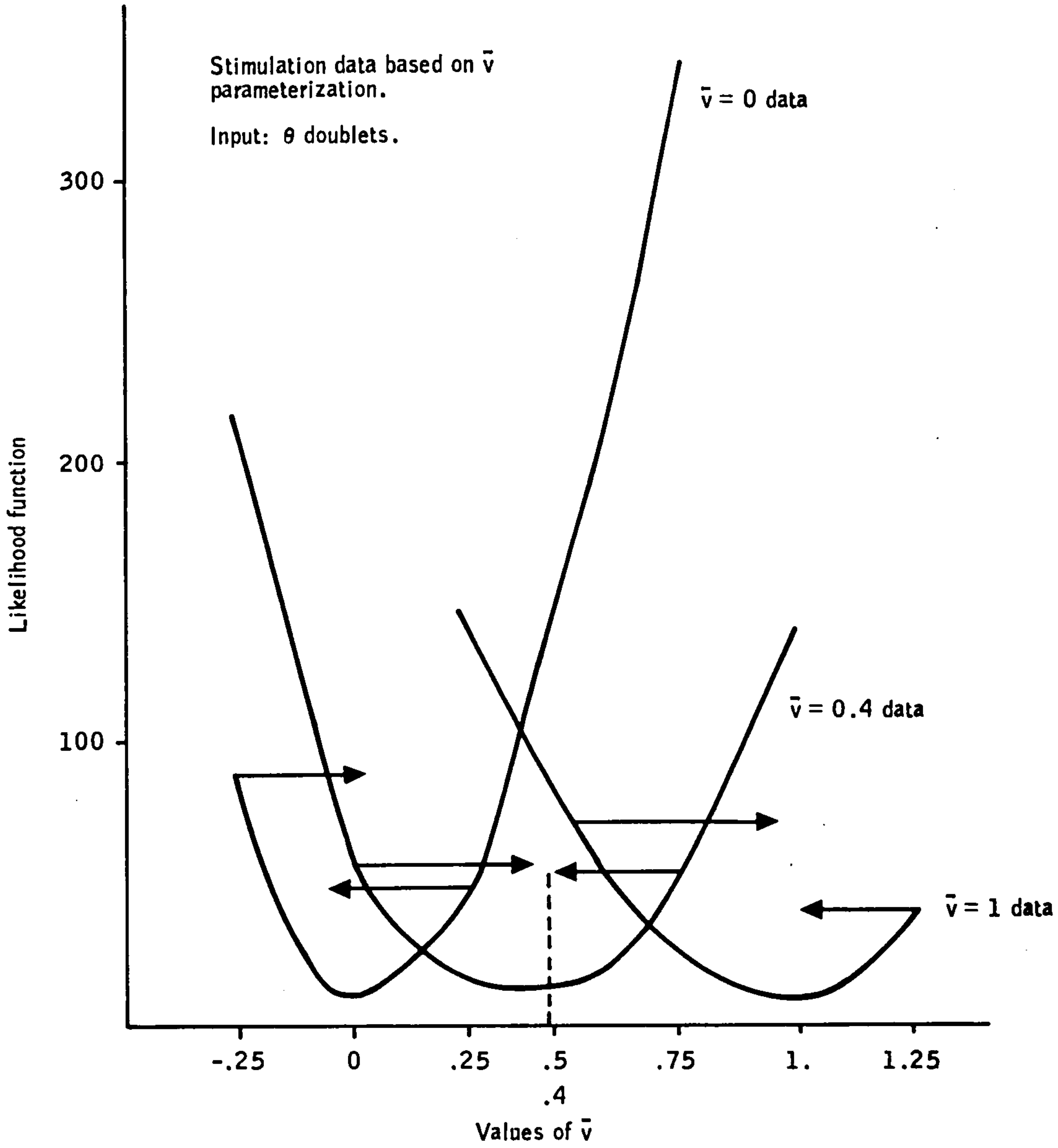

Figure 17. -Modified likelihood contours.

- Kalman filter design
- Adaptation to noise statistics
- Likelihood filters for deweighting old data.

Each of these items will be briefly discussed.

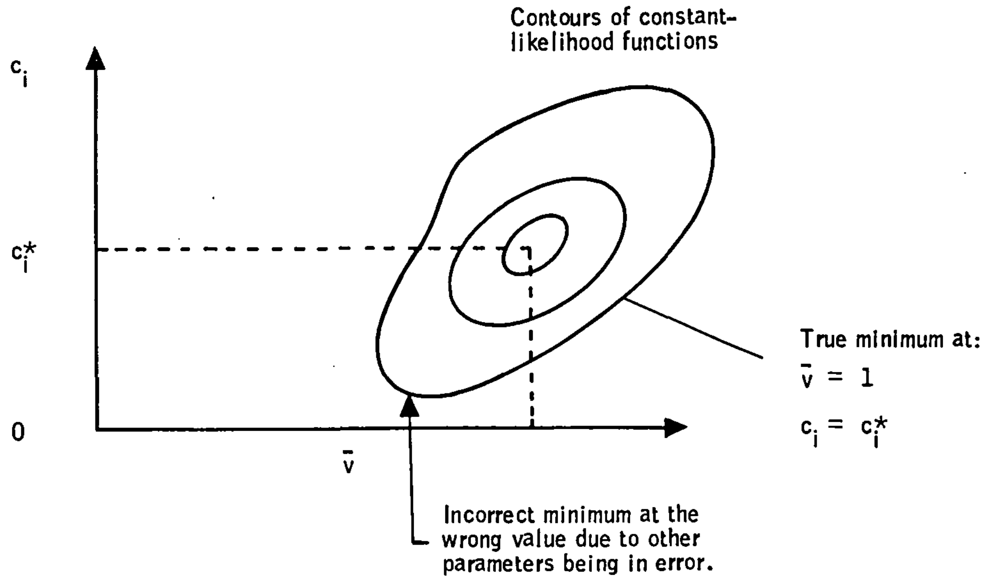

Figure 18. -Multiparameter likelihood contour.

Identification model. -Pitch-axis dynamics are modeled as:

$$\frac{d}{dt}\begin{bmatrix} V_x \\ V_z \\ q \\ \theta \end{bmatrix} = \begin{bmatrix} a_{11} & a_{12} & a_{13} & a_{14} \\ a_{21} & a_{22} & a_{23} & a_{24} \\ 0 & a_{32} & a_{33} & a_{34} \\ 0 & 0 & 1 & 0 \end{bmatrix}\begin{bmatrix} V_x \\ V_z \\ q \\ \theta \end{bmatrix} + \begin{bmatrix} b_{11} & 0 \\ b_{21} & b_{22} \\ b_{31} & b_{32} \\ 0 & 0 \end{bmatrix}\delta + \begin{bmatrix} Y_{11} & 0 & 0 \\ 0 & Y_{22} & 0 \\ 0 & 0 & Y_{33} \end{bmatrix}\eta$$

where the individual elements (a_{ij}, b_{ij}) are parameterized as given in Table 5.

The parameters Y_{11} and Y_{22} represent gust disturbances as defined below.

The Dryden gust spectrum

$$\dot{V}_g = -\frac{V}{L} V_g + \sigma \frac{2V}{L} \eta$$

was approximated by

$$\dot{V}_g \simeq \sigma \frac{2V}{L} \eta$$

A gust model was used in the x and z axes.

The bandwidth of the gust filter was set at 1 second; thus:

$$Y_{11} = \sqrt{2}\ \sigma_{x_g}$$

$$Y_{22} = \sqrt{2}\ \sigma_{z_g}$$

The Y_{33} term was added to improve the shape of the likelihood functions as described previously:

$$Y_{33} = \frac{2}{a_{33}} (0.02\ \sigma_{x_g} + 0.01\ \sigma_{z_g})$$

Measurements were modeled as

$$\begin{bmatrix} V_z \\ q \\ \theta \end{bmatrix} = \begin{bmatrix} 0 & 1 & 0 & 0 \\ 0 & 0 & 1 & 0 \\ 0 & 0 & 0 & 1 \end{bmatrix} \begin{bmatrix} V_x \\ V_z \\ q \\ \theta \end{bmatrix} + \begin{bmatrix} \sigma_{V_z} & 0 & 0 \\ 0 & \sigma q & 0 \\ 0 & 0 & \sigma_\theta \end{bmatrix} \xi_k$$

The sensor noises are modeled as independent and identically distributed random variables. Their magnitudes, σ_{V_z}, σ_q, and σ_θ, as well as the disturbance magnitudes, σ_{x_g}, σ_{z_g}, were treated as design parameters.

The trim values of the states and controls were eliminated from the identification problem by highpassing all the data with a second-order filter. The break frequency was set at 2 rad/s.

Channel selection. -The problem of channel selection is to choose both the number and location of points in parameter space. Some insight into this problem is provided by the shape of the likelihood function away from the true parameter value. The shape and curvature indicate how well interpolation can be done from each channel. Some experimentation with the simulation is also useful in selecting the channels.

The baseline design used three channels spaced at $\bar{v}$ = 0, 0.5, and 1.0, as shown in Table 7.

TABLE 7. -NOMINAL CHANNEL LOCATION

Channel	Parameters in Kalman Filter			
	$c_1(\bar{v})$	$c_2(\Delta a_{33})$	$c_3(\Delta b_{31})$	$c_4(\Delta b_{33})$
1	1.0	-0.045	-0.05	-0.07
2	.5	0	0	0
3	0	0	0	0

Kalman filter design. -According to Algorithm 2, a fixed set of Kalman filter and sensitivity equations must be operated at each set of parameter values. The design of these filters is straightforward, since steady-state gains can be used. Hence, the gains are solved off-line for their steady-state values. Stored values of K and ∇K are used in the on-line identifier.

Adaptation to proportional noise statistics. -We noted in the filter design section that fixed statistics were used to compute filter gains. This is desirable because it generates an invariant set of gains for each channel which can be computed off-line and stored for on-line use. Invariant gains are actually obtained under slightly less restrictive circumstances, namely, when the disturbance and noise statistics remain in constant relationship to one another. This means that a filter for disturbances statistics and sensor noise statistics remains unchanged when both statistics are scaled by the same factor. As a result, the total identification algorithm designed for one set of statistics can still be valid when those statistics are scaled up or down, provided only that the likelihood functions are also scaled. This was done adaptively as described by Hartmann, et al.[2] Assume that all statistics are known to within a constant scale factor, σ. This parameter is estimated and used to scale the likelihood functions before a comparison is made to select the minimum channel.

Likelihood filters. -Highpass filtering of the accumulated likelihoods in each channel keeps the accumulations current by exponentially deweighting past data. The rate at which deweighting occurs (or the choice of time constants for the highpass filter) is determined by two conflicting requirements:

1) A well-defined, correct minimum of the likelihood function requires slow deweighting.

2) Small tracking errors when aircraft parameters change requires fast deweighting.

The first requirement exists because likelihood functions do not necessarily have minima in the correct place (i.e., at $\underline{c} = \underline{c}_t$) for short data samples.[2] It should be noted that this phenomenon is not inconsistent with maximum likelihood theory. The theory guarantees correct answers only asymptomatically.

The second requirement is less esoteric. As the aircraft changes flight condition, its parameters change in ramp-like fashion. The accumulated likelihood functions will then be out of date and cause parameter estimates to lag behind the true parameter values. The faster we deweight accumulated data, the less the lag.

The design compromise for these requirements resulted in a time constant of 5 seconds.

In addition to low-frequency deweighting of accumulated likelihoods, it was also found desirable to prevent very-high-frequency data (such as sharp-edged gust or command responses) from being accumulated. This was done by adding a relatively high-frequency, lowpass filter to the accumulation and highpass network. The total likelihood filter then takes the (digital) form shown in Figure 19. The symbols $\Delta\epsilon_k$, $\overline{\Delta\epsilon}_k$, and ϵ_k denote generic inputs, intermediate states, and outputs, respectively. The filter is actually used to generate all likelihood functions, $L^{(i)}$ $i = 1, 2, \ldots N$, and all components of ∇L and $\nabla^2 L$.

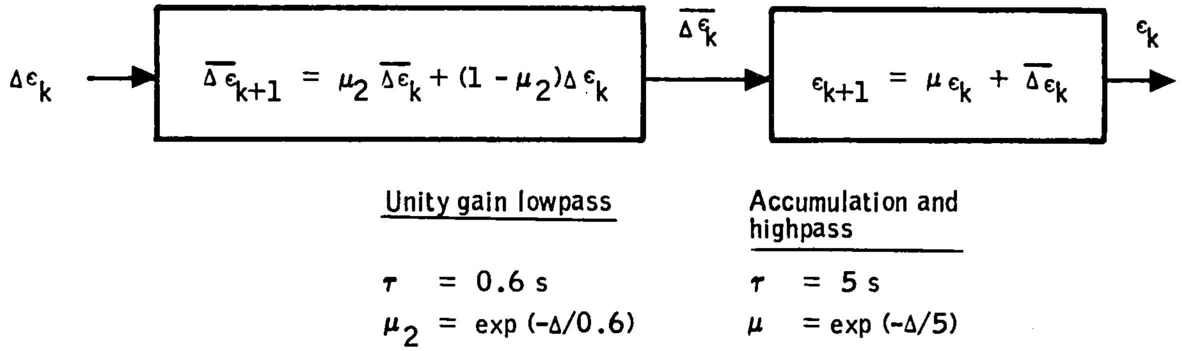

Figure 19. -Filter for likelihood functions.

Gain adjustment. -Adaptive control techniques that use explicit parameter identification require a gain schedule based on the parameter estimates. This section describes the gain adjustment portion of the PCMLE adaptive algorithm.

Derivation of gains: Since the VALT performance specification was given in terms of desired command responses, it was straightforward to specify gains to match a desired closed-loop model. A gain matrix was computed at each flight condition based on the desired closed-loop characteristics.

Plots of these gains versus flight condition (forward velocity) are contained in Appendix A (pitch axis) and Appendix B (lateral axis). Examination of the pitch-axis plots shows a strong dependence on forward airspeed for the majority of the elements. Simple functions of $\bar{v}$ (normalized velocity) were used to approximate the desired set of gains and thus define a "schedule." The schedule was given in Table 4 and was checked at a number of flight conditions.

The benefit of extending the gain calculation to a function of four variables was examined using a least-squares measure of fit. A "fit error" for each gain element was computed as the normalized sum of squares between the schedule and the desired gain value. The sum was done over 33 flight conditions and the fit error was normalized by the fit error for zero gains.

Results are given in Table 8. The first column shows the fit of the $\bar{v}$ schedule. (Note J = 1 for K_{11} and K_{21}, since the schedule is zero for V_x feedback.) Column 2 shows the improvement if all four of the parameters estimated by PCMLE are used for updating gains. Gain elements K_{12}, K_{15}, and K_{26} shows some relative improvement. Columns 3, 4, and 5 of the table show the improvement in the fit if each of the three extra parameters are used one at a time with $\bar{v}$. Consideration of these data shows that the improvement in fit is due to including parameter c_3 (∂b_{31}); thus, three gains will fit better if the basic $\bar{v}$ schedule is augmented with c_3 dependence. The new schedule was computed as:

$$K_{12} = K_{12}(\bar{v}) - 0.6071\ c_3$$

$$K_{15} = K_{15}(\bar{v}) + 0.582\ c_3$$

$$K_{26} = K_{26}(\bar{v}) + 2.574\ c_3$$

Next, the command responses with and without the c_3 function were evaluated at a number of flight conditions. Evaluation of these time histories did not show any benefit of using c_3. Thus, although c_3 improves the fit of several gains, this effect is not important in the closed-loop responses. Therefore, only the $\bar{v}$ dependence is retained.

TABLE 8. -FIT ERRORS IN PITCH-AXIS GAIN SCHEDULE

Gain	$J(v)$	$J(v + \bar{\delta})$	$J(v + \delta_1)$	$J(v + \delta_2)$	$J(v + \delta_3)$
K(1, 1)	1.0	0.61	0.88	0.75	1.0
(1, 2)	0.25	0.017	0.25	0.25	0.062
(1, 3)	0.033	0.0096	0.021	0.022	0.029
(1, 4)	0.022	0.004	0.022	0.004	0.020
(1, 5)	0.45	0.037	0.45	0.45	0.10
(1, 6)	0.020	0.002	0.02	0.002	0.02
(2, 1)	1.0	0.93	0.98	0.98	0.98
(2, 2)	0.012	0.004	0.01	0.005	0.012
(2, 3)	0.83	0.70	0.72	0.83	0.83
(2, 4)	0.0155	0.0033	0.0158	0.0167	0.004
(2, 5)	0.011	0.008	0.01	0.009	0.01
(2, 6)	0.37	0.20	0.37	0.36	0.27

Note: PCMLE estimates $\bar{v}$ and $\bar{\delta}$, where

$$\bar{\delta} = \begin{bmatrix} \delta a_{33} \\ \delta b_{31} \\ \delta b_{32} \end{bmatrix}$$

Gain schedules as a function of parameter accuracy: In the VALT design, gain adjustment is used to improve command responses and minimize cross coupling, not to maintain stability. Thus, it is logical to evaluate a "best" fixed-gain system. The best fixed gains can be determined by formally solving an optimization problem.

The function being minimized by a weighted least-squares fit was expressed as:

$$J = \Sigma_{jk} w_{jk}(A + BK - A_m)_{jk}^2$$

where

A, B = Vehicle model matrices

A_m = Desired closed-loop matrix

w_{jk} = Weight factor for jk element of matrix $(A - BK - A_m)$

K = Gain matrix

The matrix K can be determined by following the usual least-squares procedure: set $\frac{\delta J}{\delta K} = 0$ and solve for K. If only one flight condition is selected, this algorithm returns the set of gains for this condition. Summing over multiple flight conditions produces a weighted least-squares fit. In the following analysis, the $V_z = 0$ flight conditions were given three times the weight over $V_z \neq 0$ conditions in determining the gains.

The weighting factors were computed as follows. An individual weighting was applied to each of 16 gain elements. The weighting of each gain element was determined from the sensitivity of four responses to various errors in the closed-loop matrix. The four responses are:

r_1 = V_z due to V_z command (direct)

r_2 = θ due to V_z command (cross coupling)

r_3 = V_z due to θ command (cross coupling)

r_4 = θ due to θ command (direct)

Define:

$$\delta_{ijk} = \left.\frac{\delta ri}{\delta\alpha_{jk}}\right|_{\text{Evaluate at peak of response}} = \text{Sensitivity of response i to change in gain element jk}$$

and

$$w_{jk} = \Sigma_i \delta^2_{ijk} \text{ (sum over the four responses)}$$

Then W, the matrix of elements w_{jk}, is the weighting used in our least-squares algorithm.

It turned out that each a_{jk} was important to only one of the four responses. Recall also that feedback is affecting only the V_z (row 2) and the q (row 3) rows of the closed-loop system matrix. The elements of the system matrix and their respective weighting are given below:

$$\text{Closed-loop parameters} = \begin{bmatrix} a_{22} & a_{23} & a_{24} & a_{25} & a_{26} & b_{21} & b_{22} \\ a_{32} & a_{33} & a_{34} & a_{35} & a_{36} & b_{31} & b_{32} \end{bmatrix}$$

$$W = \begin{bmatrix} 0.04 & 0.25\text{E-}04 & 0.25\text{E-}04 & 0.01 & 0.6\text{E-}05 & 0.06 & 0.25\text{E-}04 \\ 16.0 & 0.01 & 0.01 & 4.0 & 0.25\text{E-}02 & 144. & 0.06 \end{bmatrix}$$

The elements of the W matrix are themselves interesting. The b_{31} element, which is the feedforward from the θ command to the collective and differential collective, is the most sensitive. Errors in this parameter show up as a large ΔV_z response to a θ command.

The gain schedules derived earlier in this section implicitly assume perfect knowledge of the scheduling parameter, $\bar{v}$. If the uncertainty level of this parameter is known, it may be desirable to modify the gain schedule. (In an extreme case, the fixed gain configuration may perform better than a schedule if the scheduling parameter is in error.) This latter possibility was examined by computing the "best" fixed gains over an interval. The interval represents a ±2-sigma bound on the estimate. In the VALT design it was found that the gain schedule should be a function of the uncertainty level of the scheduling parameter.

The accuracy of the scheduling parameter has been included by determining a family of gain schedules for different accuracies of the parameter estimates.

Three sets of gains were computed with the above procedure:

- Low-sigma - Fit gains for flight conditions over an interval $\pm 0.25\ \bar{v}$ about the nominal $\bar{v}$.
- High-sigma - Fit gains for flight conditions over an interval $\pm 0.5\ \bar{v}$ about the nominal $\bar{v}$.
- Constant-gain - Fit gains over all flight conditions.

Plots of the original $\bar{v}$ schedule, the functions for high- and low-$\bar{v}$ accuracy and the best constant value are contained in Appendix E. Note as the accuracy degrades (high sigma), the curves tend toward the best fixed-gain schedule.

Implementation: The preceding gain computation method has been implemented as a table lookup. The PCMLE $\bar{v}$ estimate and its accuracy estimate will be quantized and a gain matrix selected from the table.

Performance on adaptive controllers on VALT simulation. -The PCMLE adaptive controller for the pitch axis was evaluated on the NASA-LRC VALT simulation. The performance agreed with linear simulations run at Honeywell in Minneapolis. This section contains a number of cases to illustrate the salient performance features of the algorithm. The PCMLE estimator uses a baseline set of three filters (channels) and estimates four parameters. The three channels correspond to models at the following flight conditions:

Channel 1: $\bar{v} = 1.0$

Channel 2: $\bar{v} = 0.5$

Channel 3: $\bar{v} = 0$ (hover)

The PCMLE cases are summarized in Table 9. In these cases, the estimator was evaluated open-loop. A measured $\bar{v}$ was used by the gain schedule.

TABLE 9. -VALT SIMULATION TEST CASES

Flight condition	Input	PCMLE channel used	Time history trace
Hover	$\Delta\theta$, ΔV_z step commands	1, 2	Figs. 20, 21
V_x = 19.5 m/s (63 ft/s)	$\Delta\theta$ step commands	3	Figs. 22, 23
V_x = 41.2 m/s (135 ft/s)	$\Delta\theta$, ΔV_z step commands	1, 3	Figs. 24, 25
V_x = 41.2 m/s (135 ft/s)	$\Delta\theta$, gusts, sensor noise	2	Figs. 26, 27
V_x = 79.3 m/s (260 ft/s)	$\Delta\theta$, ΔV_z step commands	2	Figs. 28, 29

Simulation traces for each of these cases are shown in Figures 20 through 29. Figures 20, 22, 24, 26, and 28 show the helicopter variables:

θ - pitch attitude
δ_B' - differential collective command
δ_c' - collective command
δ_B - differential collective position
q - pitch rate
δ_c - collective position
$\dot{x}$ - forward velocity (earth reference)
$\dot{z}$ - vertical velocity (earth reference)

Figures 21, 23, 25, 27, and 29 show selected PCMLE variables:

CH - channel (1, 2, or 3) being used for estimate
$\hat{V}_z$ - estimate of V_z from selected channel
$\hat{q}$ - estimate of q from selected channel
TJ(1) -
TJ(2) - Likelihood functions for the three channels
TJ(3) -
$\hat{z}_1$ - estimate of $\bar{v}$ parameter
$\hat{z}_2$ - estimate of δb_{32} parameter

Figure 20 shows that θ and V_z command responses at hover meet specifications. The step responses satisfy our criteria and there is no noticeable cross-axis response. Figure 21 shows that the likelihood function is minimum for channel 3 (hover). The ^ estimate should be zero and it is close to zero when estimating from either channel 1 or 2. This confirms the gradient calculations.

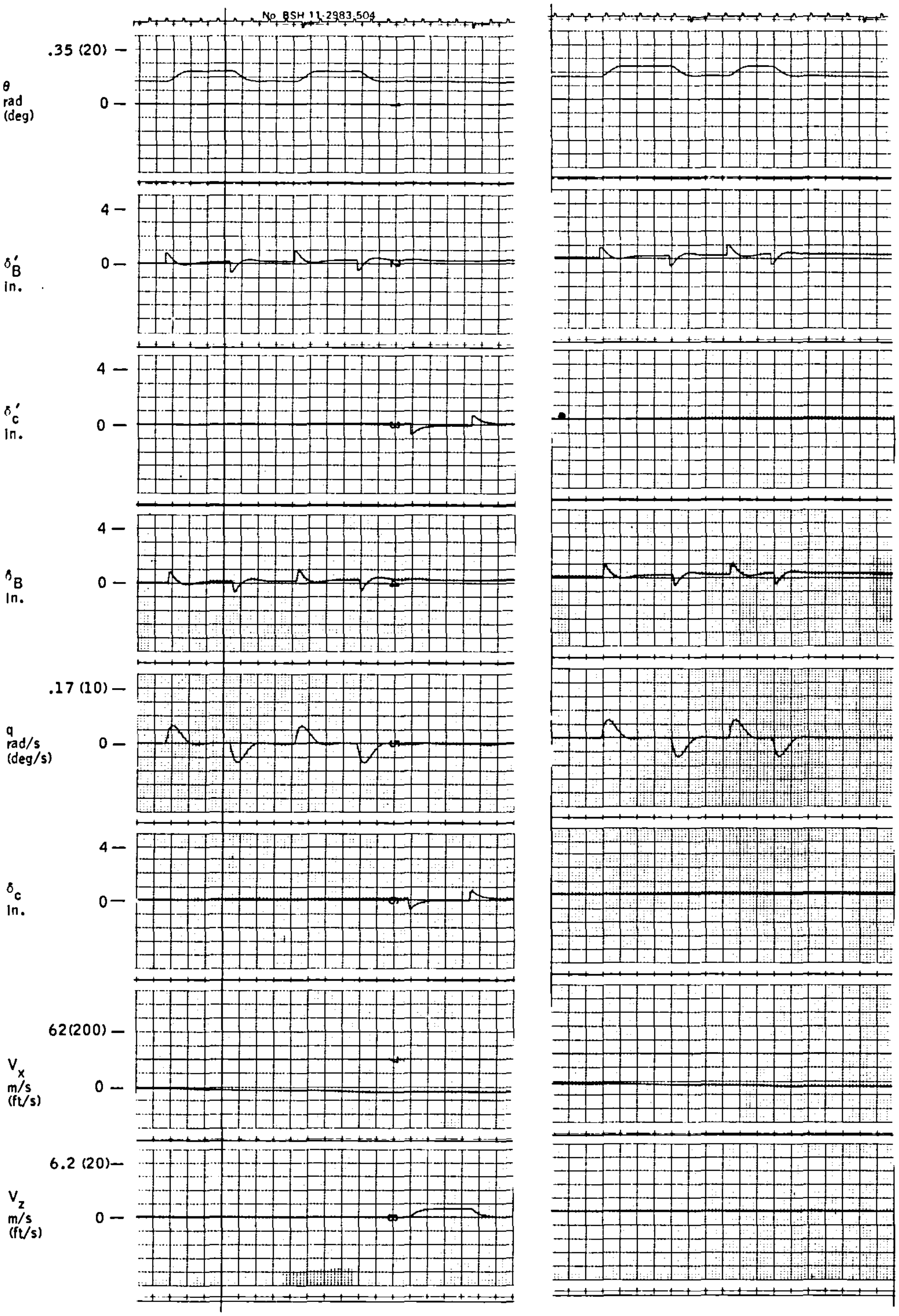

PCMLE
Trim = 3.1 m/s (10 ft/s)

Figure 20.-PCMLE time history test case 1--helicopter variables.

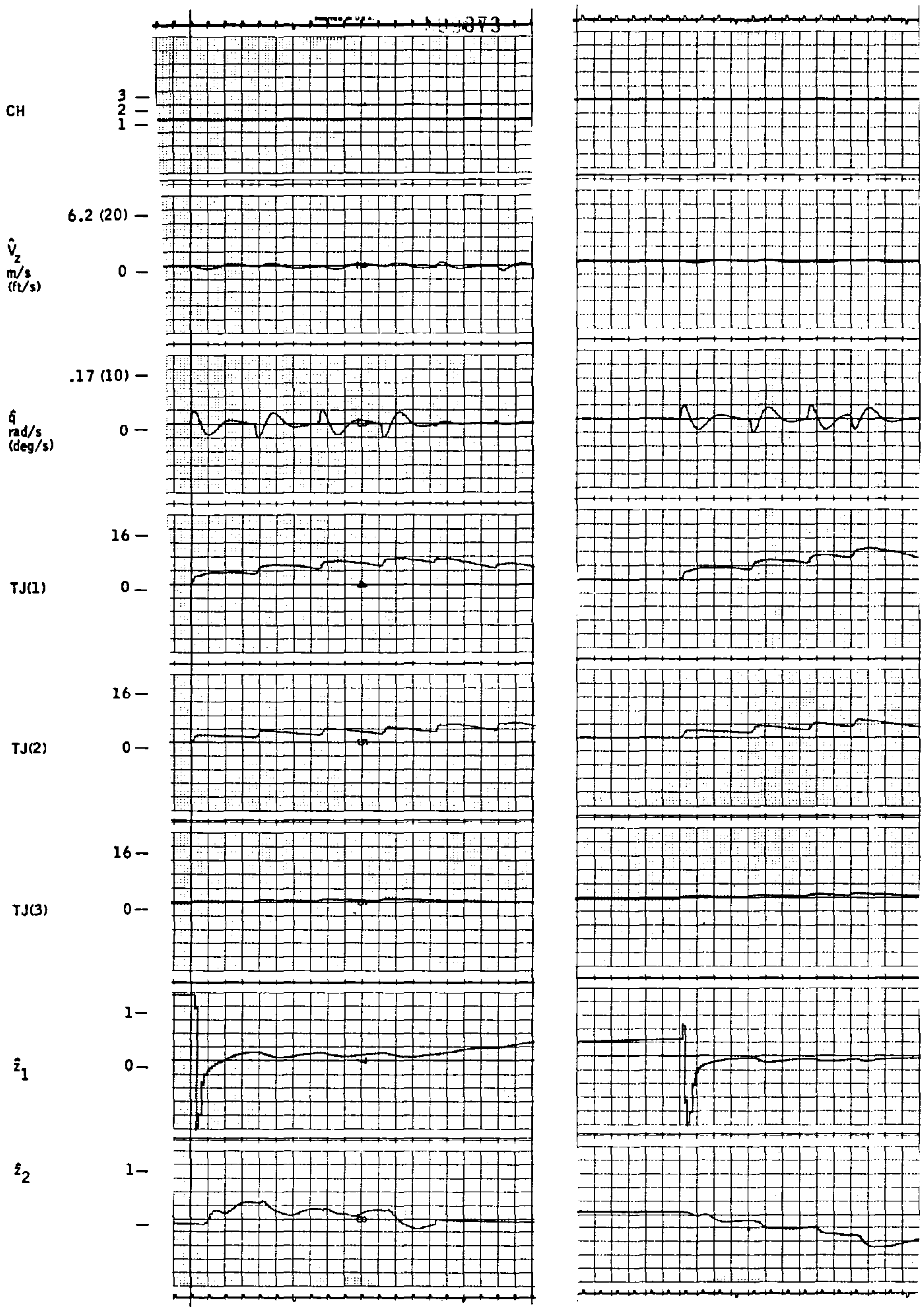

From CH 1

From CH 2

Figure 21. - PCMLE time history test case 1-- PCMLE variables.

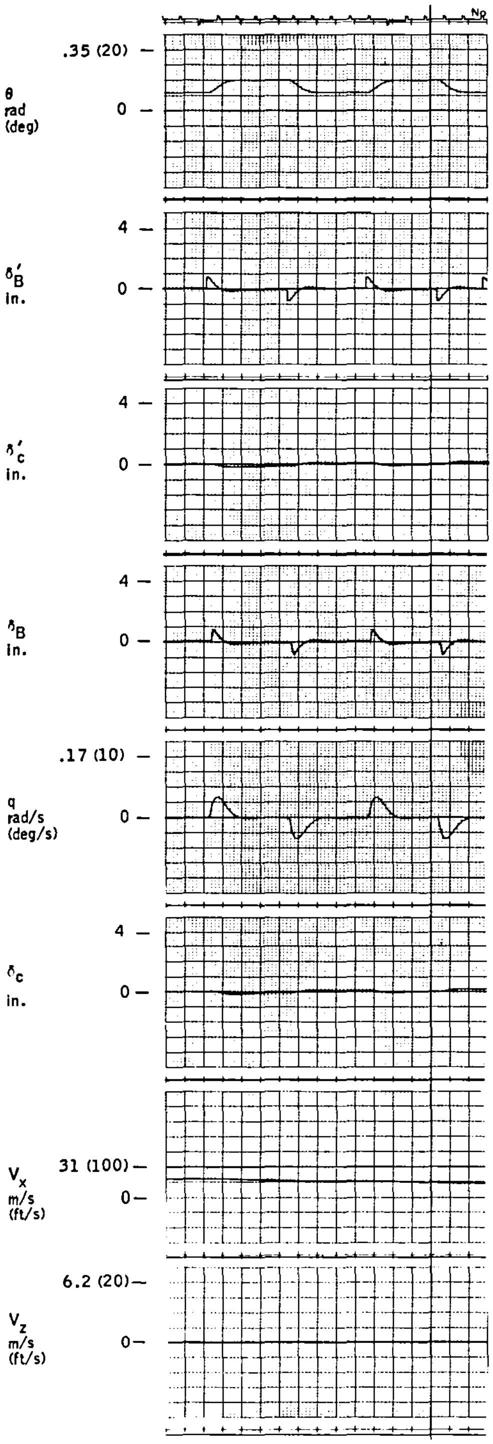

Trim = 19.5 m/s (63 ft/s)

Figure 22. - PCMLE time history test case 2-- helicopter variables.

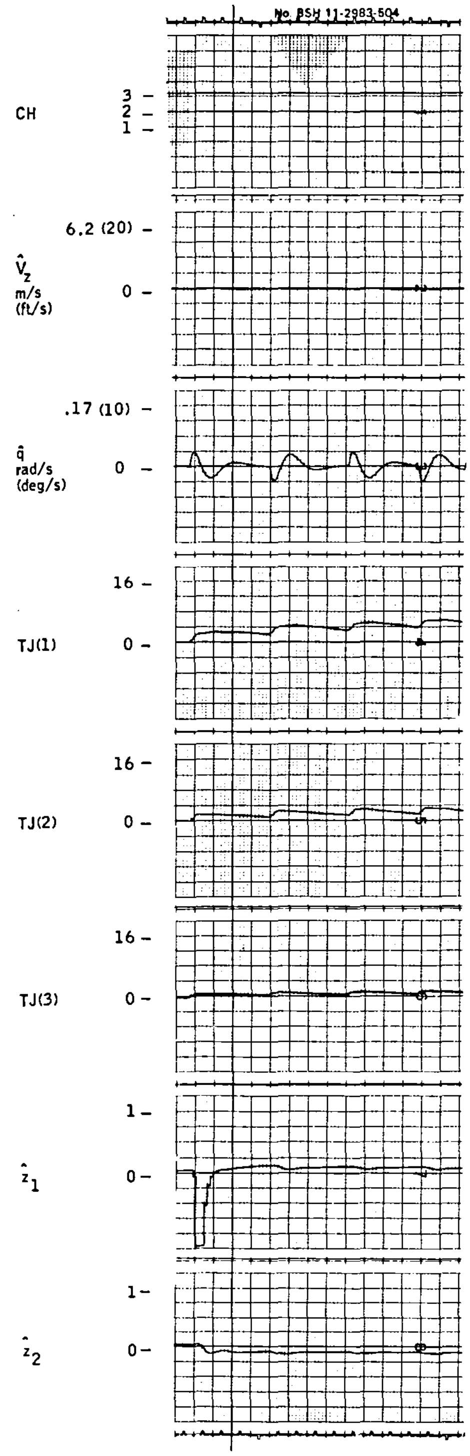

Figure 23.-PCMLE time history test case 2--
PCMLE variables.

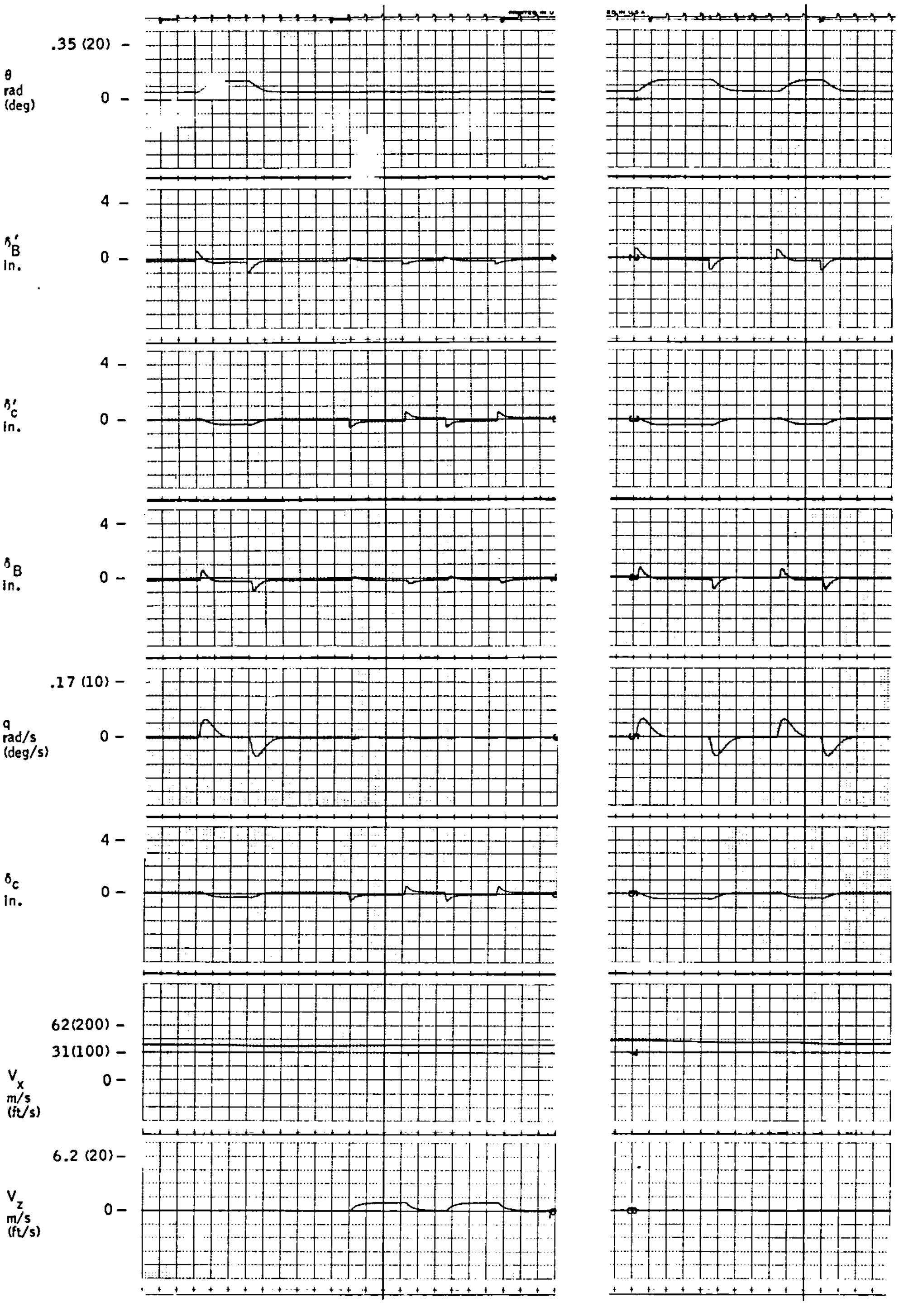

Figure 24.-PCMLE time history test case 3--helicopter variables.

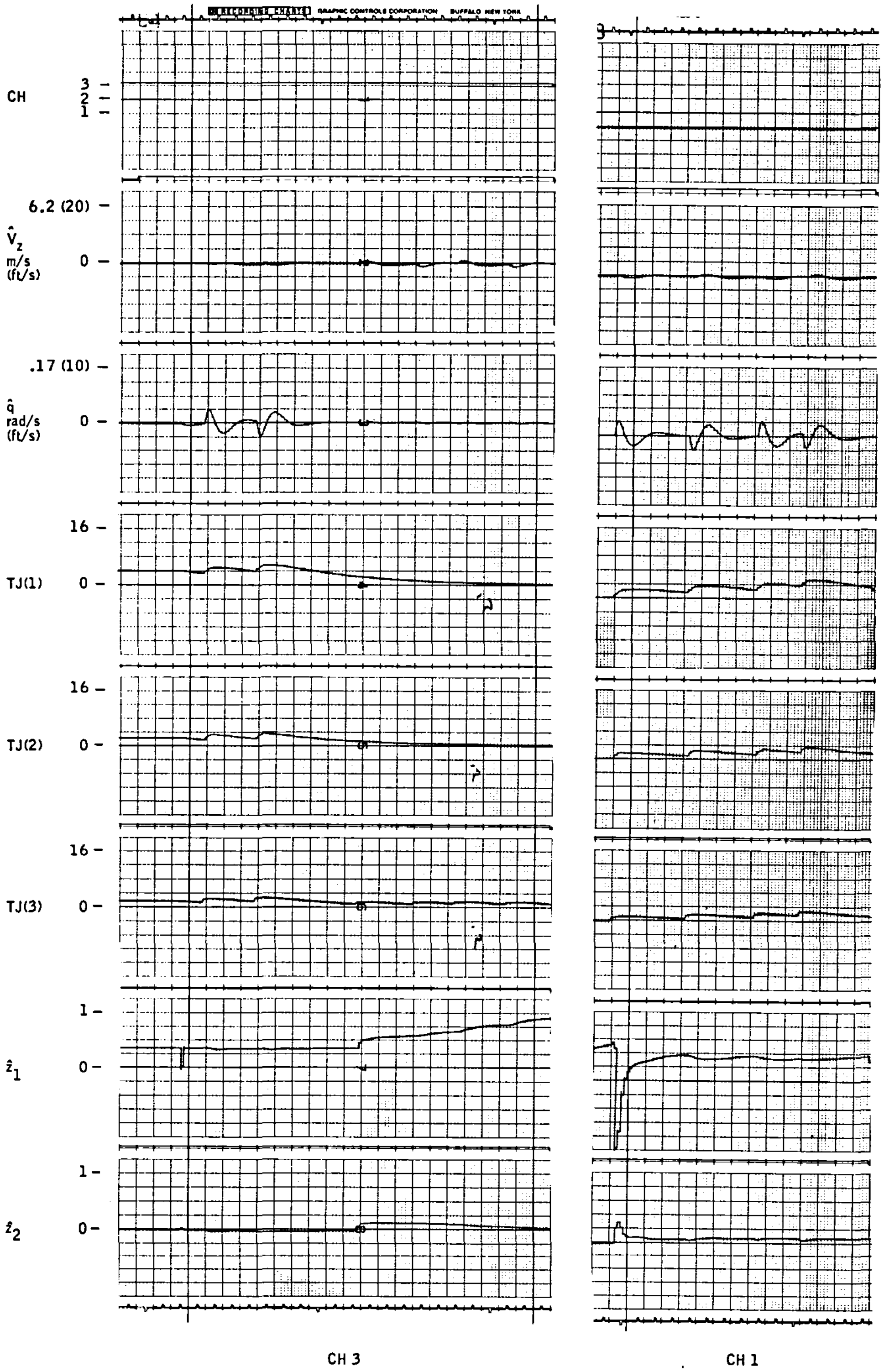

Figure 25.-PCMLE time history test case 3--PCMLE variables.

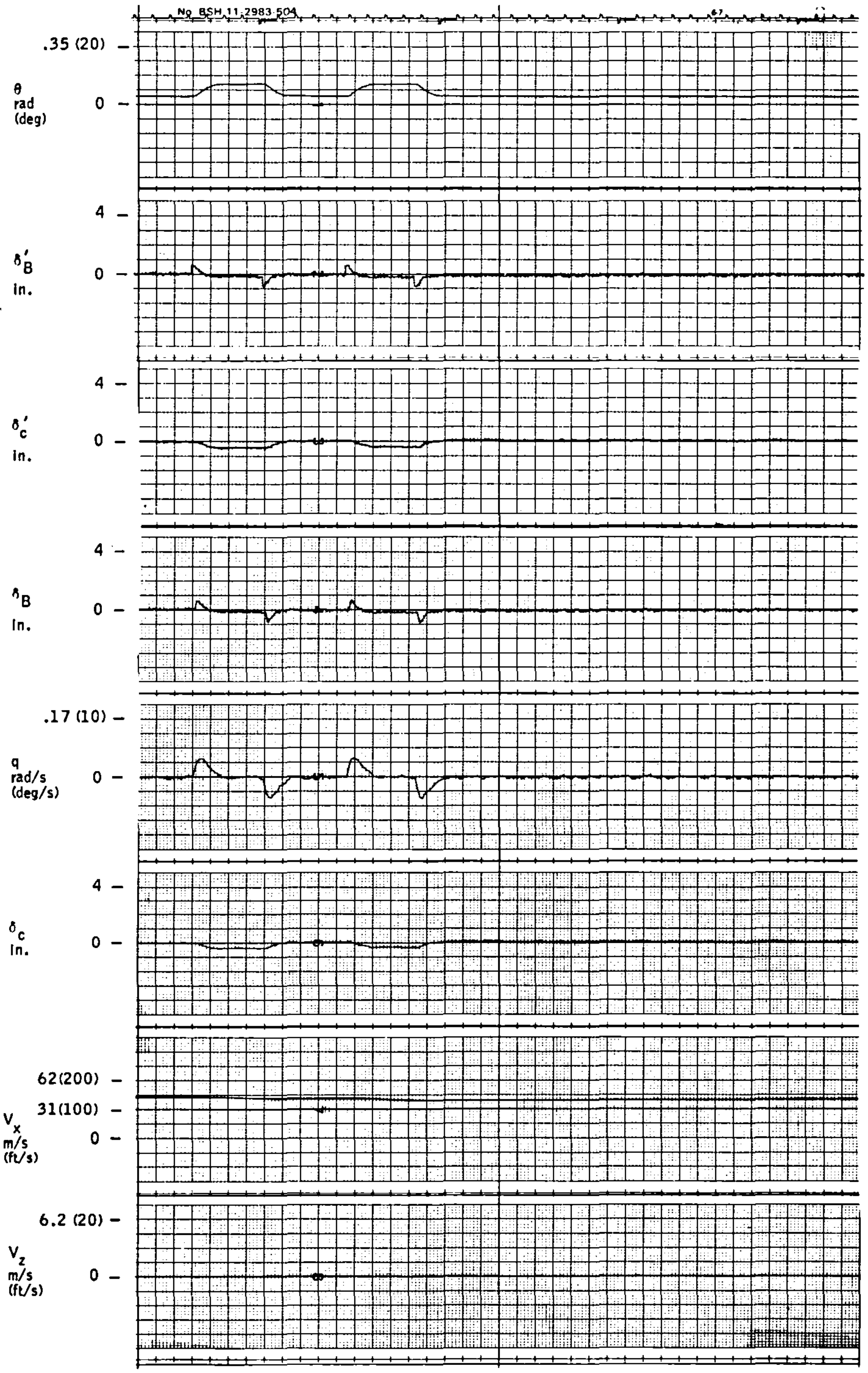

.31 m/s (1 ft/s) vertical gusts plus sensor noise

PCMLE
Trim = 41.2 (135 ft/s)

Figure 26.-PCMLE time history test case 4--helicopter variables.

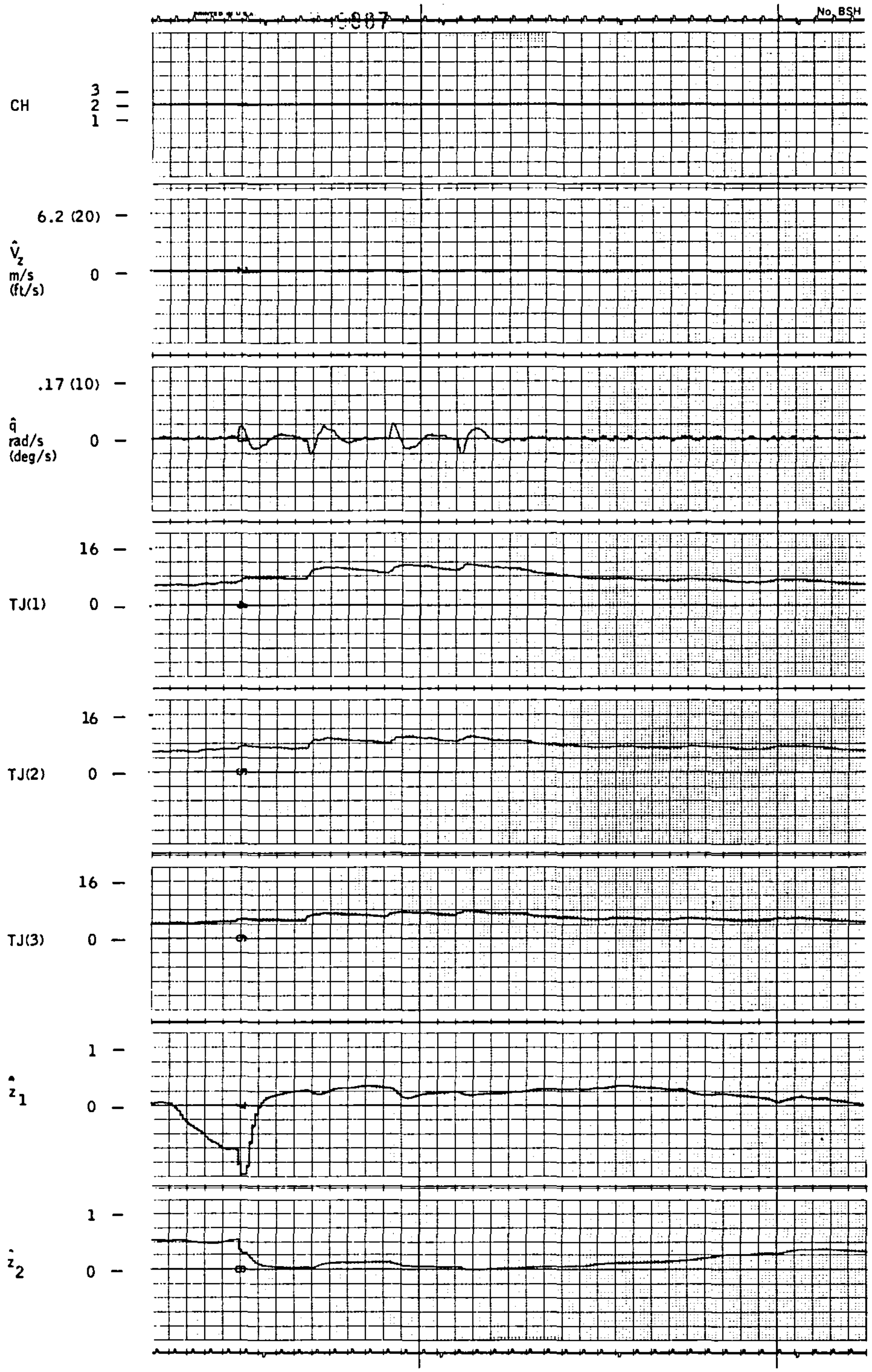

Figure 27. - PCMLE time history test case 4-- PCMLE variables.

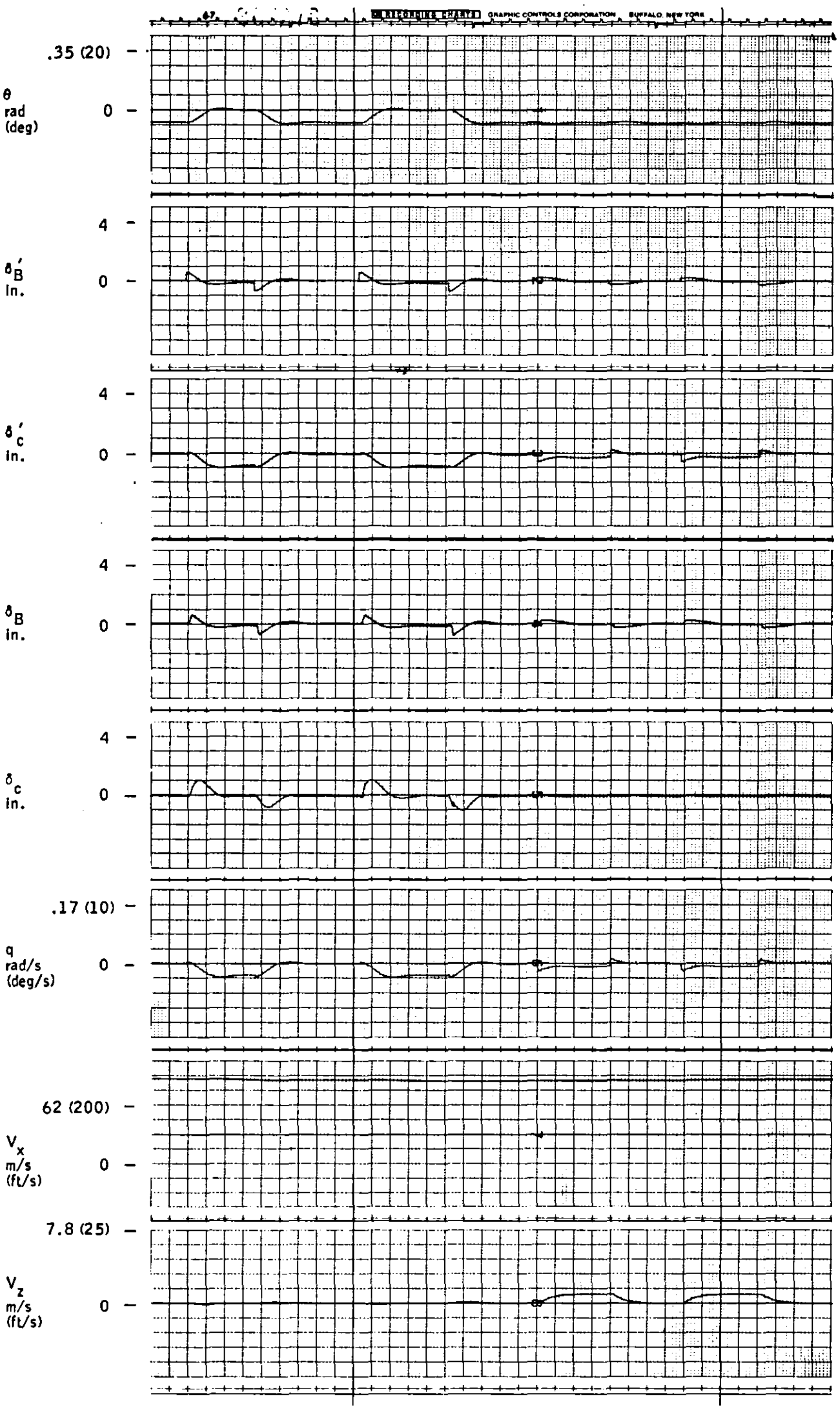

Figure 28. - PCMLE time history test case 5-- helicopter variables.

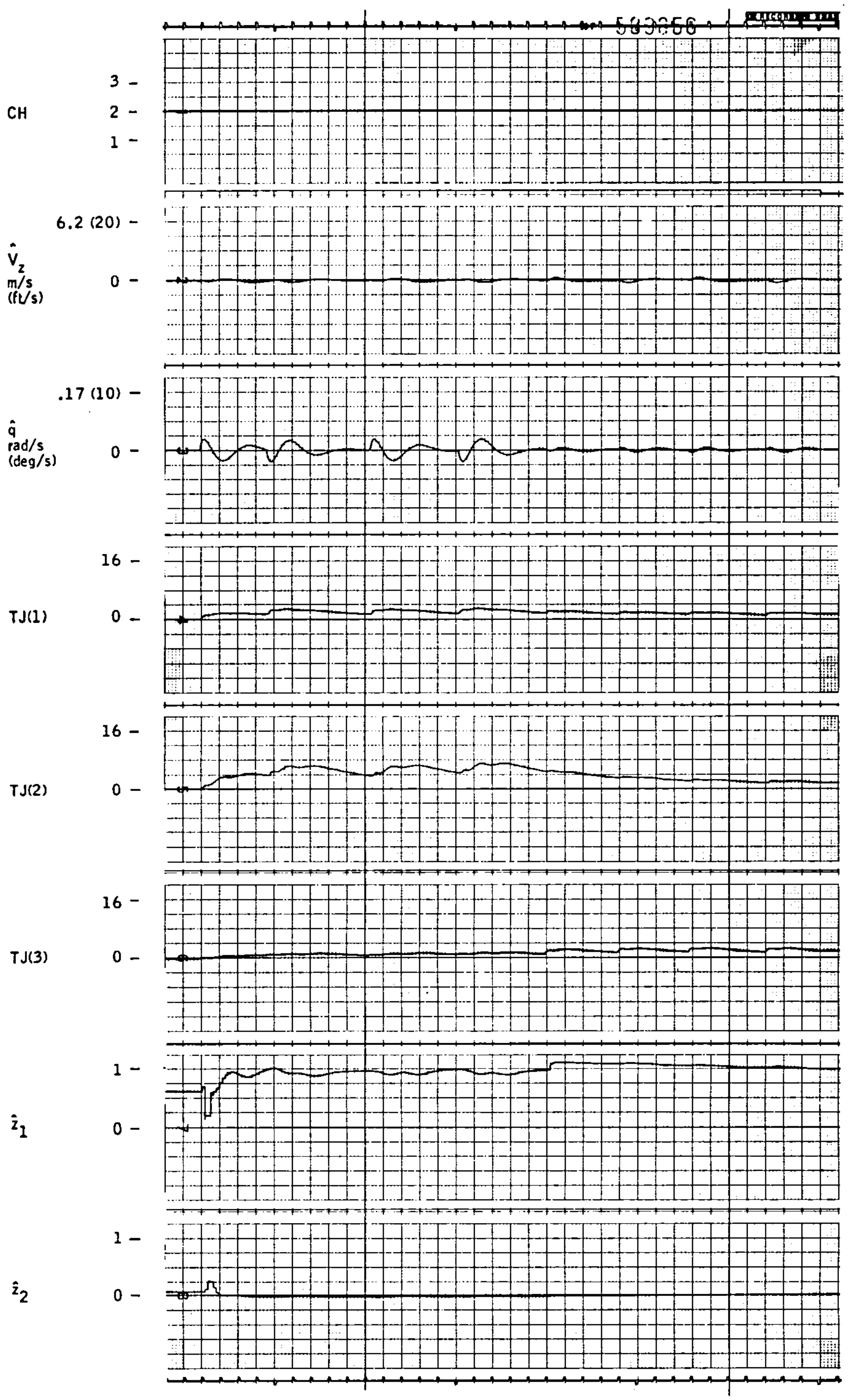

Figure 29. - PCMLE time history test case 5--
PCMLE variables.

Figures 22 and 23 show θ responses at $\bar{v} = 0.23$ (37 kt). Channel 3 still fits best as expected. The $\bar{v}$ estimate is a little low, but still acceptable.

Figure 24 shows θ and V_z command at a $\bar{v} = 0.5$ (80 kt). Again the command responses are good and there is no cross-axis response. Figure 25 shows $\bar{v}$ estimated from channel 1 and channel 3. The parameter $\bar{v}$ should be 0.5 at this condition and the estimate is reasonably close. Channel 2 should have the minimum TJ, but as a result of errors in other parameters, TJ(1) and TJ(2) are very close.

Figures 26 and 27 present a repeat of the $\bar{v} = 0.5$ flight condition with gusts and sensor noise. The $\bar{v}$ estimate is slightly lower than 0.5, but acceptable. Channel 2 should be minimum, but the likelihood function of channel 3 is slightly smaller.

Finally, Figures 28 and 29 show the performance at the maximum velocity, $\bar{v} = 1$ (160 kt). Again, θ and V_z responses are very good, with a barely detectable cross-axis response. The estimate of $\bar{v}$ is close to 1 as it should be. Again, channel 3 is minimum, although channel 1 should be at this condition.

This section has presented a design based on explicitly identifying four CH-47 pitch-axis parameters ($\bar{v}$ plus perturbation parameters on the B(3, 1), B(3, 2) and A(3, 3) coefficients). This section described the analysis used to select the parameters to be identified and the channel structure to be used in the algorithm. Next, the use of the $\bar{v}$ estimate in scheduling the gains was considered. The resulting gain schedule was implemented as a table lookup that uses the $\bar{v}$ estimate as well as its indicated accuracy. Finally, the performance of the identifier on the VALT simulation was considered. The accuracy of identifying $\bar{v}$ was consistent with predictions. It was observed that in some situations the minimum channel is not at the correct value of $\bar{v}$ (even though the estimate is reasonable). This result is investigated in Section 10 where the results of processing actual flight data are presented.

SECTION 7

MODEL REFERENCE ADAPTIVE ALGORITHM

The block diagram of the model reference (MR) algorithm as applied to the CH-47 longitudinal axis is shown in Figure 30. Note the command model is lower order than the vehicle model.

Overview of Algorithm

Consider the CH-47 longitudinal axis in the form given in Section 4:

$$\dot{x} = Ax + B\delta$$

and a model

$$\dot{x}_m = A_m x_m + B_m u$$

where

$x^T = (V_x, V_z, q, \theta)$

$\delta^T = (\delta_B, \delta_c)$ are the actuator commands

$u^T = (V_{z_c}, \theta_c)$ are the command inputs from guidance

$x_m{}^T = (V_{z_m}, q_m, \theta_m)$

The three-state model provides the desired θ_c and V_{z_c} command responses. The θ_m response is second-order, the V_{z_m} response is first-order. Including integral control on each command error adds two states to the control law.

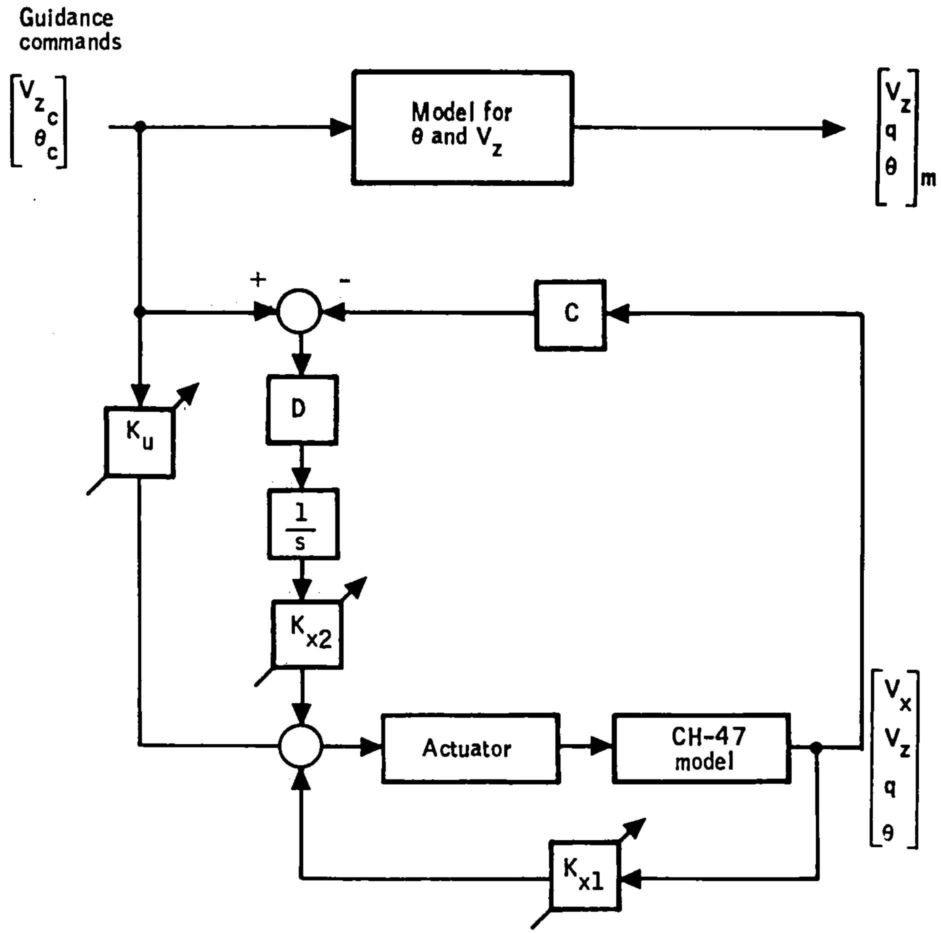

$$C = \begin{bmatrix} 0 & 1 & 0 & 0 \\ 0 & 0 & 0 & 1 \end{bmatrix} \quad \text{and} \quad D = \begin{bmatrix} 1 & 0 \\ 0 & 0.8 \end{bmatrix}$$

Starting gains:
$$\begin{array}{ccccc} \left[\begin{matrix} 0. \\ 0.3 \end{matrix}\right. & \begin{matrix} -7.6 \\ 0 \end{matrix} & \begin{matrix} -27 \\ 0 \end{matrix} & \begin{matrix} 0 \\ -0.23 \end{matrix} & \left.\begin{matrix} 17.5 \\ 0 \end{matrix}\right] \\ V_z & q & \theta & I_1 & I_2 \end{array}$$

Note: $K_x = \left[K_{x1} \,\vdots\, K_{x2} \right]$. K_x is partitioned to separate integrator states.

Figure 30. -Structure of MR algorithm.

The control law has the form discussed in Section 5:

$$\delta = K_x x + K_u u$$

which gives a closed-loop:

$$\dot{x} = (A + BK_x)\, x + BK_u u.$$

Here x includes the two command error integrator states.

The function of the adaptive algorithm is to adjust the gains so the closed-loop matrices match the model.

As A and B vary with flight conditions, K_x and K_u need to be continually adjusted for the plant to match the model. The gain matrices K_x and K_u contain a total of 10 individual terms.

In the MR algorithm, the gains are adjusted to force a Liapanov function of model-following errors and parameter errors to zero. It is well-known that a Liapanov-derived gain adjustment rule is stable in the error, e. If the parameter errors do not go to zero, they remain bounded.[3]

The first form of a Liapanov function used in the study was:

$$V = 1/2\ e^T Pe + 1/2\ \mathrm{Tr}(\Delta A \Delta A^T) + 1/2\ \mathrm{TR}(\Delta B \Delta B^T)$$

where ΔA and ΔB are the difference between the model and the vehicle.

Taking the appropriate time derivatives yields adjustment rules of the form:

$$\Delta \dot{A} = -Pex^T$$

$$\Delta \dot{B} = -Peu^T$$

where x is the measured state, u is the input and e is the error between model and plant states.

Since the adptation is implemented as an adjustment of feedforward and feedback gains, the adjustment rules need to be expressed as $\Delta\dot{K}$ functions rather than direct changes to the plants A and B matrices:

$$\frac{d}{dt}(A + BK_x) = -Pe^Tx \tag{3}$$

$$\dot{K} = -\bar{B}^{-1}Pe^Tx$$

$$\frac{d}{dt}(BK_u) = -Pe^Tu$$

$$\dot{K}_u = -\bar{B}^{-1}Pe^Tu \tag{4}$$

The above form implies a $\bar{B}^{-1}$ can be found that works sufficiently well over the flight envelope, since in this application B also varies with flight conditions.

The P matrix is determined from usual stability considerations:

$$A_m{}^TP + PA_m = Q \leq 0 \tag{5}$$

If $Q = \lambda Q_o$, where λ is an arbitrary scaling parameter, then the P matrix in Equations (3) and (4) is also scaled. Thus, P is a somewhat arbitrary design parameter [as long as Equation (5) is satisfied].

In past applications, problems with the gain adjustment equations arose because they are sensitive to the signal levels of e, x, and u.[2] (If a P was found that worked well with large commands, the adaptation was too slow with small inputs; if tuned to work well with small inputs, then it became very oscillatory with large inputs and usually diverged due to numerical difficulties.)

It was recognized that monotonic functions of the basic Liapunov function could also be used and these forms could be used to "normalize" signal levels in the K equations. Thus, by using different Liapunov functions, different forms of the gain adjustment equations are obtained. The three forms investigated are given in Table 10. The third form is the one finally selected for implementation.

TABLE 10. -MODIFIED LIAPUNOV FUNCTIONS

Liapunov function	Adjustment rule
$V = ePe^T + 1/2 \text{ Tr } \Delta A \; \Delta A^T$ $+ 1/2 \text{ Tr} \Delta B \Delta B$	$\dot{K}_1 = -B^{-1} \; Pe^T x$ $\dot{K}_2 = -B^{-1} \; Pe^T u$
$V = 1/2 \; \ell n \; (e^T Pe + 1)$ $+ 1/2 \text{ Tr} \Delta A \Delta A^T + 1/2 \text{ Tr} \Delta B \Delta B^T$	$\dot{K}_1 = - \dfrac{B^{-1}}{(e^T Pe + 1)} \; Pe^T x$ $\dot{K}_2 = - \dfrac{B^{-1}}{(e^T Pe + 1)} \; Pe^T u$
$V = \sqrt{e^T Pe + 1}$ $+ 1/2 \text{ Tr} \Delta A \Delta A^T + 1/2 \text{ Tr} \Delta B \Delta B^T$	$\dot{K}_1 = - \dfrac{B^{-1}}{\sqrt{e^T Pe + 1}} \; Pe^T x$ $\dot{K}_2 = - \dfrac{B^{-1}}{\sqrt{e^T Pe + 1}} \; Pe^T u$

Simulation Results

A number of experiments were conducted using the CH-47 longitudinal model to develop the MR algorithm. This included considerations for model-following errors caused by states not being controlled and the effects of various design parameter on performance.

The model is

$$\frac{V_z}{V_{z_c}} = \frac{2}{s + 2}$$

$$\frac{\theta}{\theta_c} = \frac{7}{s^2 + 4s + 7}$$

$$\omega = 7 \text{ rad/s}$$

$$\rho = 0.76$$

$$P = \lambda \begin{bmatrix} 0.25 & 0 & 0 \\ 0 & 0.1944 & 0.0833 \\ 0 & 0.0833 & 1.4167 \end{bmatrix}$$

$$\lambda = 300$$

A fixed set of K_1 and K_2 is used as starting gains at each flight condition. (They are given in Figure 30.) These gains then adjust based on the update rules. K_1 and K_2 are presently adjusted with the rule shown in row 3 of Table 11.

TABLE 11. -VALT SIMULATION TEST CASES

Flight condition	Input	Model reference mode	Time history trace
Hover	V_z, θ step commands	Fixed gain	Fig. 31
V_x = 41.2 m/s (135 ft/s)	V_z, θ step commands	Fixed gain	Figs. 32, 33
V_x = 79.3 m/s (260 ft/s)	V_z, θ step commands	Fixed gain	Figs. 34, 35
V_x = 79.3 m/s (260 ft/s)	θ, V_z step commands	Adapting	Figs. 36, 37
V_x = 79.3 m/s (260 ft/s)	θ, Gusts and sensor noise	Adapting	Figs. 38, 39

Performance of MR Algorithm on VALT Simulation

The performance of this algorithm on NASA-LRC's simulation is summarized in this subsection. This algorithm adjusts gains based on errors between the model states and three measured helicopter states (V_z, q, θ). The starting set of gains was selected to work well at hover. In practice, they work well up to forward speeds of 41.2 m/s (80 kt). The major performance degradation occurs at the maximum forward speed of 79.3 m/s (160 kt) and is manifested primarily by large cross-axis responses. Thus, the model reference adaptation is shown at the high-speed condition, since its effects are most apparent there.

Simulation traces for these cases are shown in Figures 31 through 37. Figures 31, 32, 34, and 36 show the same helicopter variables as the PCMLE runs do. Figures 33, 35, and 37 show the following variables:

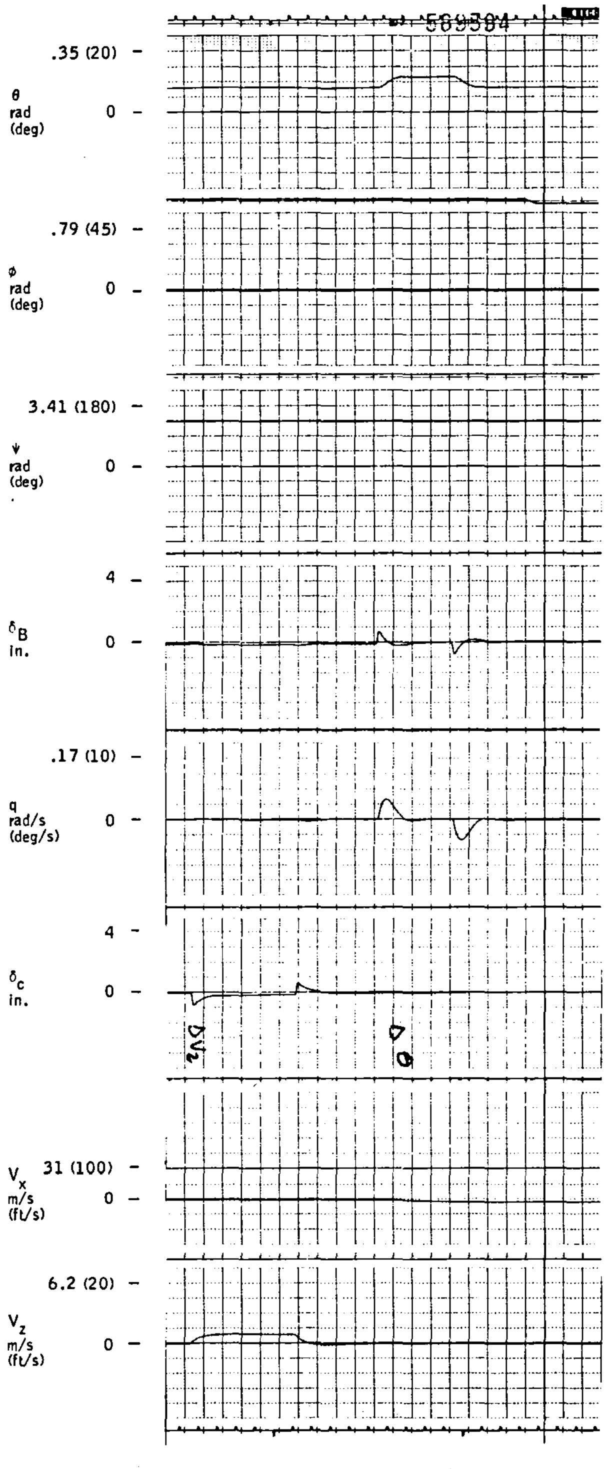

Trim = 3.1 m/s (10 ft/s)

Figure 31.- MR time history test case 1--helicopter variables.

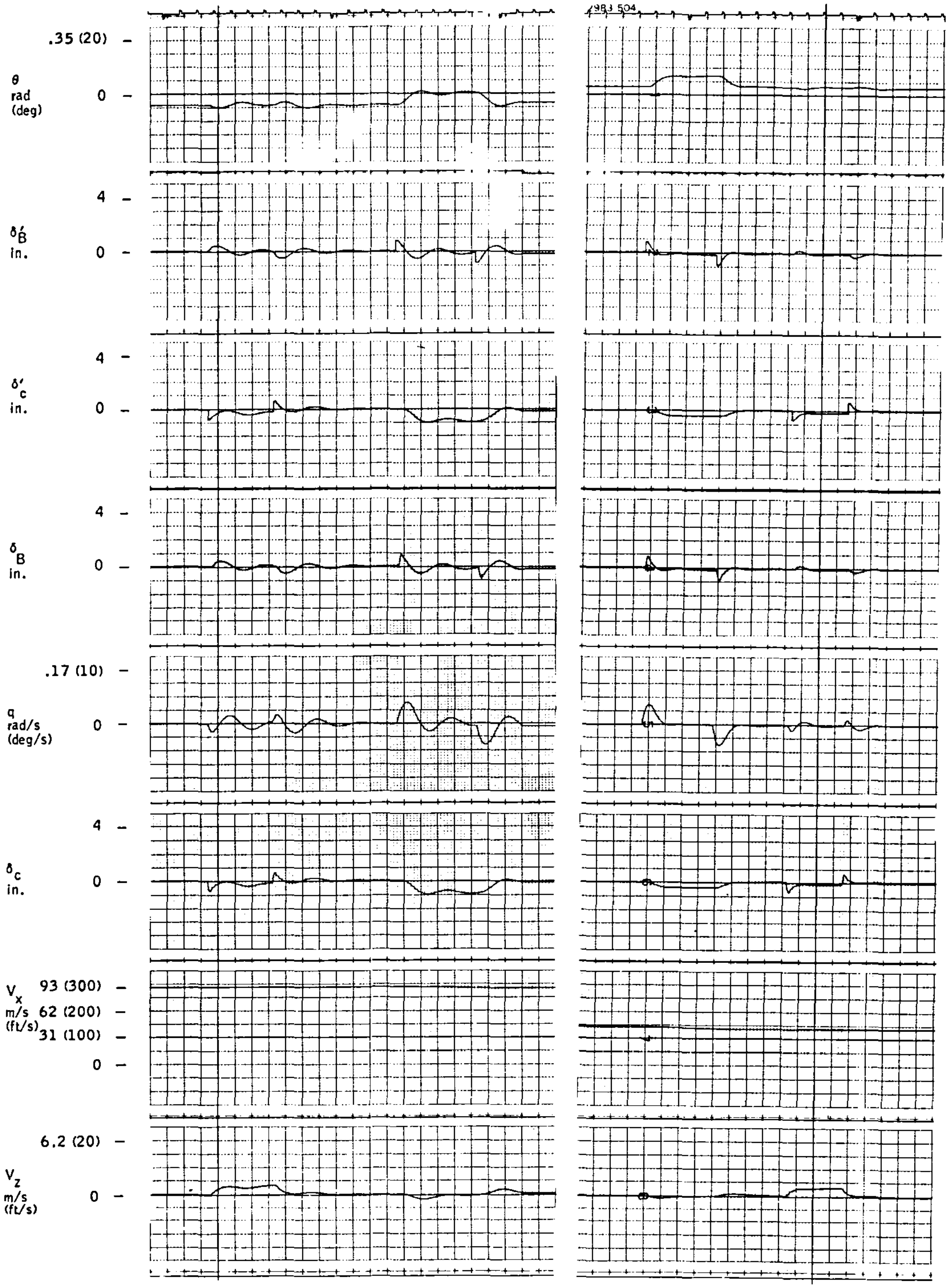

Trim = 79.3 m/s (260 ft/s)

Trim = 41.9 m/s (135 ft/s)

Fixed gain

Figure 32. -MR time history test case 2--helicopter variables.

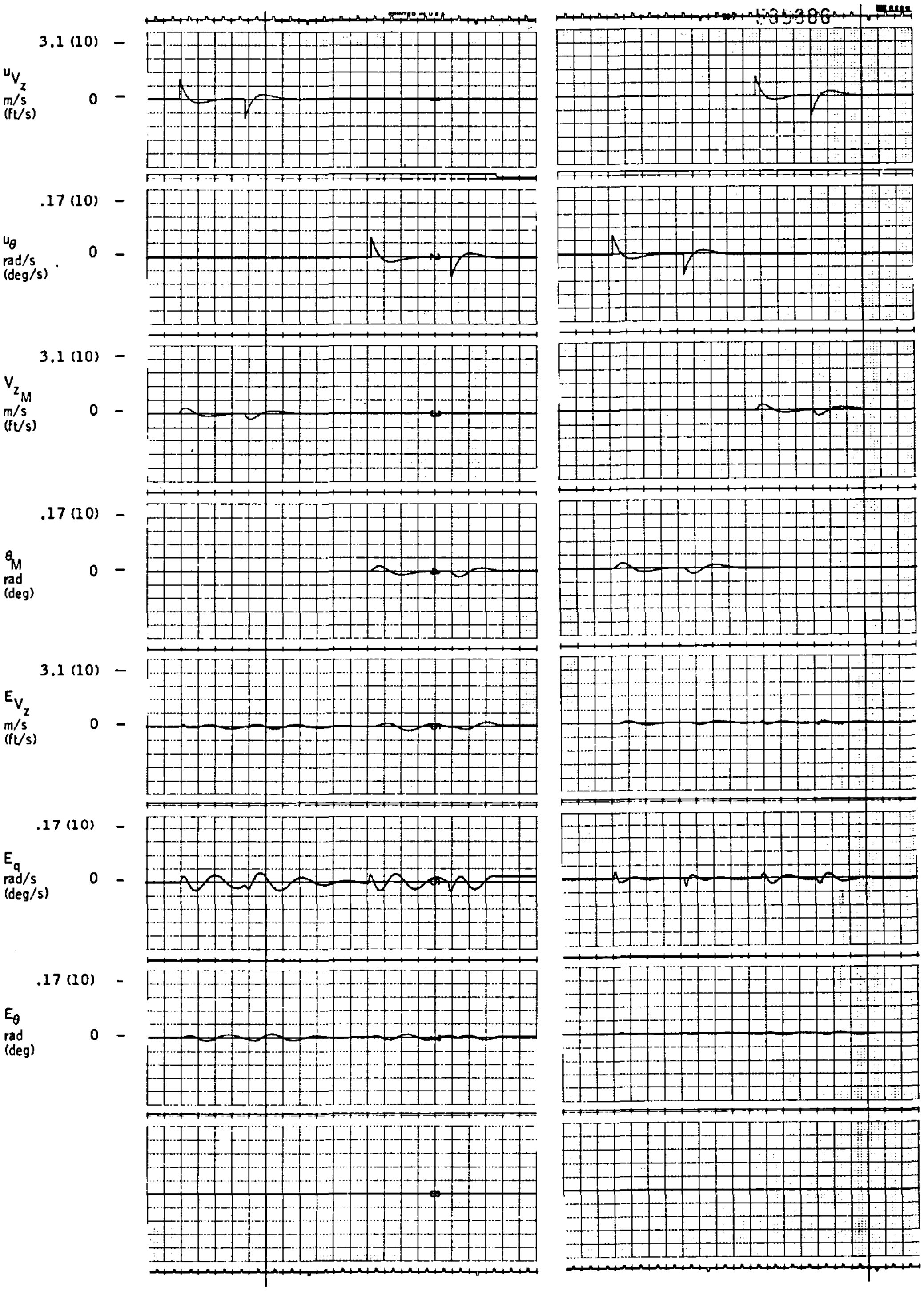

Figure 33.-MR time history test case 2--command input, model state, and error variables.

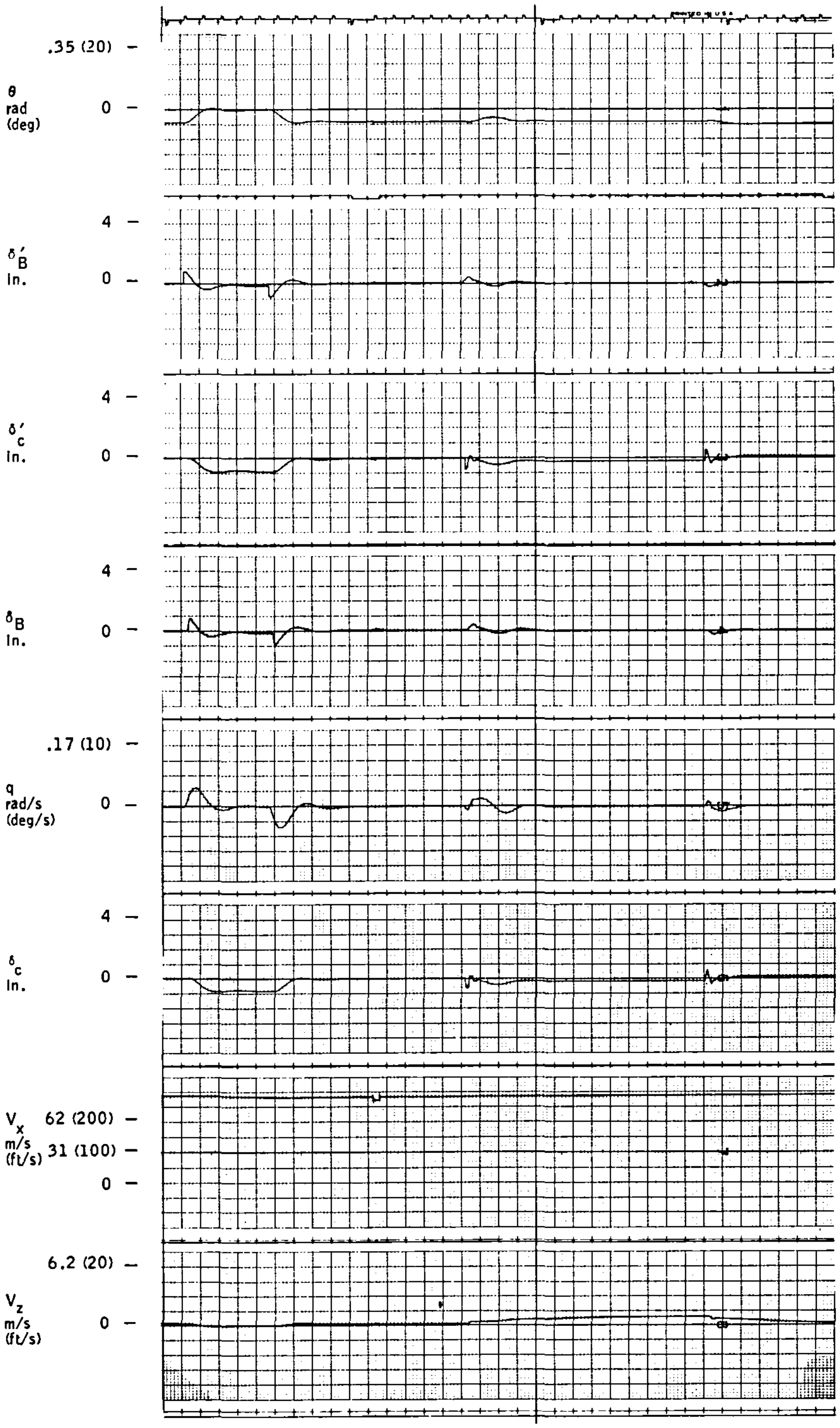

Trim = 79.3 m/s (260 ft/s)

MR adapt

Figure 34. -MR time history test case 3-- helicopter variables.

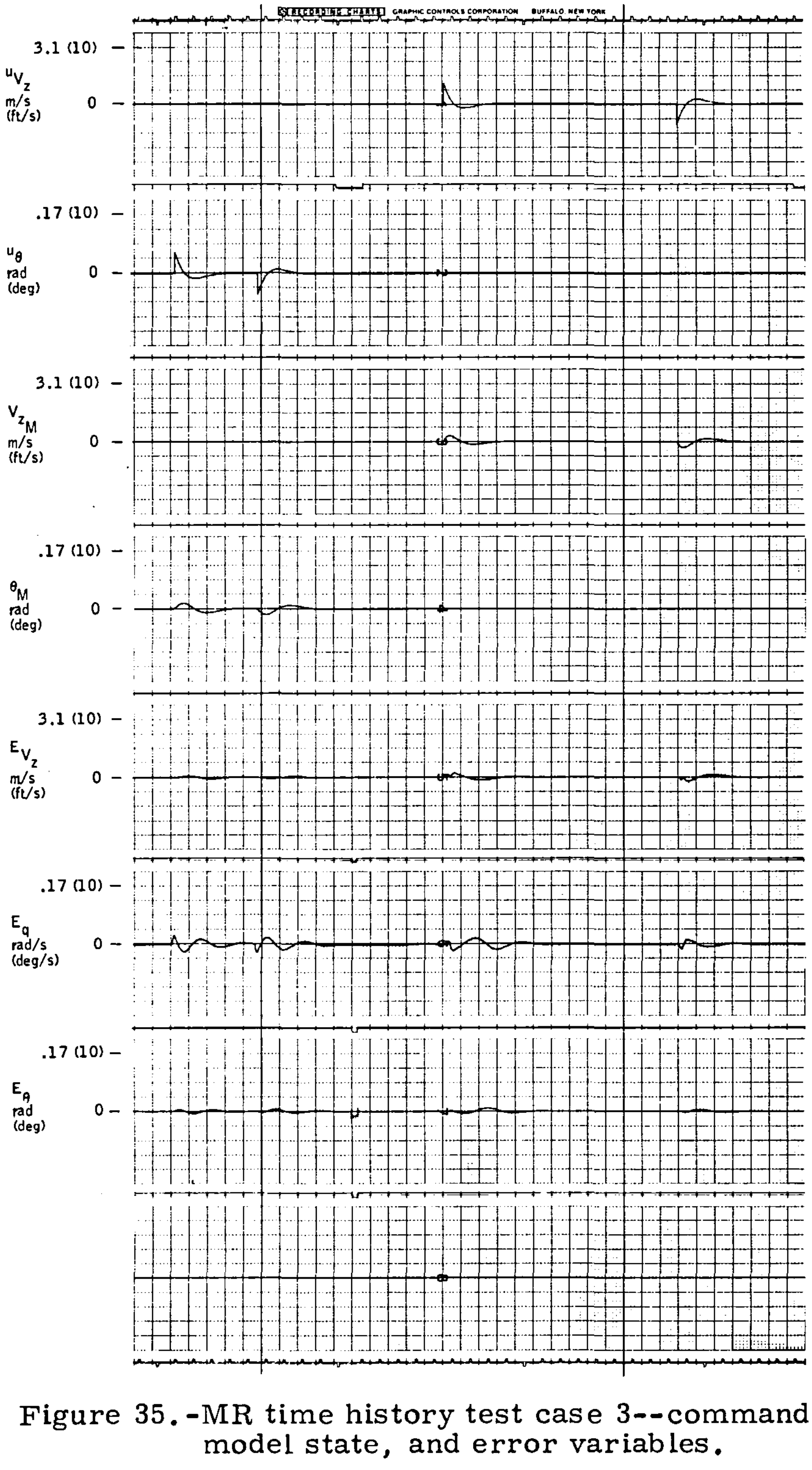

Figure 35.-MR time history test case 3--command input, model state, and error variables.

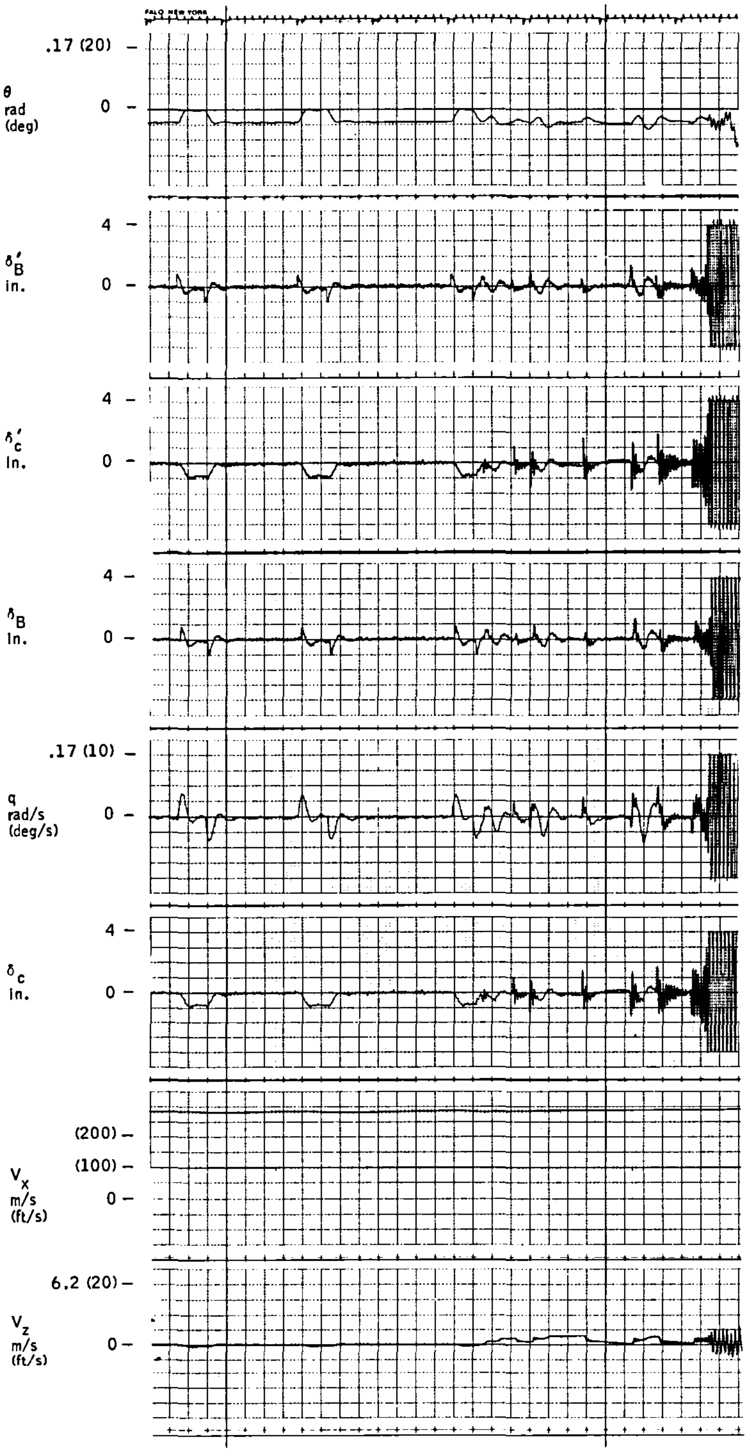

Trim = 79.3 m/s (260 ft/s)

Gusts and sensor noise

Figure 36.-MR time history test case 4--helicopter variables.

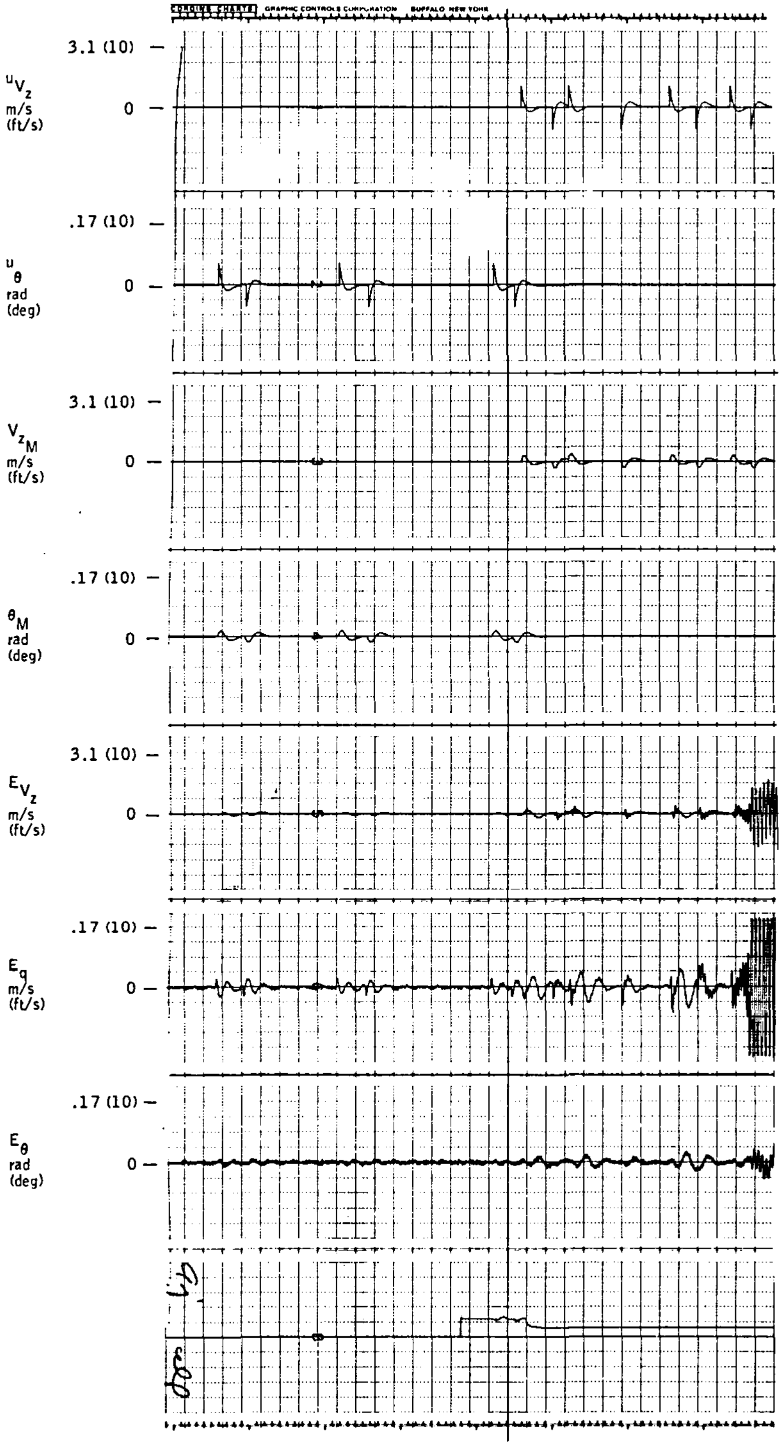

Figure 37.-MR time history test case 4--command input, model state, and error variables.

U_{v_z} - V_z command input to model

U_θ - θ command input to model

V_{z_m} - V_z model state

θ_m - θ model state

E_{v_z} - V_z error between model state and helicopter

E_q - q error between model state and helicopter

E_θ - θ error between model state and helicopter

It should be noted that the inputs to the model are high-passed so steady-states do not appear on the traces. (Basically, this is required to remove trim effects.)

Figure 31 shows V_z and θ command responses at hover. They meet requirements and show no cross-axis response.

Figures 32 and 33 show θ and V_z command responses at the 41.2 m/s (80 kt) and 79.3 m/s (160 kt) with the starting gains fixed. At the 79.3 m/s condition, some cross-axis response is present; otherwise, the command responses are reasonable.

Figures 34 and 35 show the 79.3 m/s condition with the gains adapting. Note the reduction in the cross-axis response for θ command. Also note that the V_z command that follows has a very slow response because some gain values moved to accommodate the θ command.

Figures 36 and 37 illustrate the fundamental problem with this algorithm. The system is at the high-speed (79.3 m/s) condition with gusts and sensor noise. After operating for several minutes, a sequence of θ

commands is applied. The random disturbances had caused the gains to drift sufficiently that an unstable combination resulted.

This section has presented the design of a model reference algorithm. The structure of the control law is identical to the adaptive design of Section 6. The difference lies in the method used for determining the gain matrices. In this design, the gain is adjusted with a Liapunov procedure to drive the response errors toward zero. Simulation studies indicated good performance except when measurement noise is present. In this situation, the gains continue to drift in response to the measurement noise. This result is discussed further in the next section which compares the two candidate adaptive designs.

SECTION 8
CONCEPT COMPARISON AND SELECTION

The two designs from Sections 6 and 7 are compared in Table 12. This comparison summarizes the simulation performance, the design process, the complexity of the algorithm, and its simulation performance.

The PCMLE adaptive design was recommended for flight evaluation based on its superior performance with gust and sensor noise present. In addition, the digital formulation of the algorithm offers better numerical stability than discretization of the model-following equations.

The PCMLE algorithm for real-time parameter estimation is relatively complex compared with current flight control software. The various PCMLE subroutines are written in FORTRAN with an emphasis on speed of execution. During development, the software was run on a CDC-6600 and a Honeywell H-6080 computer in Minneapolis.

Load maps from CDC-6600 compilations show that about 5K of memory are required (about 1.6K of this represents labeled common blocks). Timing checks made on the H-6080 indicate a maximum of 5.6 ms, with minor variation between the five subcycles.

TABLE 12. -CONCEPT COMPARISON

Parameter	PCMLE adaptive controller	Model reference adaptive controller
a) Command responses (ΔV_z, $\Delta\theta$)	Both designs satisfy response specifications. Command responses are nearly identical for nominal conditions (no gusts or sensor noise).	
b) Stability of controller	Equal for nominal operation.	
c) Stability of adaptive portion of algorithm	Estimator stable and unbiased. Only plants that do not exhibit approximately linear perturbation responses would cause problems.	Theoretical. In practice, numerical problems can cause algorithm to diverge. Related to item f below.
d) Effects of turbulence	No problem. It is accounted for in Kalman filter design.	Causes drift in some gain elements.
e) Effects of sensor noise	No problem. It is accounted for in Kalman filter design.	Causes drift and biases in some gain elements.
f) Implementation philosophy	a) Explicit gain adjustment. Requires designing a gain schedule based on parameter estimates. b) Direct digital formulation. c) Offers the lowest sample rate.	a) Implicit gain adjustment. b) Discretization of analog equations. Problems in integrating continuous equations with large Δt. c) Problem not well-posed if perfect model-following is not possible.
g) Complexity (real-time code only)	1602 core FORTRAN code. 1608 core common blocks.	452 core FORTRAN code. 256 core common blocks.
h) Computation time	6 ms per cycle (3 channels - 4 parameters estimated).	Less than 1 ms per cycle.

SECTION 9
GUIDANCE INTERFACE

As discussed previously, the controller was designed for θ, ϕ, ψ, and V_z commands. Since the existing VALT guidance algorithm generates velocity commands, an interface was required to convert velocity commands to attitude commands. The guidance interface is shown in Figure 38.

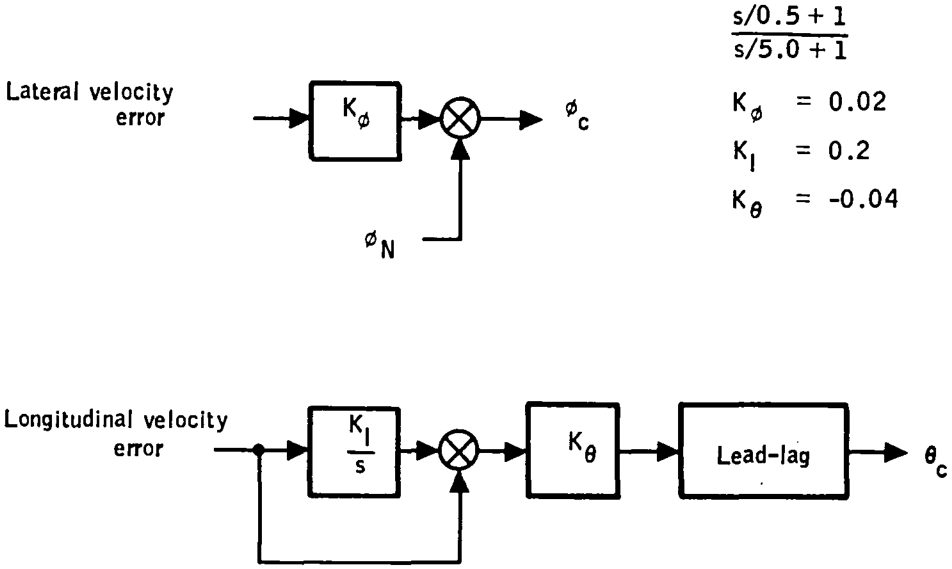

$$\frac{s/0.5+1}{s/5.0+1}$$

$K_\phi = 0.02$
$K_I = 0.2$
$K_\theta = -0.04$

Figure 38. -Guidance interface.

The bank-angle command is generated from a sum of lateral velocity error and the nominal bank angle computed by the guidance law.

The pitch-attitude command is more difficult to generate, since a nominal θ is not available. The longitudinal velocity error is applied to a proportional plus integral and used as the attitude command. A lead-lag filter was added to improve the dynamic response of the coupled guidance/control system. A root-locus analysis predicted the closed-loop response to a velocity command should have a damping ratio of 0.5.

A time history of trajectory-following using the attitude controller and the guidance coupler is shown in Figure 39. The performance is satisfactory. An overshoot of approximately 20 percent can be observed in the forward-velocity trace as the vehicle completes the trajectory and comes to a hover.

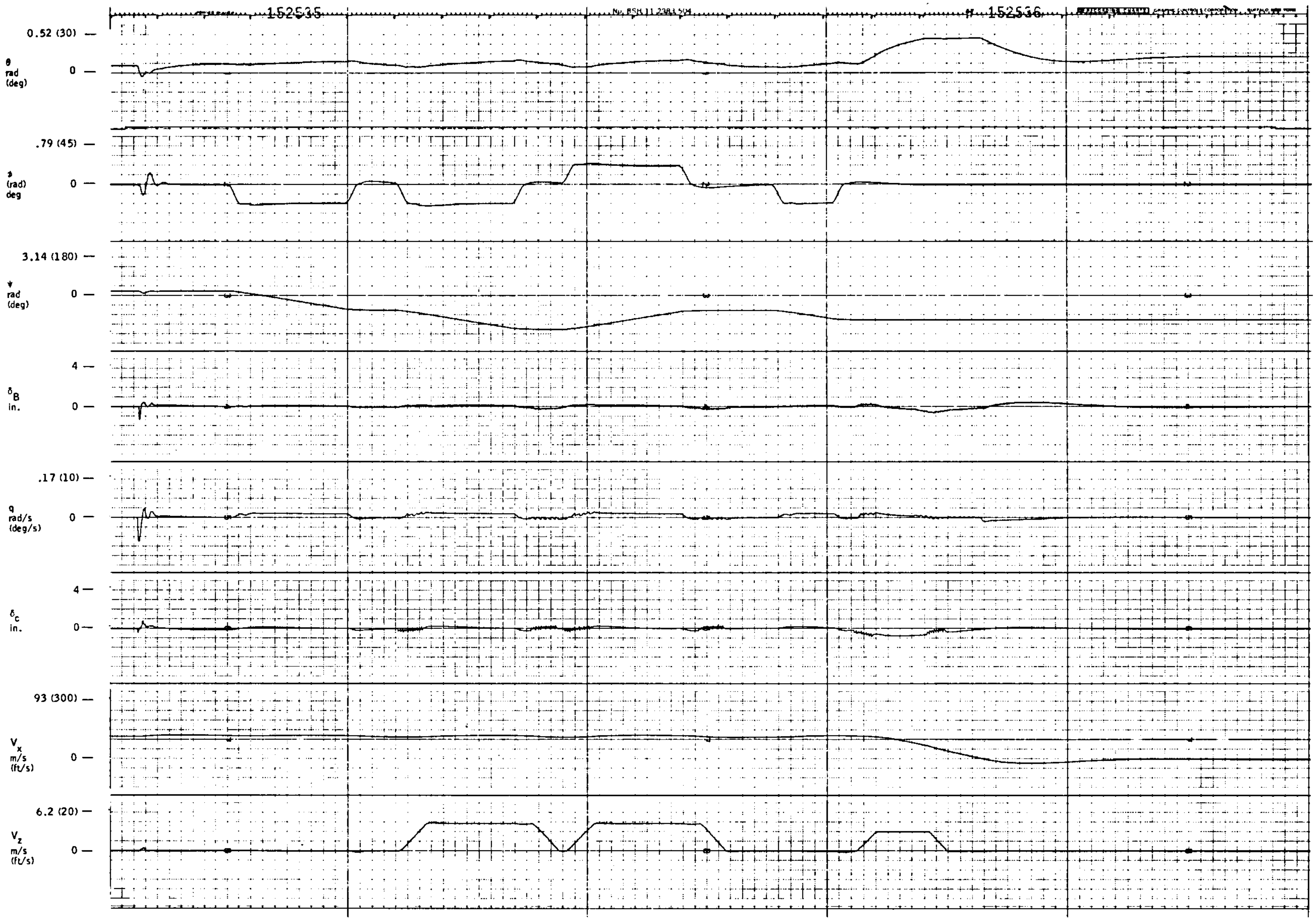

HI Controller/Guidance

K_ϕ = .02

K_θ = -.01

Figure 39. - Time history of trajectory-following.

SECTION 10

ESTIMATION OF PARAMETERS FROM FLIGHT DATA

The PCMLE algorithm was evaluated against prerecorded flight data to assess the performance of the explicit identifier. Multiple iterations of the Newton-Raphson parameter steps were used to obtain the best possible convergence. This section describes the sensor data, the procedure used to obtain parameter estimates, and draws conclusions from the results.

Analysis of Sensor Data

Recorded flight data for a number of maneuvers was available from an earlier flight test program. The variables of interest for the PCMLE algorithm are vertical velocity, pitch rate, pitch attitude, and the two controls, differential collective and collective. A functional diagram of the pitch axis is shown in Figure 40. The variables Z13, Z16, and Z19 were used to obtain approximations for δ_c and δ_B by assuming the actuators have unity transfer functions.

Thus, $\delta_c = Z19$ and $\delta_B = Z16 + Z13$.

The flight data, which had been recorded at 40 sps, was highpass filtered to eliminate unwanted trim values in both control inputs and measurements. (This highpass operation is part of the PCMLE algorithm.) Initial processing was performed to validate scale factors and establish reasonable sensor noise levels.

Since the stability augmentation system (SAS) had not been cancelled in these flight tests, its effect had to be included. The recorded variable Z13 was compared with an estimate computed from the SAS transfer function and the measured pitch rate.

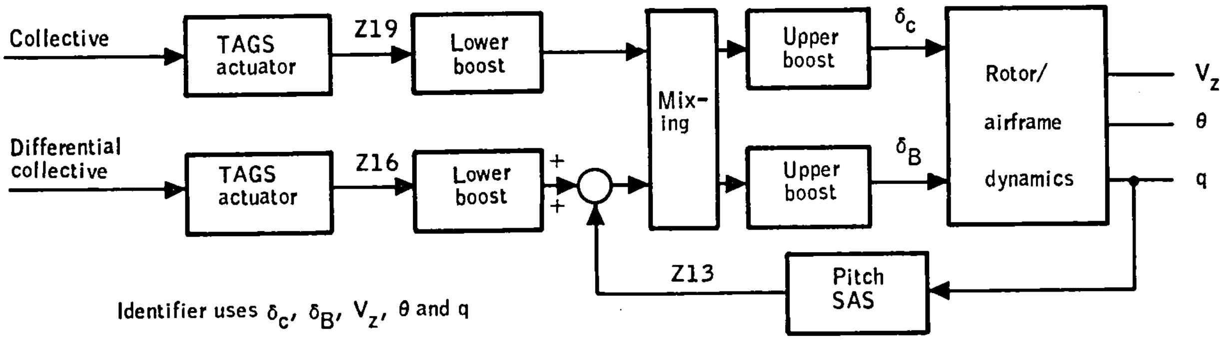

Figure 40. -Recorded sensor outputs from flight records.

The two signals differed by a scale factor which changed with maneuver. The decision to retain the recorded version was made following test cases in which its use resulted in better matches to the recorded measurements. Further analysis of the measurement residuals showed that in these calibration runs they were dominated by the vertical velocity measurement. Removal of this term from the observation equations resulted in acceptable residuals for the two remaining sensors: pitch rate and pitch attitude. The estimation process was insensitive to assumed noise statistics for these measurements over a wide range of values.

A processing rate of 10 sps (every fourth data point) was investigated to reduce computation time. Although this rate seemed well within required sampling limits, there were significant residuals that indicated that a higher rate was required. Therefore, the original sample rate of 40 sps was used.

Procedure

The basic MLE algorithm used in the identifiability analysis was used. Some numerical problems were encountered in finding solutions to the Ricatti equation. This occurred since our algorithm for solving the Ricatti equation requires that the initial set of Kalman gains stabilize the system. This was often difficult to do in view of the parameter adjustments occurring at each iteration. In retrospect, it would have been more efficient to solve the Ricatti equations with a method such as Potter's algorithm which removes the requirement for initial stabilizing gains.

Because of the apparent small gust levels, a number of runs were made using zero filter gains. Using zero gains often caused the parameter errors to diverge. This occurs because the pitch-axis model is unstable at a number of flight conditions. In this situation, the residuals diverge and the likelihood functions have such steep sides that it is very difficult from a numerical viewpoint to locate the minimum with Newton-Raphson steps. The "zero gain" procedure was modified as follows.

Once an initial set of parameters was obtained, gains were added, with the hope that parameter updates would be small enough to allow use of the same stabilizing initial gains. In most cases this proved to be true. However, for the final parameter identification experiments, the "zero-gain" procedure was not used.

The ill-behaved nature of the likelihood function necessitated careful attention to the allowable search directions in maximization. After a number of unsuccessful attempts at parameter localization with various data runs, it was decided to abandon $\overline{v}$ (forward speed estimate) as the fundamental parameter for purposes of function optimization. Perturbation parameters on a_{33} and b_{31} appeared to be much more closely related to the quality of fit. In the final set of parameter identification runs, $\overline{v}$ was set to nominal value and a_{33}, b_{31} were allowed to find their best values. Once localized in the parameter space in this manner, all the other perturbation parameters plus initial conditions were estimated. The final model used in the Kalman filter consisted of a fourth-order state representation of the longitudinal-axis dynamics with two control inputs as in the baseline PCMLE algorithm. A third "control" was added to simulate the effect of highpass filtering the contribution due to the initial conditions.

The final noise model was developed to account for uncertainties in the control inputs and the two sensors used (pitch rate and pitch attitude). State noise with an rms value of 2 percent of the control matrix was added to account for random perturbations of the recorded control inputs. Response measurements of pitch rate and pitch attitude were assigned noise statistics $\sigma_q = 0.01$ rad/s and $\sigma\theta = 0.01$ rad, respectively.

Results

The final set of 12 maneuvers analyzed is defined in Table 13.

The procedure described resulted in the parameter estimates shown in Table 14 for each of the 12 maneuvers analyzed. The quality of fit is rather good. Plots of fit for each maneuver are contained in Appendix F. Three plots are used to describe each maneuver. The first plot shows the two control inputs. The second and third plots show the highpassed measurements of θ and q and their corresponding residuals for the final iteration. It should be emphasized that only two parameters significantly improve over their a priori uncertainty. Table 15 illustrates the reduction in parameter uncertainty for a typical case (maneuver 7). Note that only a_{33} and b_{31} (plus two initial conditions) are significantly improved.

TABLE 13. -MANEUVERS ANALYZED WITH FLIGHT DATA

No.	Data run	Serial no. of file	Flight condition	
			V_x (m/s)	V_z (m/s)
1	5	34007	0	0
2	9	31017	0	0
3	13	34031	0	0
4	17	35001	10.3	+7.63
5	25	31005	20.6	0
6	27	35008	20.6	-5.08
7	29	31017	20.6	-2.54
8	31	31023	20.6	+2.54
9	33	31026	20.6	+5.08
10	39	33010	30.9	0
11	41	30010	30.9	+2.54
12	43	33012	30.9	+2.54

The basic conclusions are that near the correct value of $\bar{v}$, good parameter estimates can be obtained. If $\bar{v}$ is wrong, the algorithm may find another local minimum and erroneous parameter estimates are obtained. It appears that reasonably good fits can be obtained at a number of values of $\bar{v}$. When the baseline PCMLE algorithm was simulated, similar results were obtained.

Based on our analysis of flight data, we have concluded that $\bar{v}$ is probably not a good dominant parameter. If the baseline PCMLE algorithm had been flight-tested, it probably would have experienced problems with

TABLE 14. -PARAMETER VALUES FOR PITCH-AXIS IDENTIFICATION

No.	$\bar{v}$	a_{11}	a_{12}	a_{13}	a_{14}	a_{21}	a_{22}	a_{23}	a_{24}	a_{31}	a_{32}	a_{33}	a_{34}	b_{11}	b_{12}	b_{21}	b_{22}	b_{31}	b_{32}
1	0	-0.0181	-0.000134	2.41	-32.2	-0.180	-0.499	0.00594	-0.0685	0.0113	0.000324	0.460	0.981	0.121	-0.000818	0.0000724	-7.80	0.272	0.000119
2	0	-0.0181	-0.000069	2.41	-32.2	-0.180	-0.500	0.00151	-0.0141	0.0144	0.0000988	0.313	0.974	0.121	0	-0.0000254	-7.80	0.272	0
3	0	-0.0181	-0.000136	2.40	-32.2	-0.180	-0.499	0.00281	-0.0293	0.0109	0.000308	0.369	0.929	0.120	-0.000562	0.0000347	-7.80	0.277	-0.0115
4[a]	0.125	-0.0186	-0.000814	2.41	-32.0	-0.150	-0.494	0.00231	-22.4	0.000823	0.00227	-0.167	1.46	0.120	-0.000703	0.0870	-8.18	0.269	0.0289
5	0.25	-0.0202	-0.00318	2.40	-31.3	-0.120	-0.549	0.00108	-45.3	0.00764	-0.00333	0.128	1.07	0.121	0.00953	0.176	-8.60	0.285	-0.0110
6	0.25	-0.0198	-0.00403	2.42	-31.3	-0.122	-0.825	-0.0144	-53.7	0.0216	0.0000202	0.198	2.12	0.119	-0.163	0.211	-8.20	0.298	0.0189
7	0.25	-0.0203	-0.00328	2.42	-31.3	-0.120	-0.498	0.00201	-45.0	0.0201	0.000373	0.284	2.18	0.122	0.00228	0.175	-8.55	0.295	0.00597
8	0.25	-0.0203	-0.00368	2.40	-31.3	-0.120	-0.989	-0.00705	-43.7	0.0142	-0.0186	0.151	1.19	0.124	-0.0189	0.136	-0.40	0.265	-0.00277
9	0.25	-0.0203	-0.00429	2.40	-31.3	-0.120	-1.19	-0.0256	-42.7	0.0222	-0.0245	0.209	0.783	0.128	-0.0164	0.117	-9.83	0.258	0.00740
10[a]	0.375	-0.0229	-0.00286	2.37	-30.2	-0.0899	-0.0671	-0.0664	-66.4	-0.00499	-0.00114	0.282	2.56	0.121	0.158	0.242	-8.84	0.295	0.0409
11[a]	0.375	-0.0229	-0.00286	2.37	-30.2	-0.0899	-0.0671	-0.0664	-66.4	-0.00499	-0.00114	0.282	2.56	0.121	0.158	0.242	-8.84	0.295	0.0409
12[a]	0.375	-0.0229	-0.00286	2.37	-30.2	-0.0899	-0.0671	-0.0664	-66.4	-0.00499	-0.00114	0.282	2.56	0.121	0.158	0.242	-8.84	0.295	0.0409

[a] Unable to find filter gain solution for next update. Error has probably not been minimized.

TABLE 15. -PARAMETER UNCERTAINTIES FOR TYPICAL CASE (A PRIORI AND A POSTERORI)

Parameter	σ_o	σ_f
a_{11}	0.0045	0.00460
a_{12}	0.009	0.00914
a_{13}	0.4	0.401
a_{14}	3.0	3.00
a_{21}	0.04	0.0400
a_{22}	0.25	0.250
a_{23}	1.6	1.600
a_{24}	10.0	10.0
a_{31}	0.02	0.0531
a_{32}	0.006	0.00913
a_{33}	1.25	0.102
a_{34}	0.5	1.82
b_{11}	0.06	0.0609
b_{12}	0.3	0.322
b_{21}	0.25	0.250
b_{22}	0.8	0.800
b_{31}	0.25	0.0471
b_{32}	0.08	0.119
X0(1)	1.0	0.855
X0(2)	1.0	1.00
X0(3)	0.017	0.133
X0(4)	0.017	0.00873

local minimum as our off-line processing did. Perhaps, better parameterization would use the control effectiveness parameters (b_{31}, b_{32}) as dominant, since they are most easily identified.

One of the reasons $\bar{v}$ was selected as the dominant parameter was that analysis of the gains over the flight envelope showed a $\bar{v}$ dependence. In fact, a gain schedule based on velocity was evaluated and it performed well. The performance differences of the attitude control system with and without gain scheduling are primarily in the area of decoupling. Use of a gain schedule improves the decoupling of the $\Delta\theta$ and ΔV_z responses. Since the decoupling is dominated by the control input matrix, it is expected that a gain schedule could be expressed in terms of the B matrix. This would then be a more natural schedule to use with an explicit parameter identifier.

SECTION 11
CONCLUSIONS

Good command responses exhibiting desired speed of response and minimal cross coupling were obtained in the pitch axis with simple gain schedules based on forward airspeed. In the lateral-directional axes no gain adjustment was required. These control laws were successfully flight tested at the Wallops Island facility using the CH-47.

Use of velocity guidance with an attitude command system generally did not result in as tight a trajectory-following capability as may be desired. The guidance algorithm should be designed in conjunction with the control system for optimum performance.

Adaptation for vehicles like the CH-47 is marginally useful and marginally successful. The identifiability analyses based on computed Cramer-Rao lower bounds showed that only about 7 of 26 longitudinal parameters can be extracted from the sensor data. Relatively large maneuvers are required to obtain significant improvement over a priori knowledge. The dominant scheduling parameter (forward airspeed) can be found to an accuracy no better than 20 to 30 kt (about 15 to 20 percent of maximum speed). Off-line evaluation of the identifier supported these identifiability results. This evaluation also indicated that the fundamental parameter identification problem is plagued with local minima. Initial estimates must be reasonably close in order to converge to the correct parameter set.

These experiments suggest real-time parameter estimation is feasible in modern flight control. Whether it offers benefits for a particular application depends on the nature and magnitude of plant uncertainties and alternate methods available to achieve successful control.

APPENDIX A
GAINS FOR LONGITUDINAL AXIS

Actuator commands have the form:

$$\delta = K_x x + K_u u$$

This appendix contains design values for K_x and K_u for 33 flight conditions plus the $\bar{v}$ gain schedule. The design values were computed using the procedure described in Section 5. The two columns of matrix K_u equal columns 5 and 6 of matrix K_x so only K_x is plotted. Thus, individual terms are denoted as

$$\begin{vmatrix} \delta_B \\ \delta_c \end{vmatrix} = \begin{bmatrix} K_{11} & K_{12} & K_{13} & K_{14} & K_{15} & K_{16} \\ K_{21} & K_{22} & K_{23} & K_{24} & K_{25} & K_{26} \end{bmatrix} \begin{vmatrix} V_x \\ V_z \\ q \\ \theta \\ I_1 \\ I_2 \end{vmatrix} + \begin{bmatrix} K_{15} & K_{16} \\ K_{25} & K_{26} \end{bmatrix} \begin{vmatrix} V_{z_c} \\ \theta_c \end{vmatrix}$$

The data, in the form of computer plots, are presented in Figures 41 through 52.

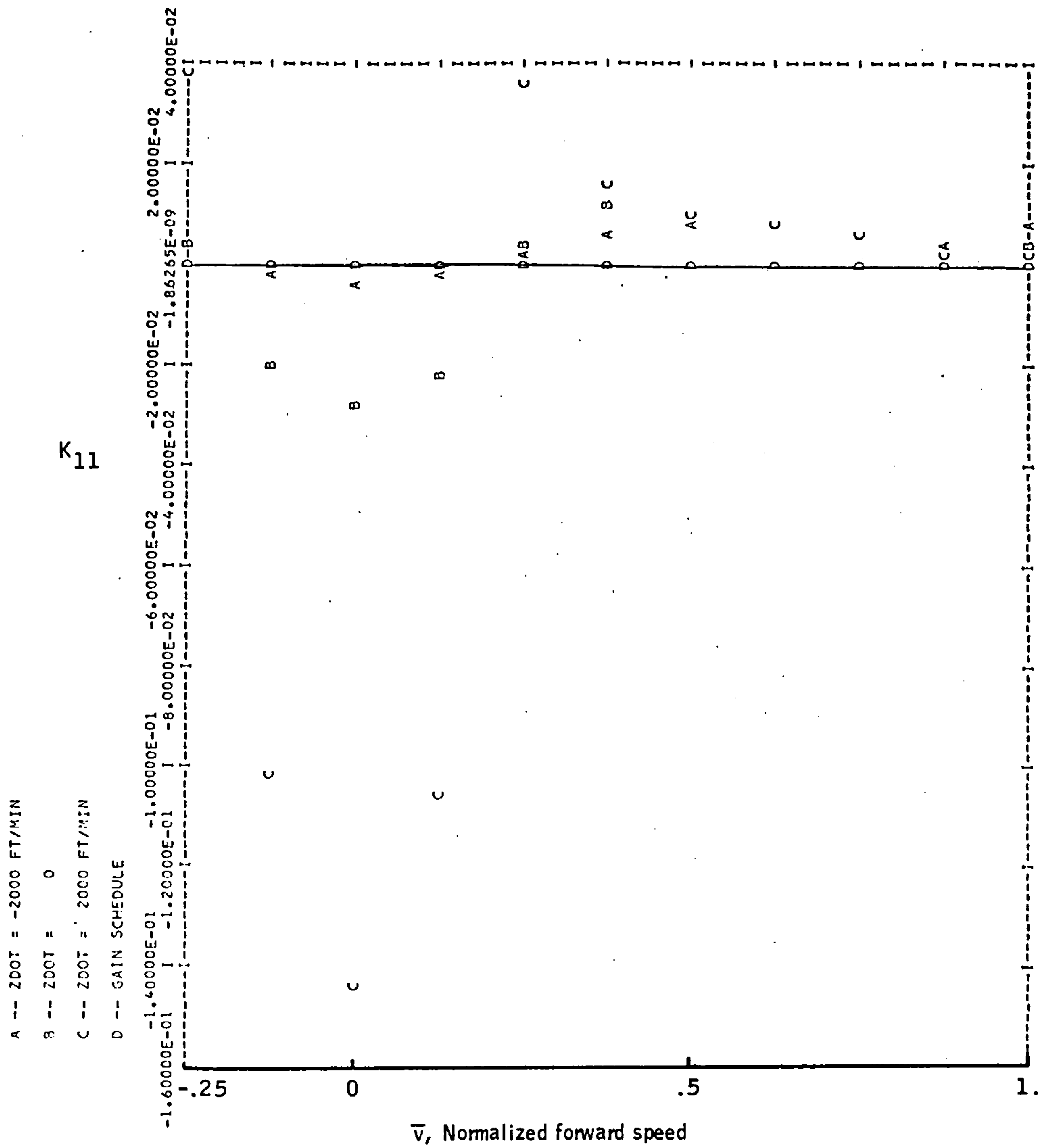

Figure 41. -Element K_{11} versus $\bar{v}$ -- longitudinal axis.

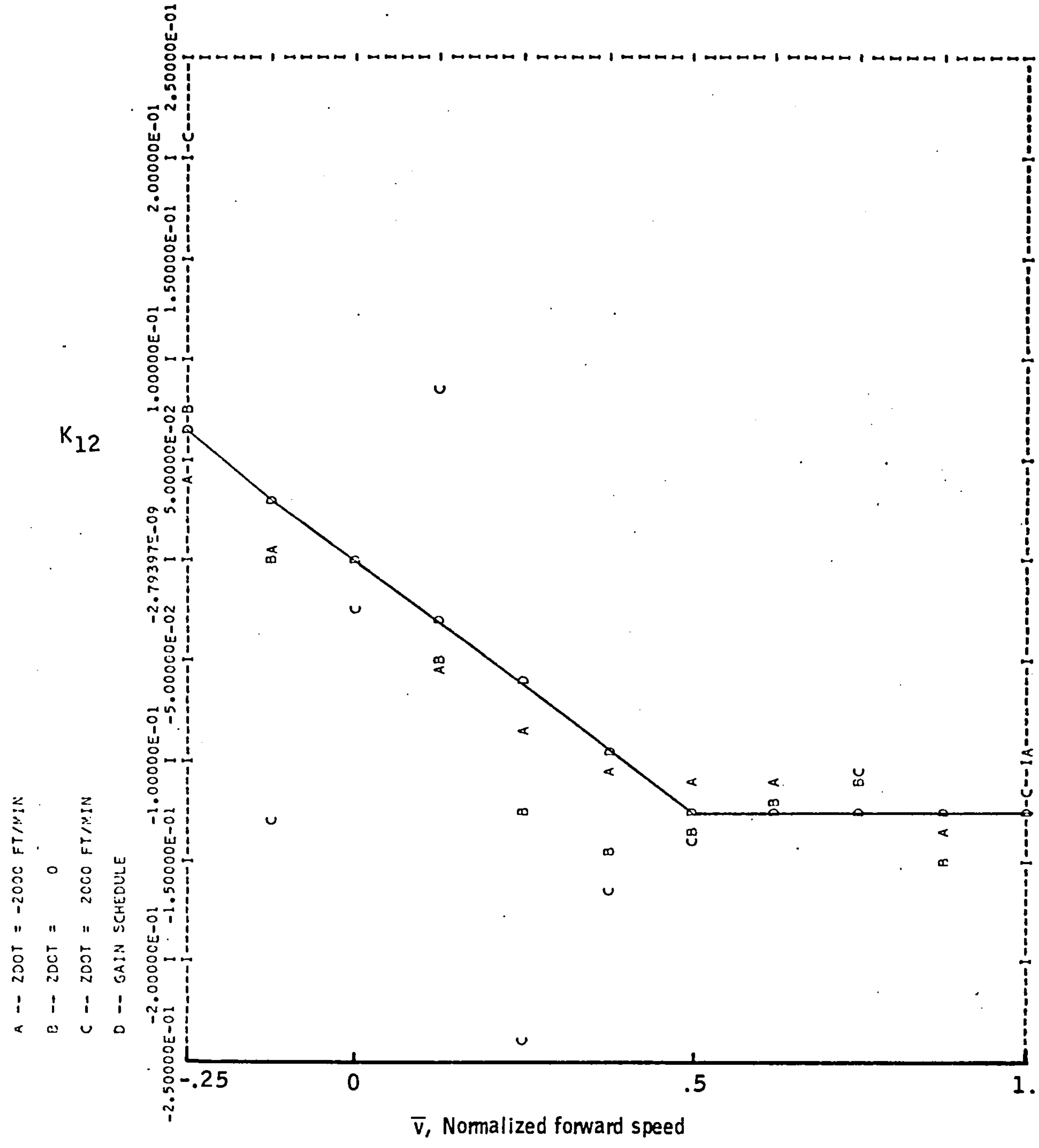

Figure 42. -Element K_{12} versus $\bar{v}$ -- longitudinal axis.

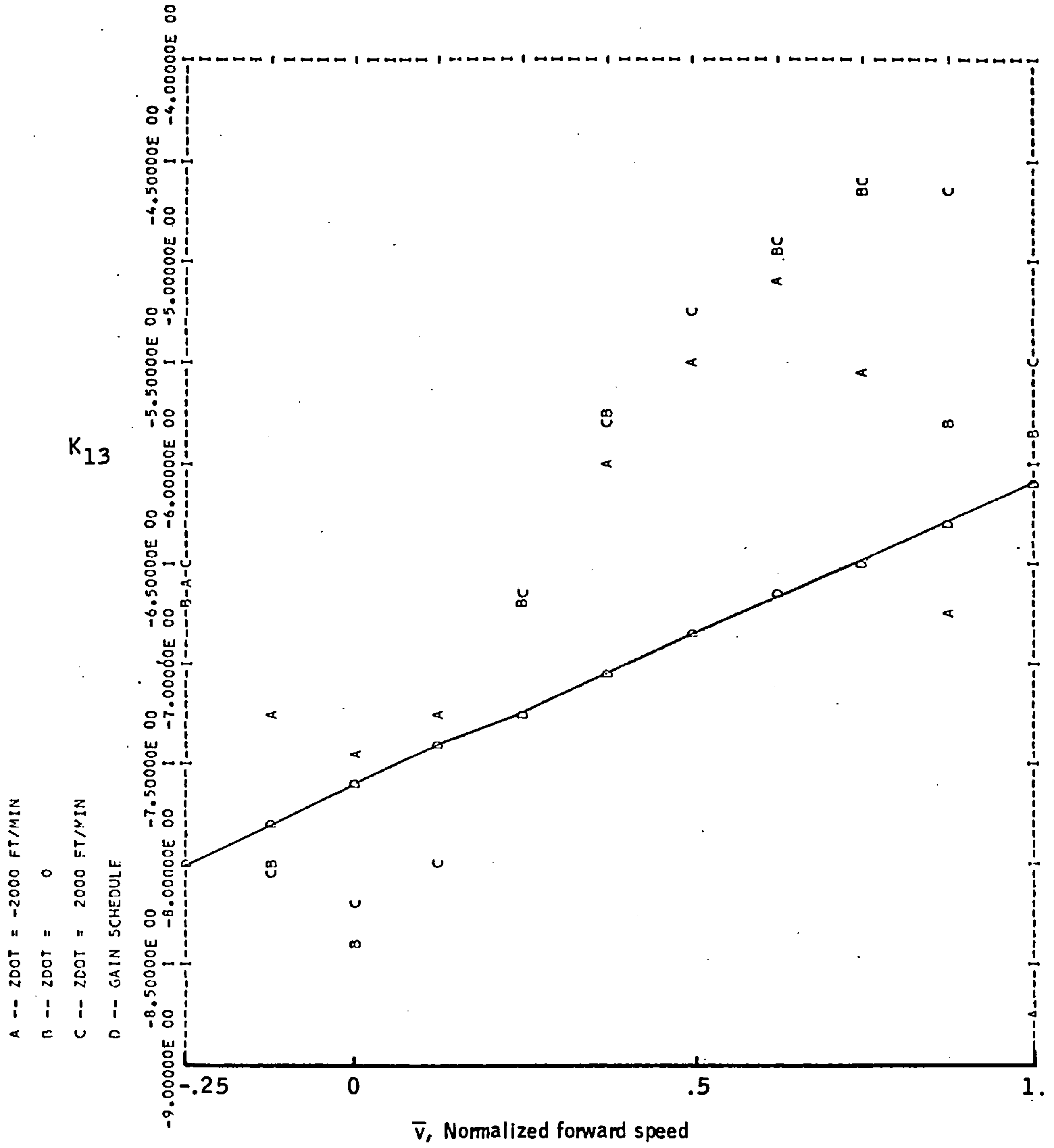

Figure 43. -Element K_{13} versus $\bar{v}$ -- longitudinal axis.

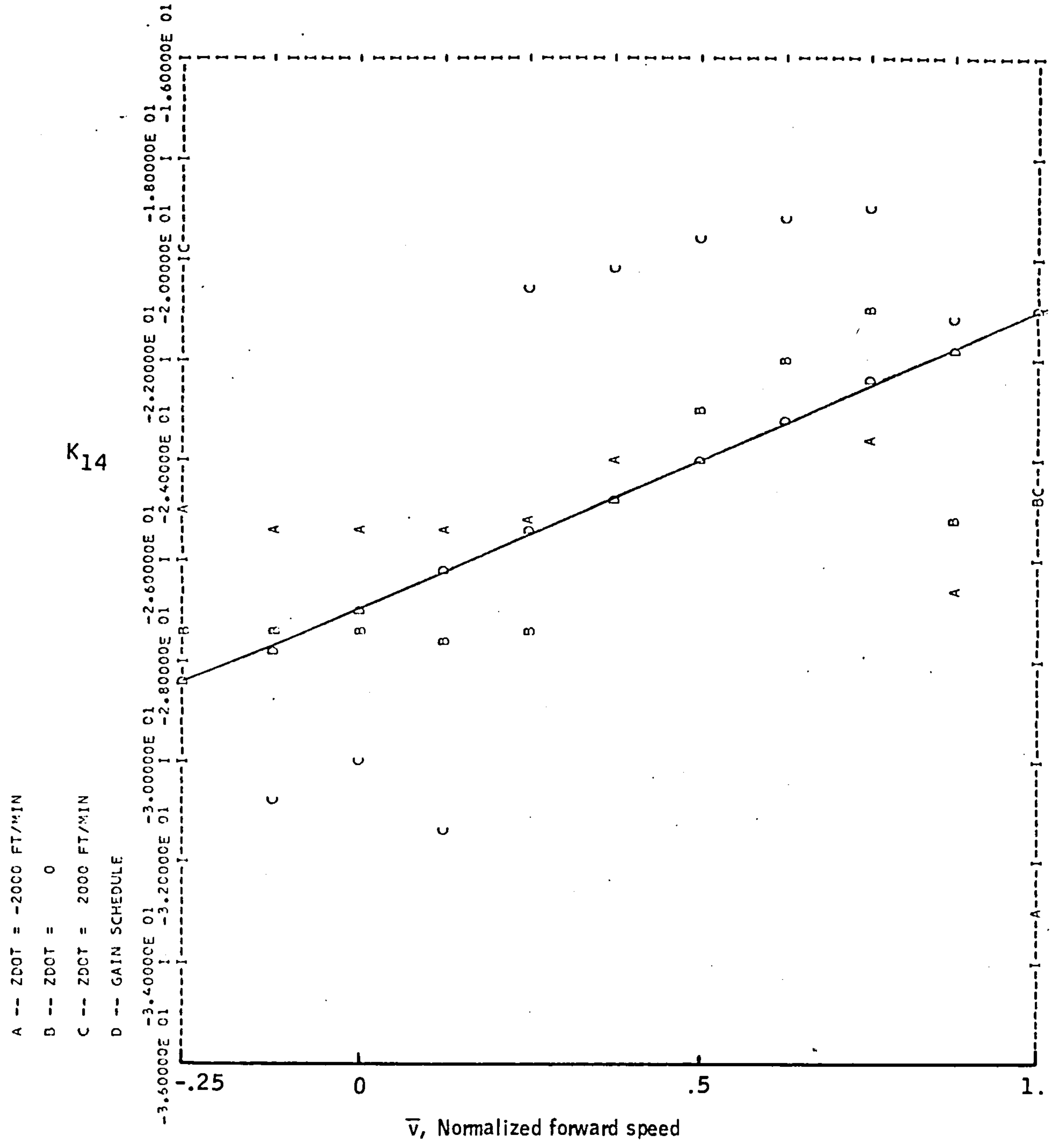

Figure 44. -Element K_{14} versus $\bar{v}$ -- longitudinal axis.

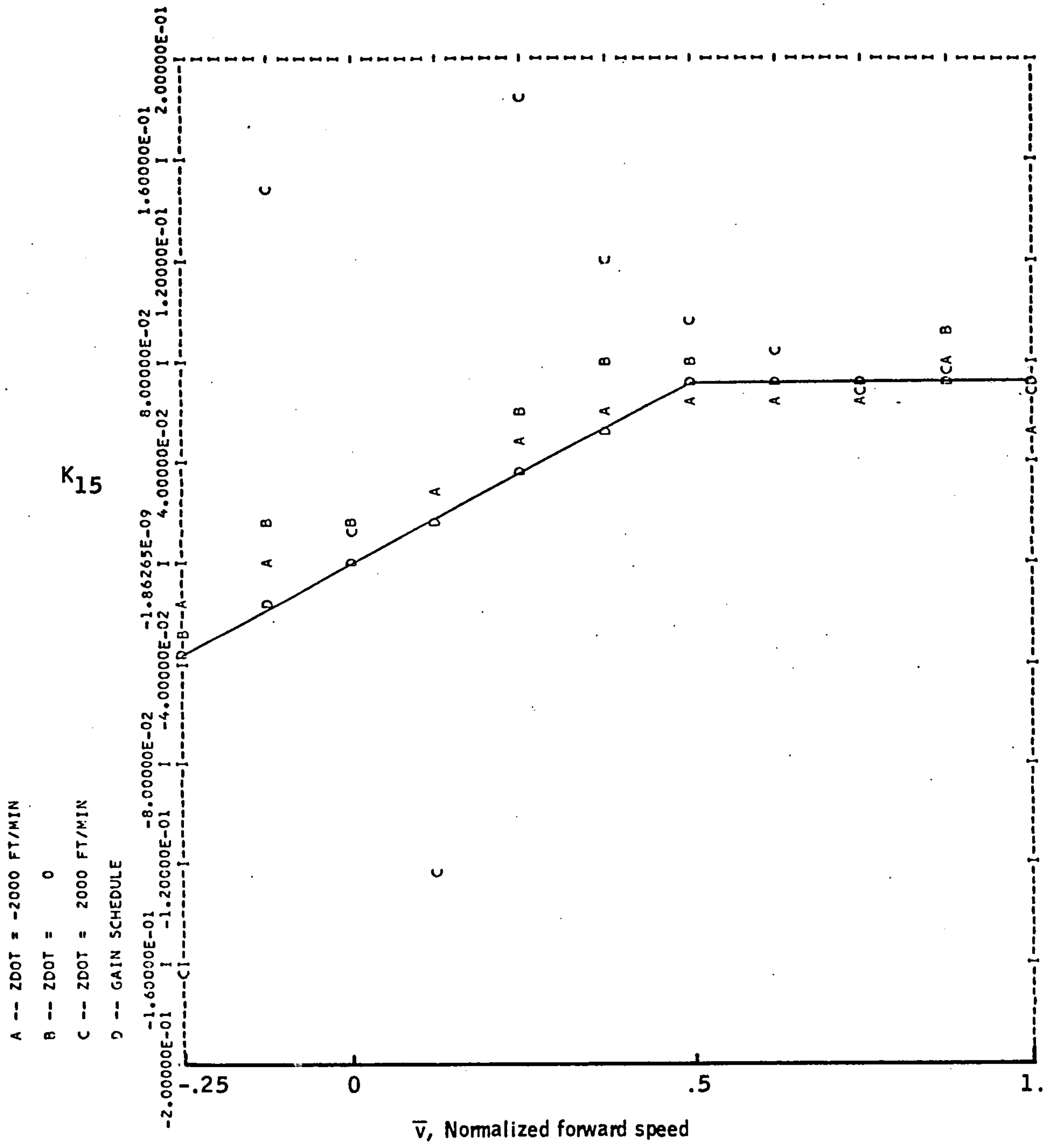

Figure 45. -Element K_{15} versus $\bar{v}$ -- longitudinal axis.

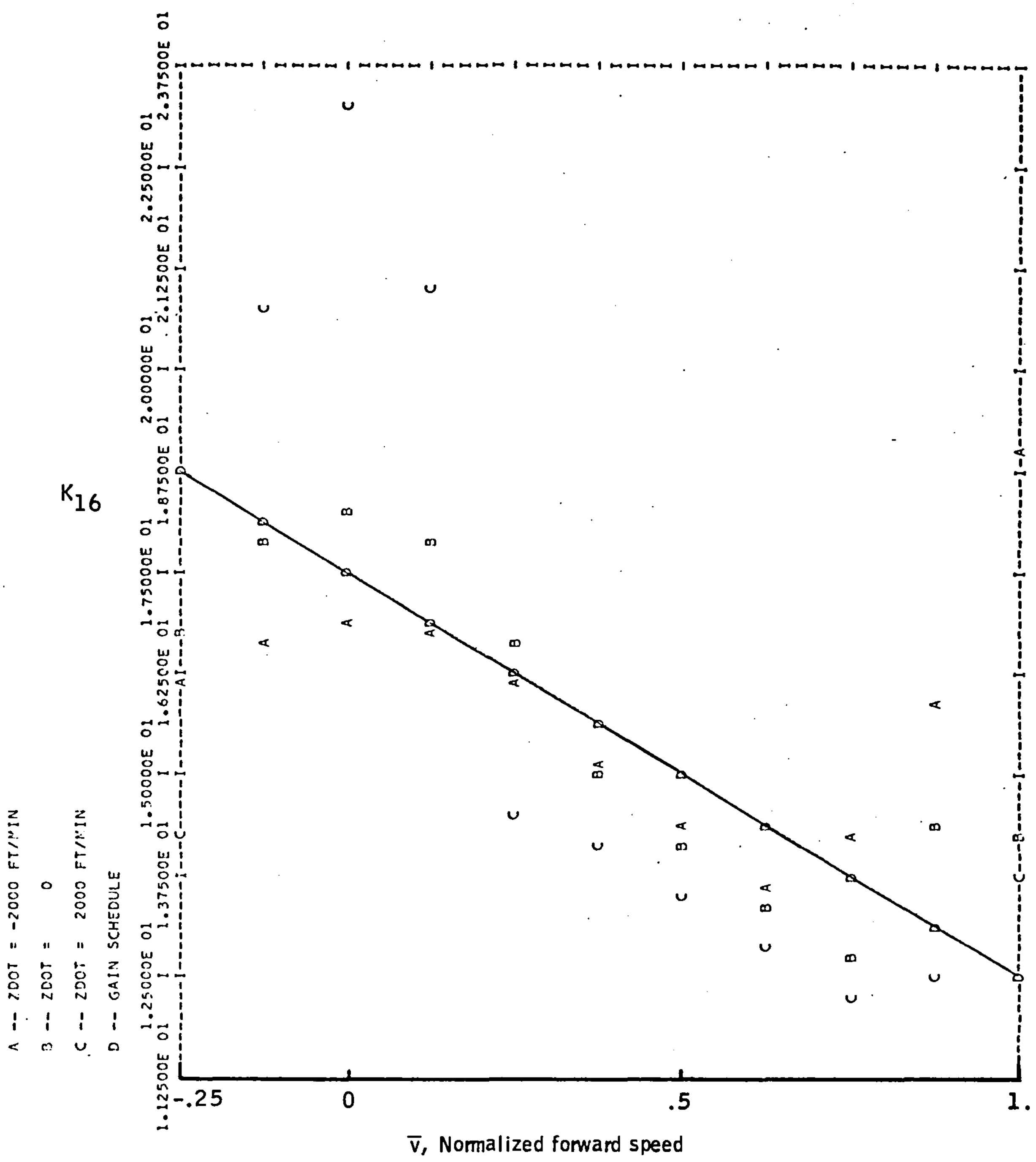

Figure 46. -Element K_{16} versus $\bar{v}$ -- longitudinal axis.

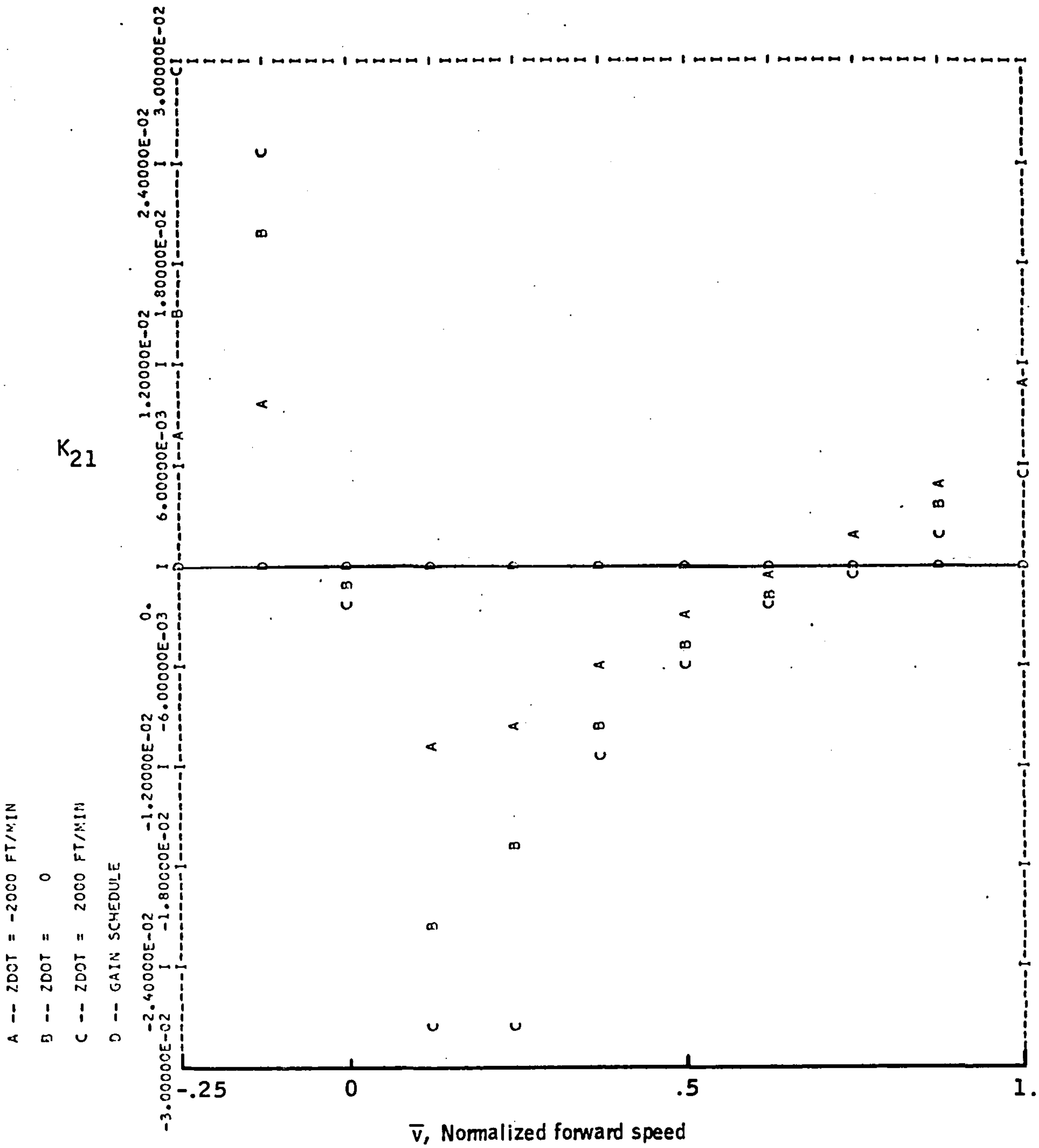

Figure 47. -Element K_{17} versus $\bar{v}$ -- longitudinal axis.

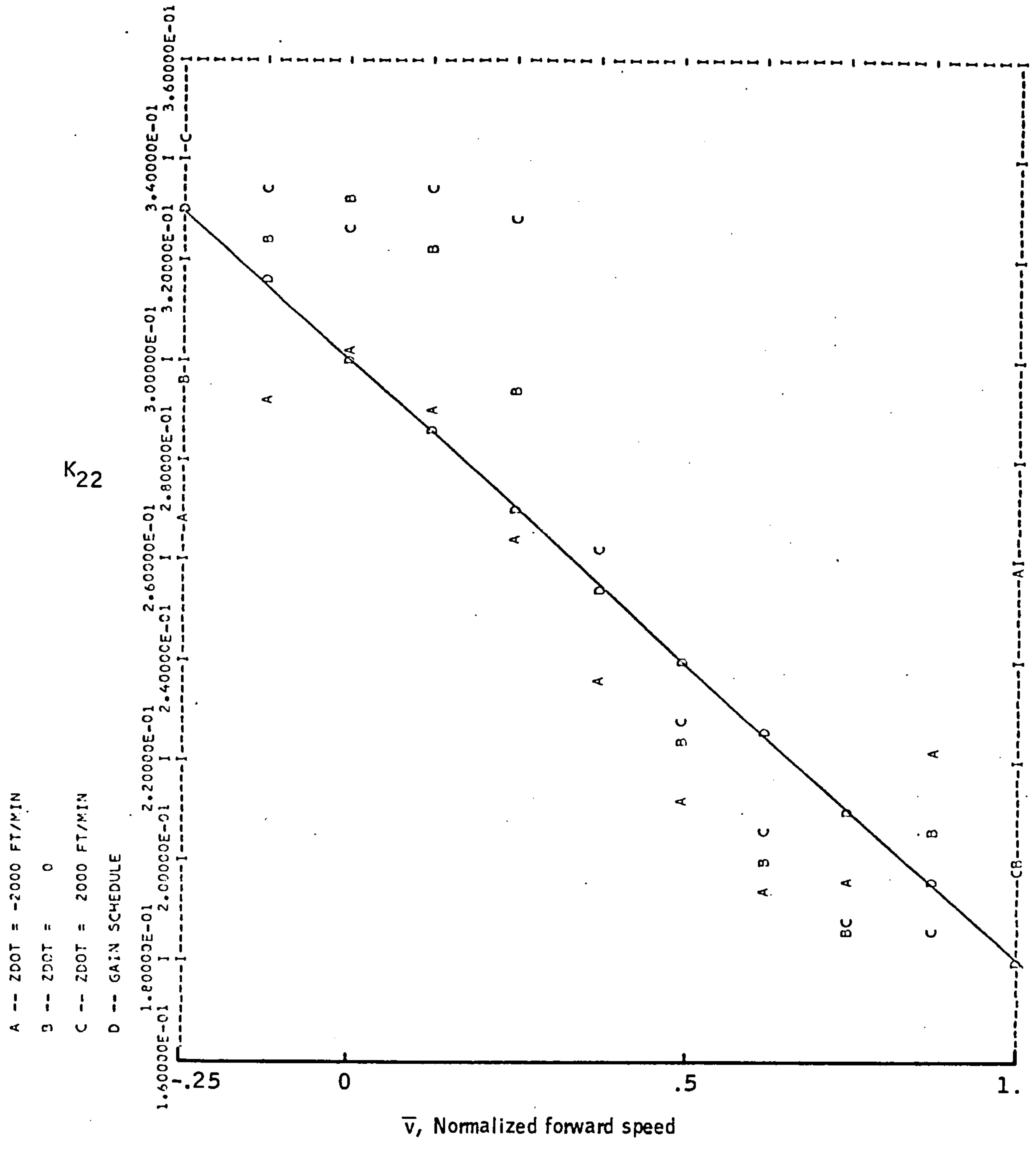

Figure 48. -Element K_{22} versus $\bar{v}$ -- longitudinal axis.

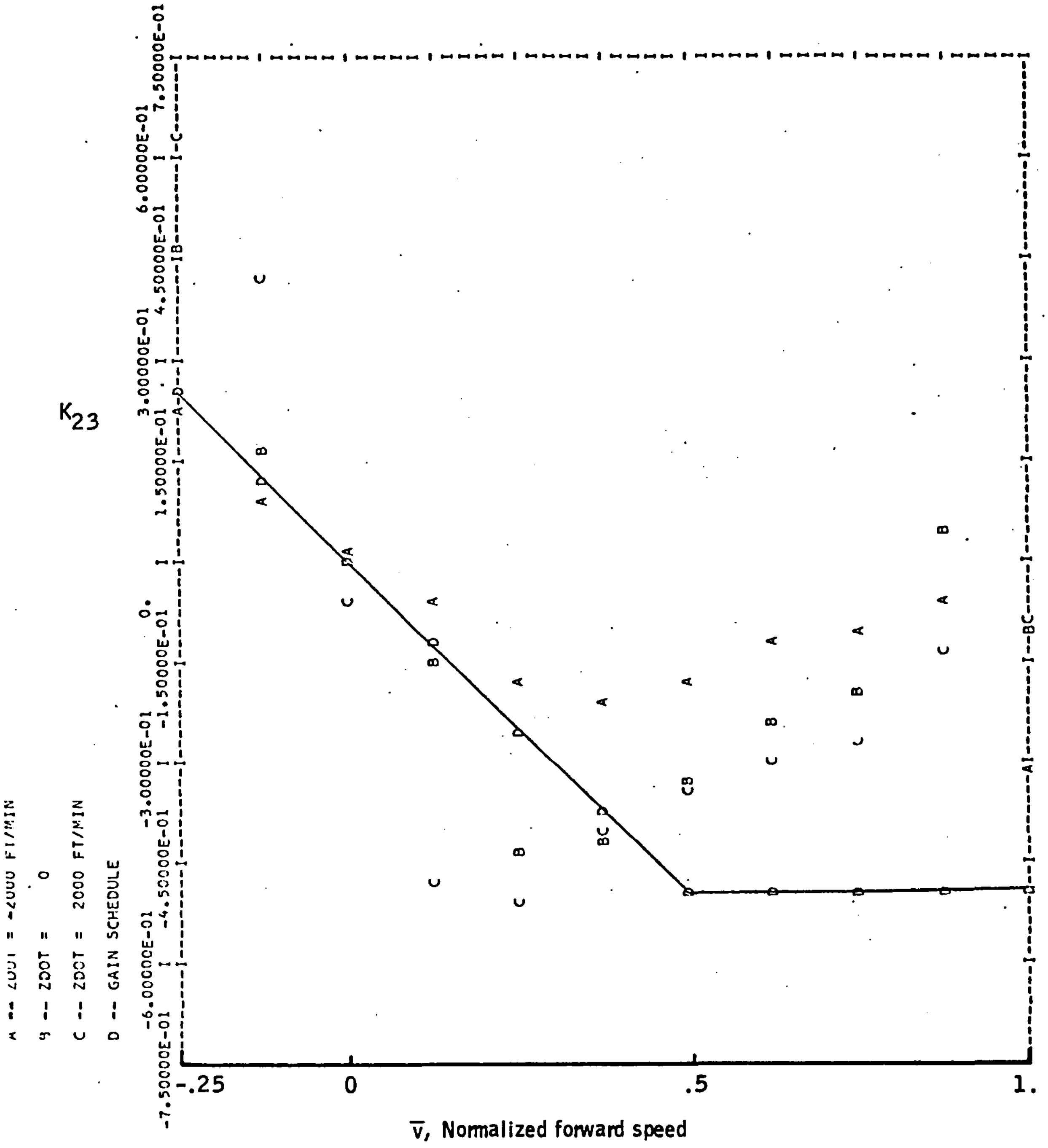

Figure 49. -Element K_{23} versus $\bar{v}$ -- longitudinal axis.

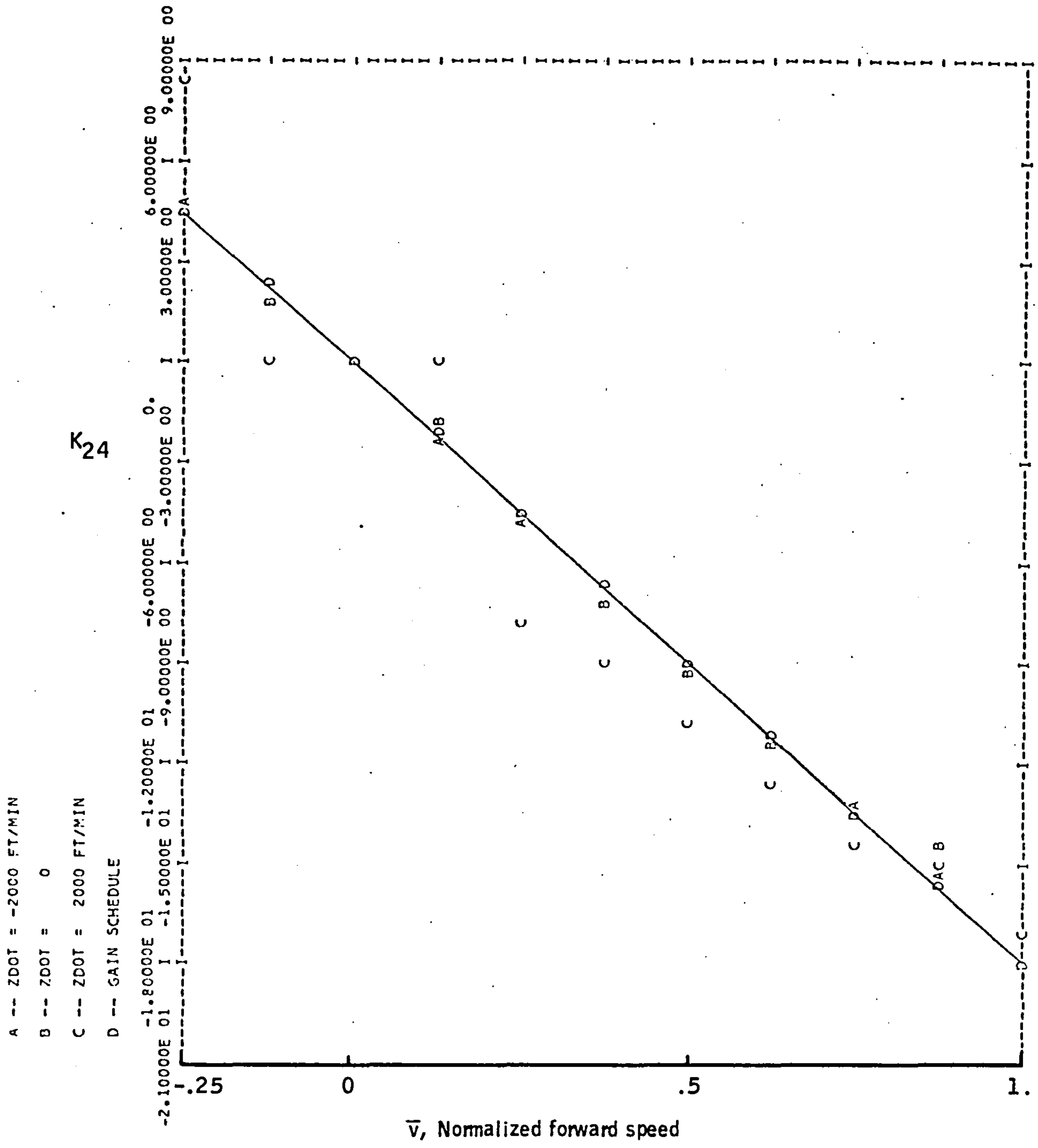

Figure 50.-Element K_{24} versus $\bar{v}$ -- longitudinal axis.

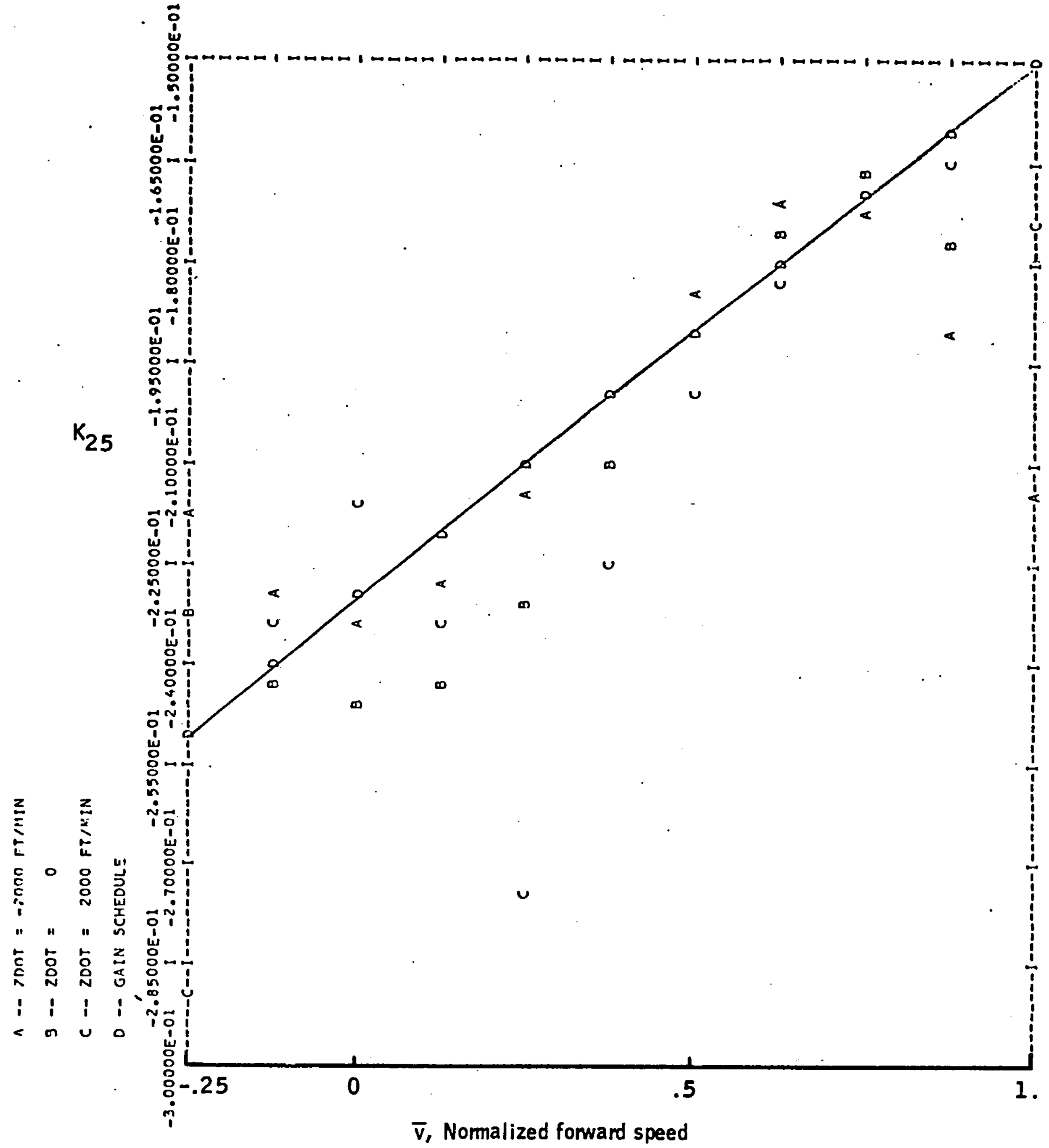

Figure 51. -Element K_{25} versus $\bar{v}$ -- longitudinal axis.

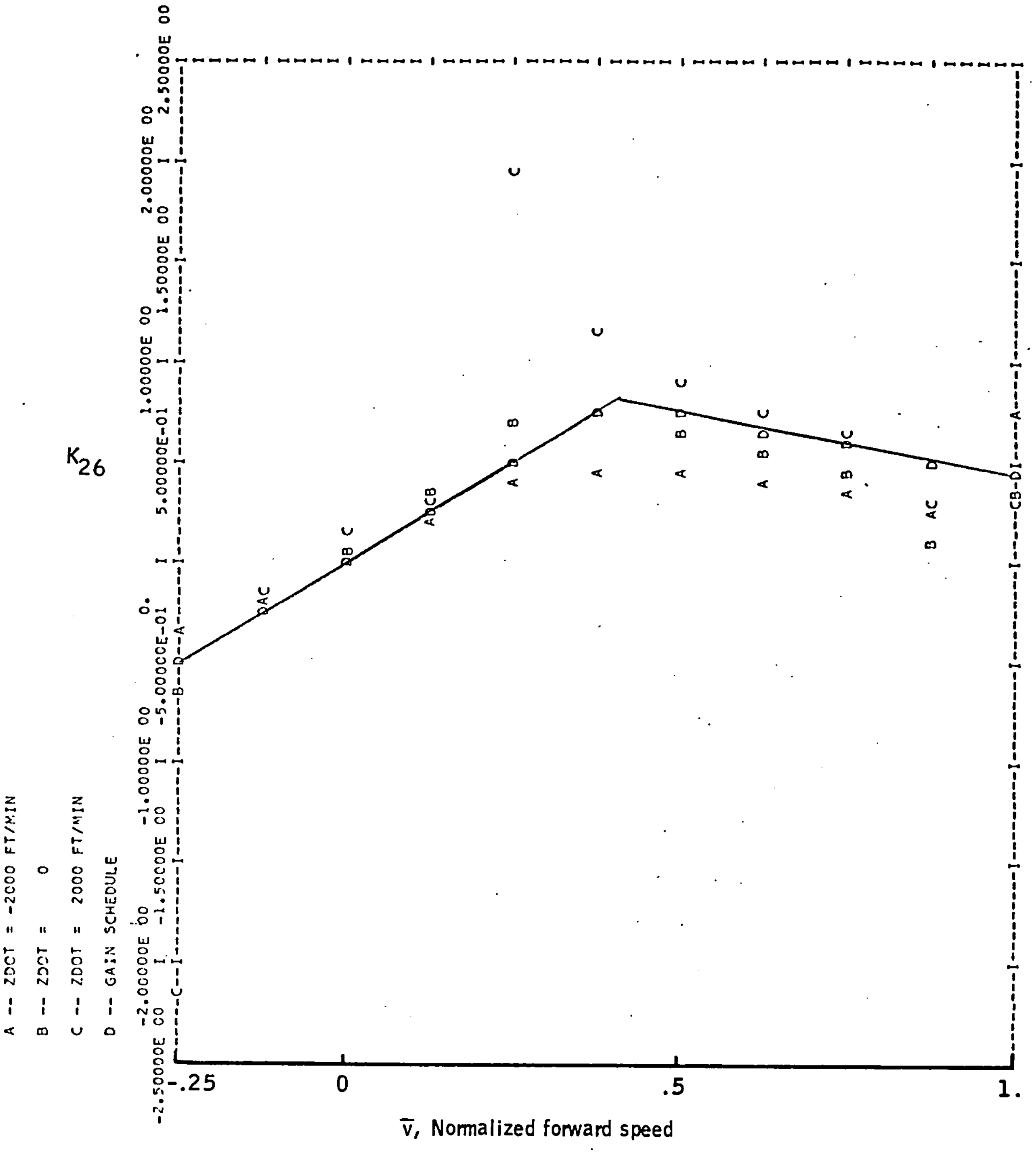

Figure 52. -Element K_{26} versus $\bar{v}$ -- longitudinal axis.

APPENDIX B
GAINS FOR LATERAL-DIRECTIONAL AXES

Actuator commands have the form:

$$\delta = K_x x + K_u u$$

This appendix contains design values for K_x and K_u for 33 flight conditions plus the $\bar{\bar{v}}$ gain schedule. The design values were computed using the procedure described in Section 5. The two columns of matrix K_u equal columns 6 and 7 of matrix K_x so only K_x is plotted. Thus, individual terms are denoted as

$$\begin{vmatrix} \delta_s \\ \delta_R \end{vmatrix} = \begin{bmatrix} K_{11} & K_{12} & K_{13} & K_{14} & K_{15} & K_{16} & K_{17} \\ K_{21} & K_{21} & K_{23} & K_{24} & K_{25} & K_{26} & K_{27} \end{bmatrix} \begin{vmatrix} v \\ p \\ r \\ \phi \\ \psi \\ I_1 \\ I_2 \end{vmatrix} + \begin{bmatrix} K_{16} & K_{17} \\ K_{26} & K_{27} \end{bmatrix} \begin{vmatrix} \phi_c \\ \psi_c \end{vmatrix}$$

The data, in the form of computer plots, are presented in Figures 53 through 66.

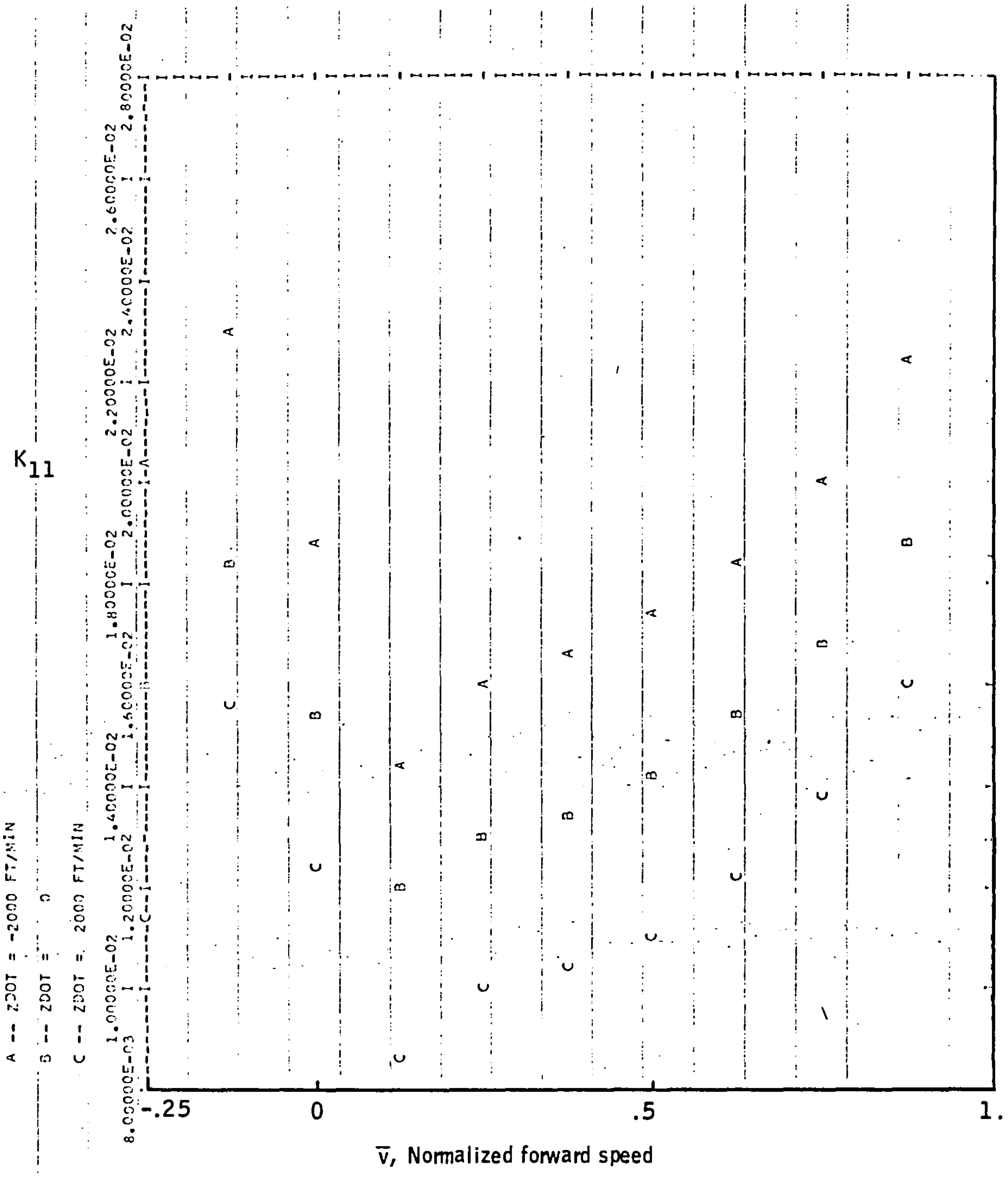

Figure 53. -Element K_{11} versus $\bar{v}$ -- lateral-directional axes.

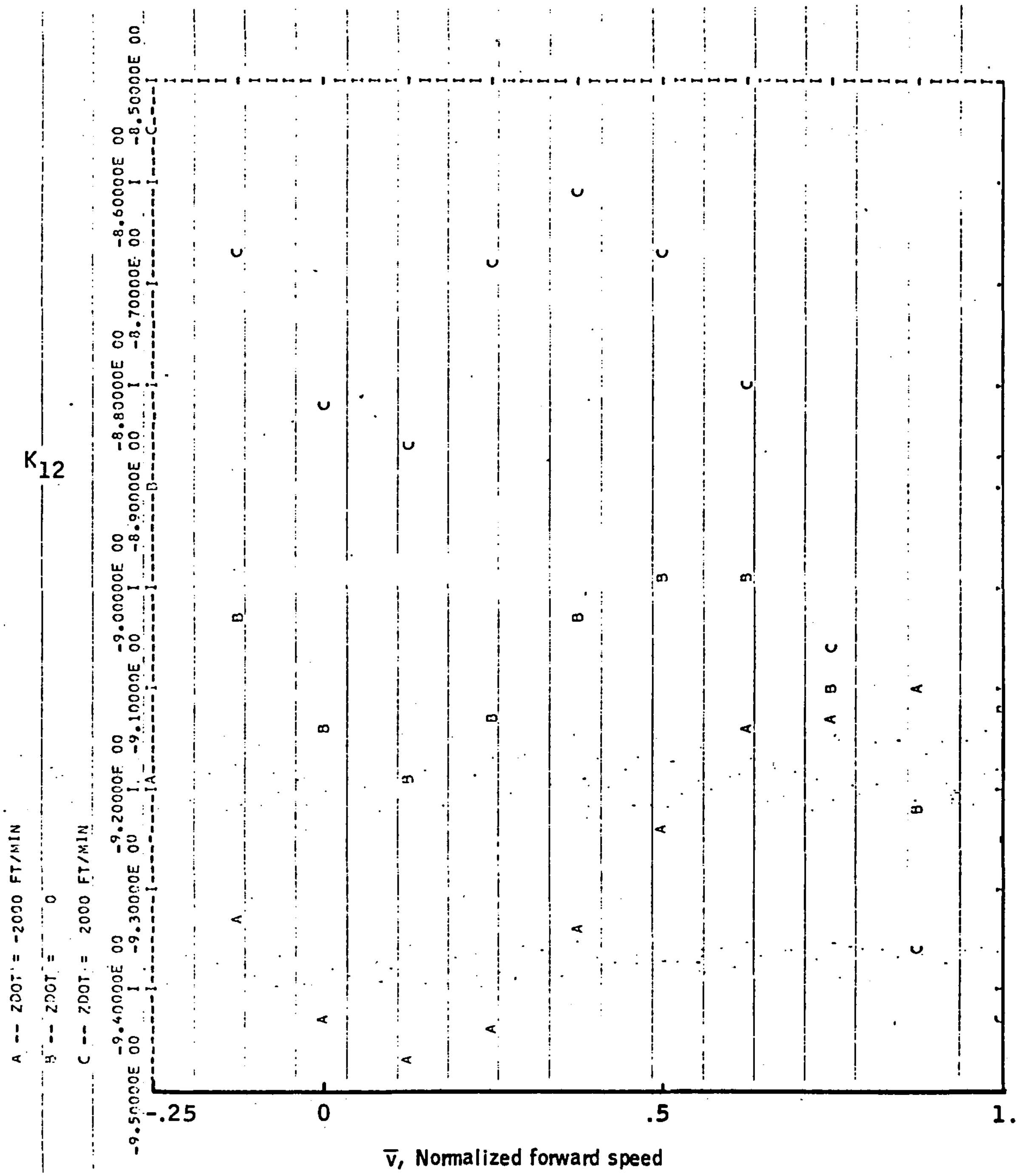

Figure 54. -Element K_{12} versus $\bar{v}$ -- lateral-directional axes.

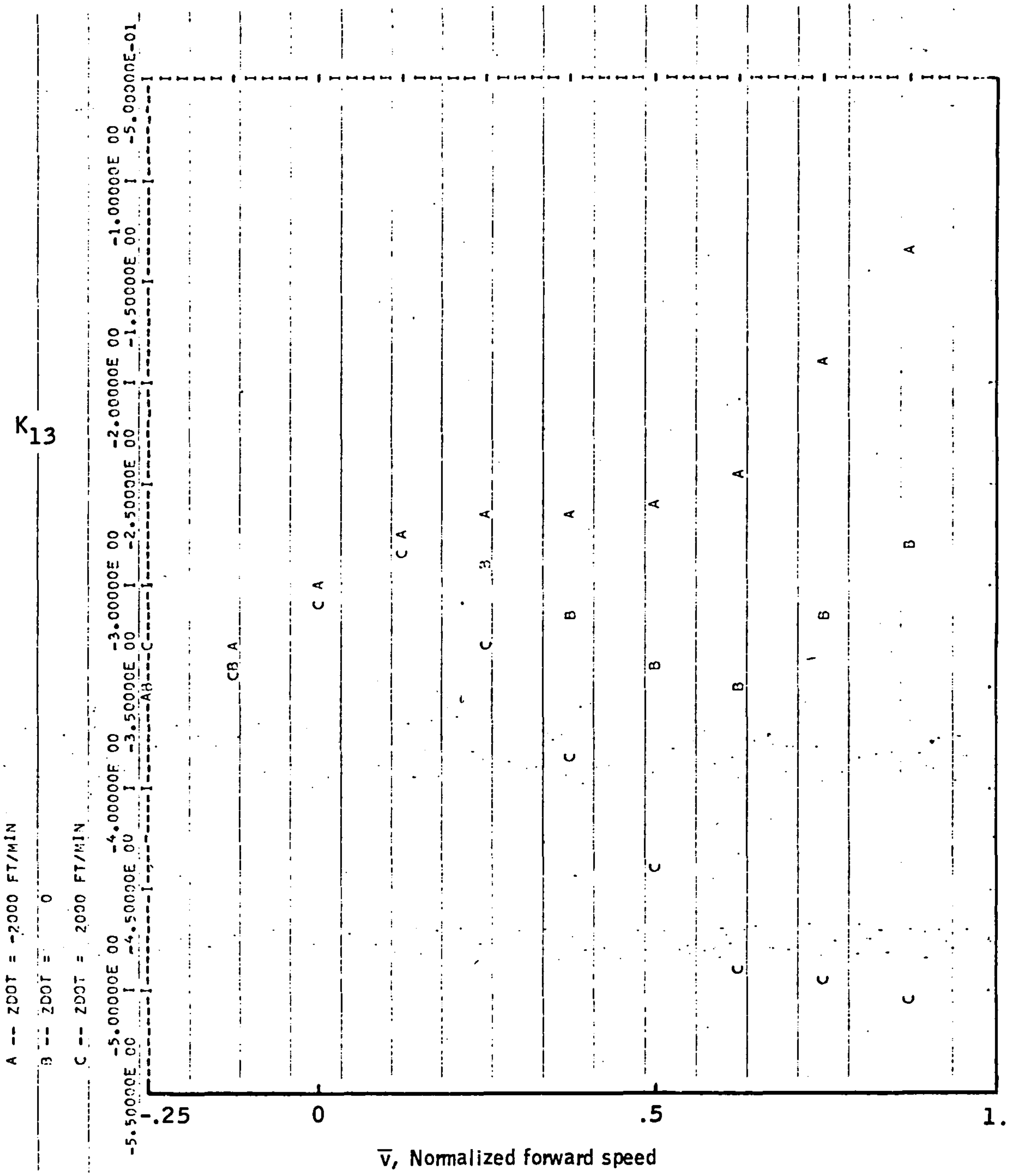

Figure 55. -Element K_{13} versus $\bar{v}$ -- lateral-directional axes.

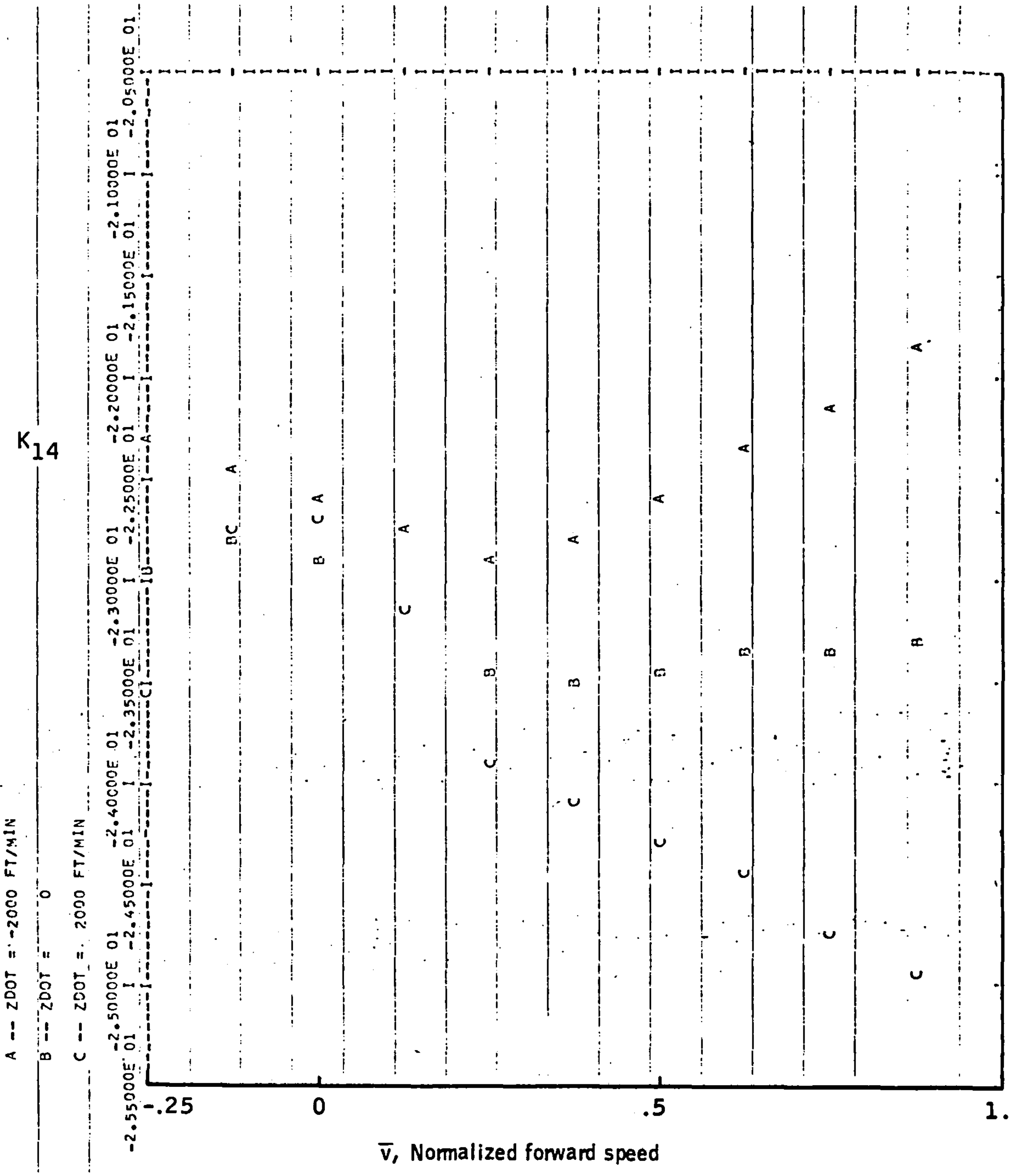

Figure 56. -Element K_{14} versus $\bar{v}$ -- lateral-directional axes.

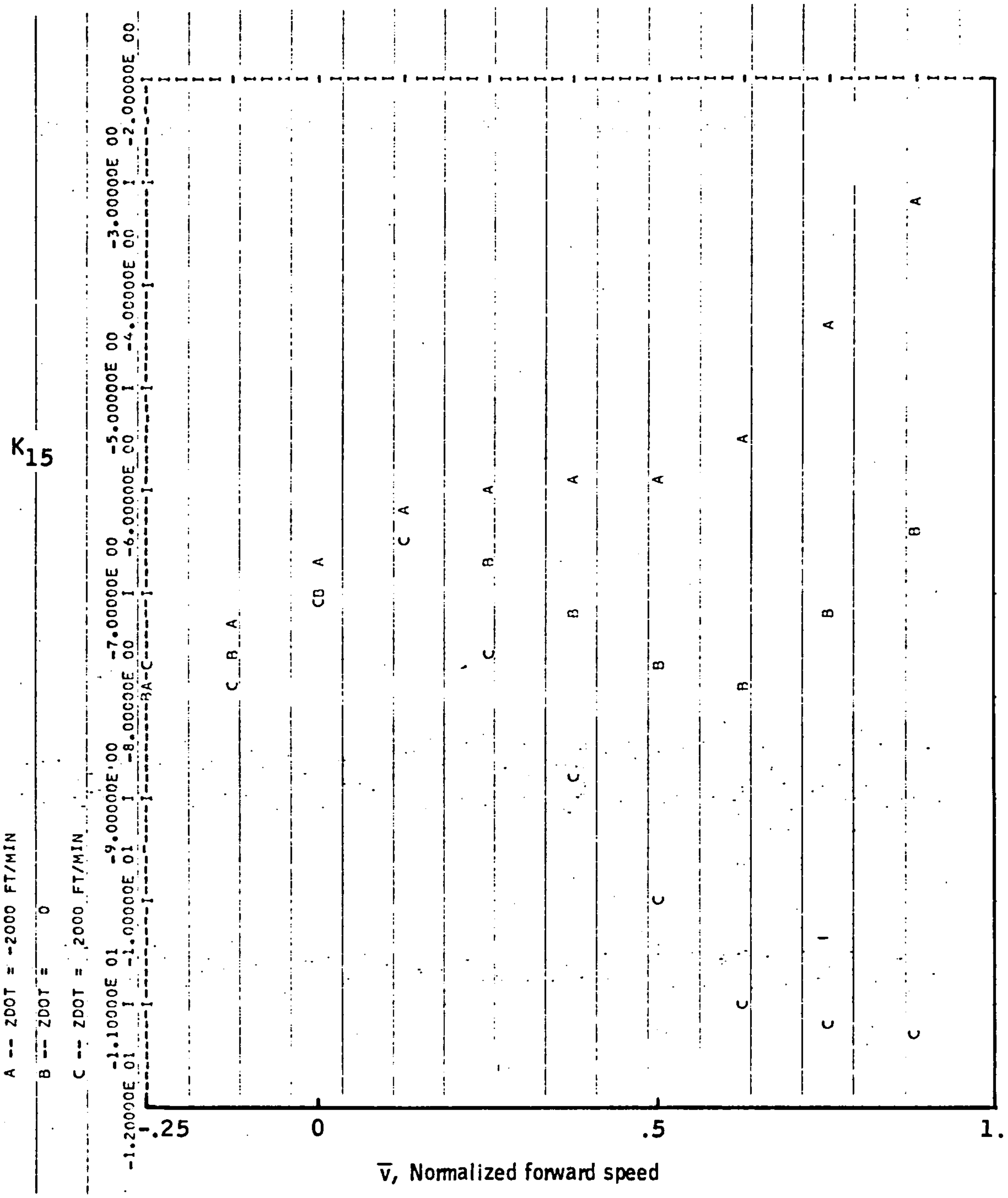

Figure 57. -Element K_{15} versus $\bar{v}$ -- lateral-directional axes.

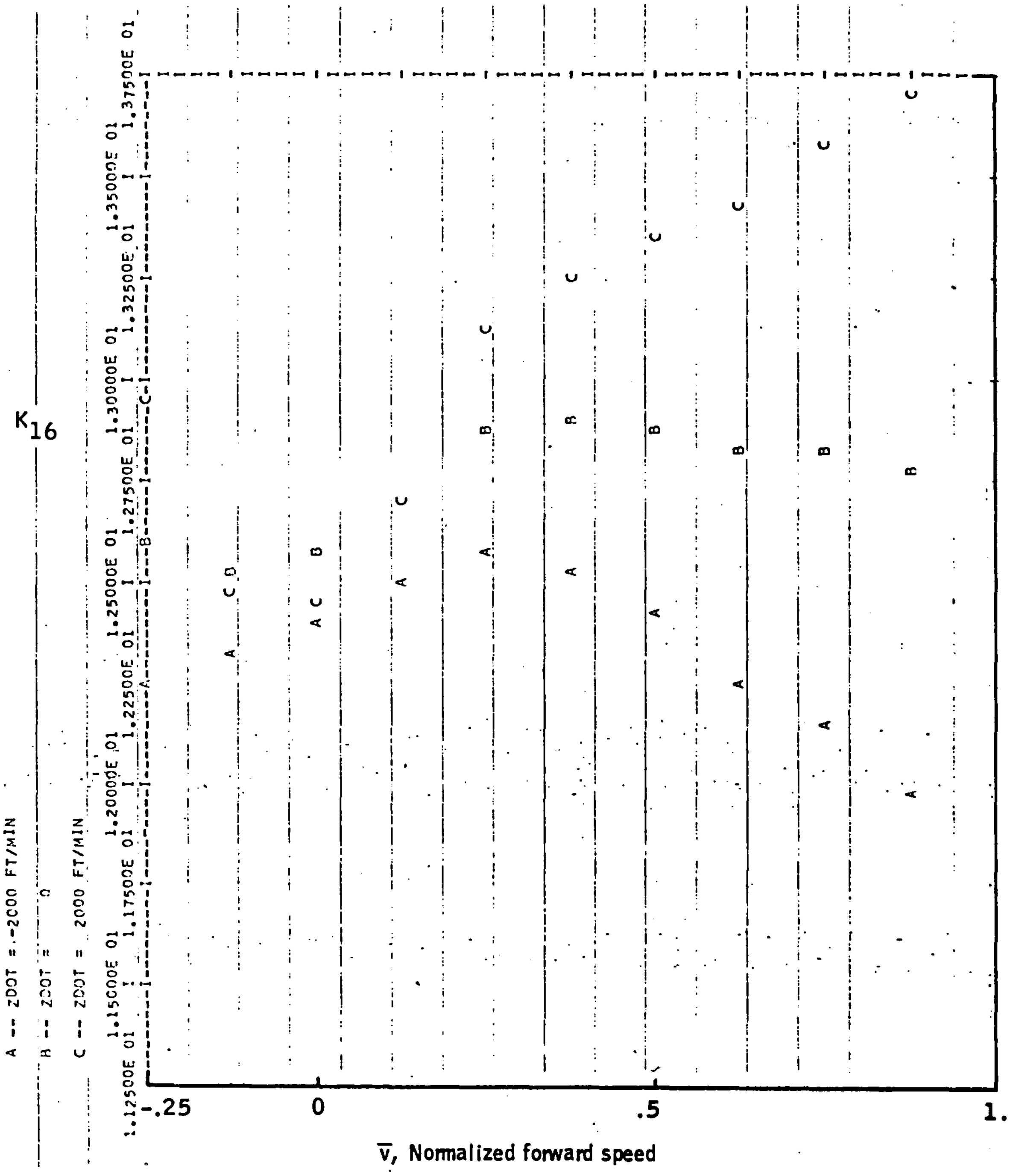

Figure 58. -Element K_{16} versus $\bar{v}$ -- lateral-directional axes.

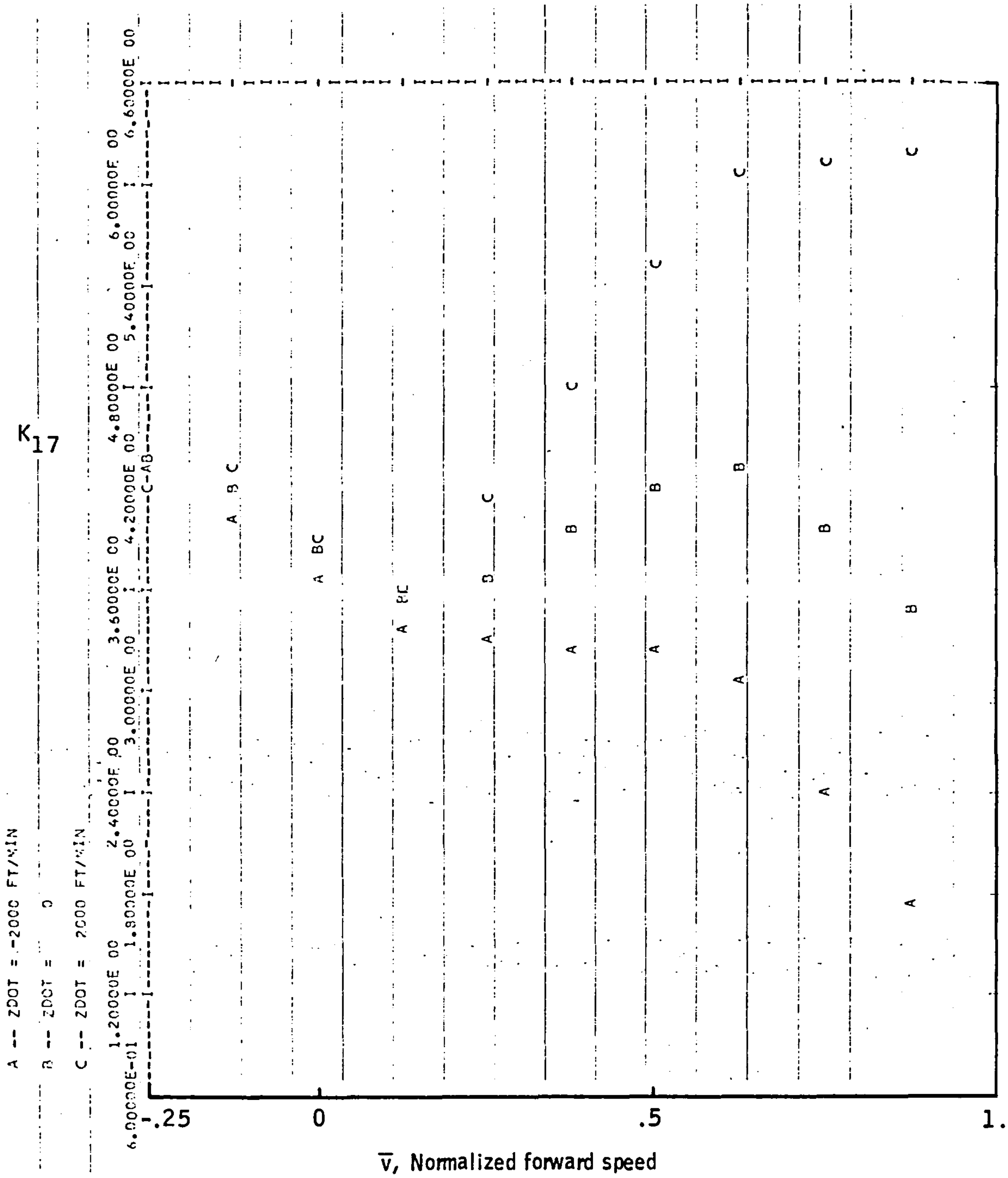

Figure 59. -Element K_{17} versus $\bar{v}$ -- lateral-directional axes.

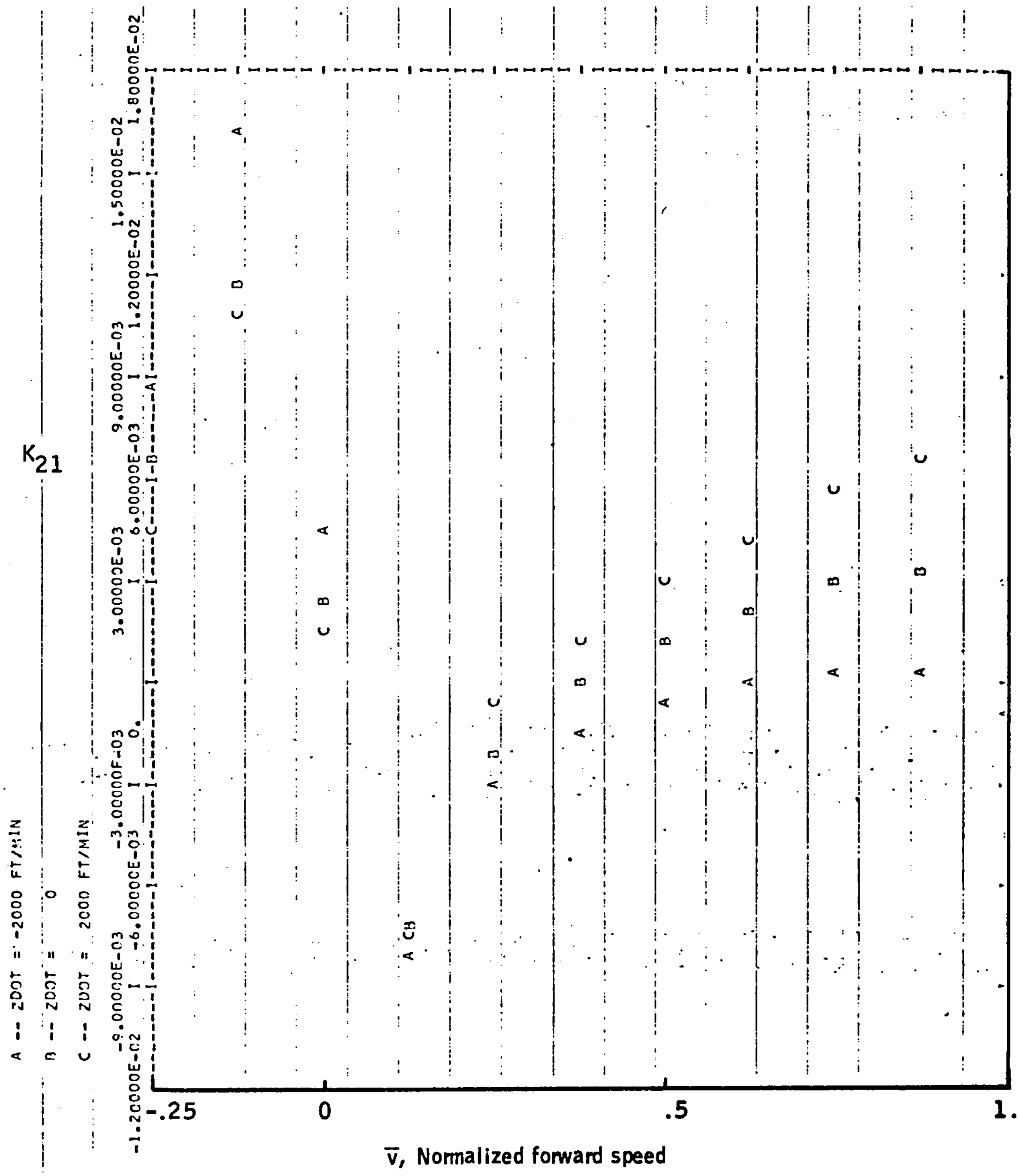

Figure 60. -Element K_{21} versus $\bar{v}$ -- lateral-directional axes.

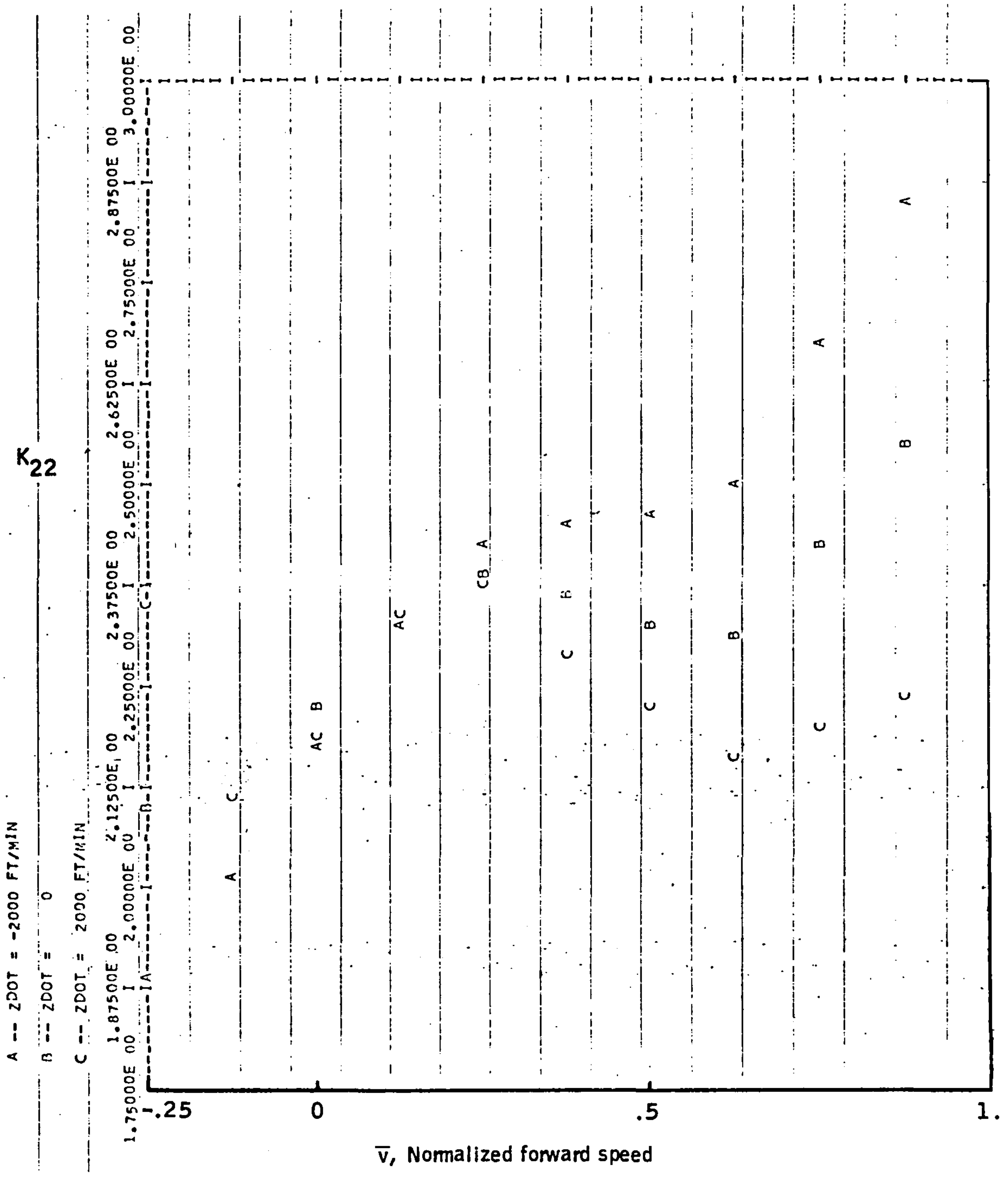

Figure 61. -Element K_{22} versus $\bar{v}$ -- lateral-directional axes.

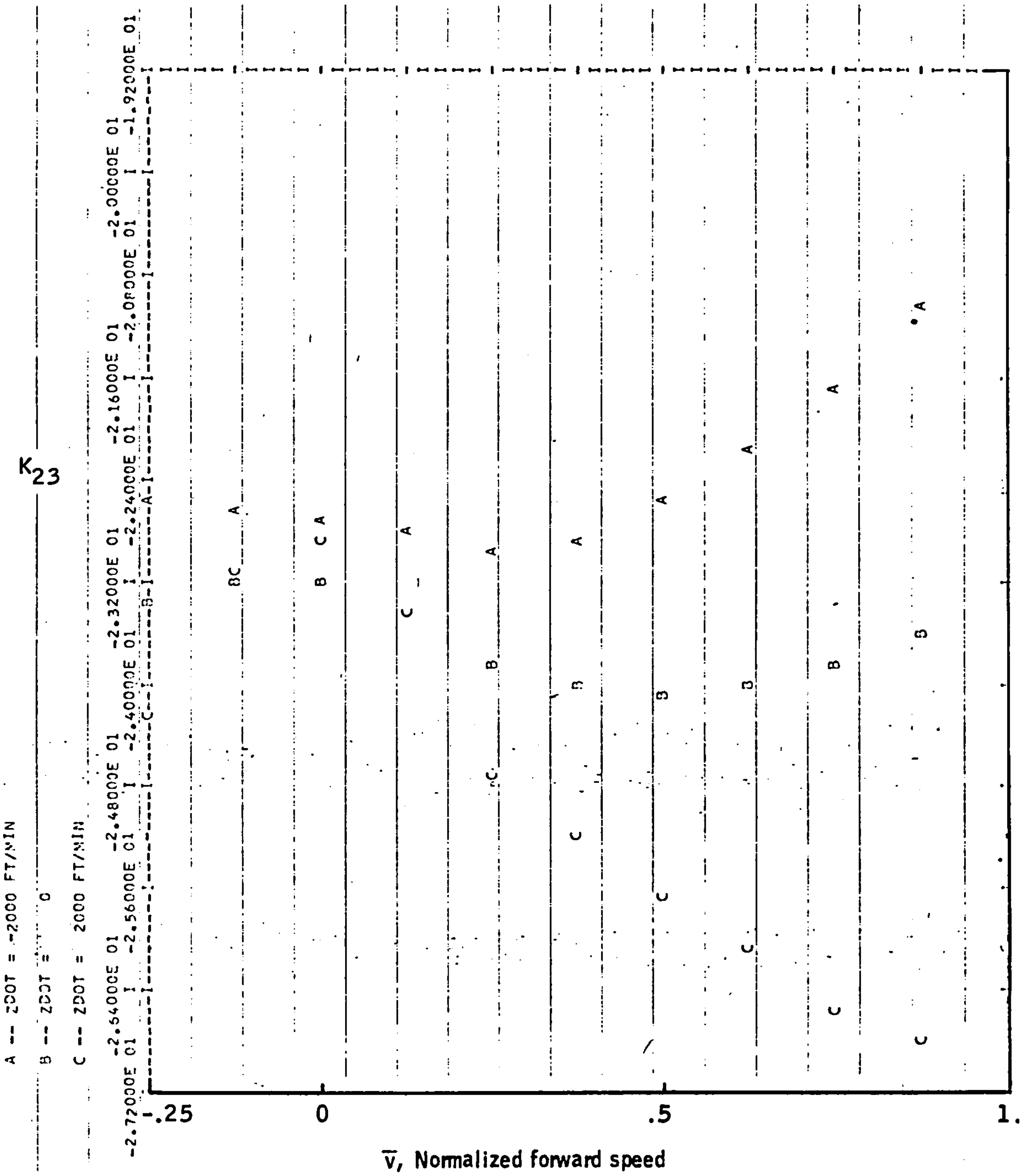

Figure 62. -Element K_{23} versus $\bar{v}$ -- lateral-directional axes.

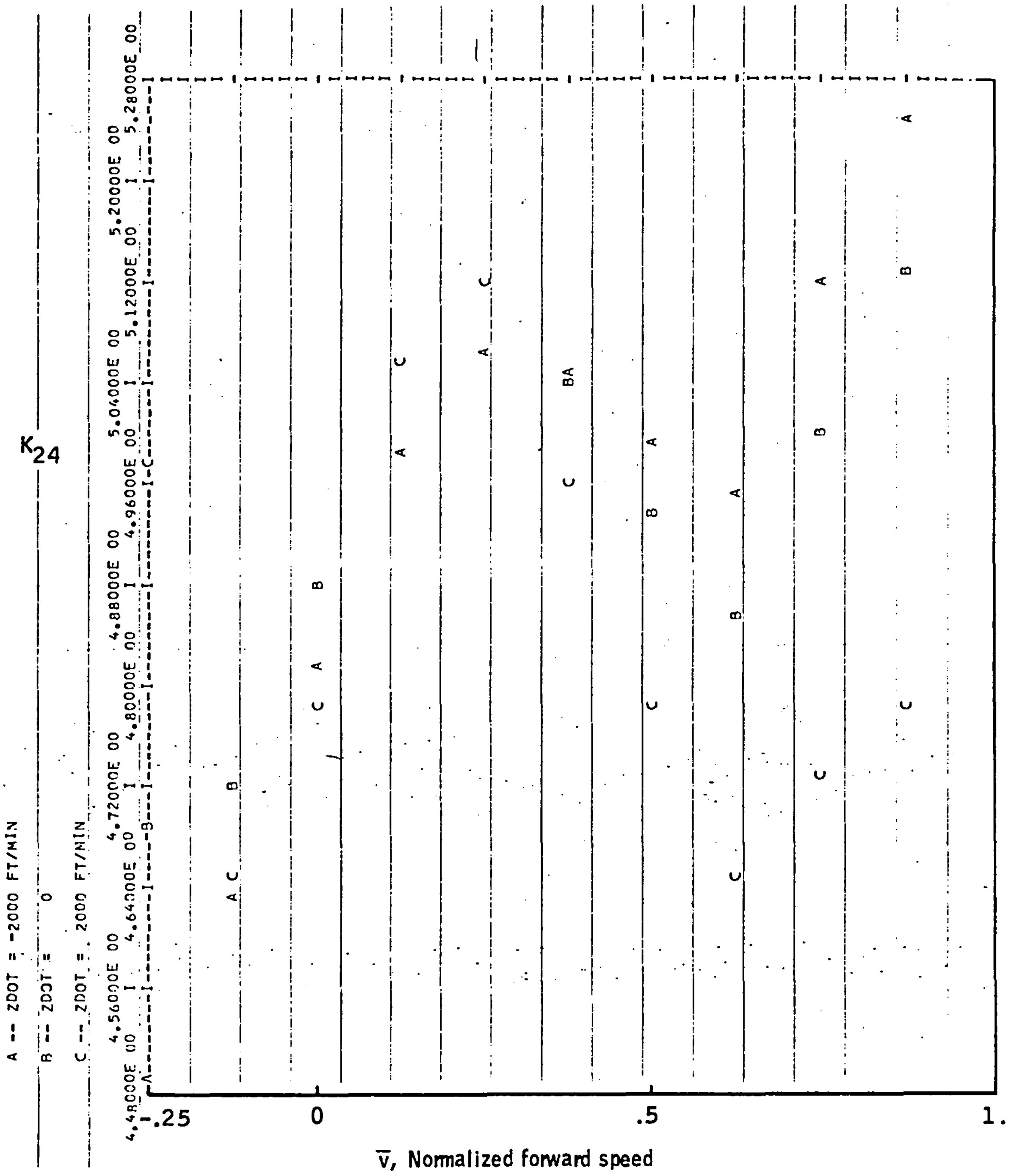

Figure 63. -Element K_{24} versus $\bar{v}$ -- lateral-directional axes.

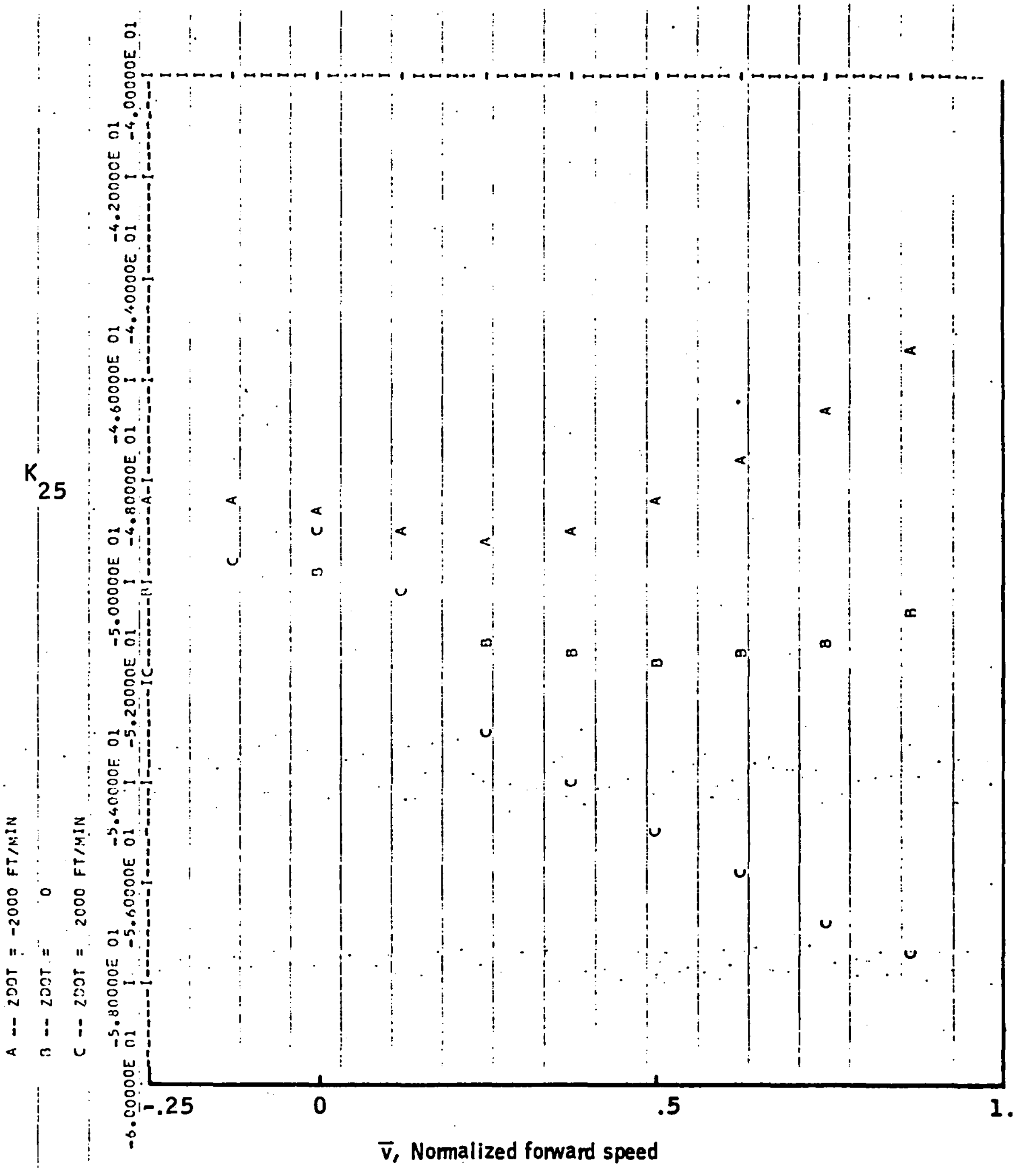

Figure 64. -Element K_{25} versus $\bar{v}$ -- lateral-directional axes.

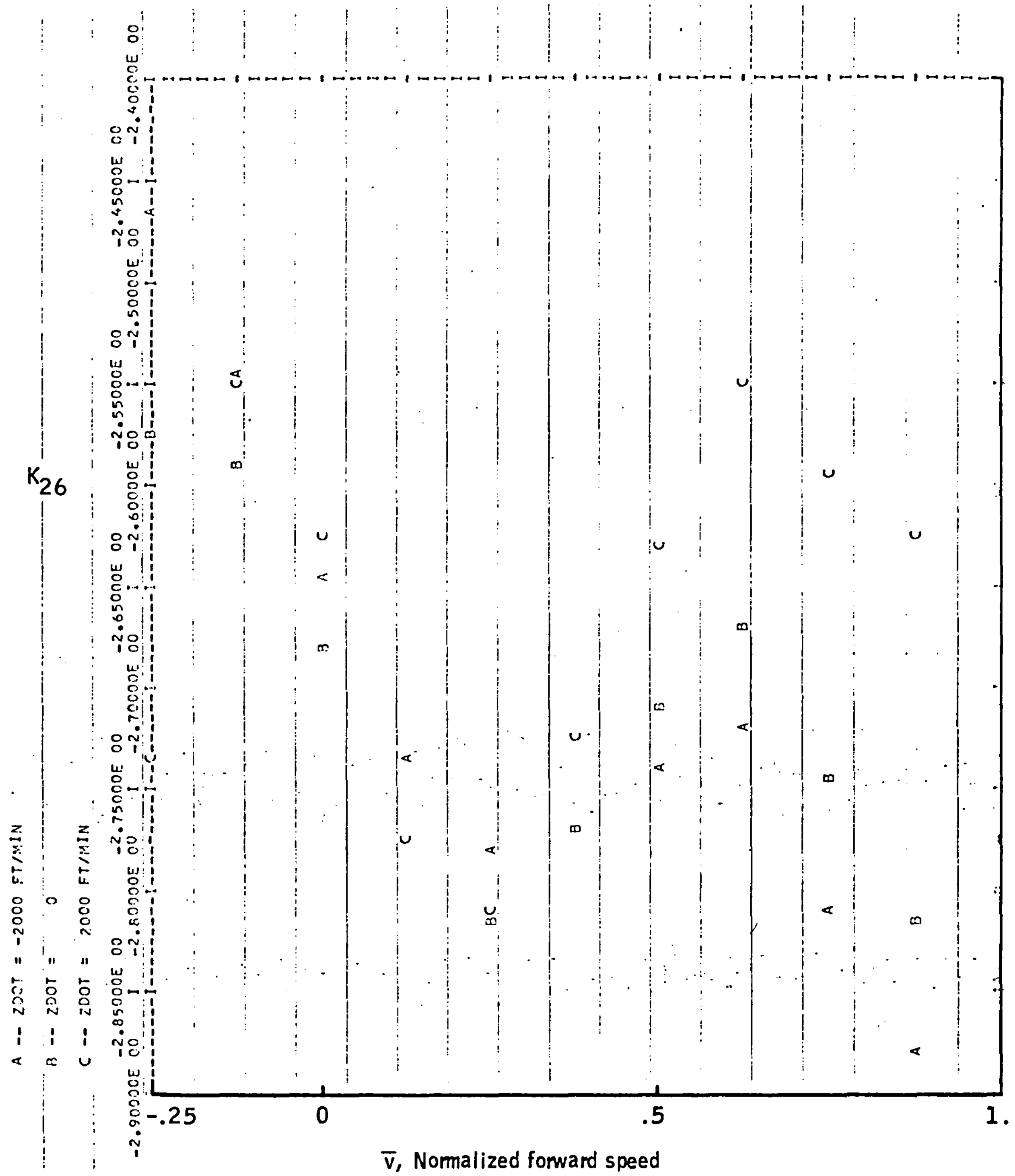

Figure 65. -Element K_{26} versus $\bar{v}$ -- lateral-directional axes.

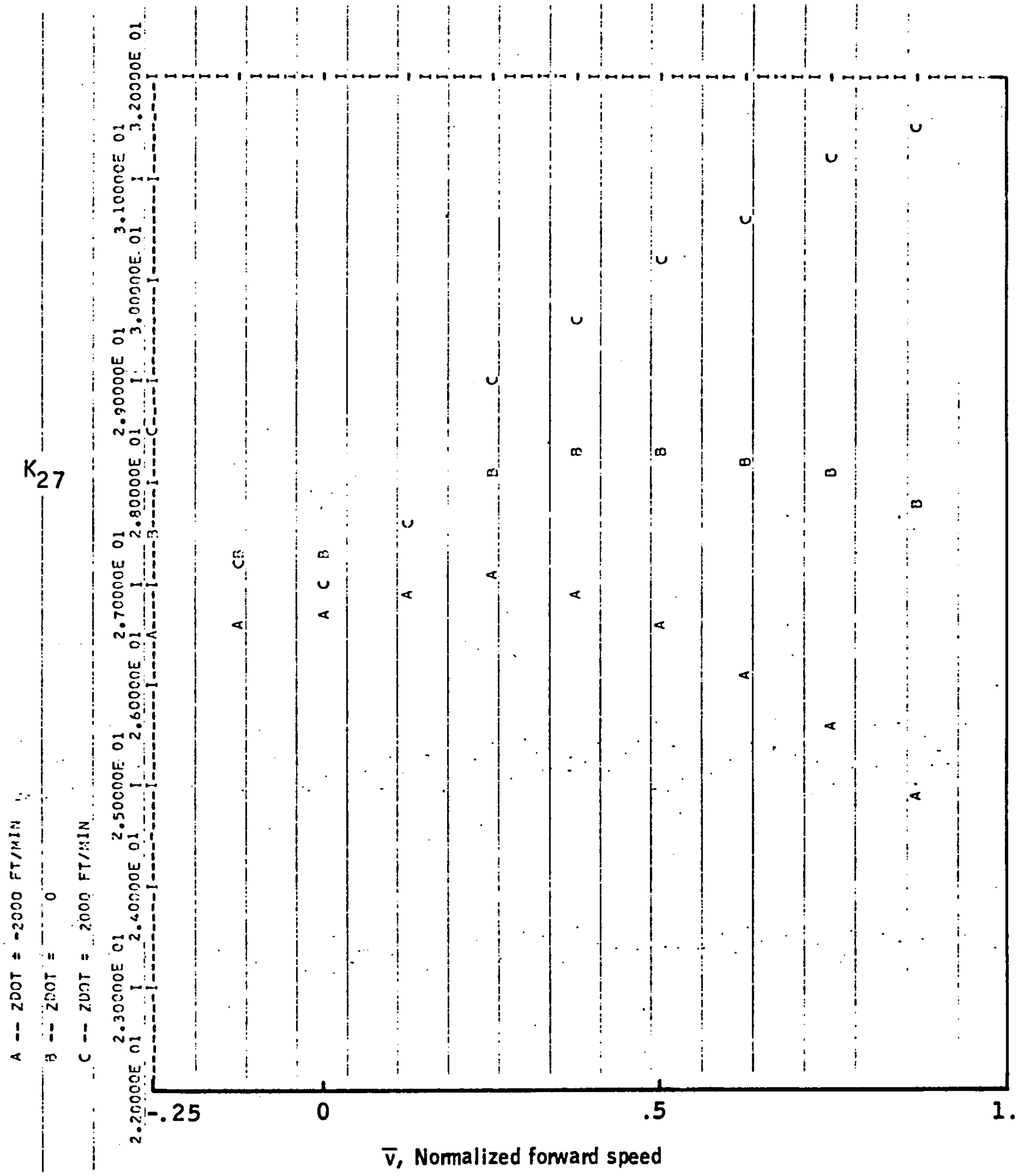

Figure 66. -Element K_{27} versus $\bar{v}$ -- lateral-directional axes.

APPENDIX C

LATERAL-DIRECTIONAL TIME HISTORIES

This appendix contains time histories of the lateral-axis controller in response to ϕ and ψ commands. The traces were generated with the VALT simulation at NASA-LRC. Three flight conditions are given: hover, 41.2 m/s forward velocity, and 79.3 m/s forward velocity.

The data are presented in Figures 67, 68, and 69.

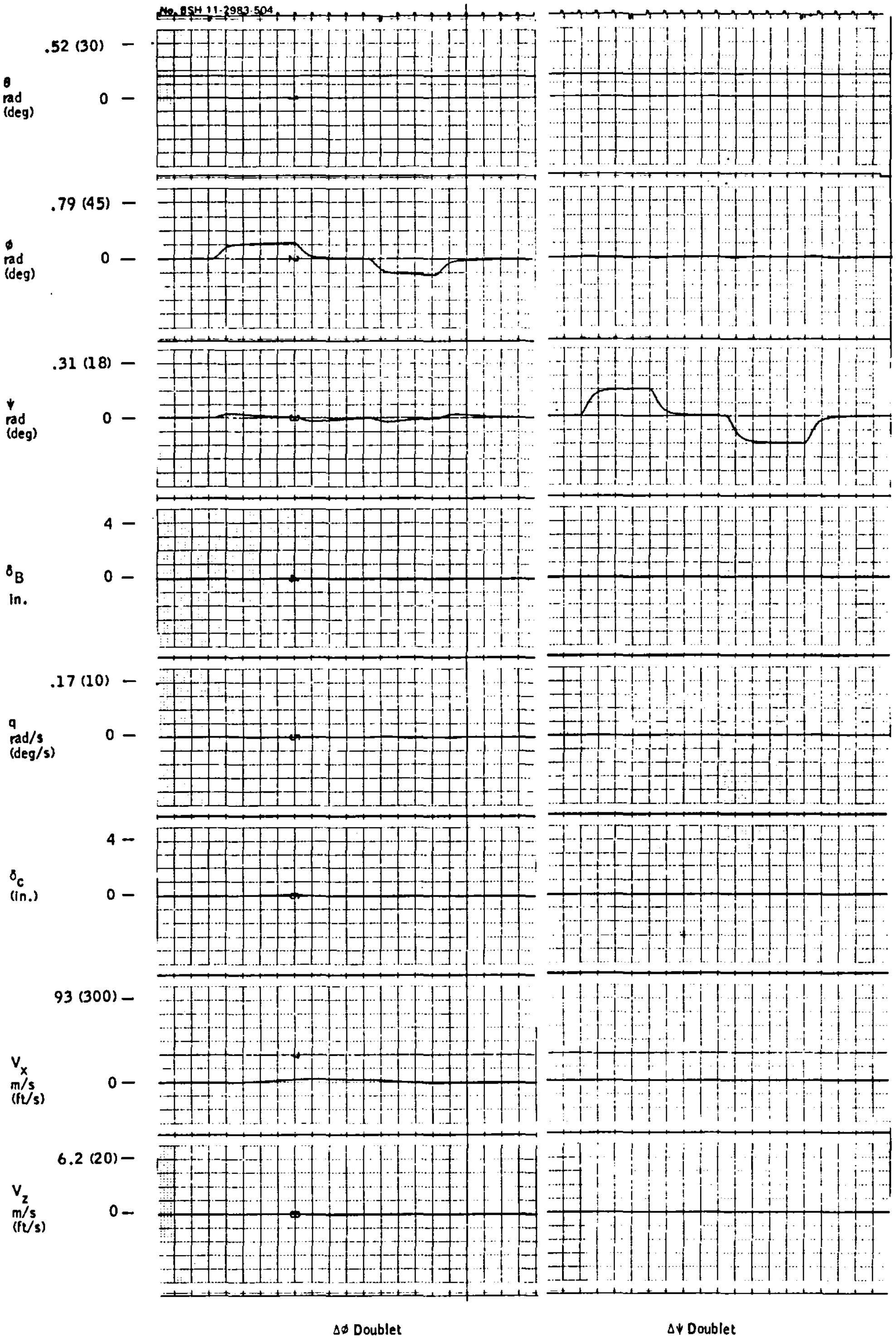

Trim = 3.1 m/s (10 ft/s)

Figure 67.-Lateral-axis controller response to ϕ and ψ commands--hover flight condition.

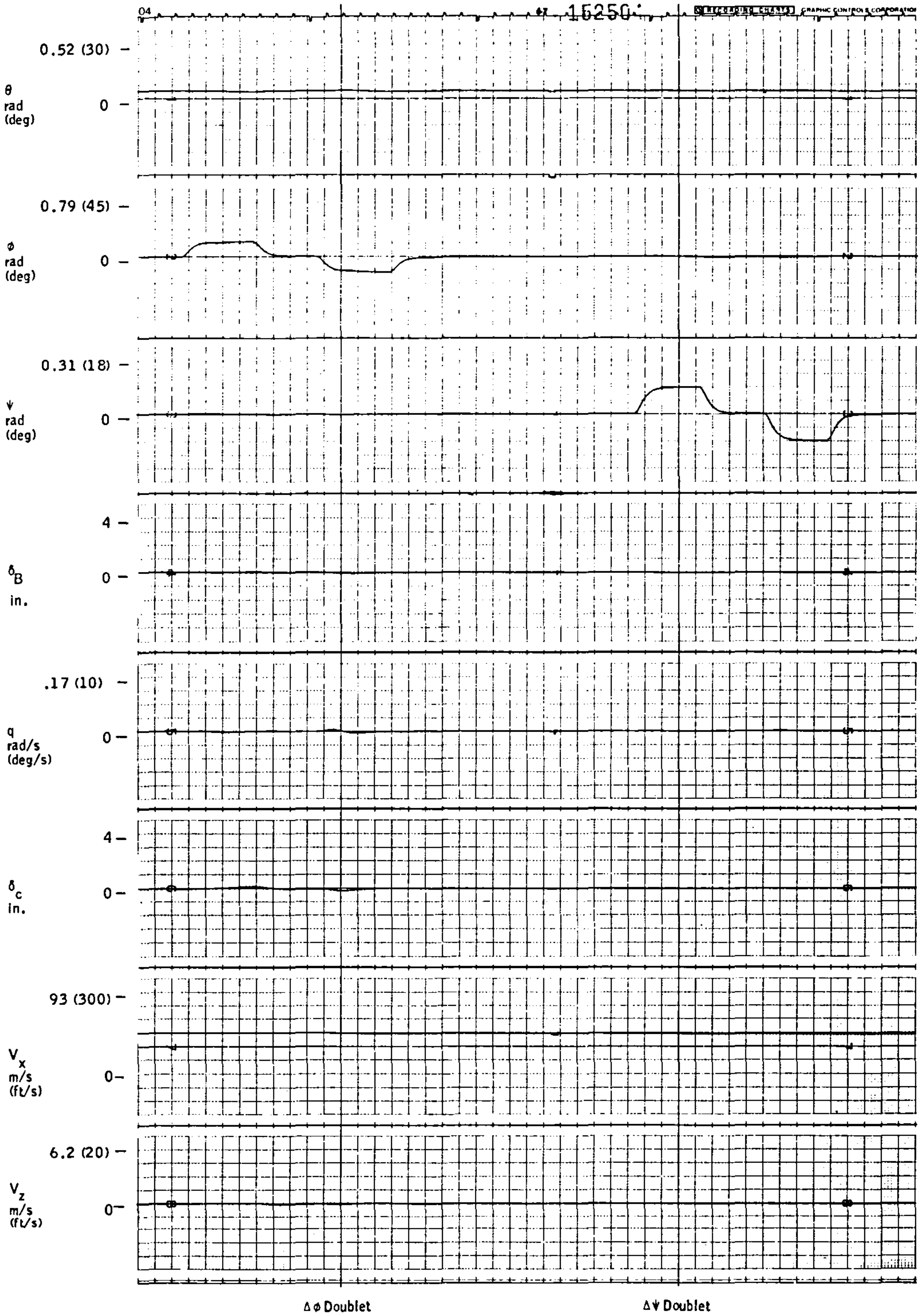

Trim = 41.2 m/s (135 ft/s)

Figure 68.-Lateral-axis controller respone to φ and ψ commands--41.2 m/s forward velocity flight condition.

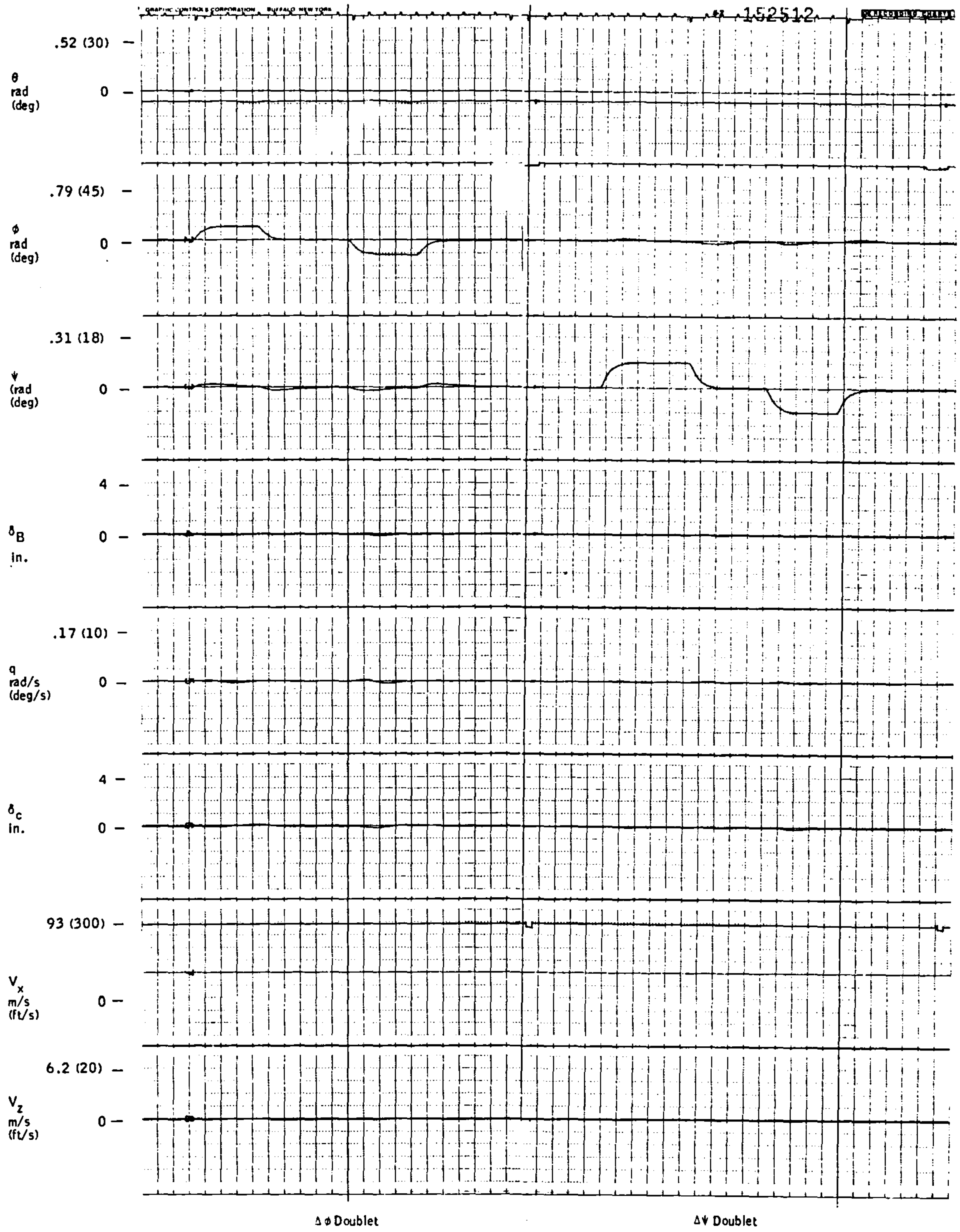

Trim = 79.3 m/s (260 ft/s)

Figure 69.-Lateral-axis controller response to ϕ and ψ commands-- 79.3 m/s forward velocity flight condition.

APPENDIX D
CH-47 MODEL PARAMETERS

This appendix contains plots of the elements of the A and B matrices for the longitudinal axis of the CH-47. The parameterization of these elements in terms of $\bar{v}$ (normalized forward airspeed) is also shown.

The vehicle model has the form (see ref. 4):

$$\frac{d}{d_t}\begin{vmatrix} V_x \\ V_z \\ q \\ \theta \end{vmatrix} = \begin{vmatrix} a_{11} & a_{12} & a_{13} & a_{14} \\ a_{21} & a_{22} & a_{23} & a_{24} \\ a_{31} & a_{32} & a_{33} & a_{34} \\ 0 & 0 & 1 & 0 \end{vmatrix} \begin{vmatrix} V_x \\ V_z \\ q \\ \theta \end{vmatrix} + \begin{vmatrix} b_{11} & b_{12} \\ b_{21} & b_{22} \\ b_{31} & b_{32} \end{vmatrix} \begin{vmatrix} \delta_B \\ \delta_c \end{vmatrix}$$

The data, in the form of computer plots, are presented in Figures 70 through 87.

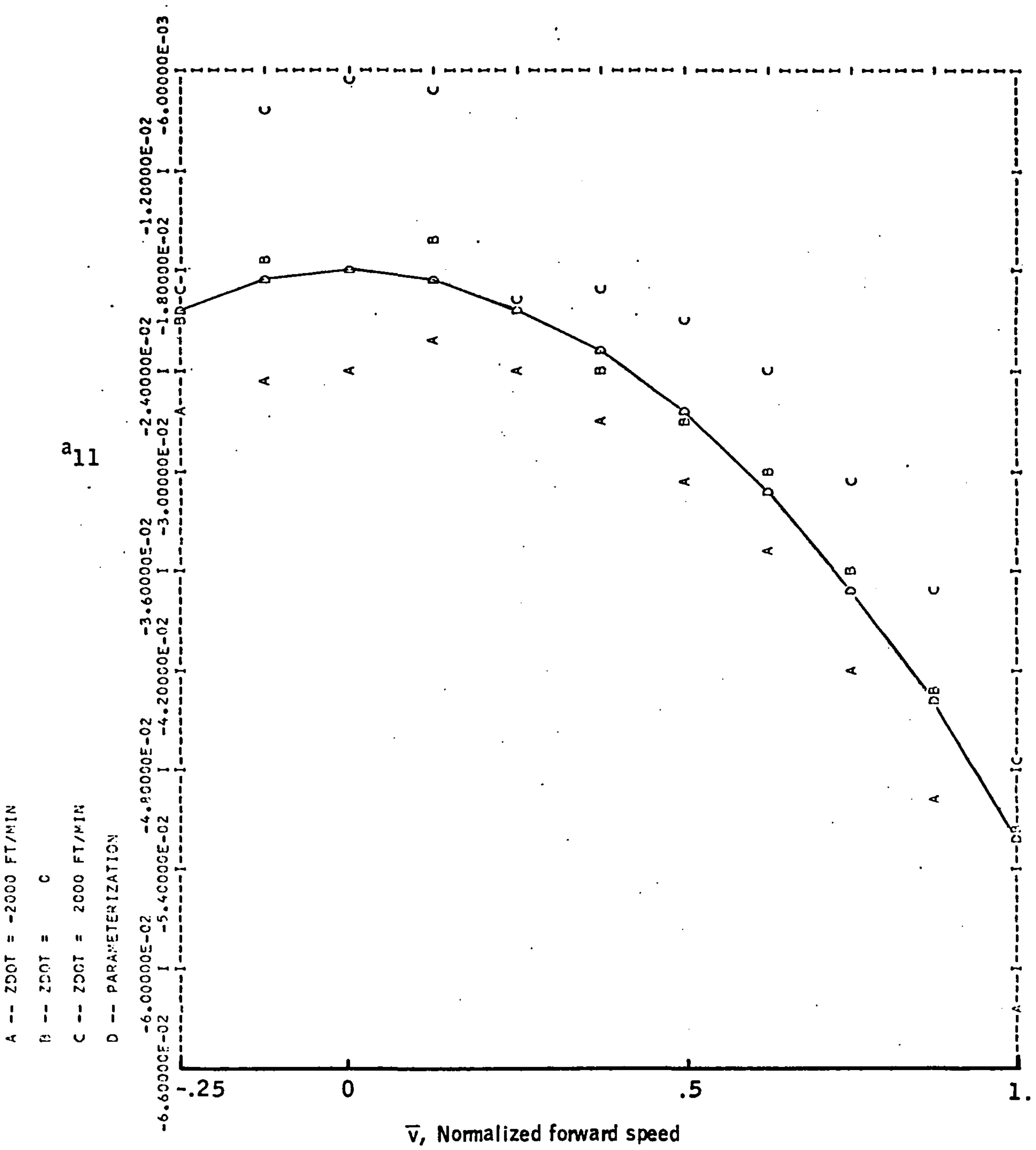

Figure 70. -Element a_{11} versus $\bar{v}$ -- CH-47 longitudinal axis.

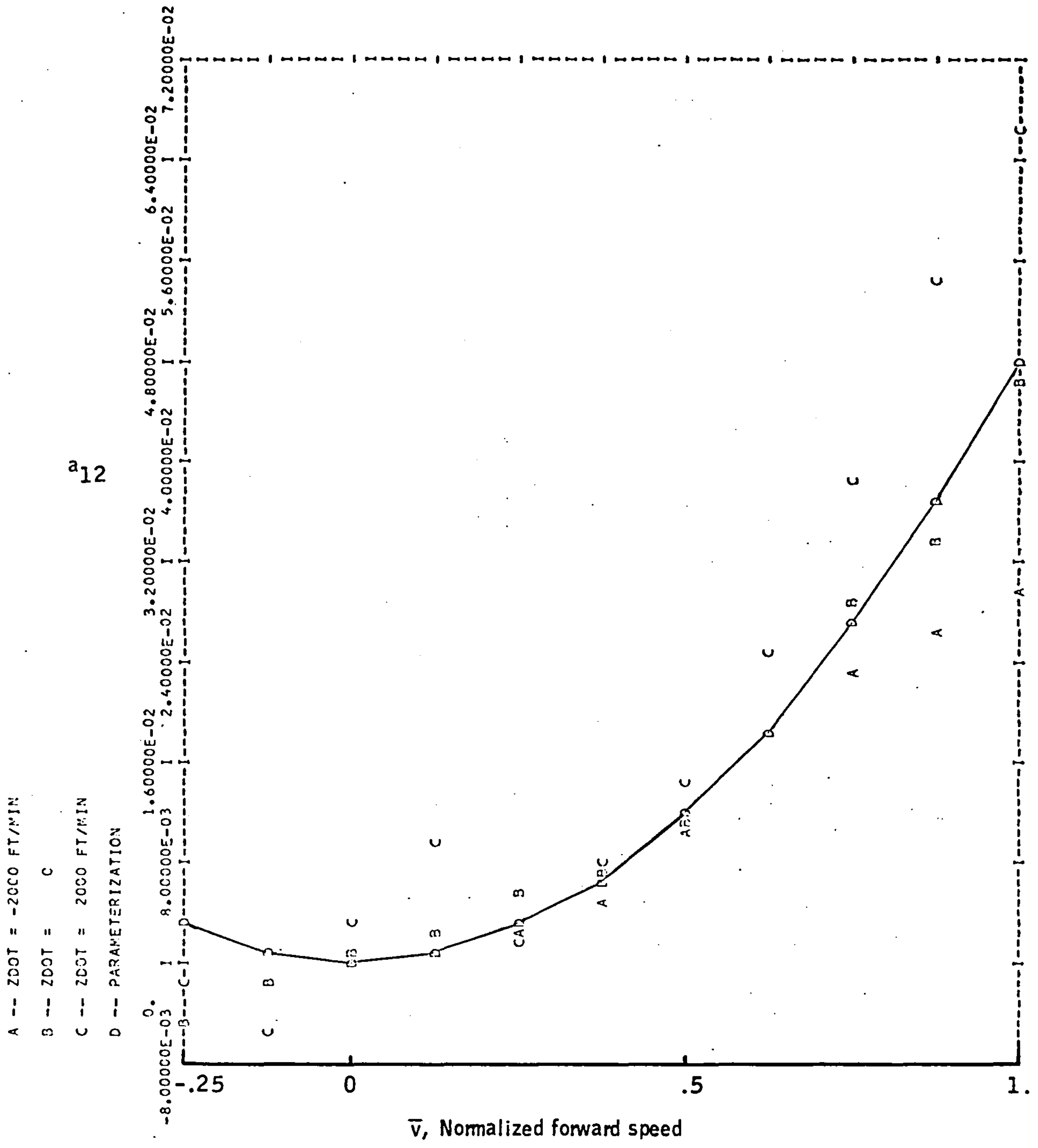

Figure 71. Element a_{12} versus $\bar{v}$ -- CH-47 longitudinal axis.

]

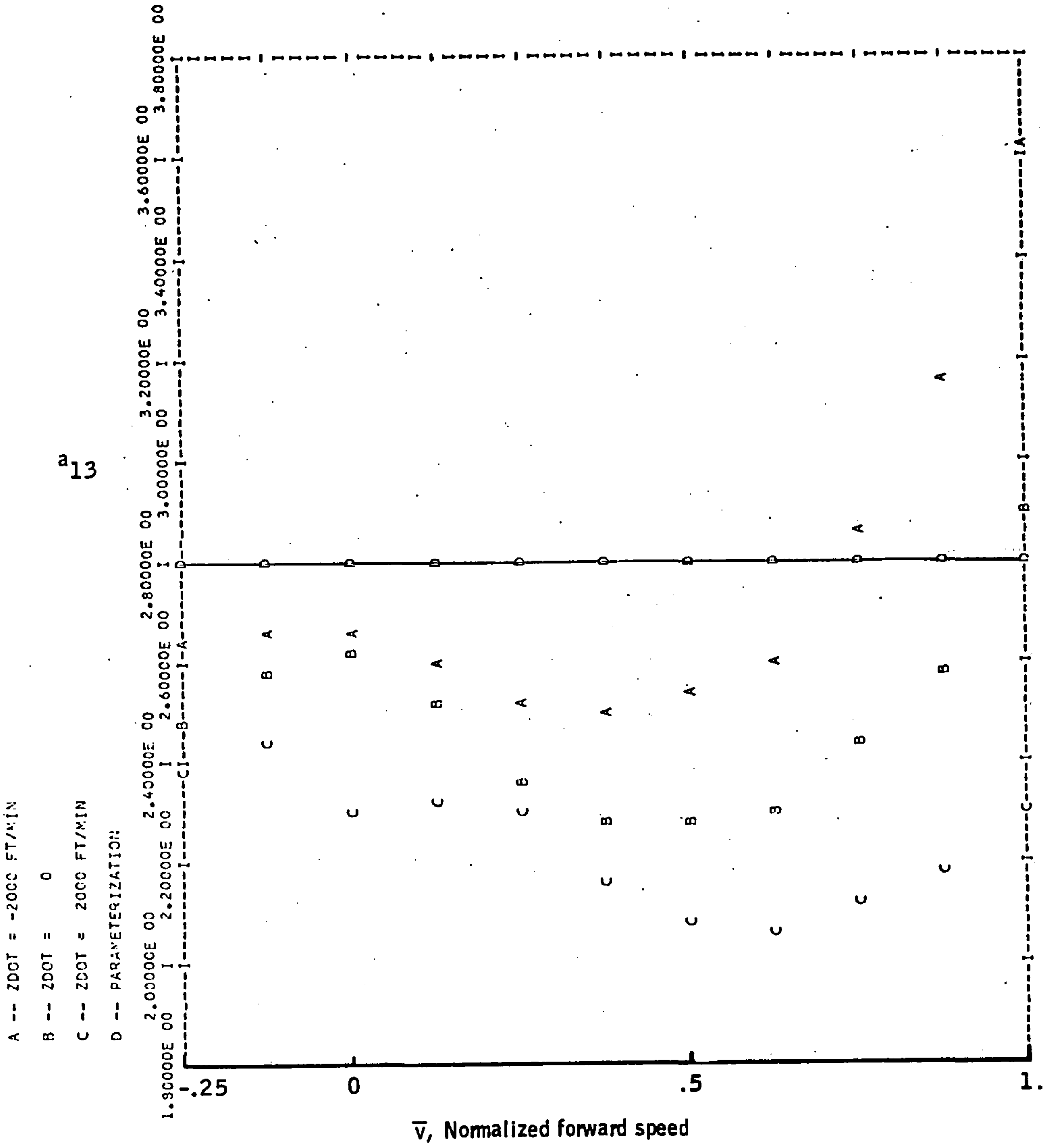

Figure 72. Element a_{13} versus $\bar{v}$ -- CH-47 longitudinal axis.

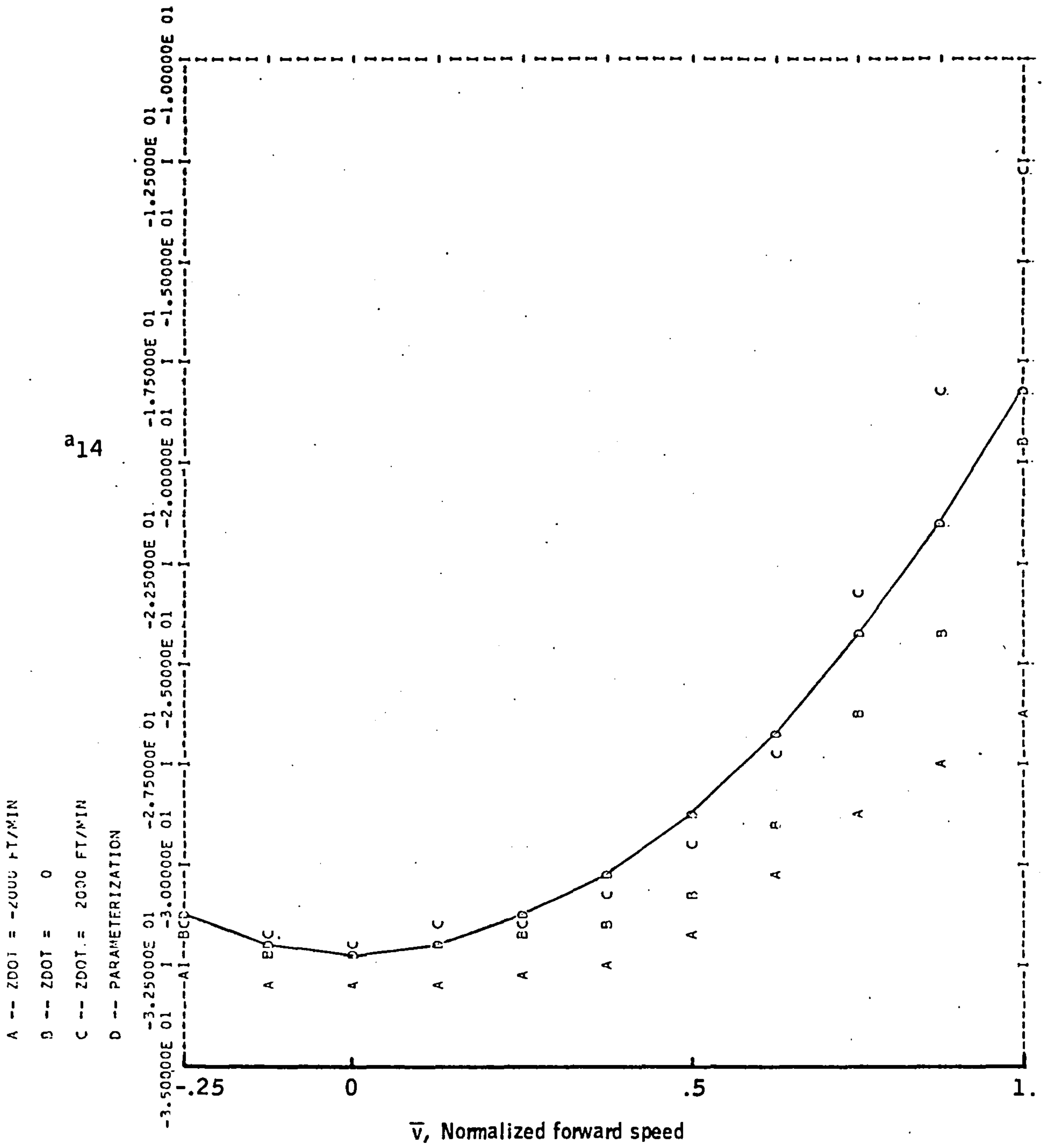

Figure 73. -Element a_{14} versus $\bar{v}$ -- CH-47 longitudinal axis.

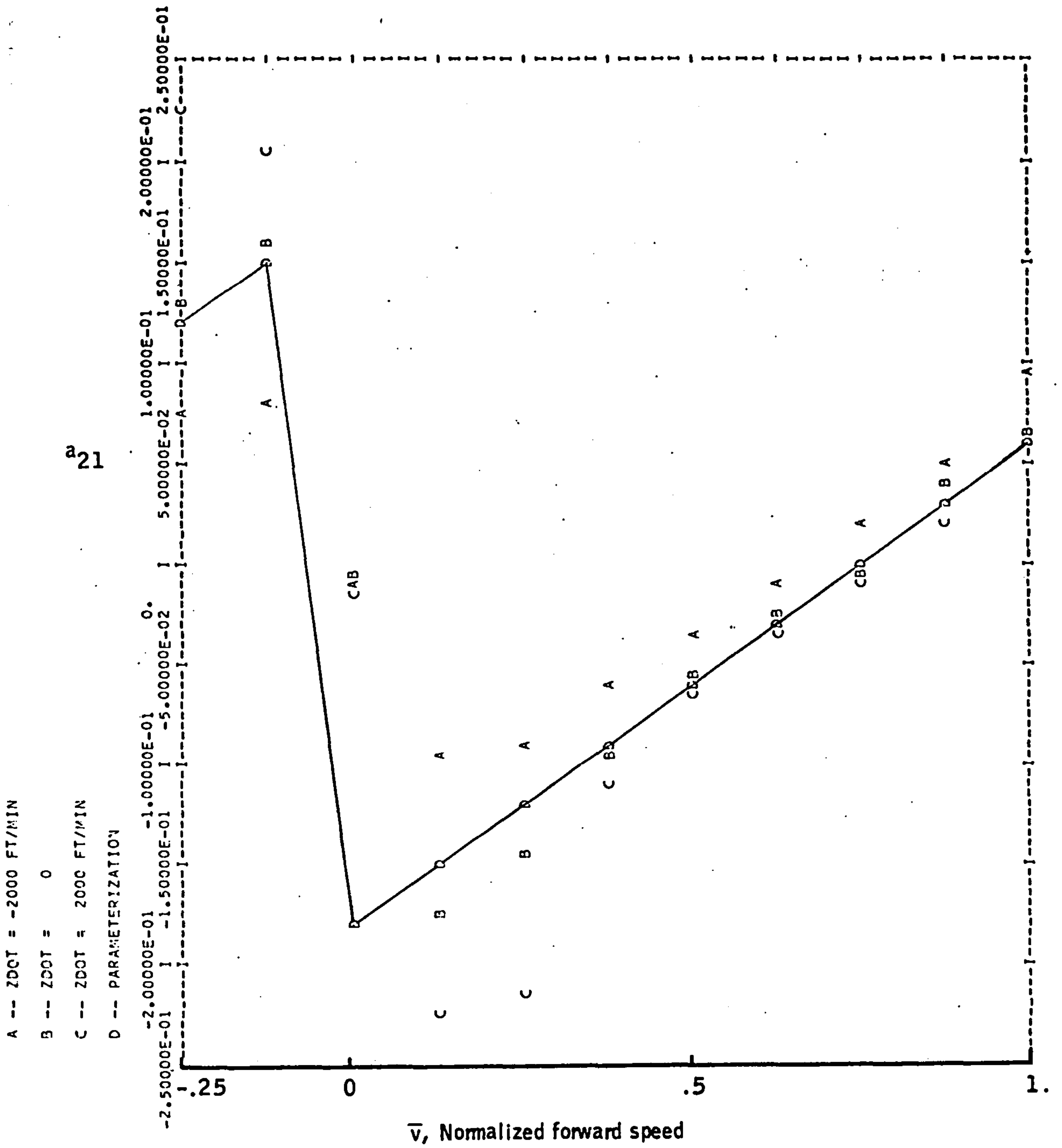

Figure 74. -Element a_{21} versus $\bar{v}$ -- CH-47 longitudinal axis.

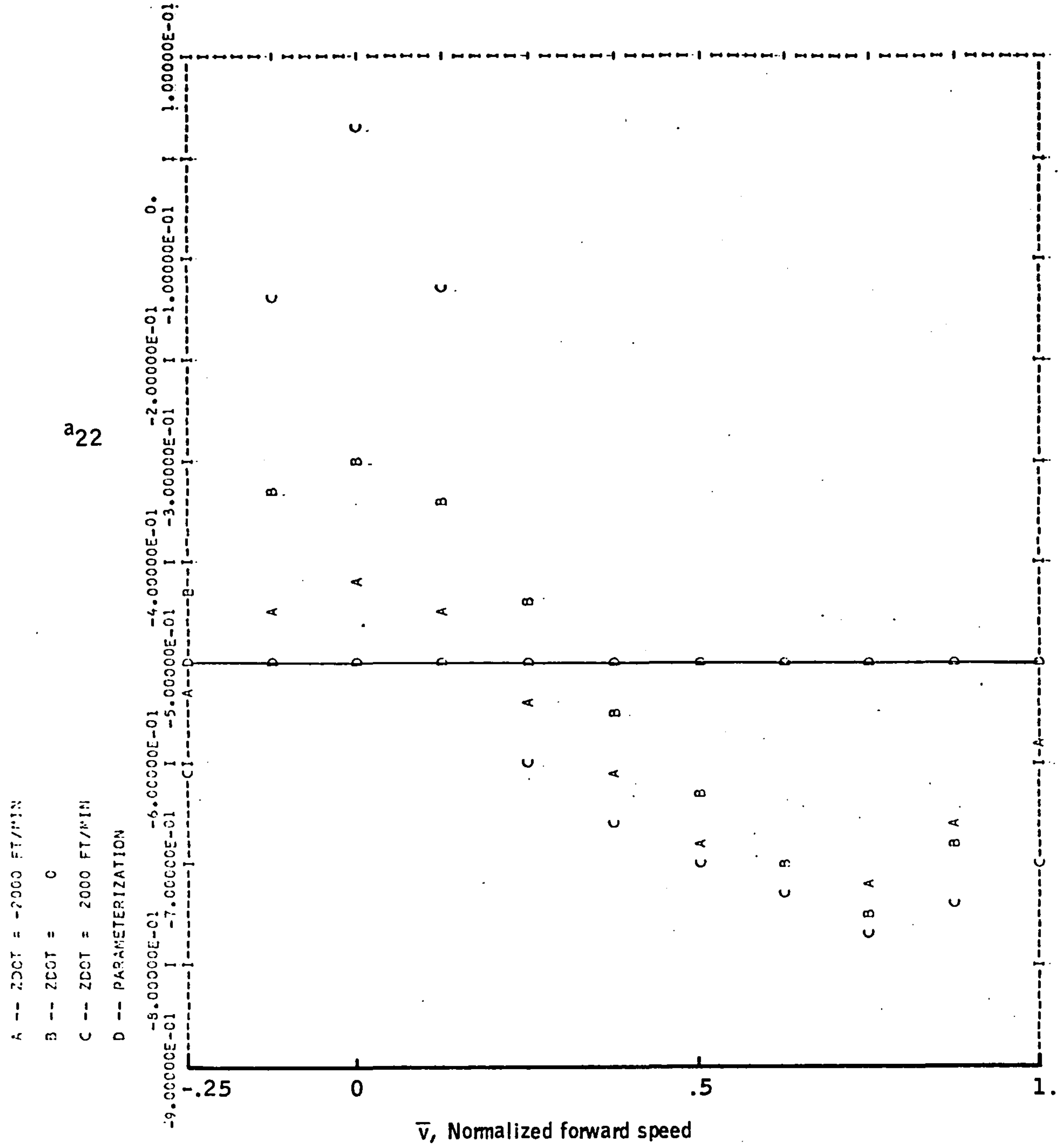

Figure 75. -Element a_{22} versus $\bar{v}$ -- CH-47 longitudinal axis.

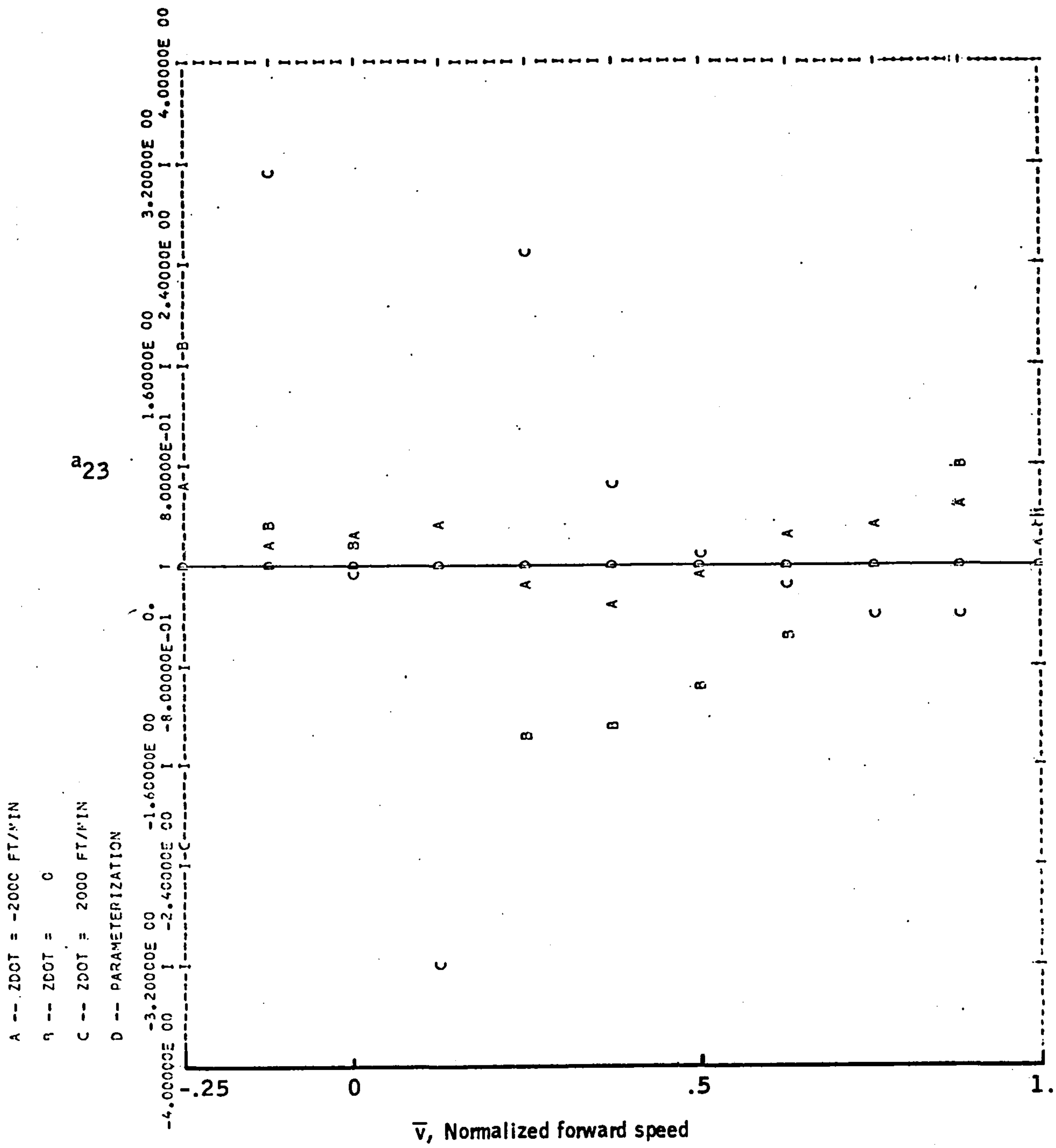

Figure 76. -Element a_{23} versus $\bar{v}$ -- CH-47 longitudinal axis.

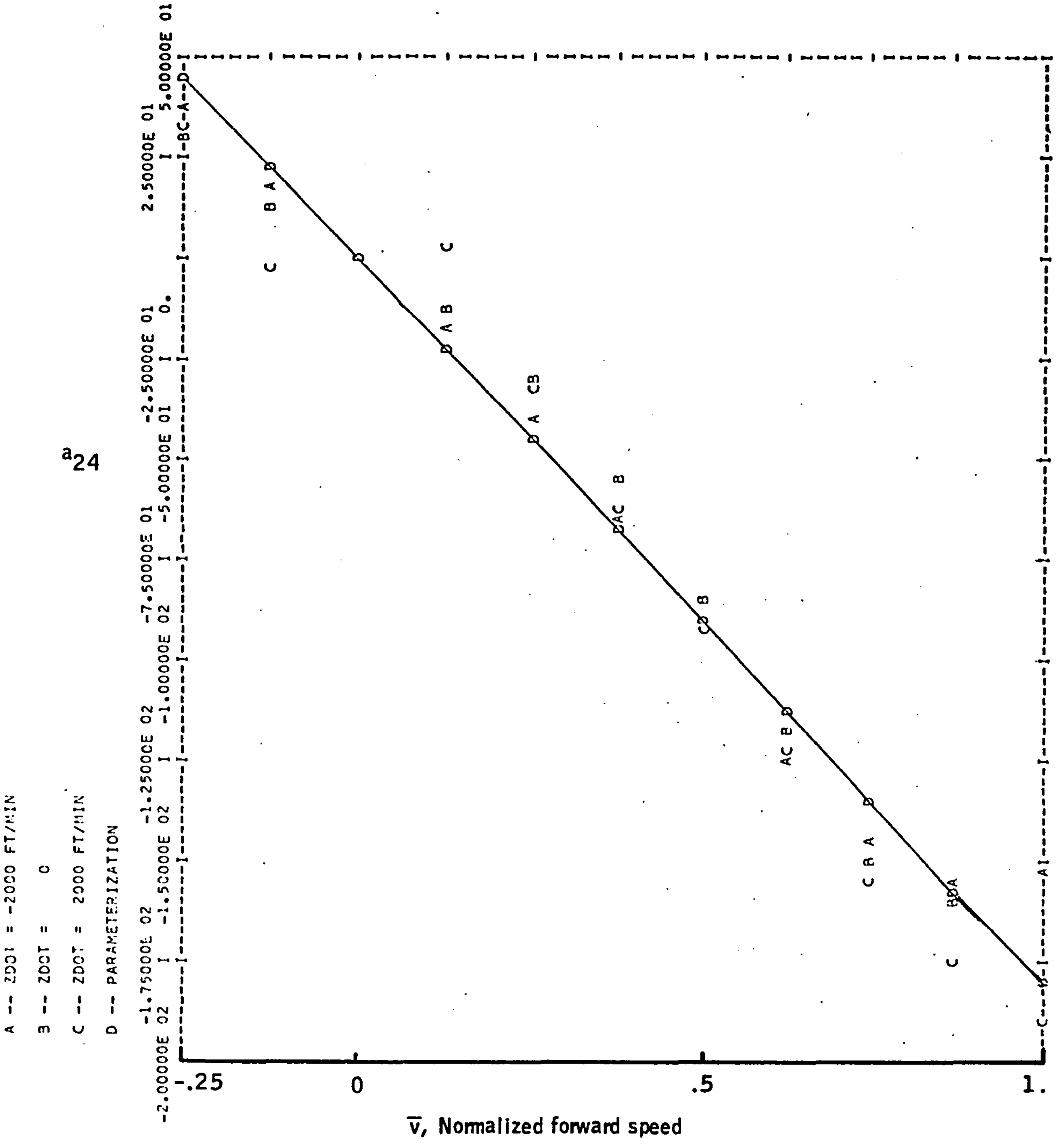

Figure 77. -Element a_{24} versus $\bar{v}$ -- CH-47 longitudinal axis.

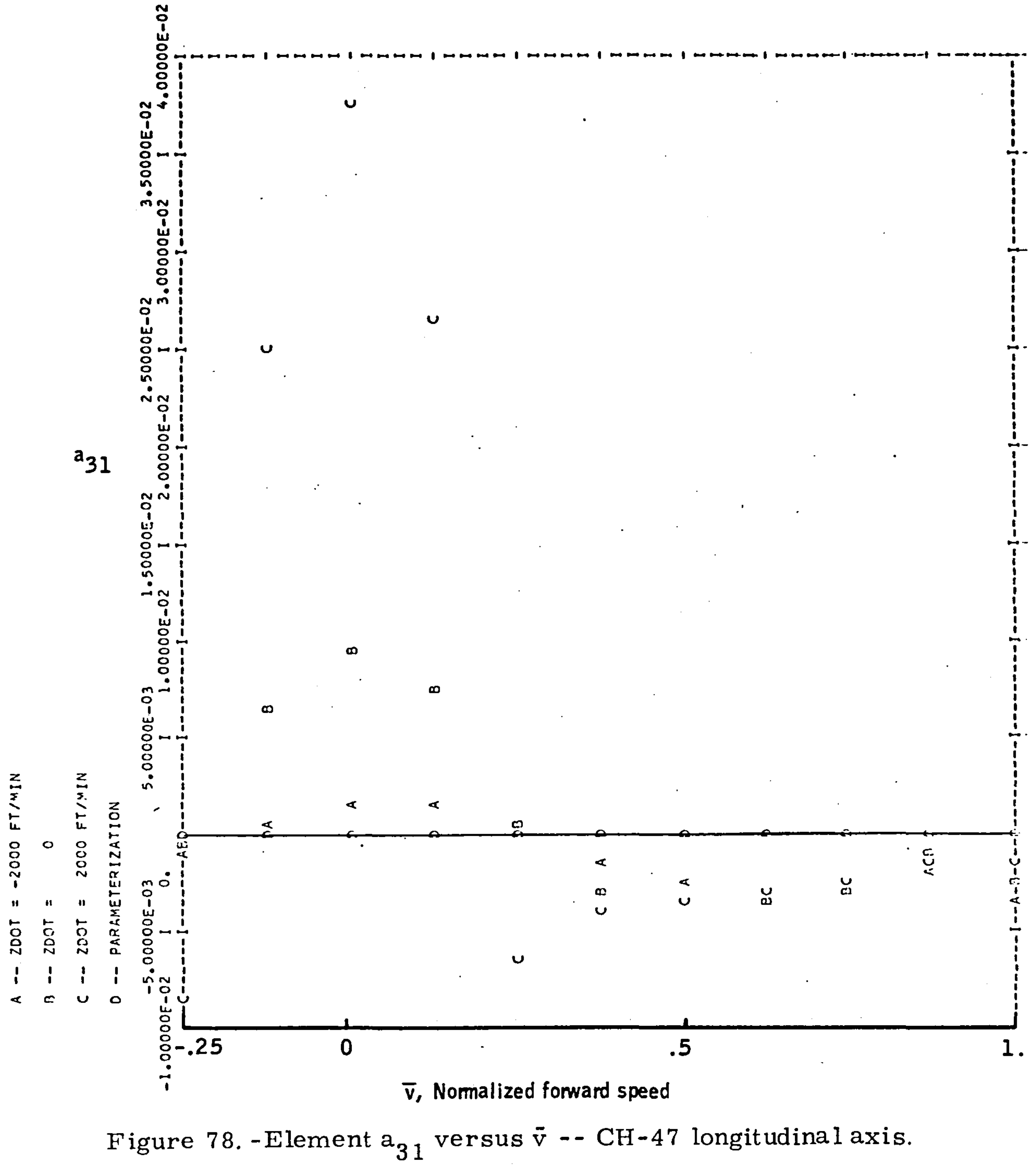

Figure 78. -Element a_{31} versus $\bar{v}$ -- CH-47 longitudinal axis.

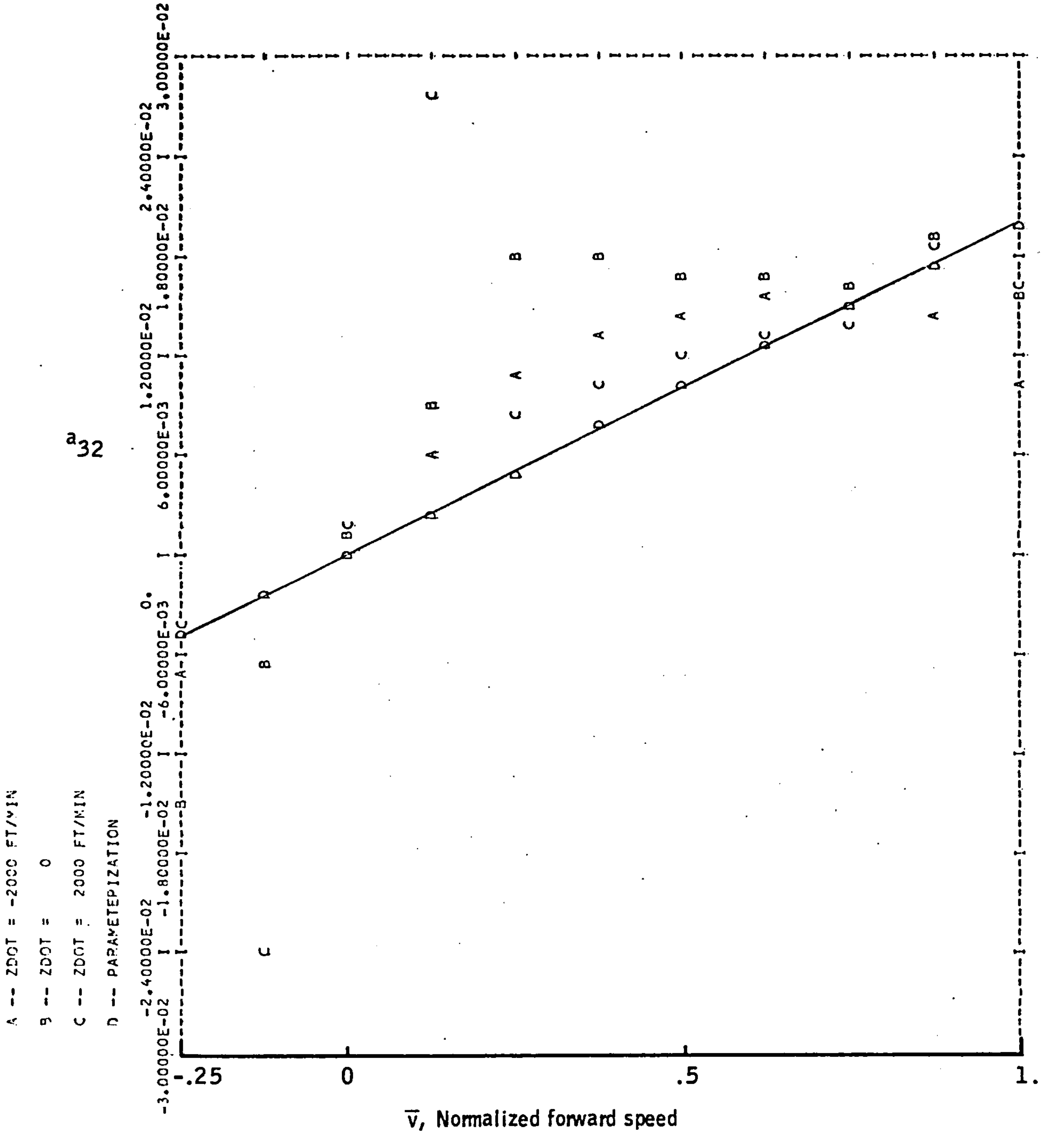

Figure 79. -Element a_{32} versus $\bar{v}$ -- CH-47 longitudinal axis.

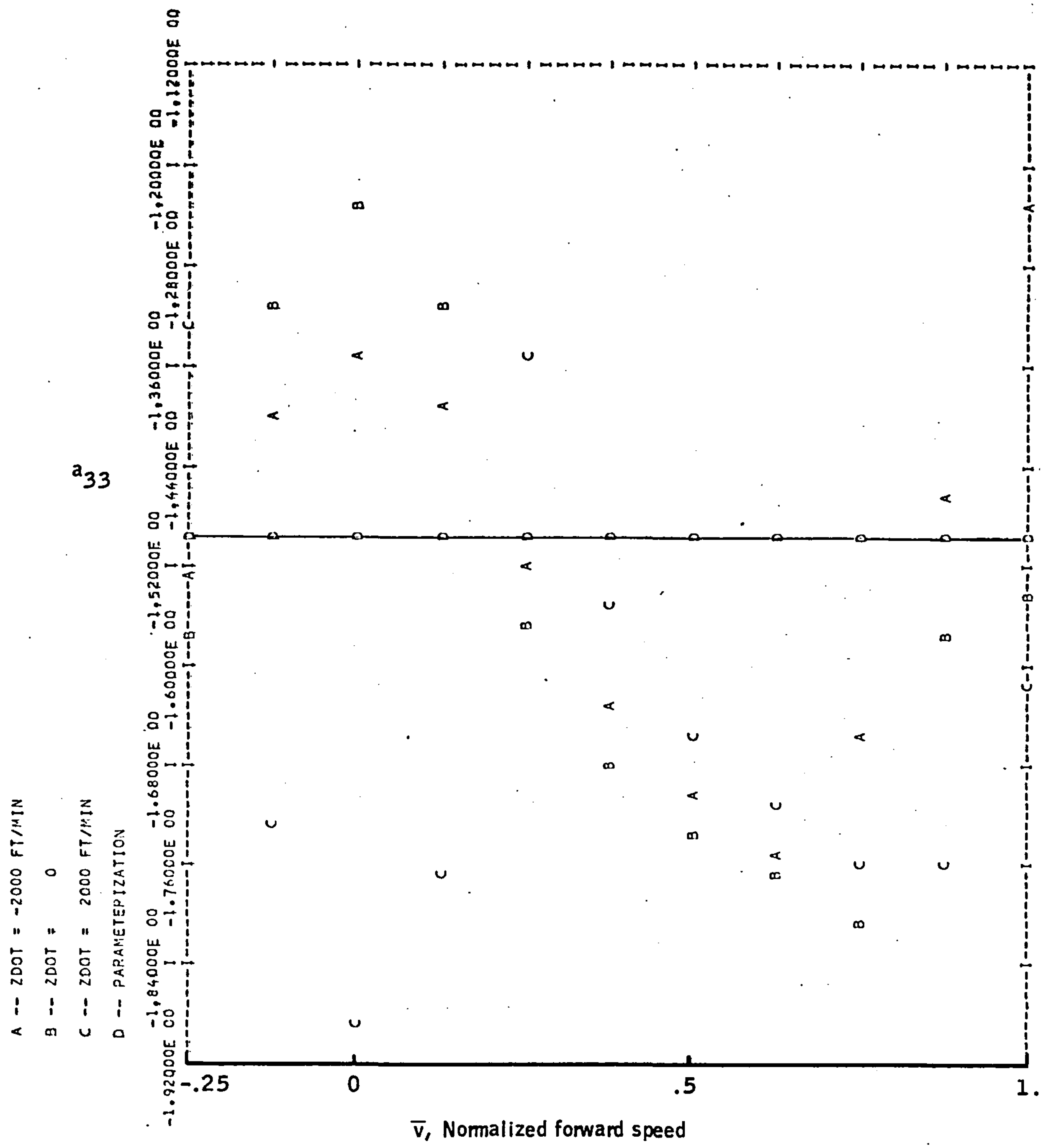

Figure 80. -Element a_{33} versus $\bar{v}$ -- CH-47 longitudinal axis.

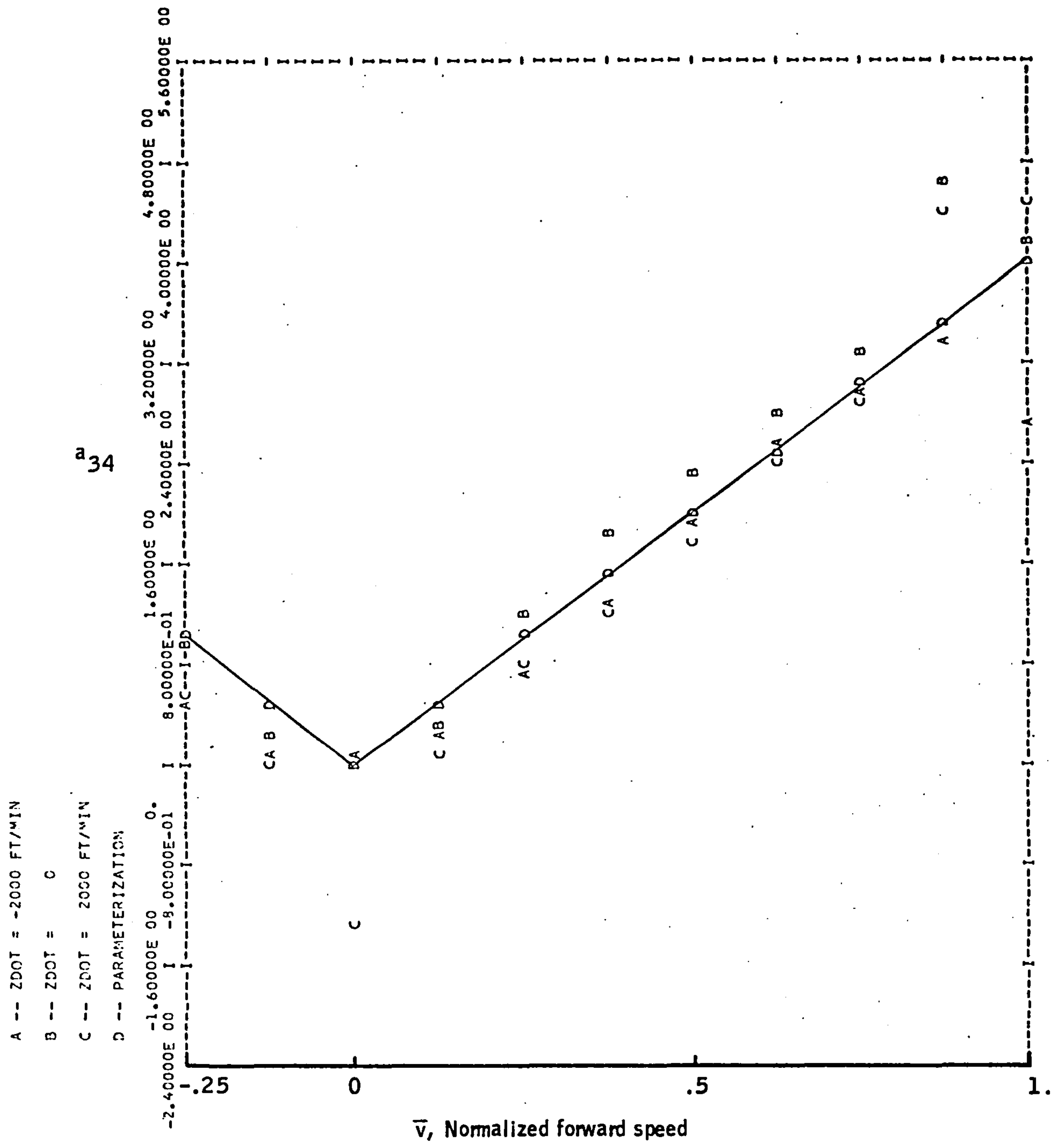

Figure 81. -Element a_{34} versus $\bar{v}$ -- CH-47 longitudinal axis.

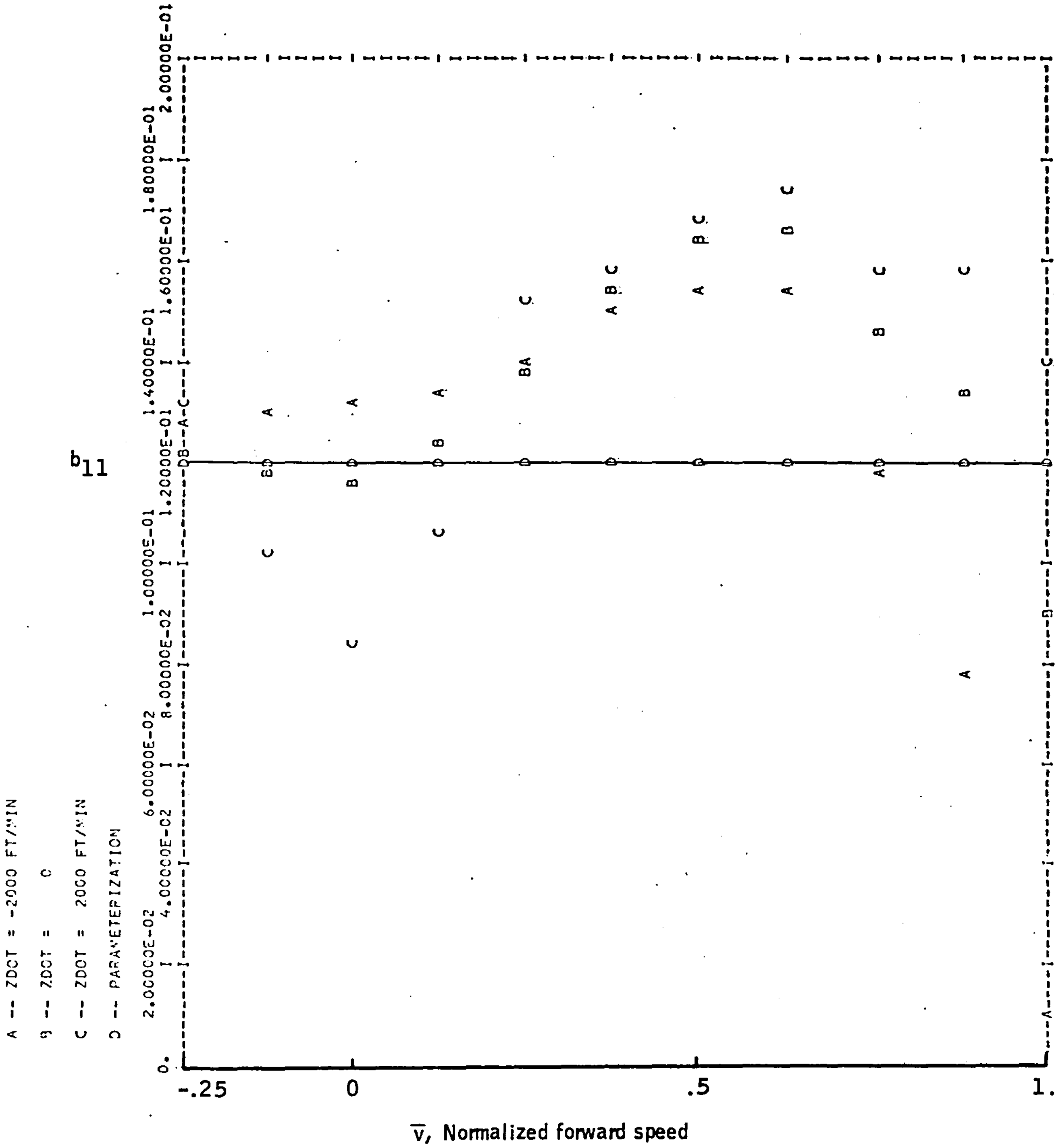

Figure 82. -Element b_{11} versus $\bar{v}$ -- CH-47 longitudinal axis.

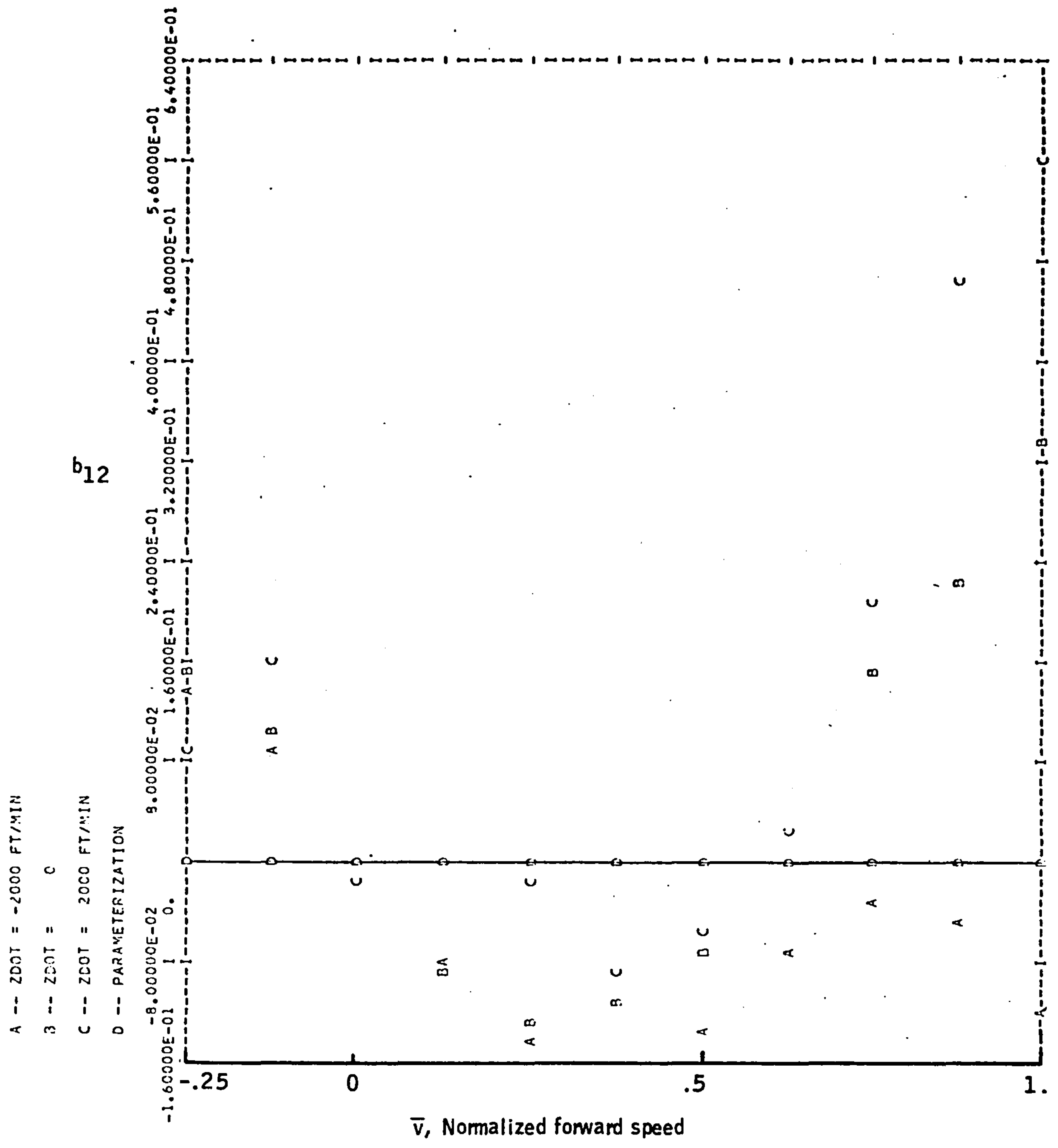

Figure 83. -Element b_{12} versus $\bar{v}$ -- CH-47 longitudinal axis.

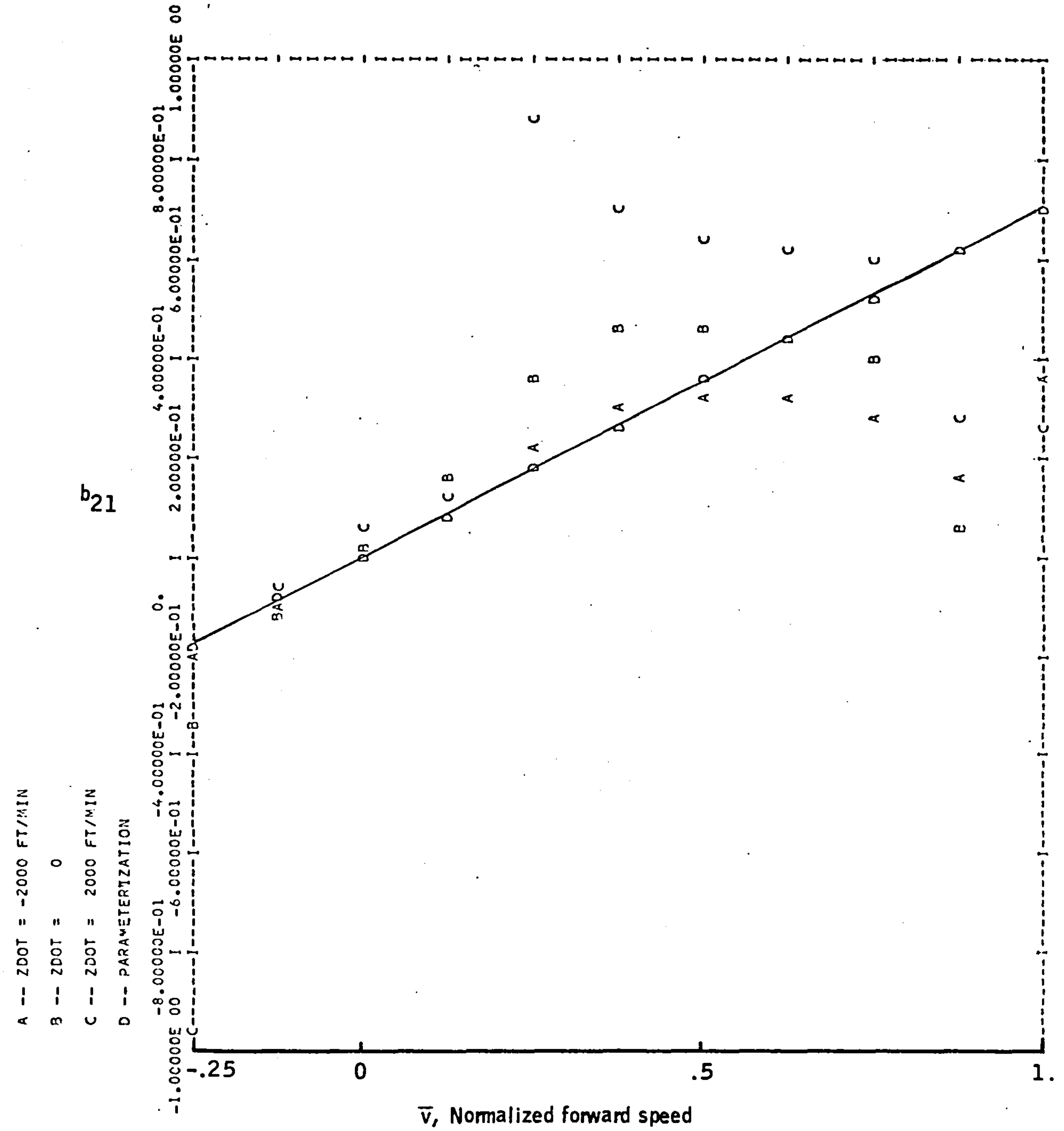

Figure 84. -Element b_{21} versus $\bar{v}$ -- CH-47 longitudinal axis.

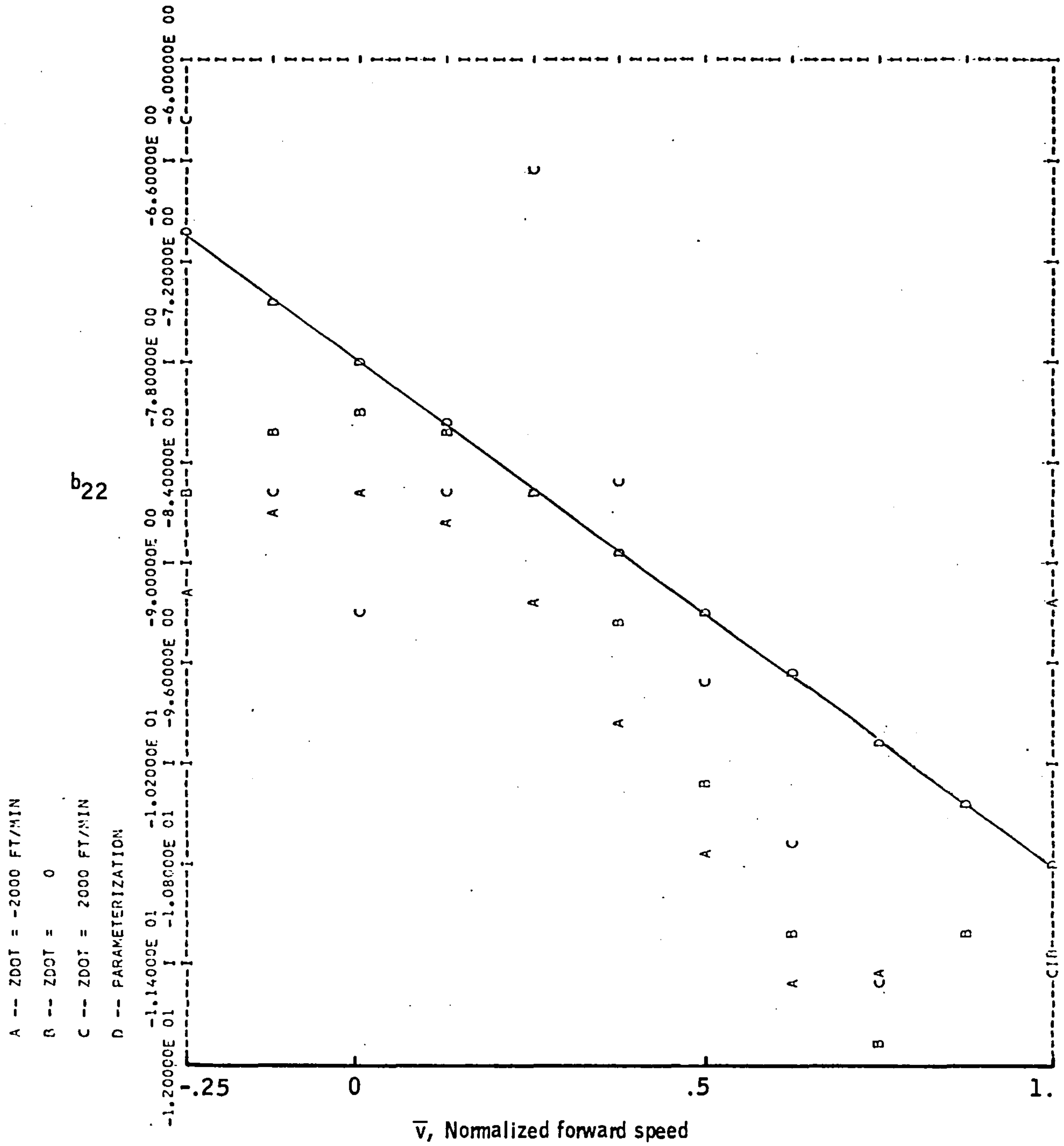

Figure 85. -Element b_{22} versus $\bar{v}$ -- CH-47 longitudinal axis.

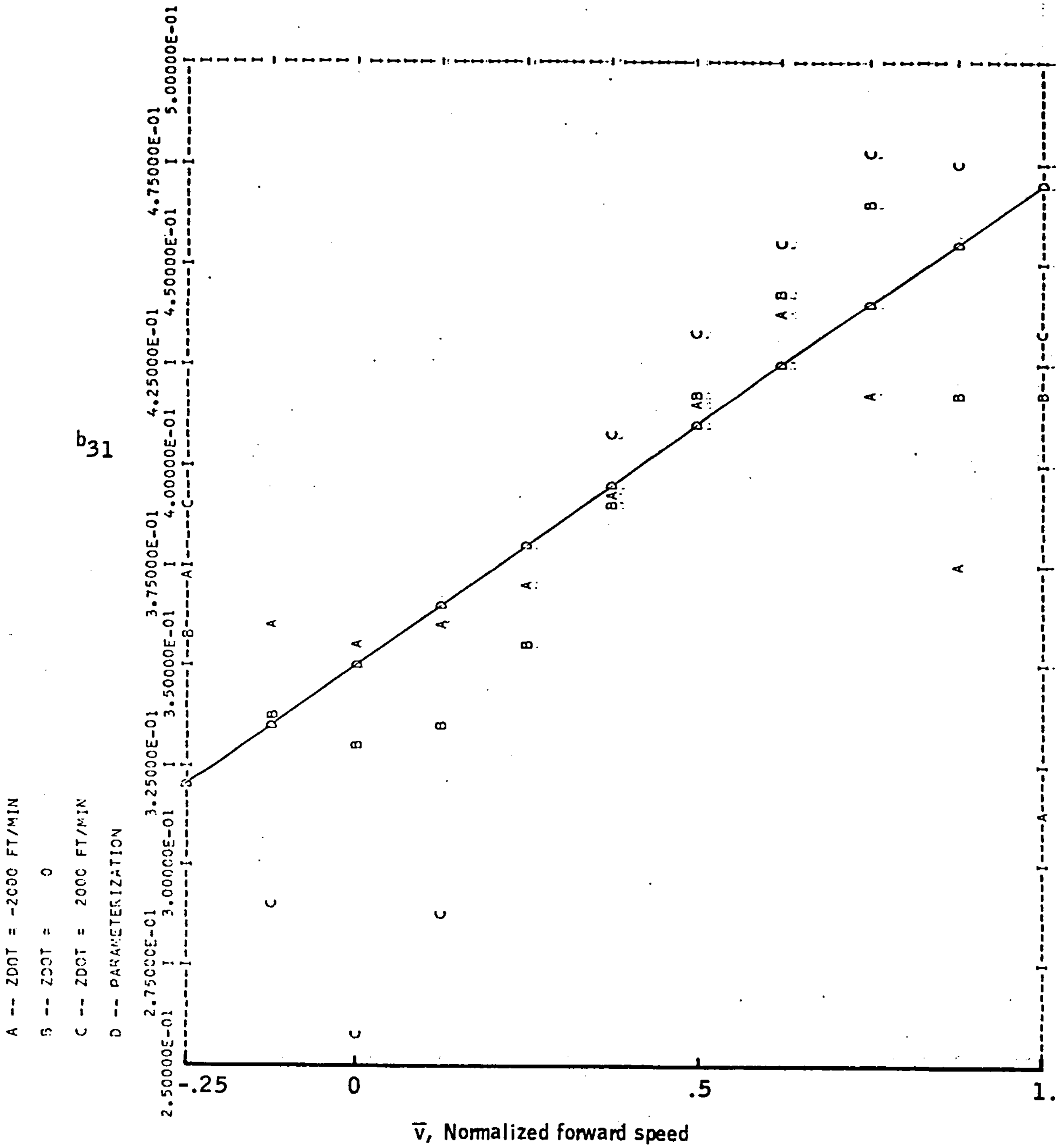

Figure 86. -Element b_{31} versus $\bar{v}$ -- CH-47 longitudinal axis.

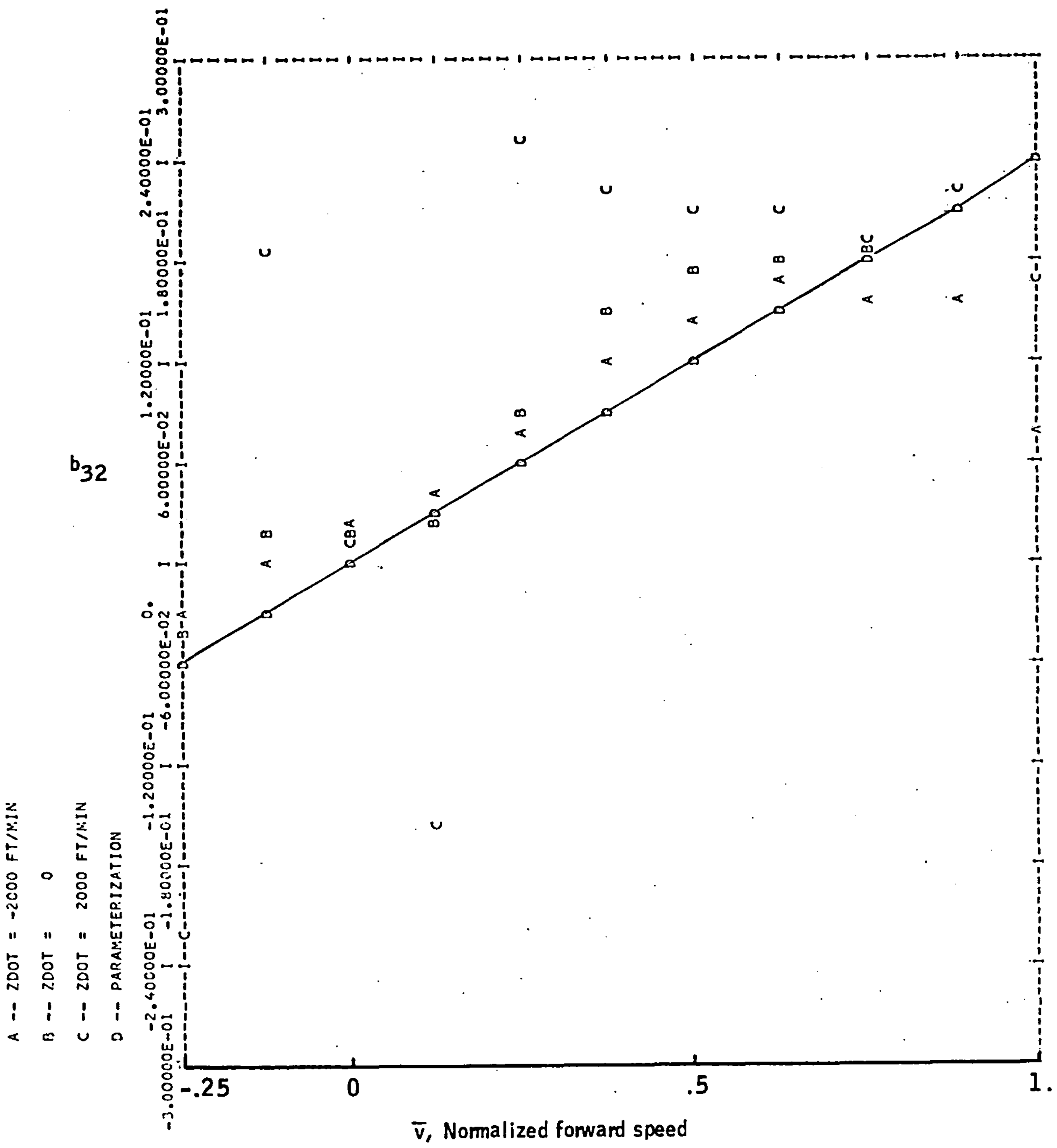

Figure 87. -Element b_{32} versus $\bar{v}$ -- CH-47 longitudinal axis.

APPENDIX E

LONGITUDINAL-AXIS GAIN SCHEDULE WITH ESTIMATED VELOCITY

This appendix presents the ideal gain schedule, the best fixed gains, and the gain schedules for two levels of uncertainty in the scheduling parameter ($\bar{v}$). This analysis is described in Section 6.

The data, in the form of computer plots, are presented in Figures 88 through 101.

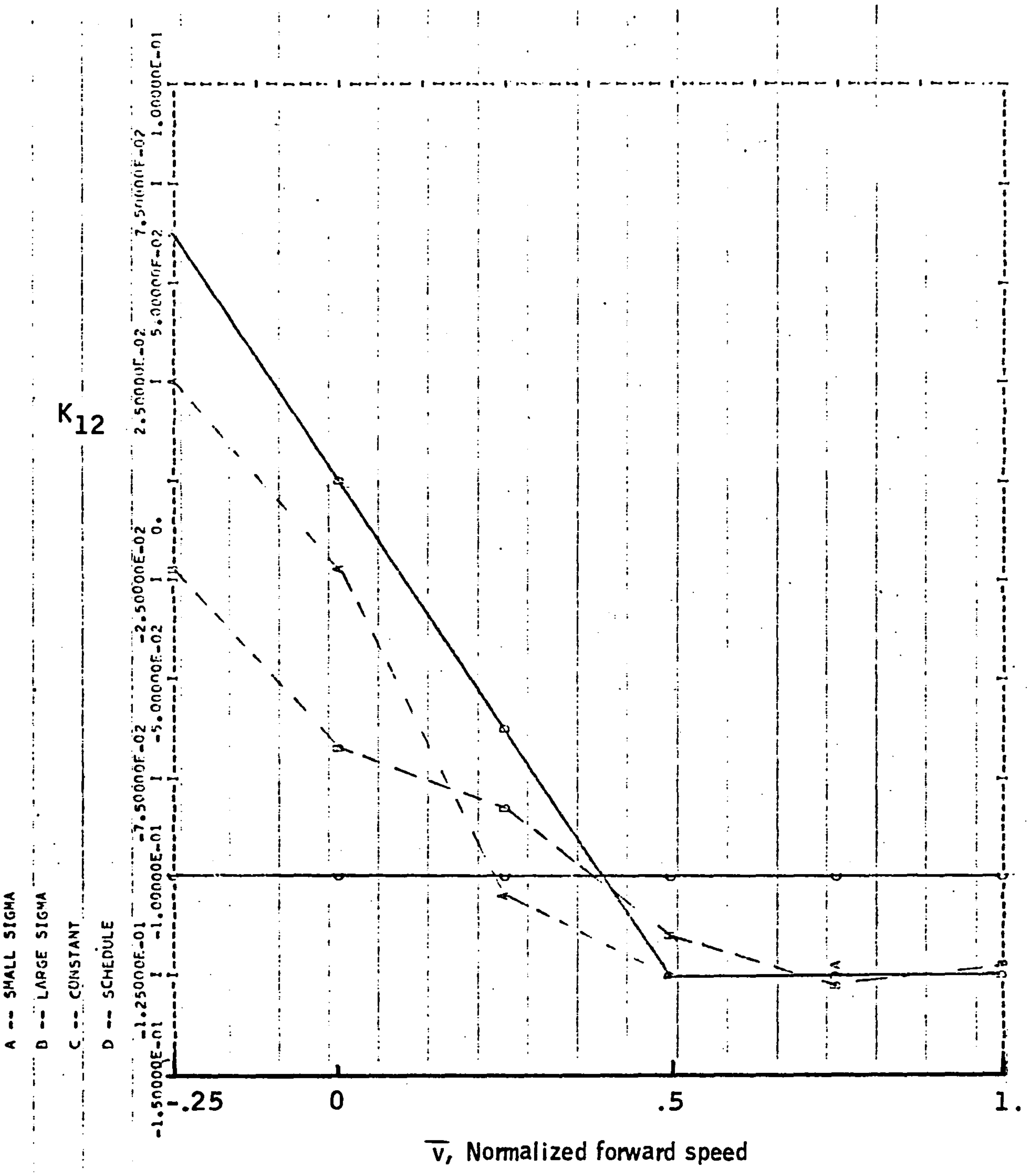

Figure 88. -Element K_{12} versus $\bar{v}$ -- longitudinal-axis gain schedule.

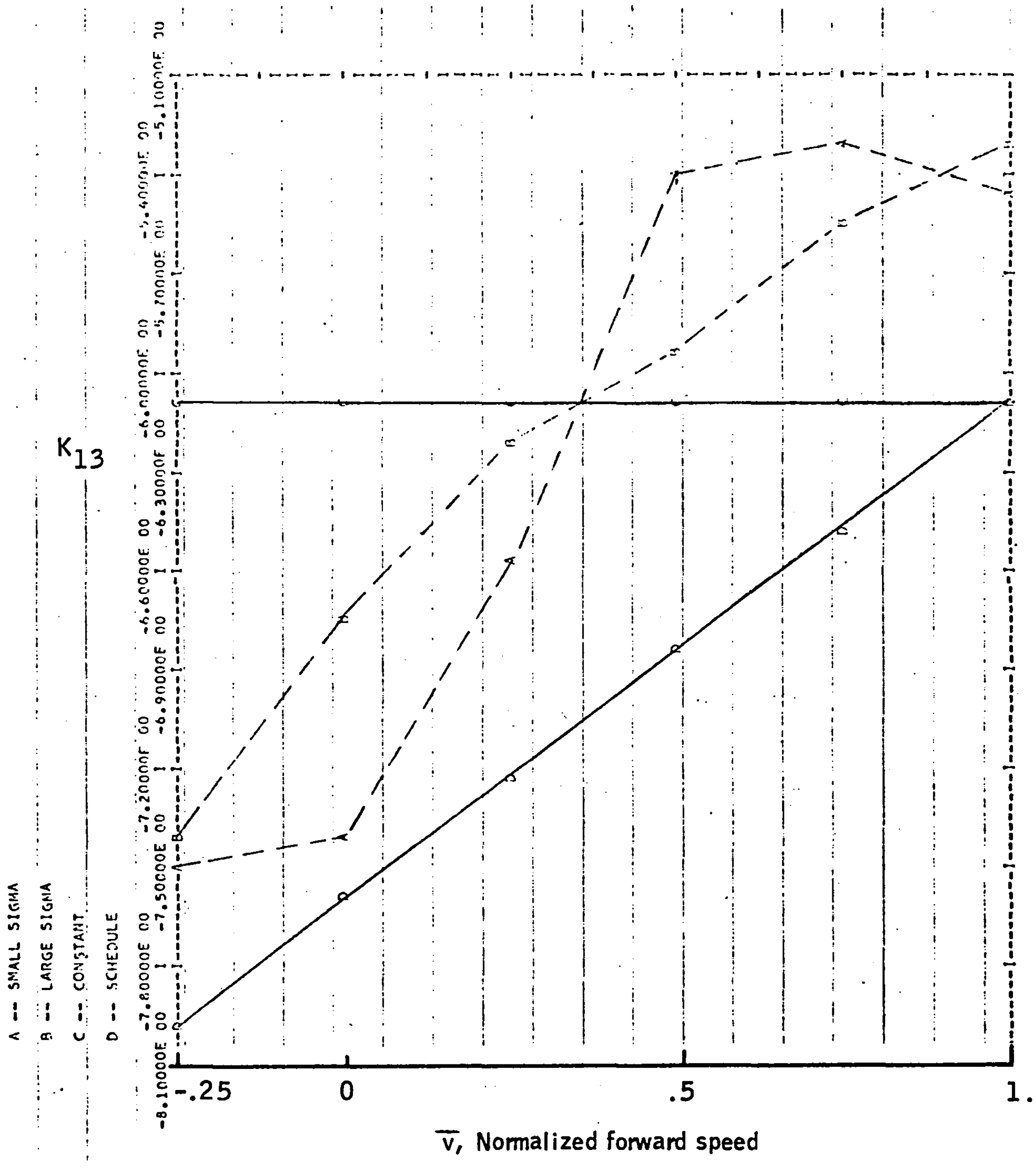

Figure 89. -Element K_{13} versus $\bar{v}$ -- longitudinal-axis gain schedule.

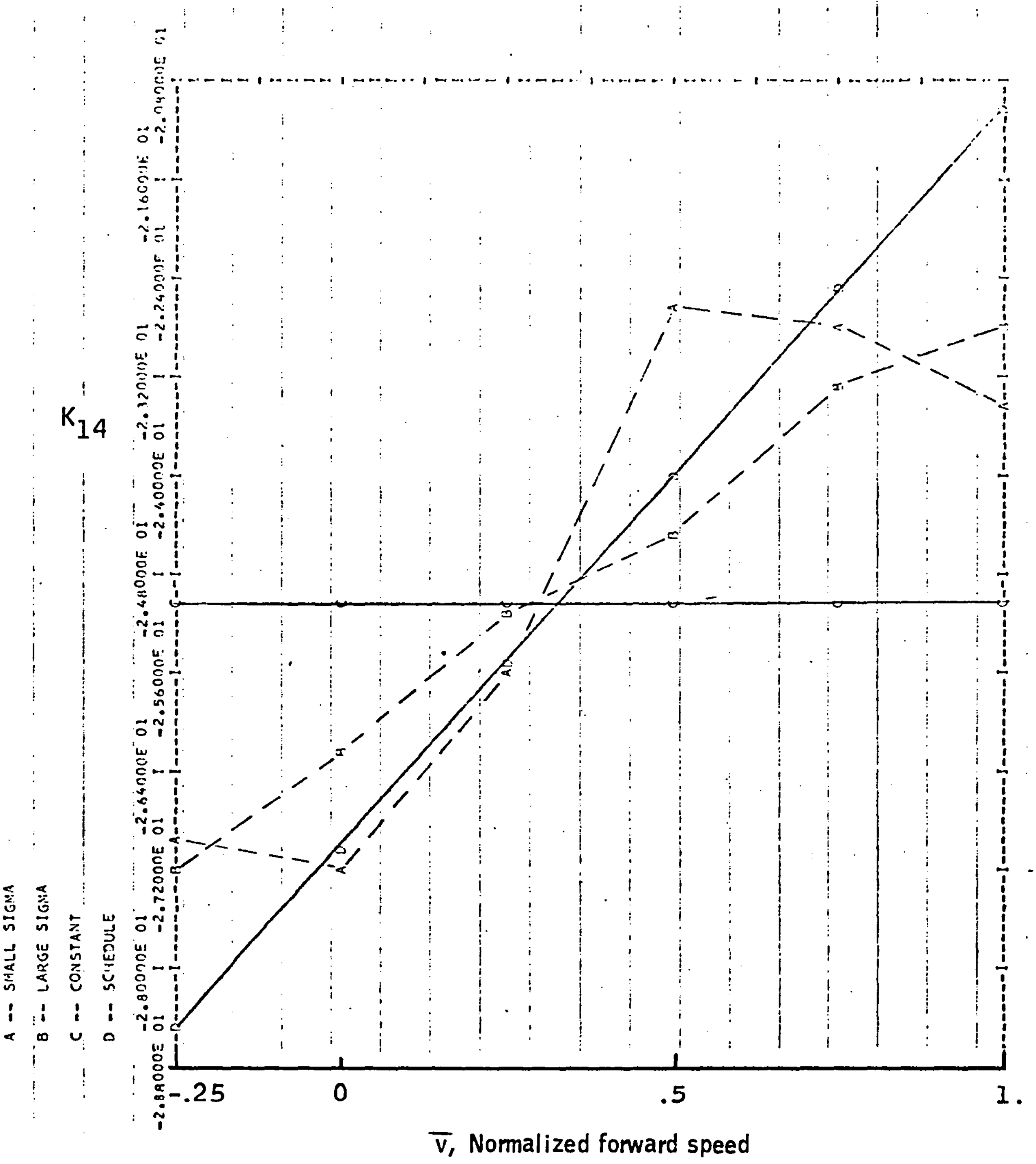

Figure 90. -Element K_{14} versus $\bar{v}$ -- longitudinal-axis gain schedule.

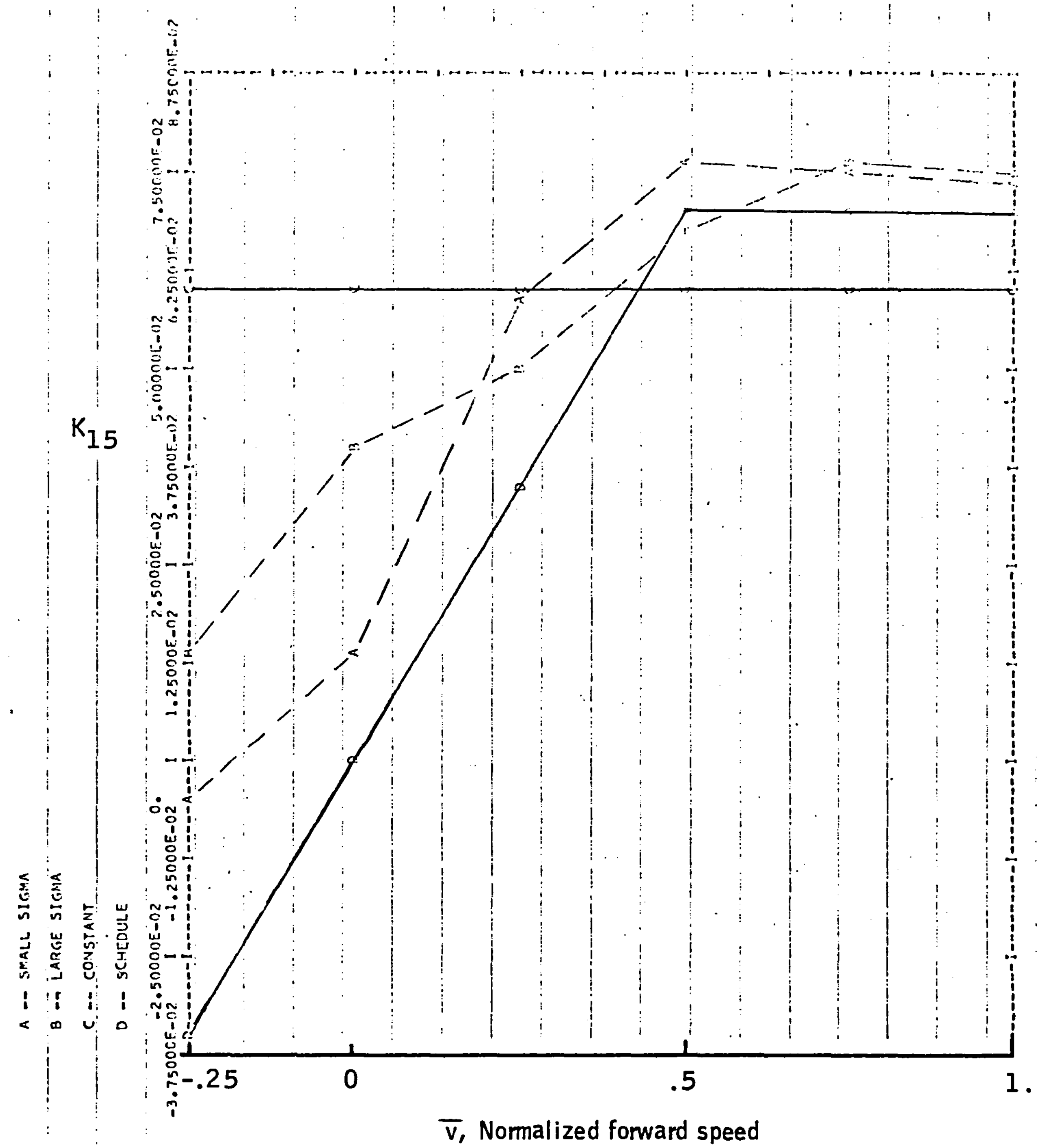

Figure 91. -Element K_{15} versus $\bar{v}$ -- longitudinal-axis gain schedule.

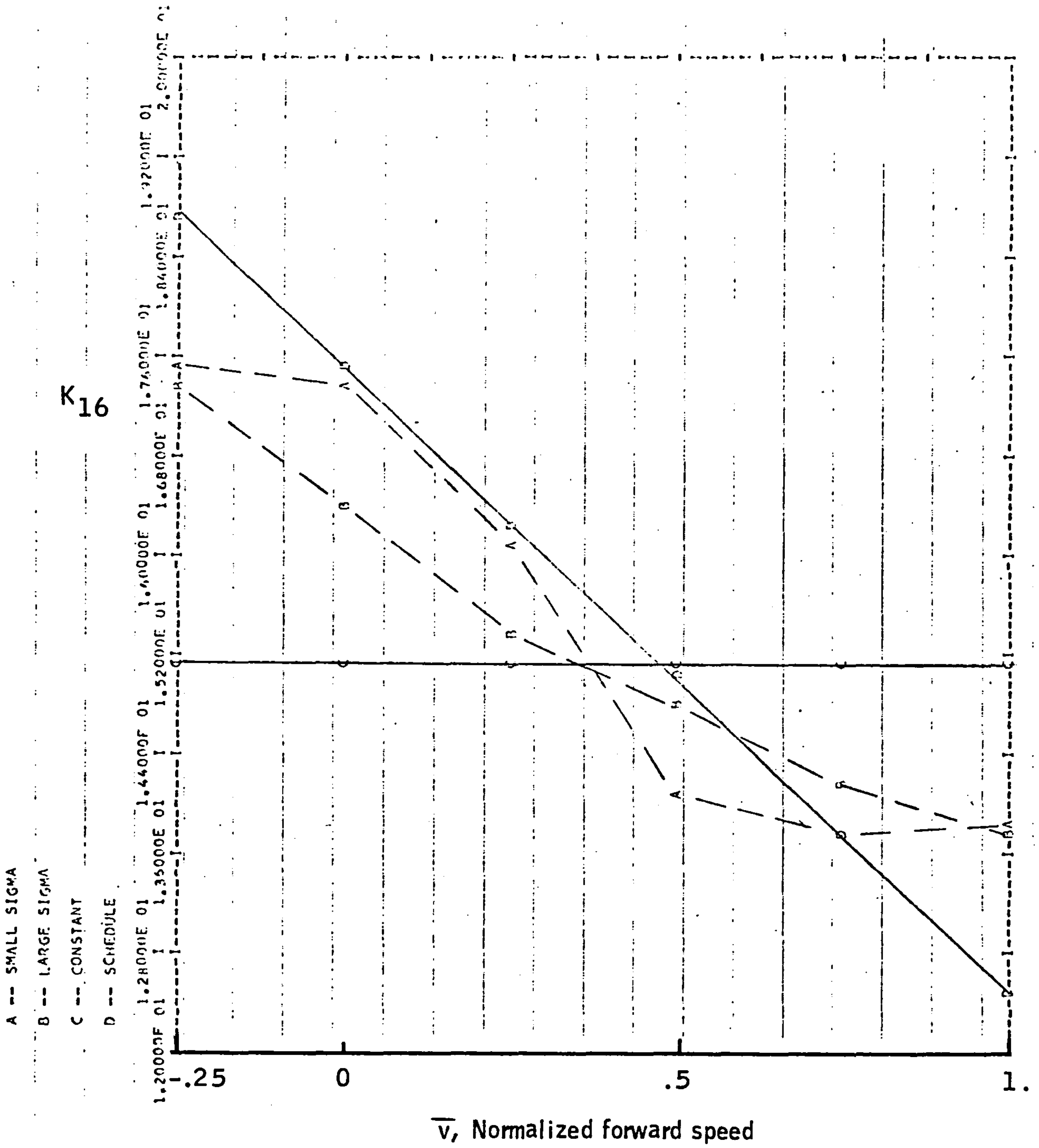

Figure 92. -Element K_{16} versus $\bar{v}$ -- longitudinal-axis gain schedule.

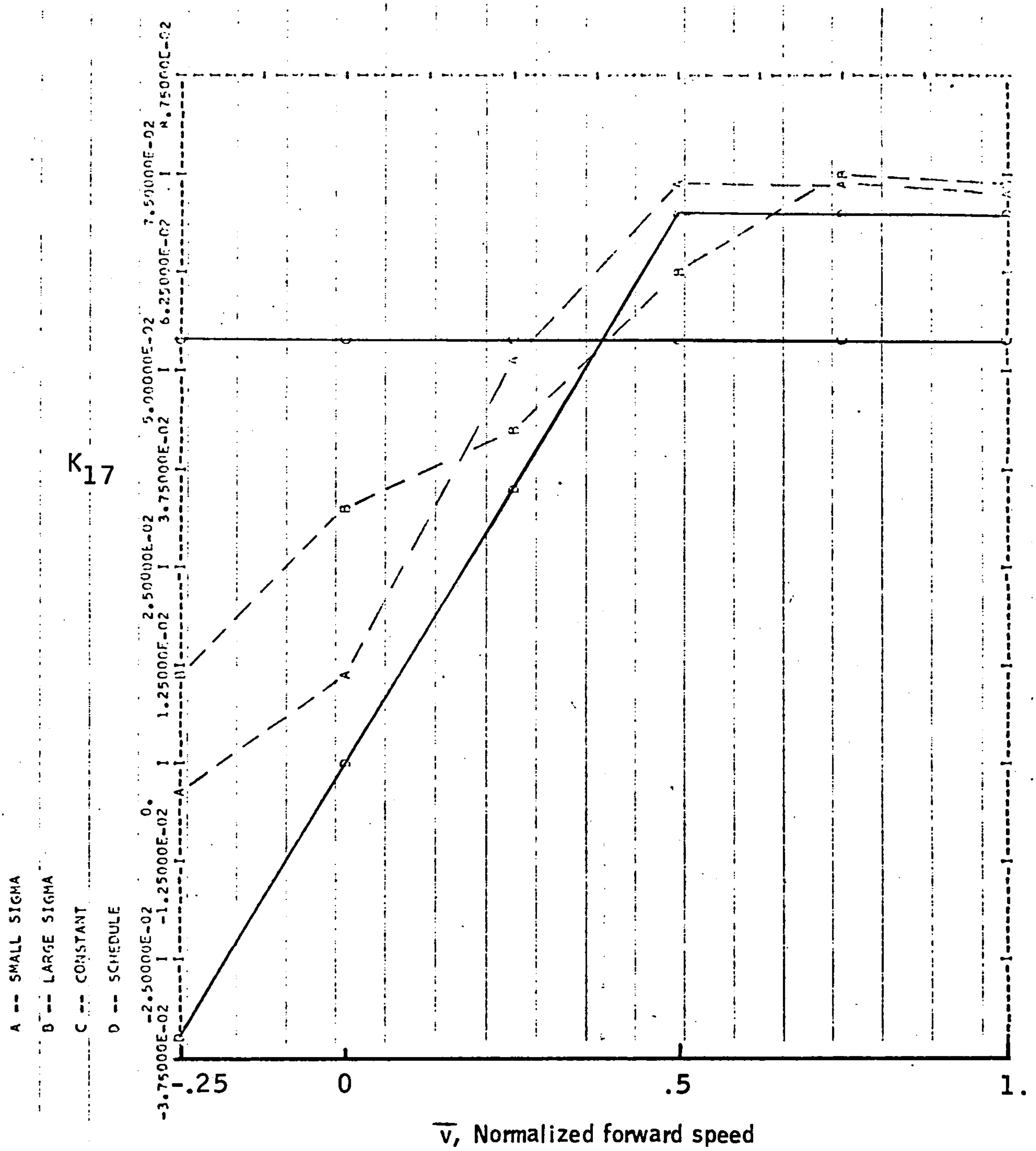

Figure 93. -Element K_{17} versus $\bar{v}$ -- longitudinal-axis gain schedule.

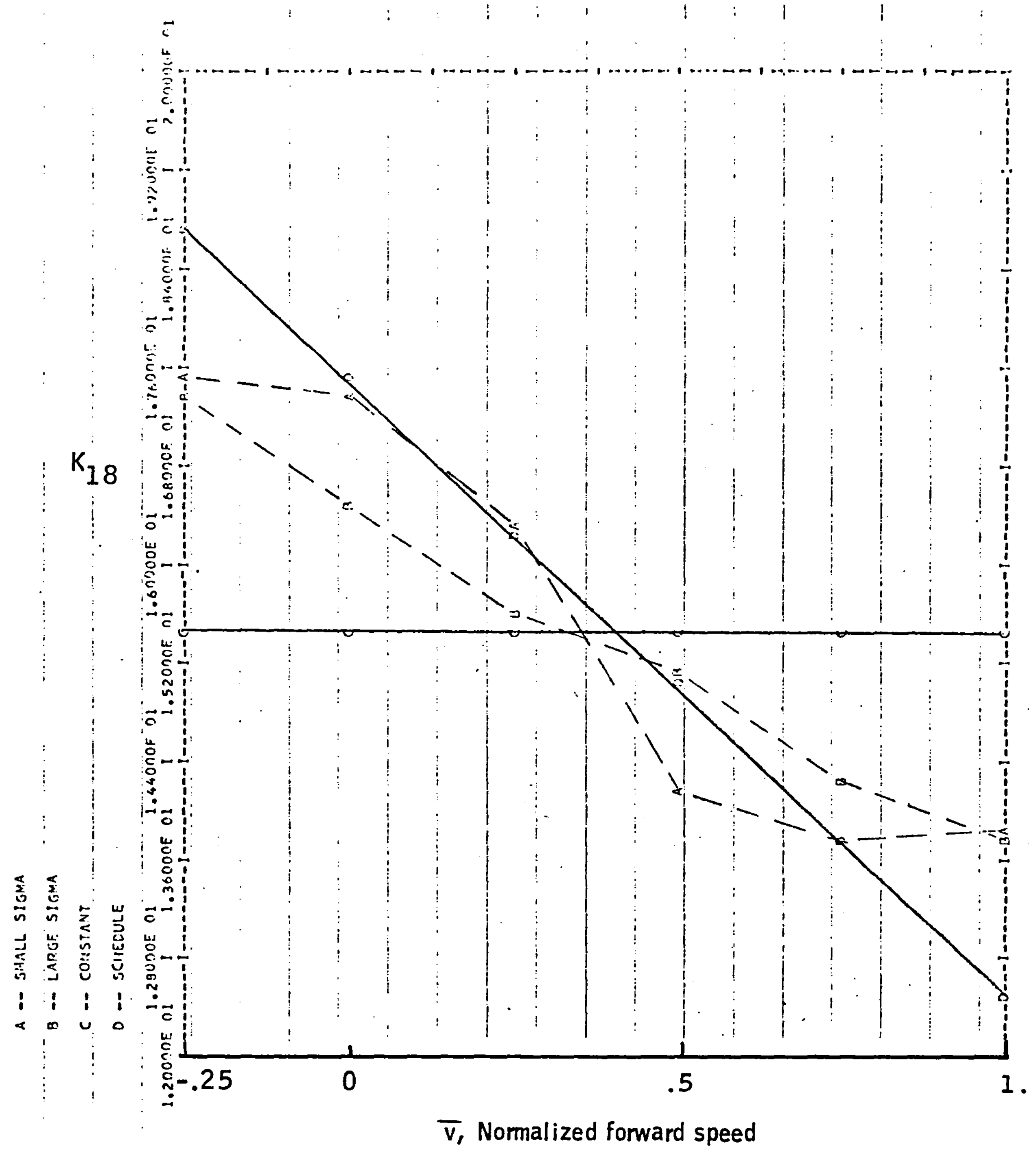

Figure 94. -Element K_{18} versus $\tilde{v}$ -- longitudinal-axis gain schedule.

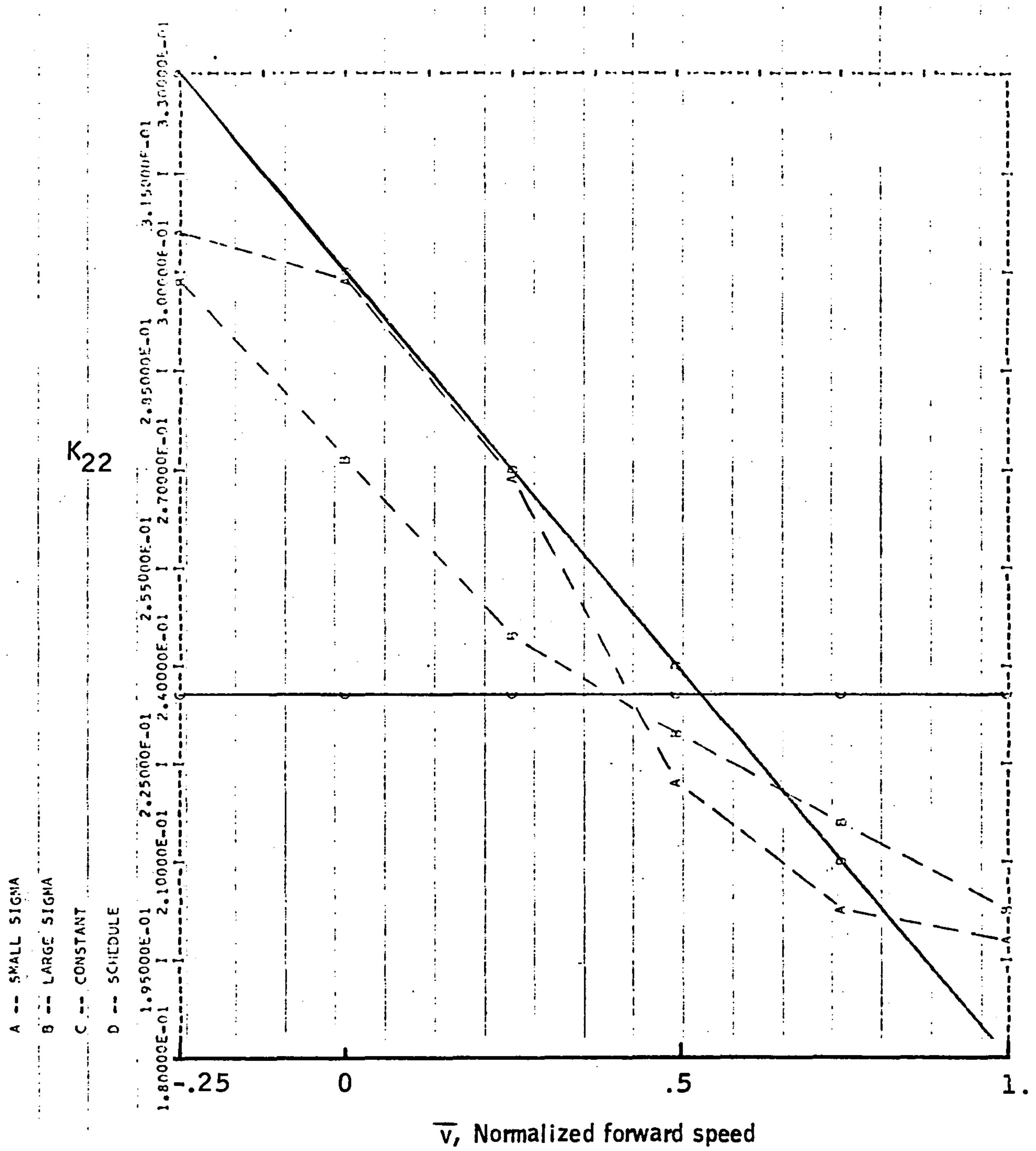

Figure 95. -Element K_{22} versus $\tilde{v}$ -- longitudinal-axis gain schedule.

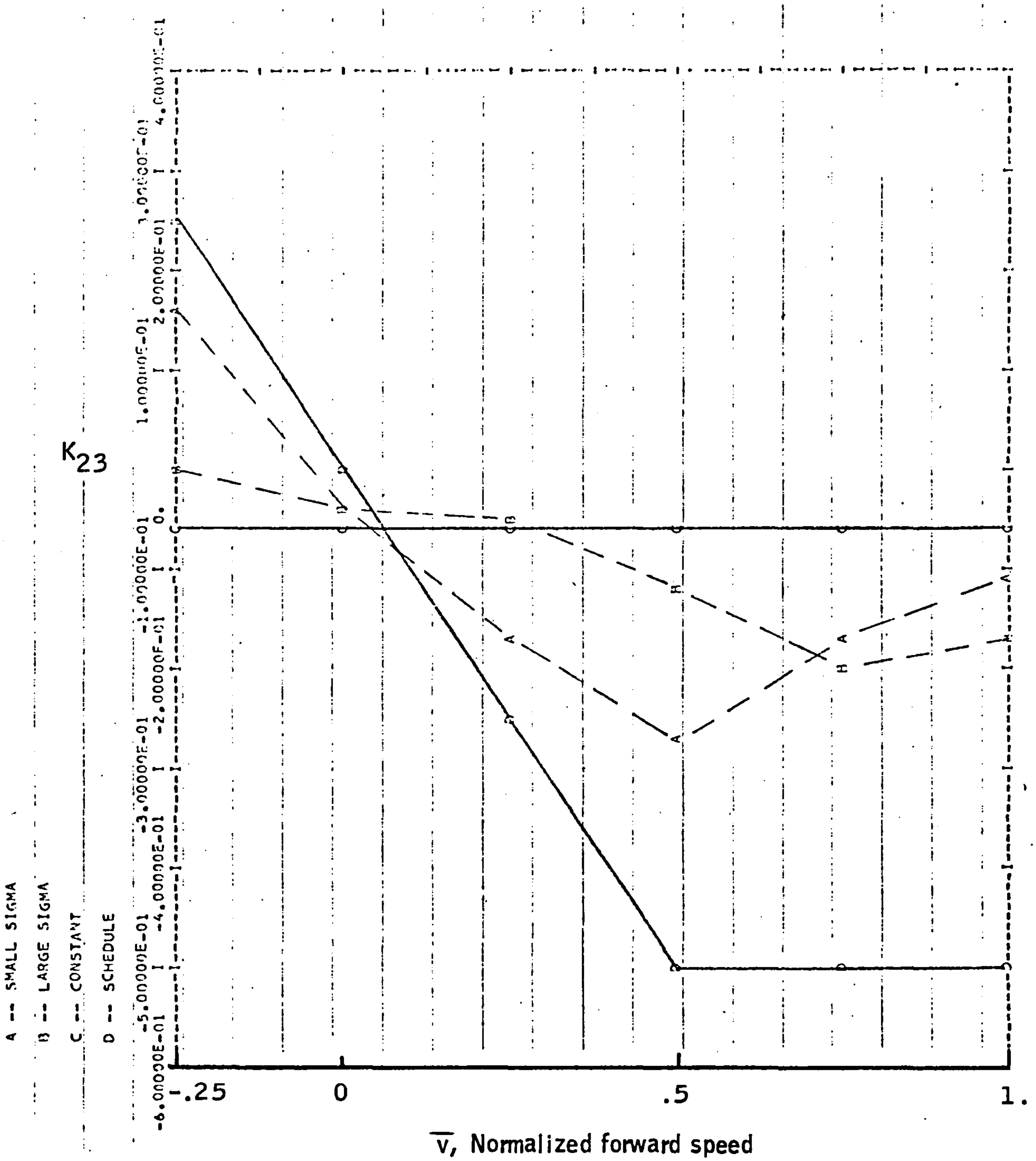

Figure 96. -Element K_{23} versus $\bar{v}$ -- longitudinal-axis gain schedule.

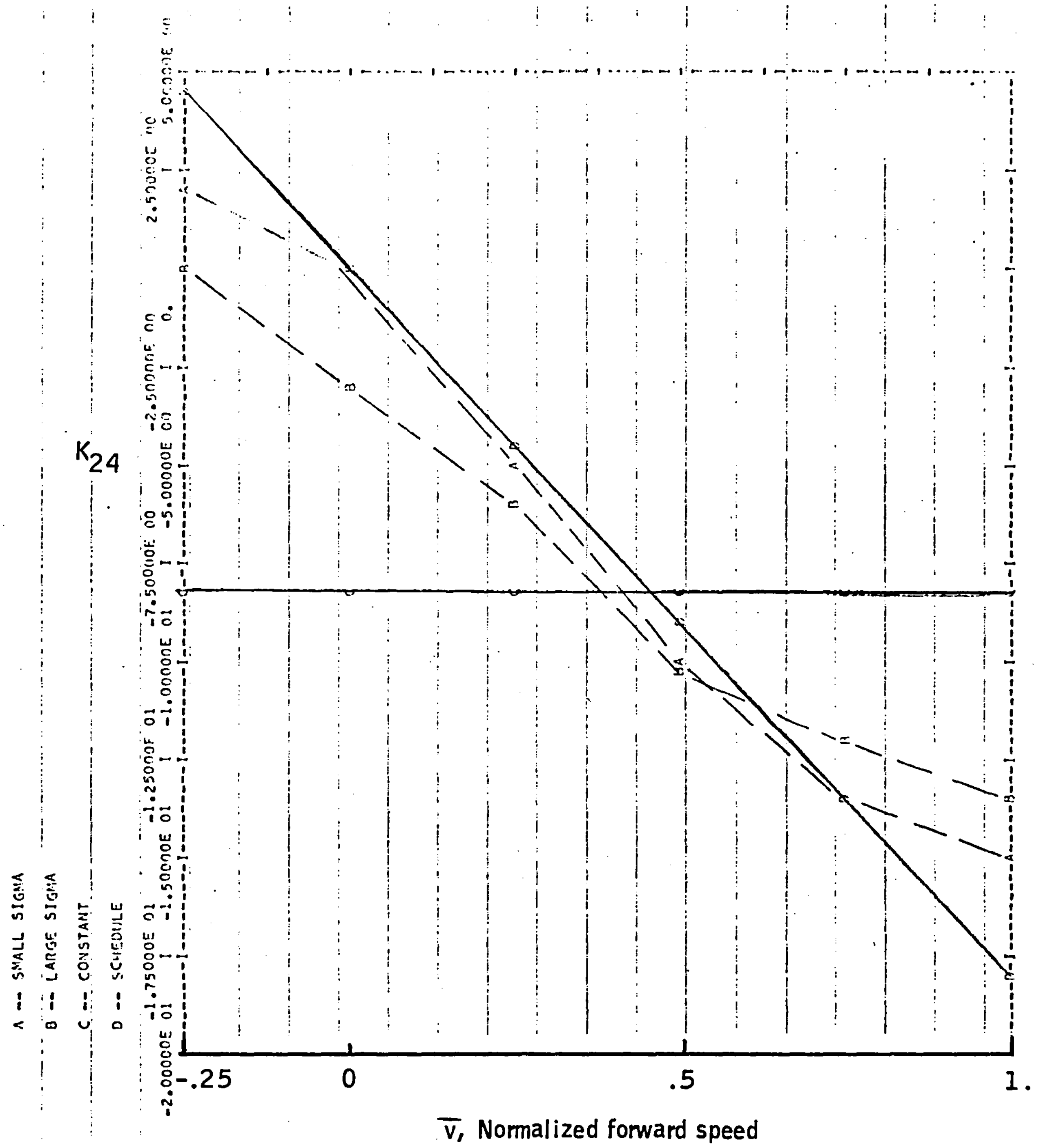

Figure 97. -Element K_{24} versus $\bar{v}$ -- longitudinal-axis gain schedule.

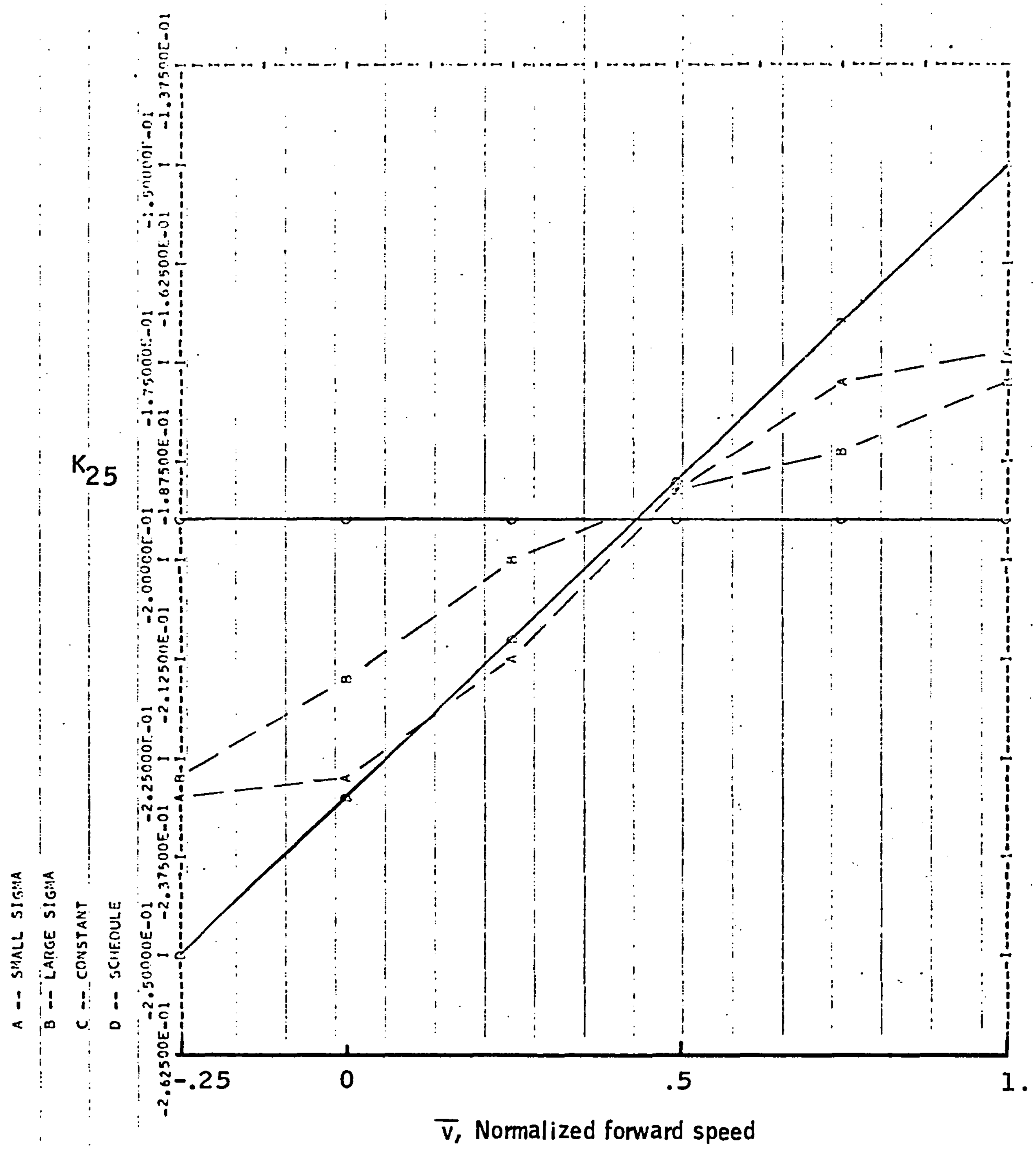

Figure 98. -Element K_{25} versus $\bar{v}$ -- longitudinal-axis gain schedule.

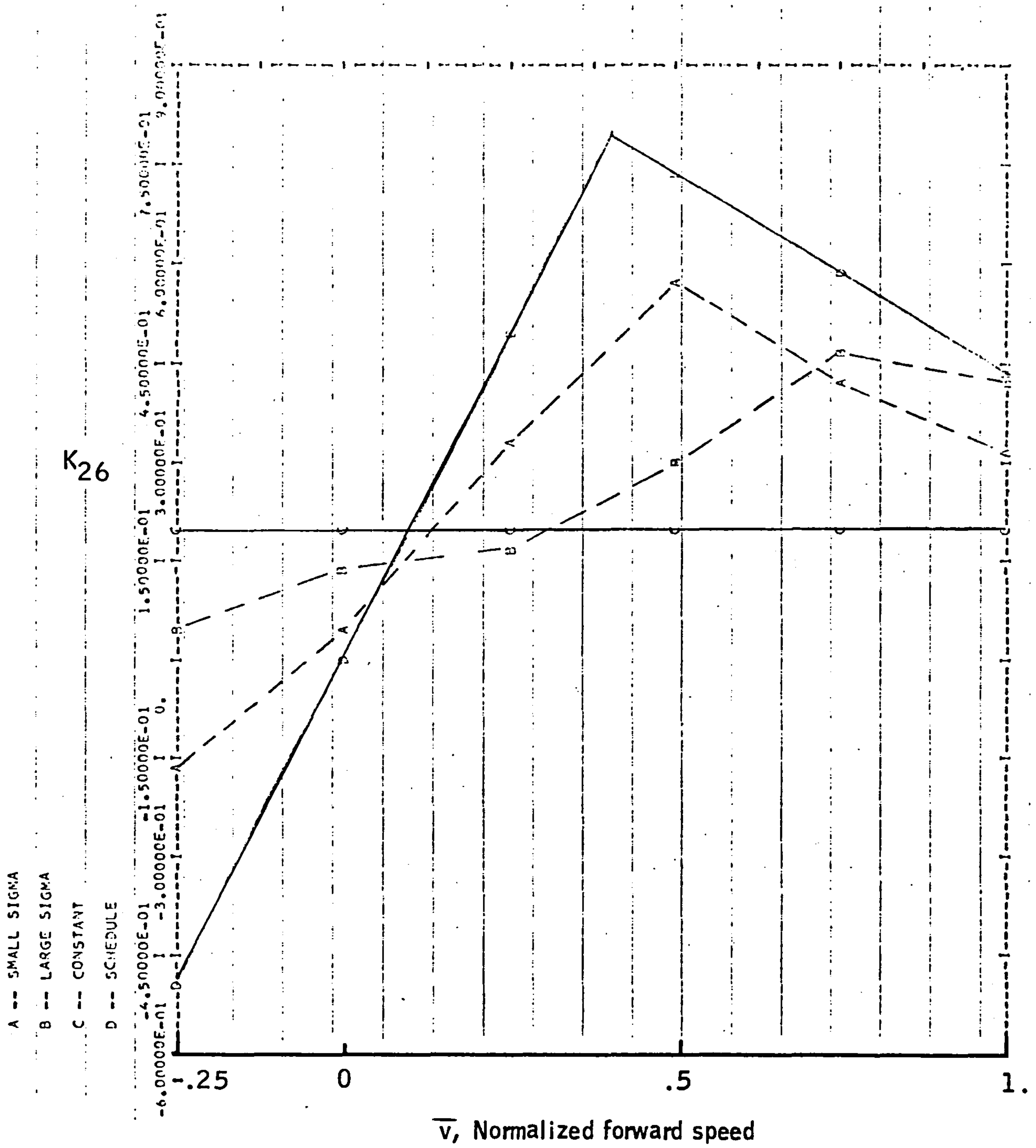

Figure 99. -Element K_{26} versus $\bar{v}$ -- longitudinal-axis gain schedule.

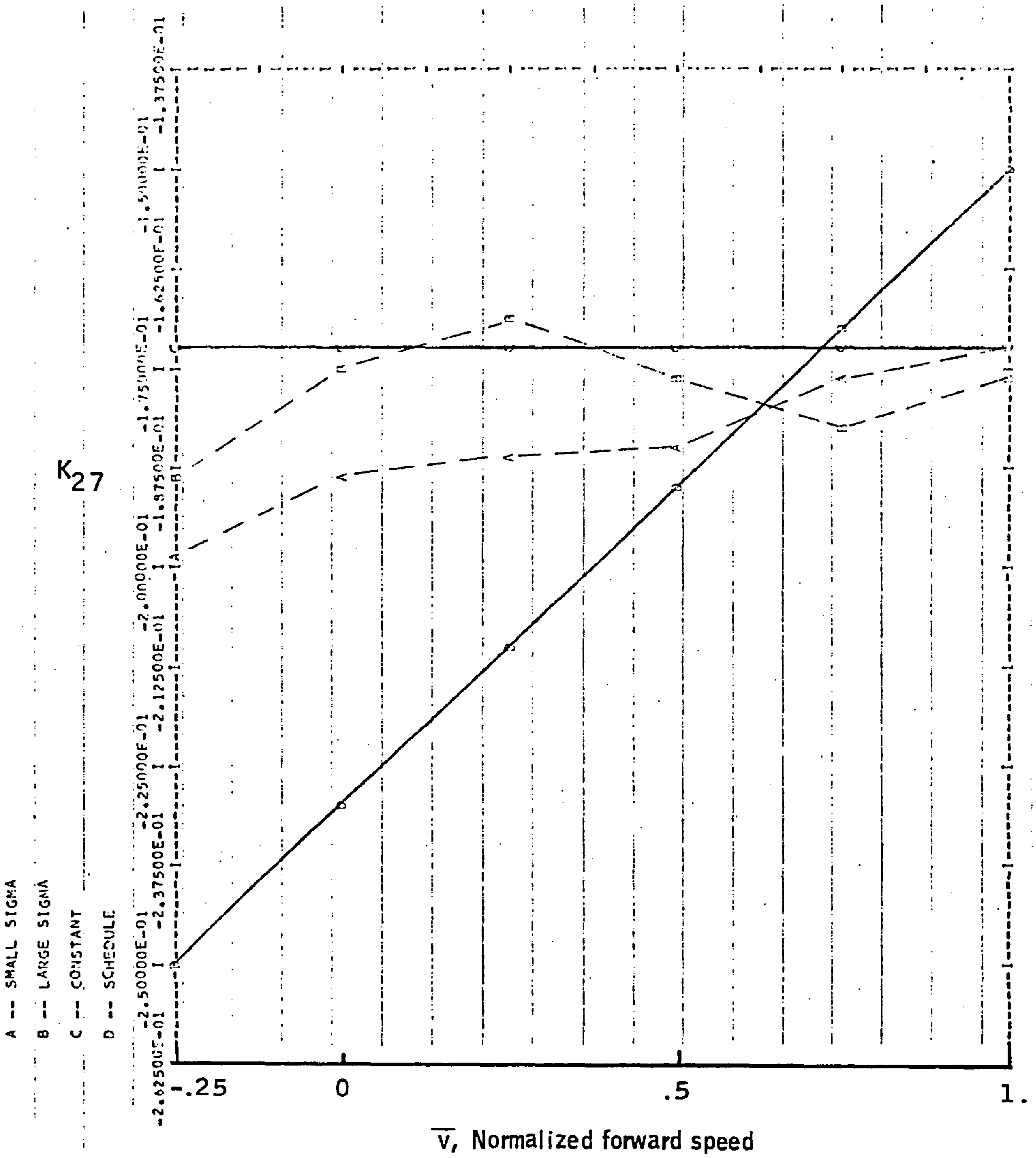

Figure 100. -Element K_{27} versus $\bar{v}$ -- longitudinal-axis gain schedule.

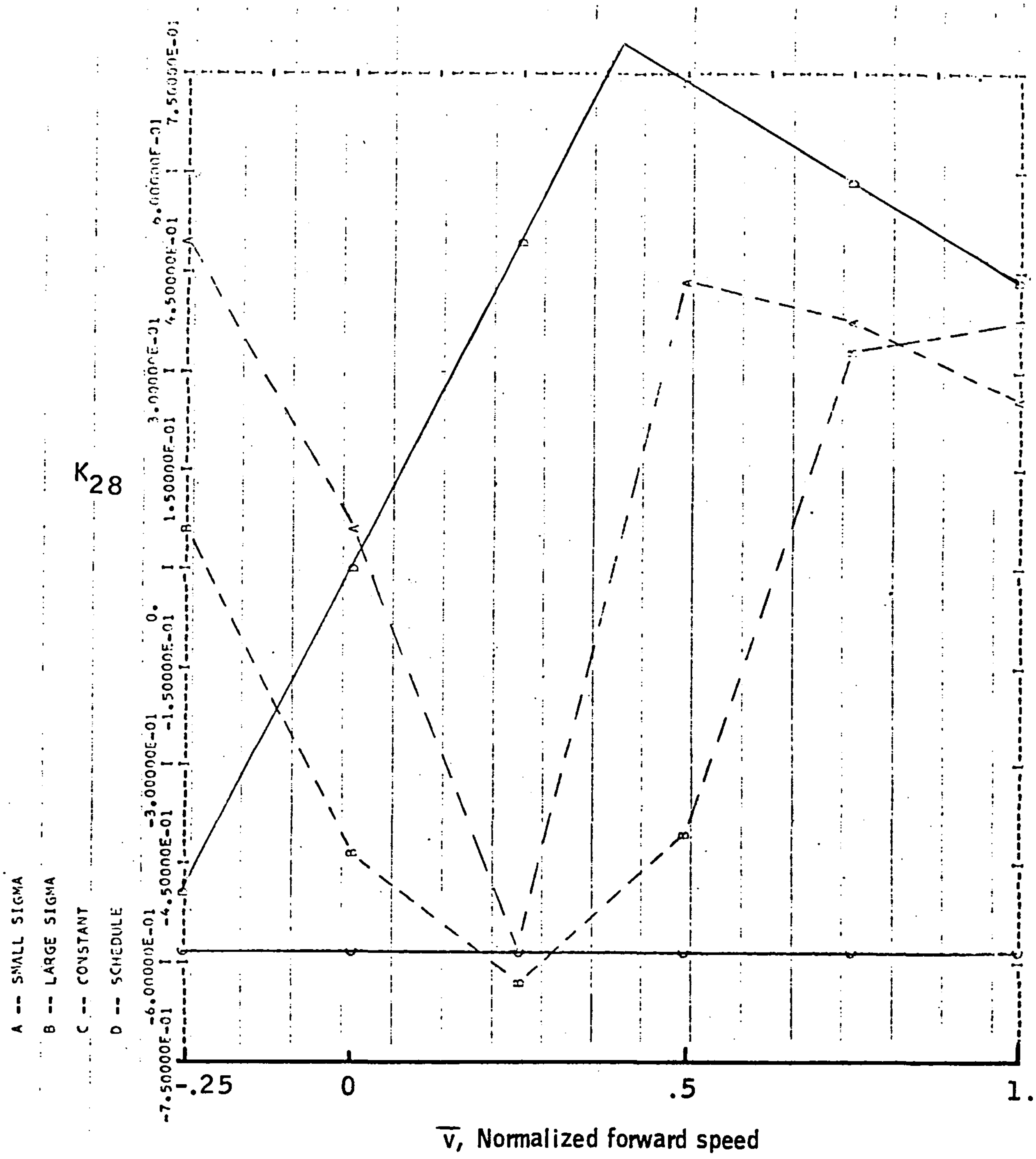

Figure 101. -Element K_{28} versus $\bar{v}$ -- longitudinal-axis gain schedule.

APPENDIX F

PARAMETER ESTIMATION USING RECORDED FLIGHT DATA

This appendix presents plots of 12 maneuvers analyzed in Section 10. For each maneuver the two controls, pitch rate and its residual and pitch attitude and its residual, are plotted. These plots have been normalized. The normalization factors are

Controls (δ_B, δ_c): 1 = 2.54 cm

Pitch rate: 1 = 1 rad/s

Pitch attitude: 1 = 1 rad

The data, in the form of computer plots, are presented in Figures 102 through 137.

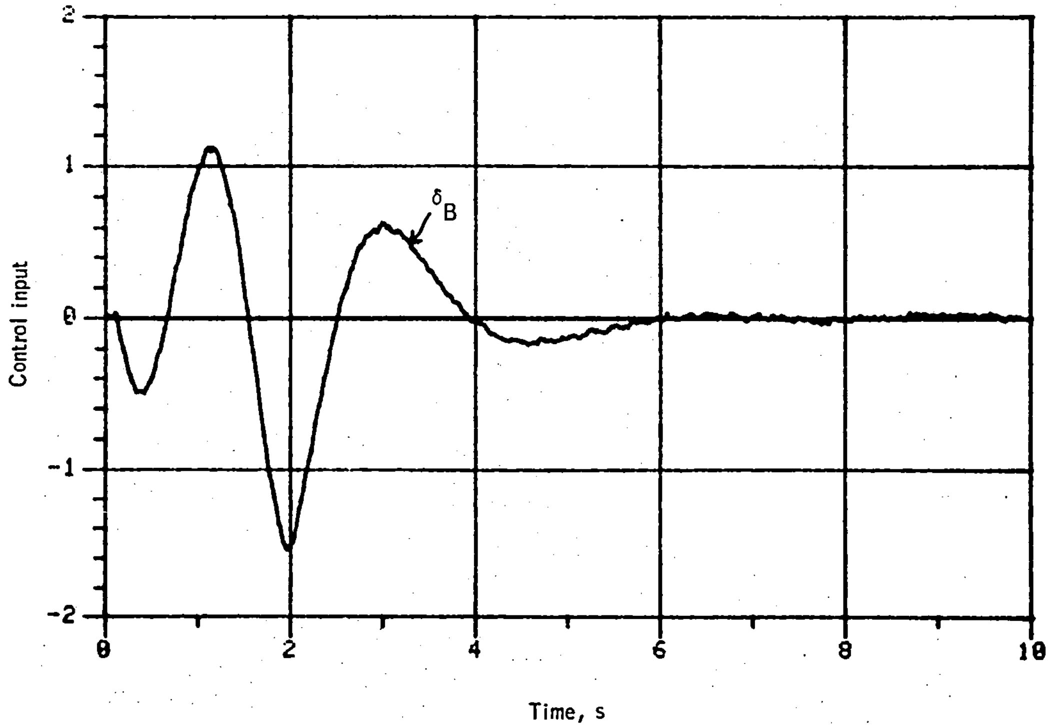

Figure 102. -Control input versus time -- maneuver no. 1.

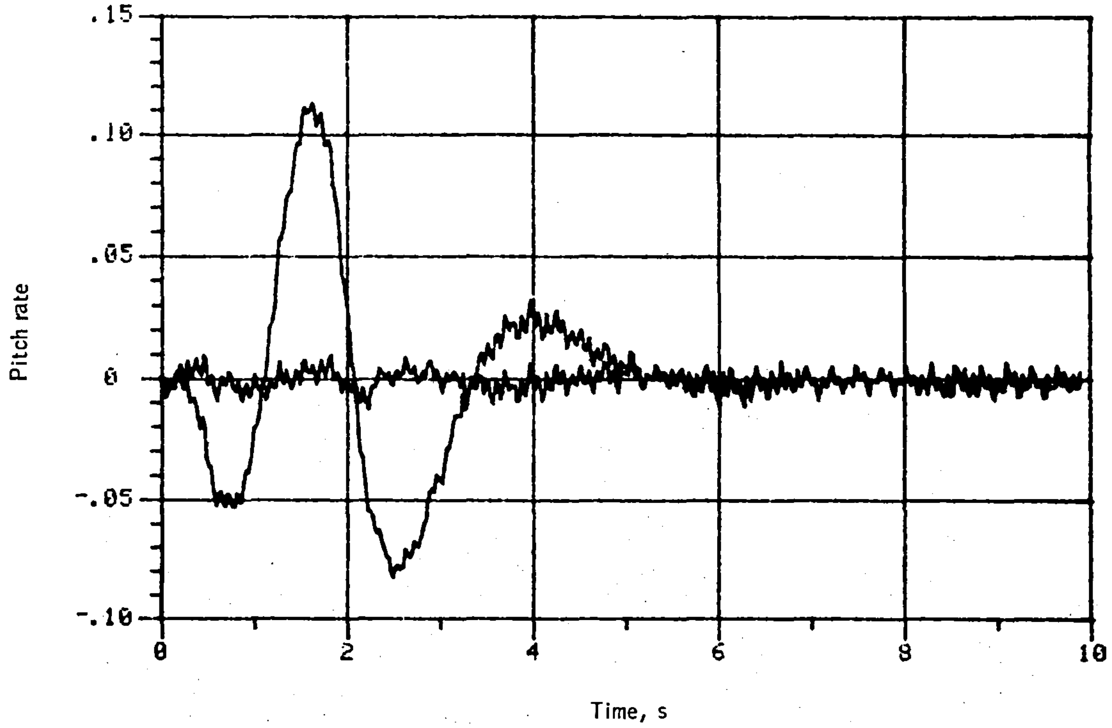

Figure 103. -Pitch rate versus time -- maneuver no. 1.

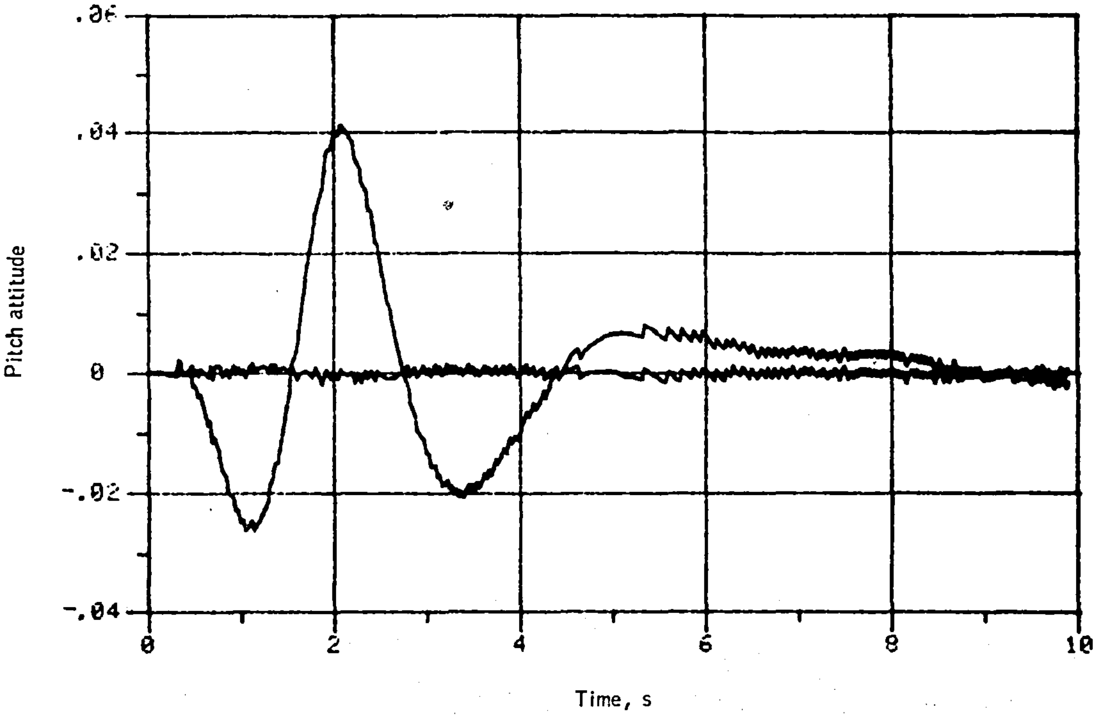

Figure 104. -Pitch attitude versus time -- maneuver no. 1.

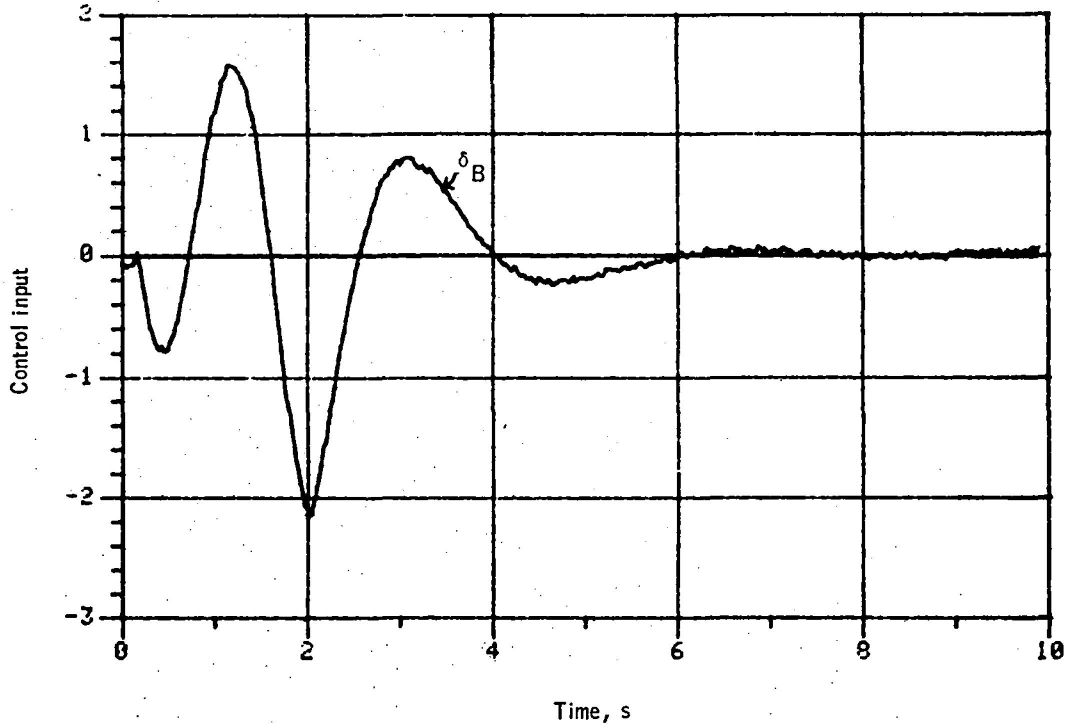

Figure 105. -Control input versus time -- maneuver no. 2.

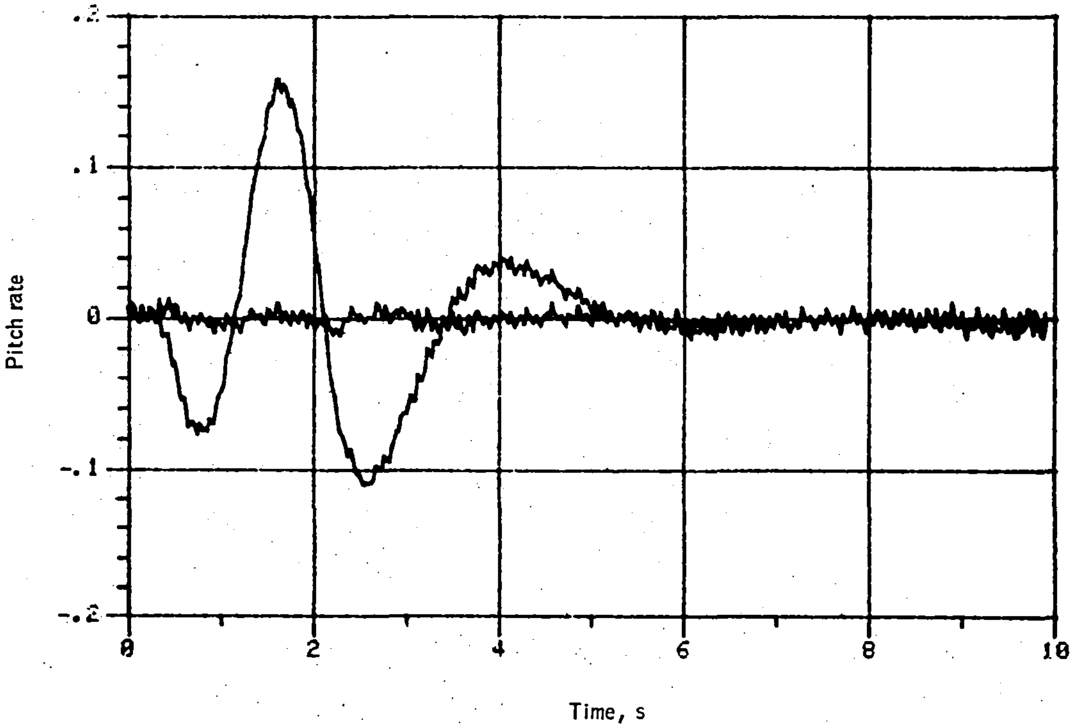

Figure 106. -Pitch rate versus time -- maneuver no. 2.

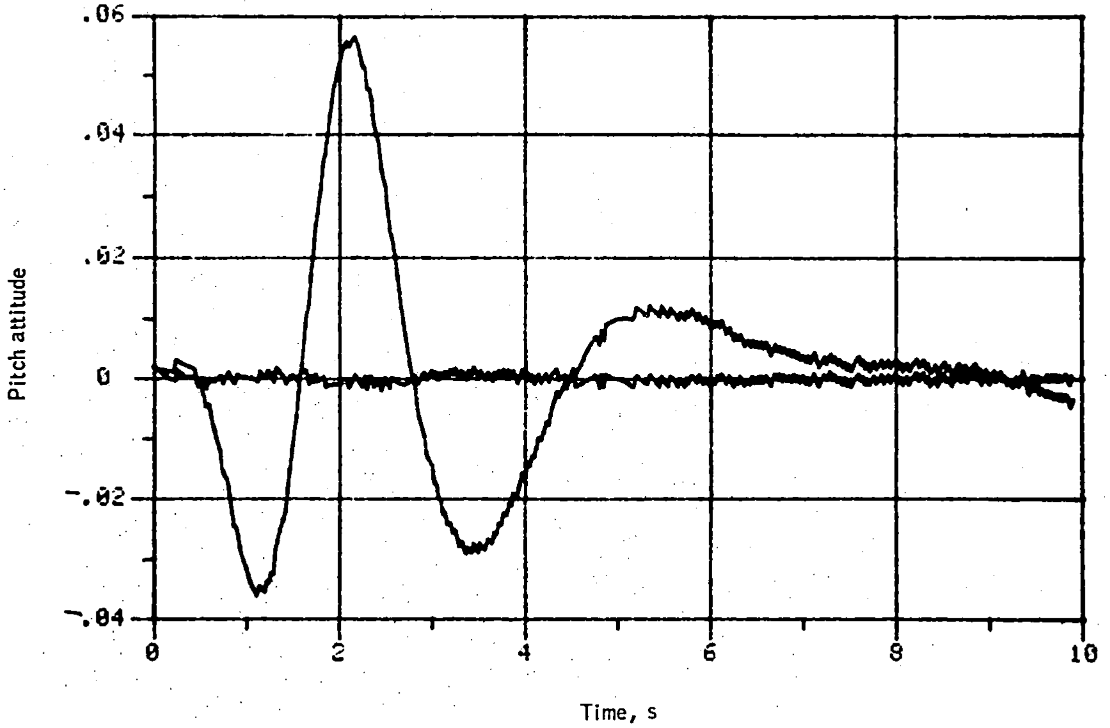

Figure 107. -Pitch attitude versus time -- maneuver no. 2.

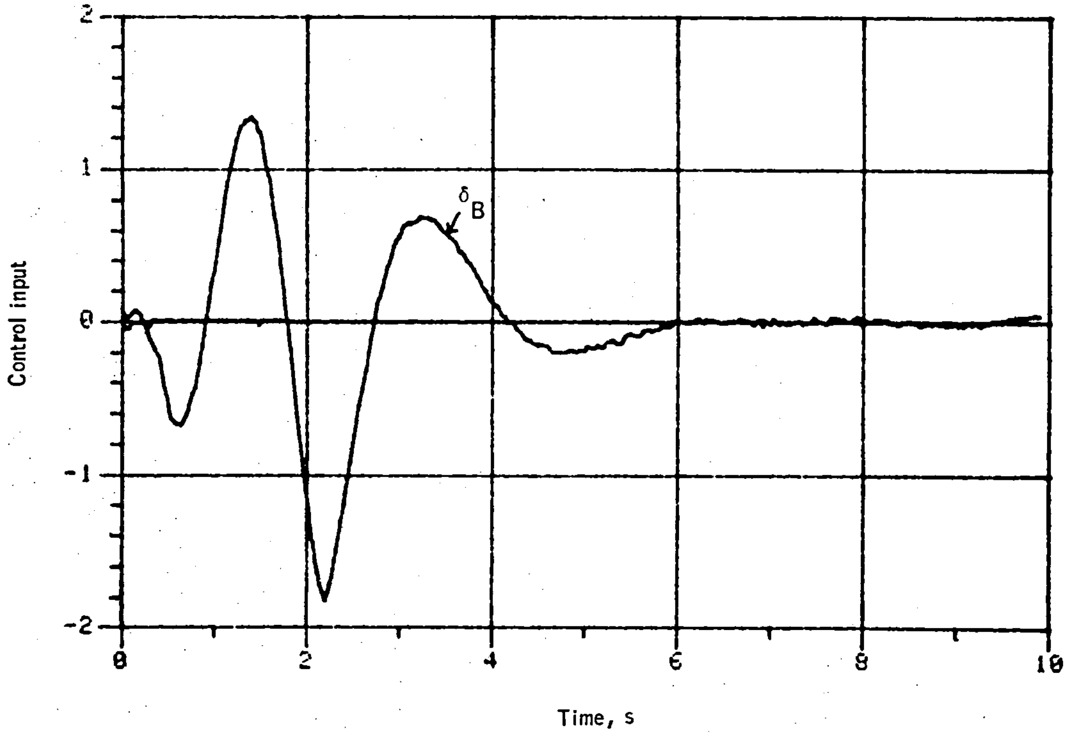

Figure 108. -Control input versus time -- maneuver no. 3.

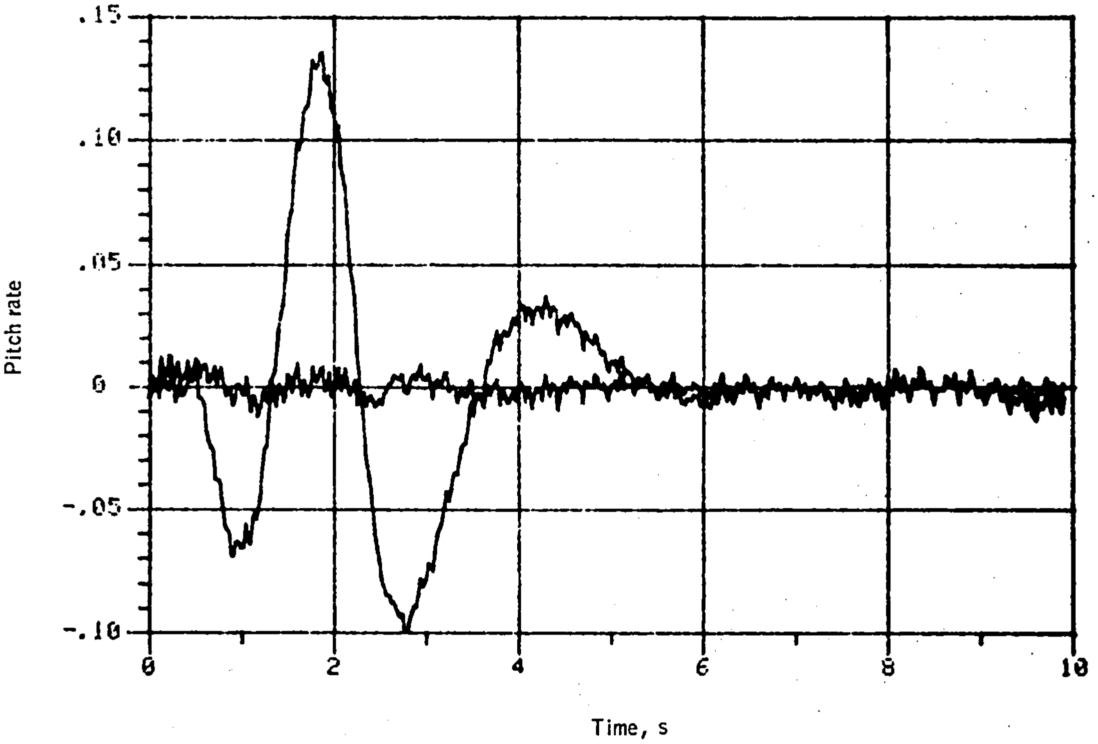

Figure 109. -Pitch rate versus time -- maneuver no. 3.

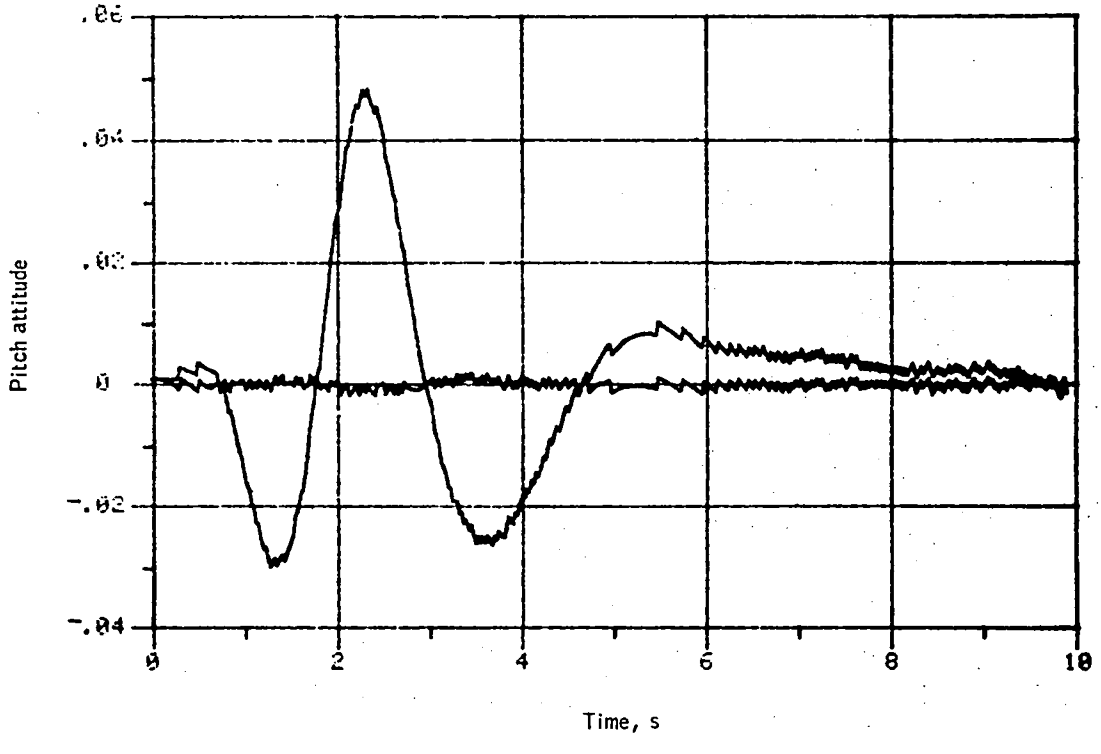

Figure 110. -Pitch attitude versus time -- maneuver no. 3.

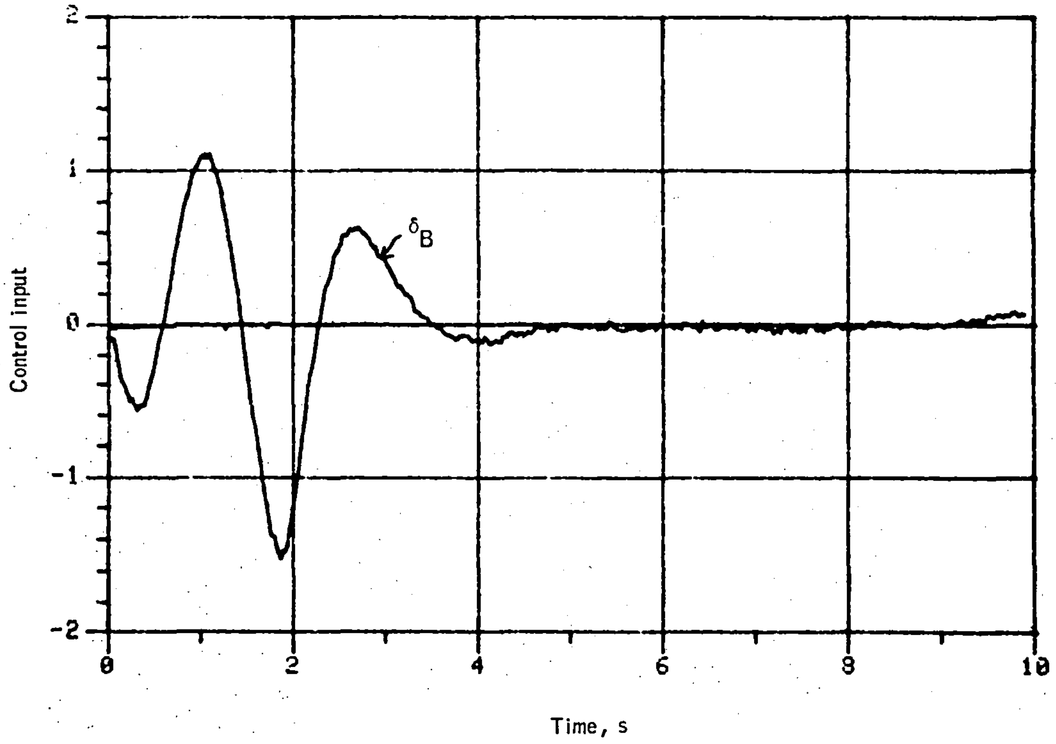

Figure 111. -Control input versus time -- maneuver no. 4.

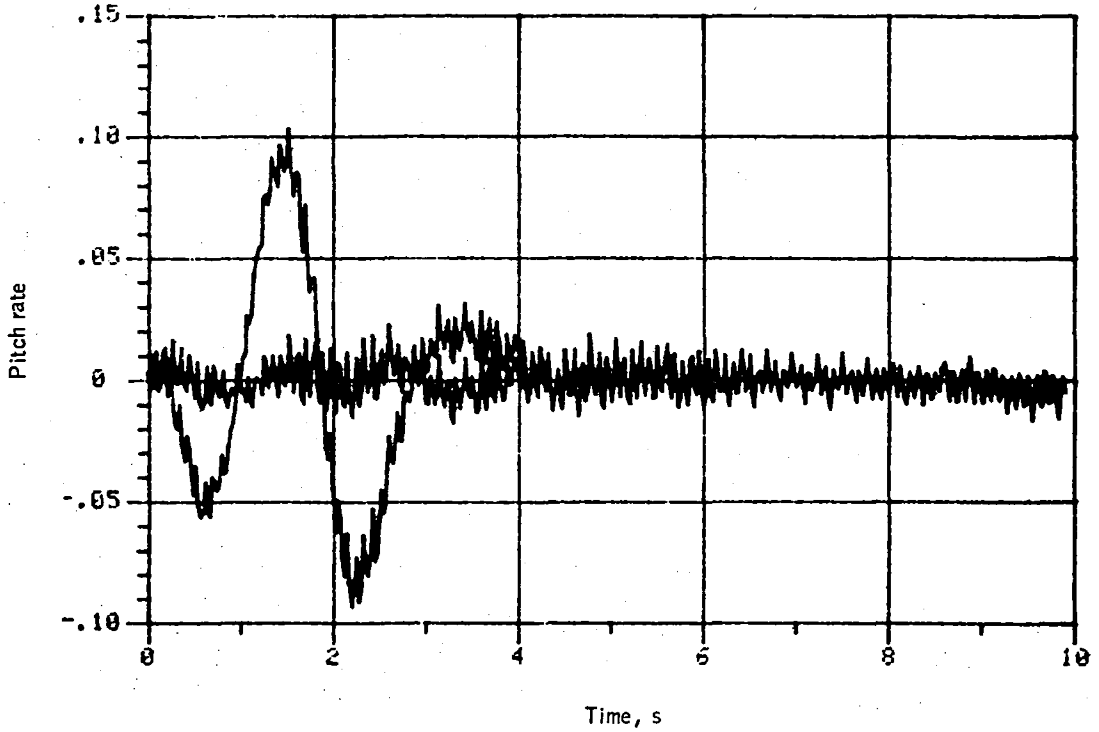

Figure 112. -Pitch rate versus time -- maneuver no. 4.

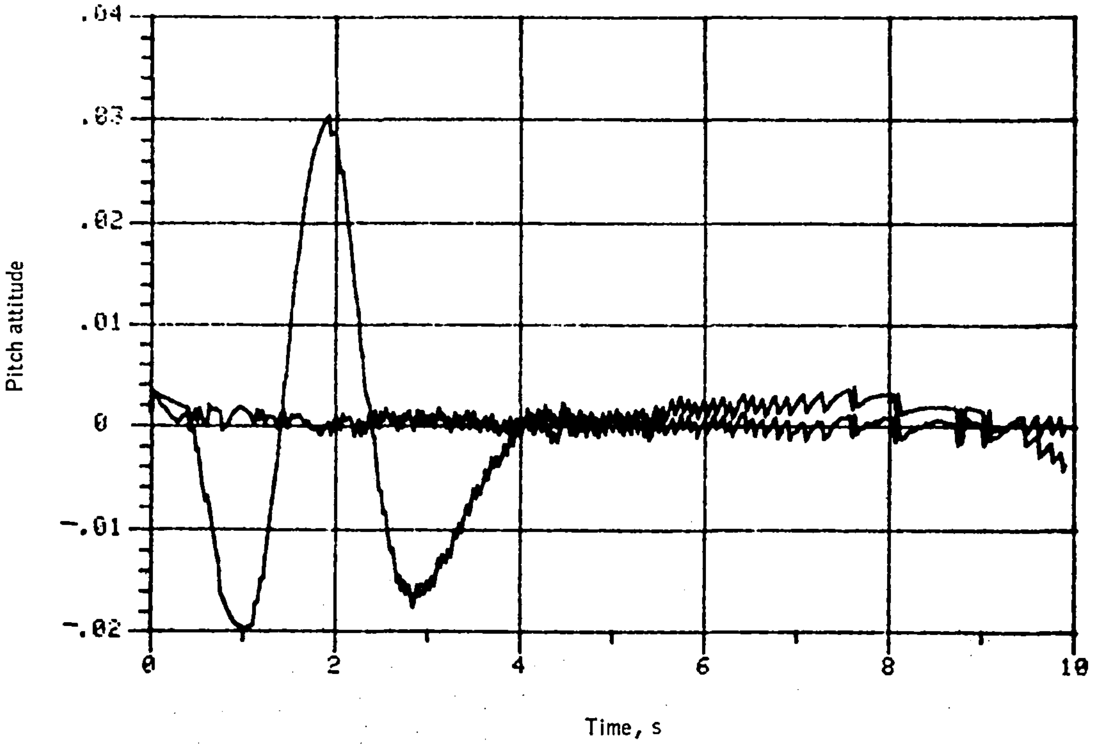

Figure 113. -Pitch attitude versus time -- maneuver no. 4.

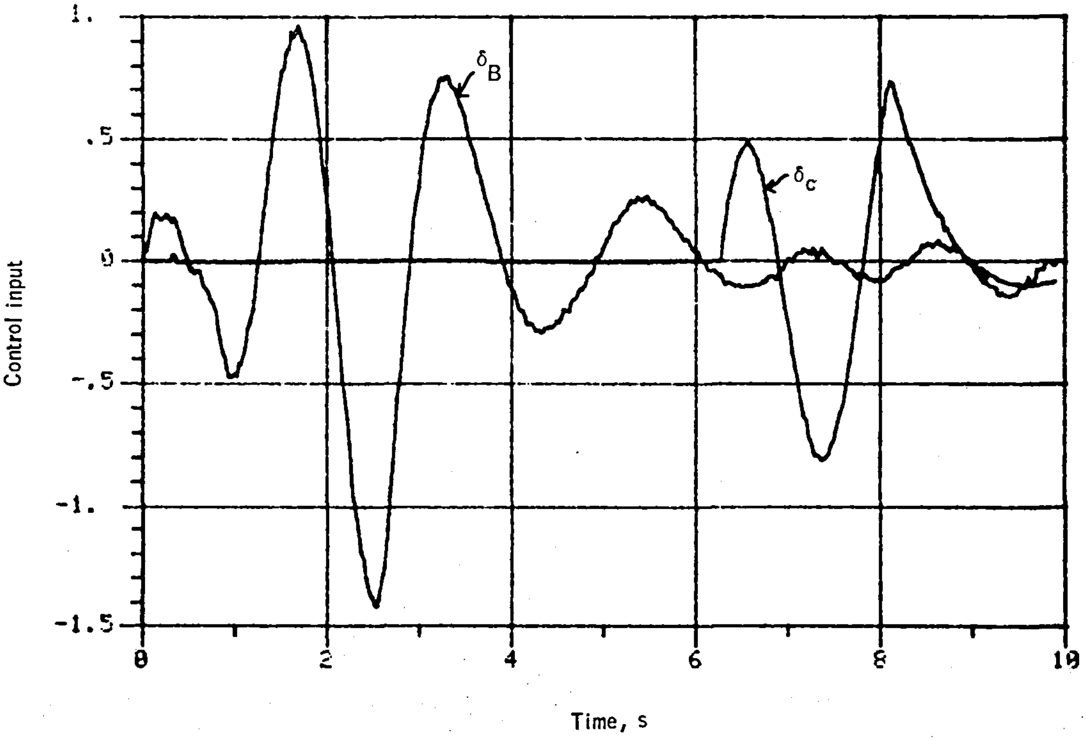

Figure 114. -Control input versus time -- maneuver no. 5.

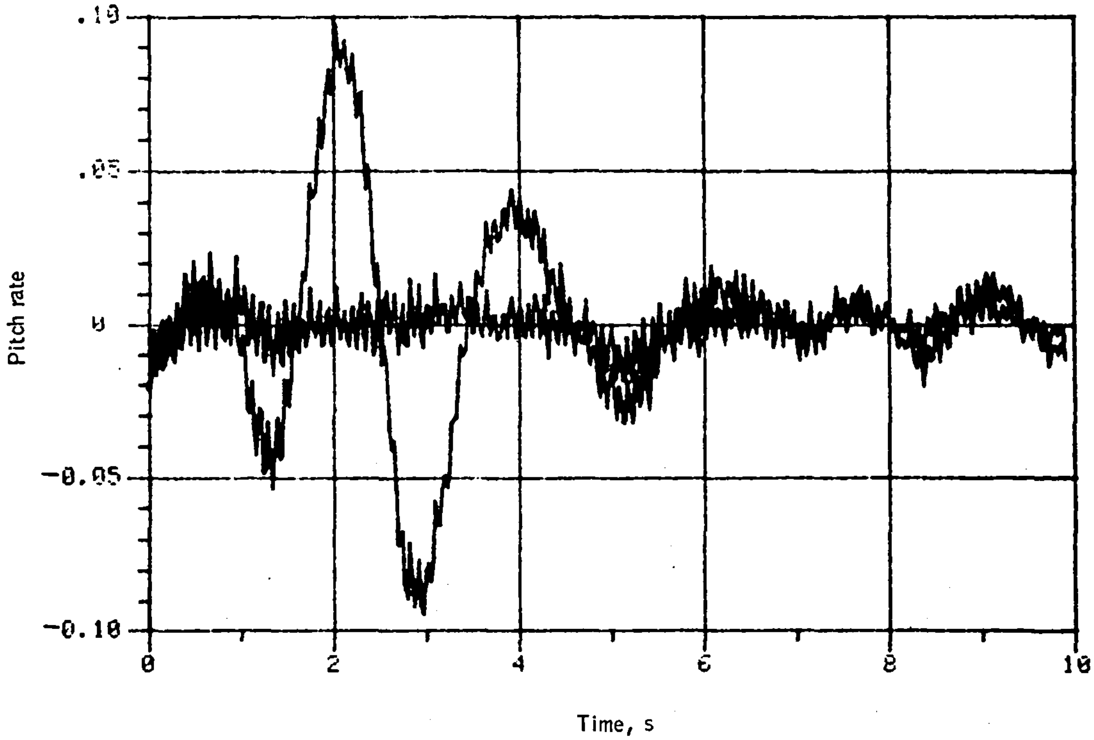

Figure 115. -Pitch rate versus time -- maneuver no. 5.

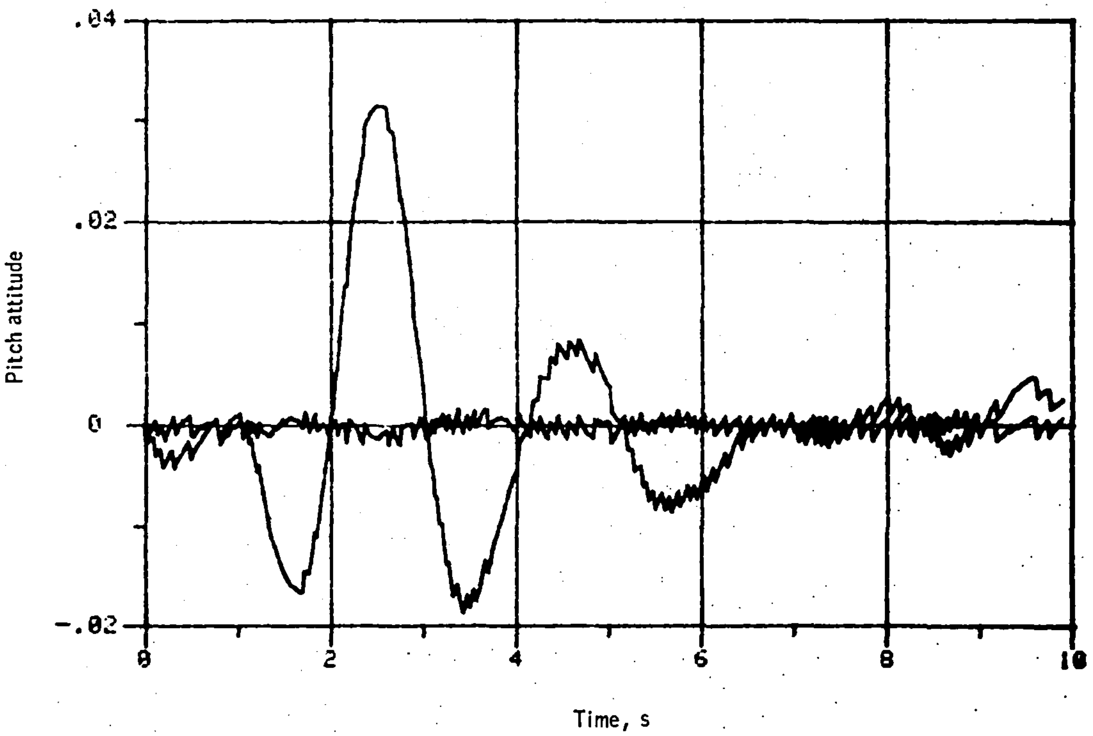

Figure 116. -Pitch attitude versus time -- maneuver no. 5.

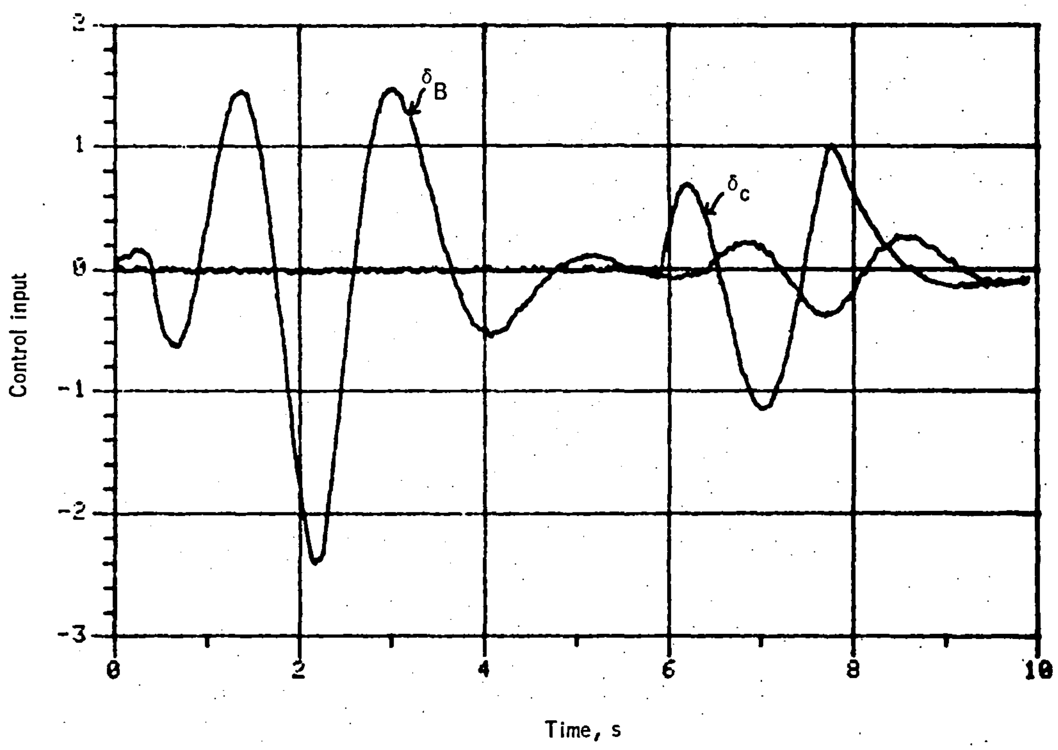

Figure 117. -Control input versus time -- maneuver no. 6.

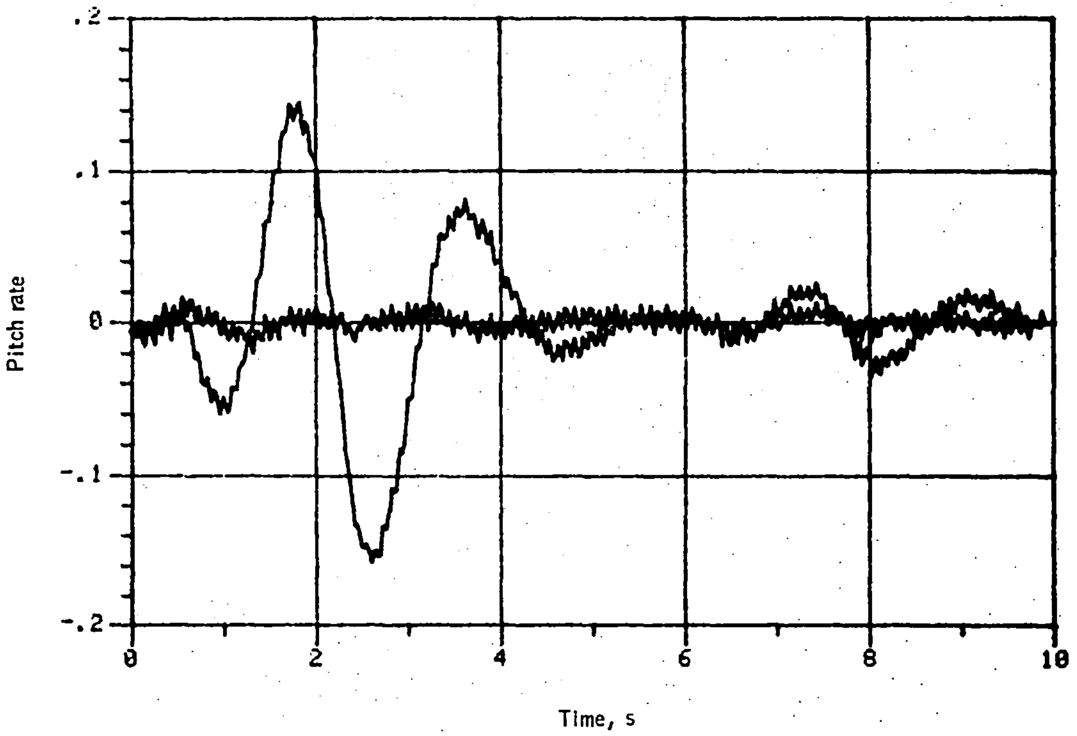

Figure 118. -Pitch rate versus time -- maneuver no. 6.

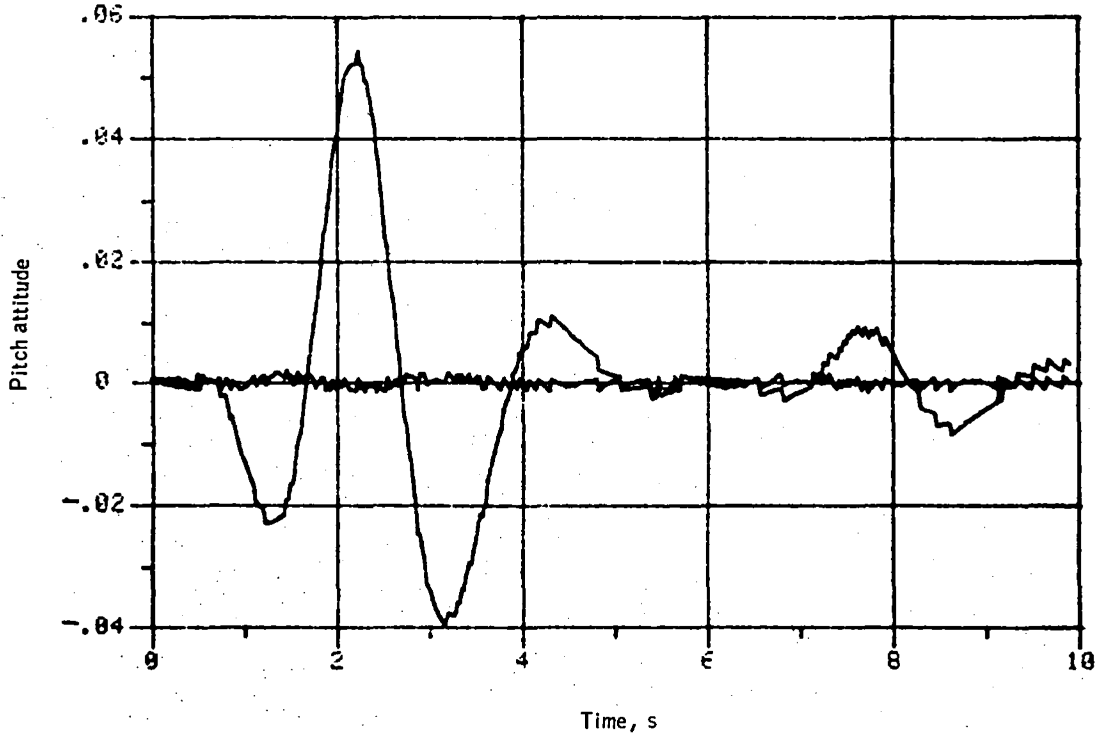

Figure 119. -Pitch attitude versus time -- maneuver no. 6.

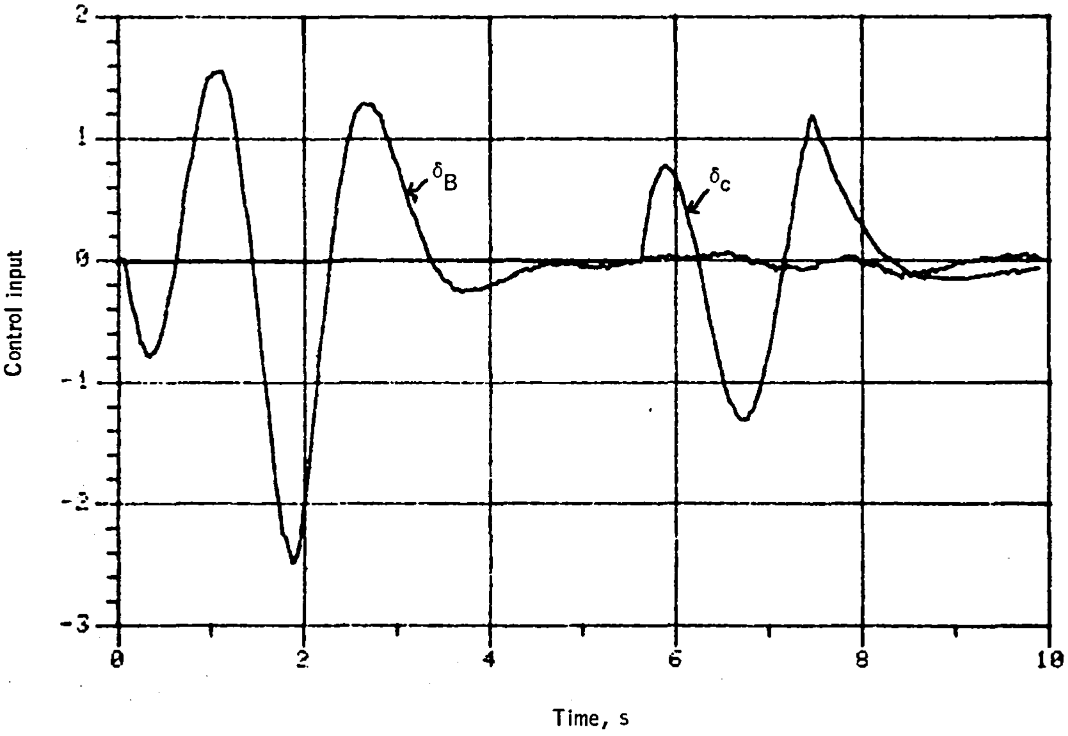

Figure 120. -Control input versus time -- maneuver no. 7.

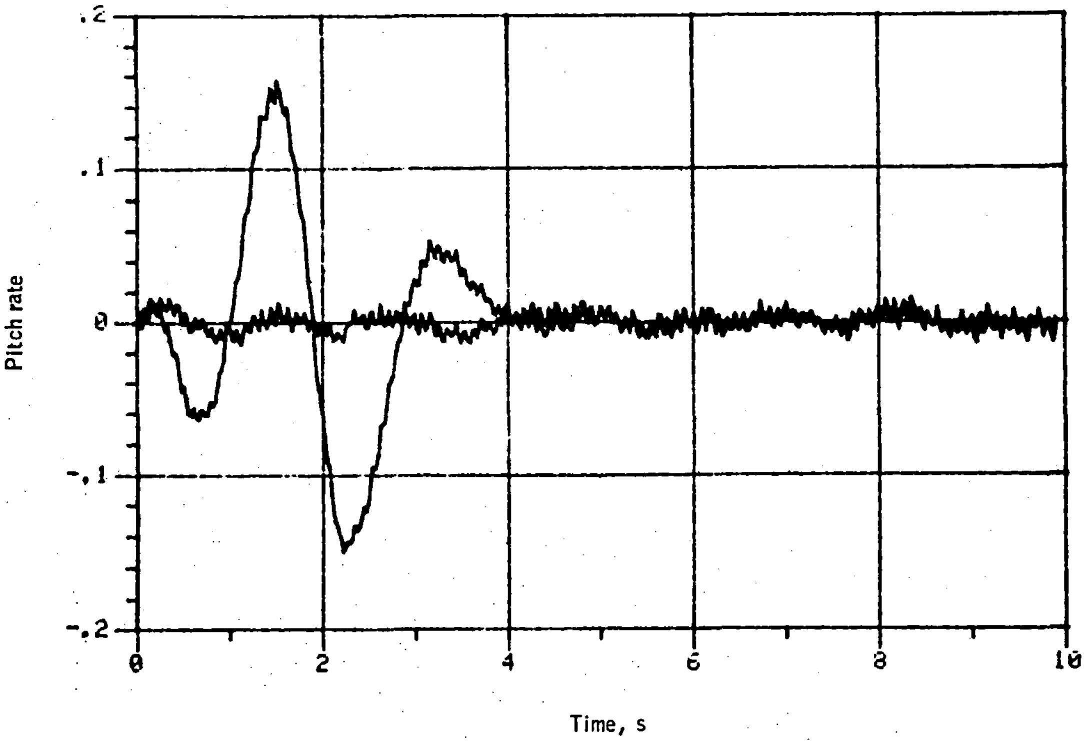

Figure 121. -Pitch rate versus time -- maneuver no. 7.

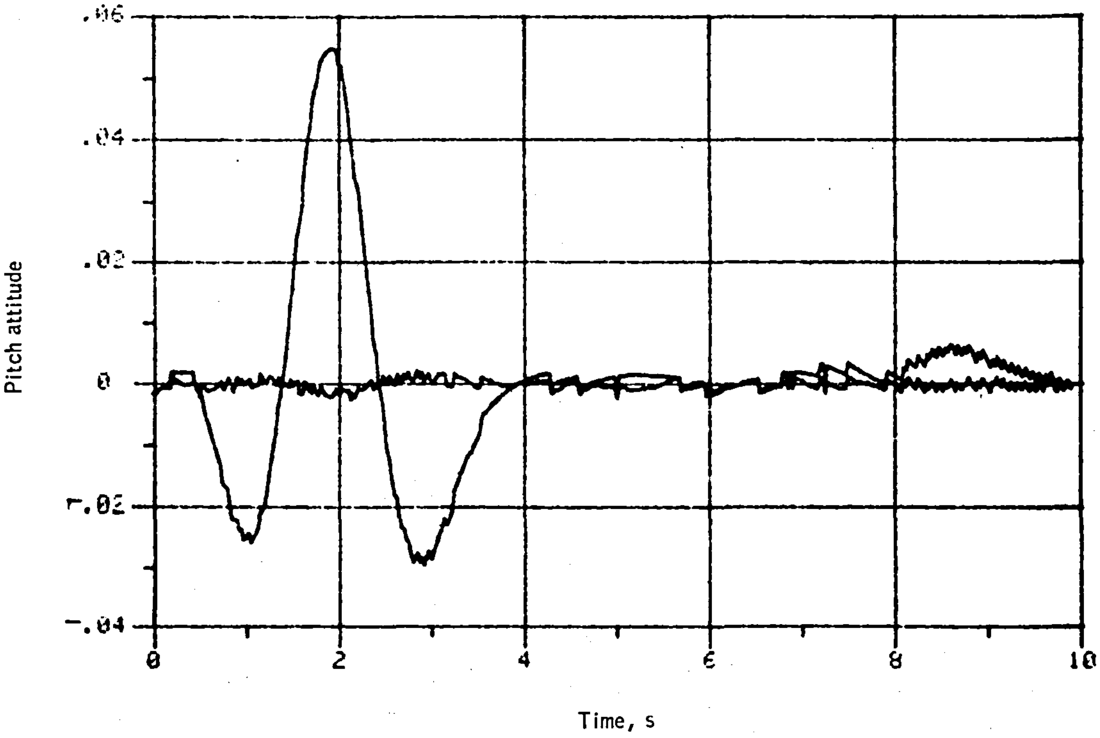

Figure 122. -Pitch attitude versus time -- maneuver no. 7.

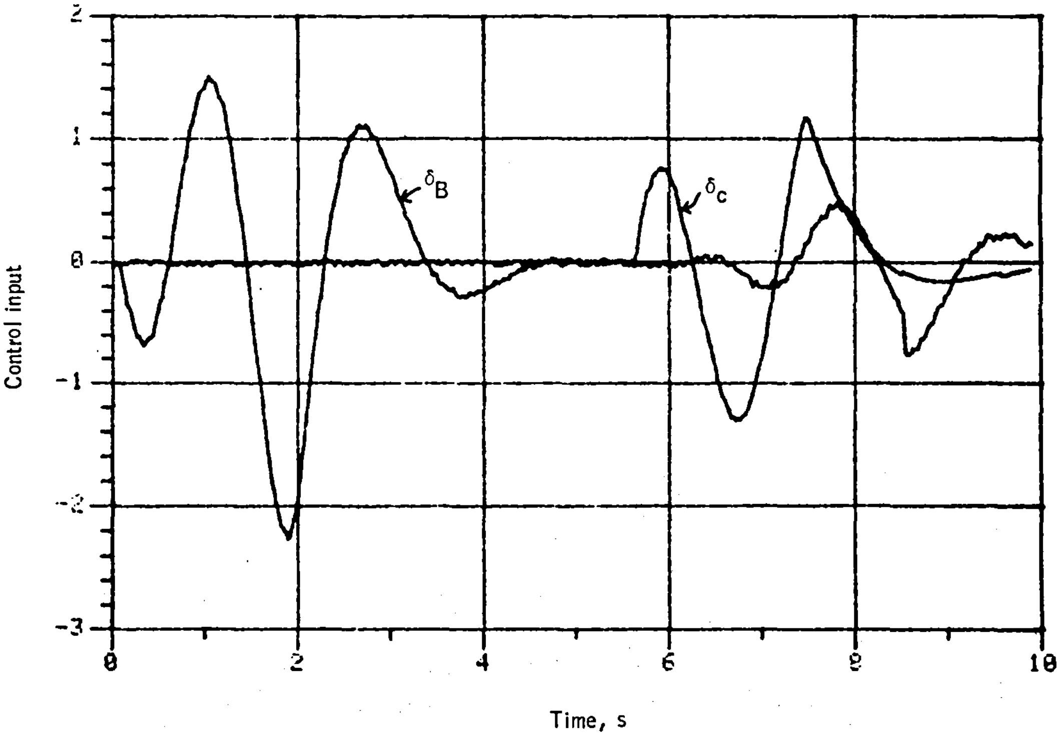

Figure 123. -Control input versus time -- maneuver no. 8.

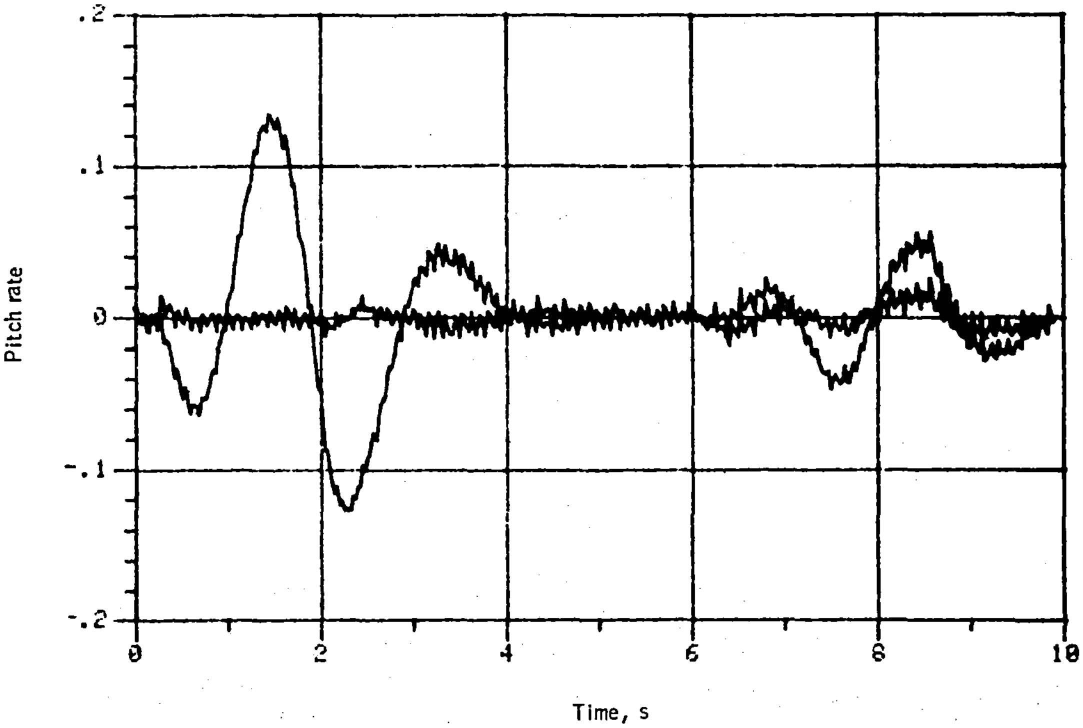

Figure 124. -Pitch rate versus time -- maneuver no. 8.

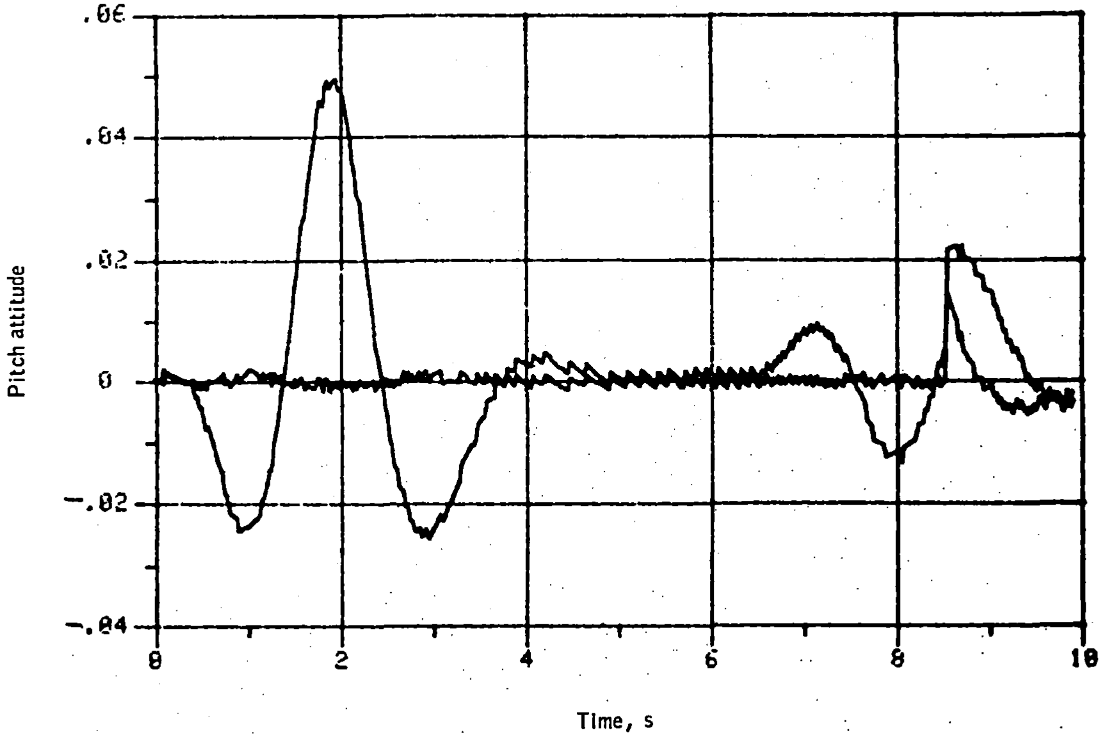

Figure 125. -Pitch attitude versus time -- maneuver no. 8.

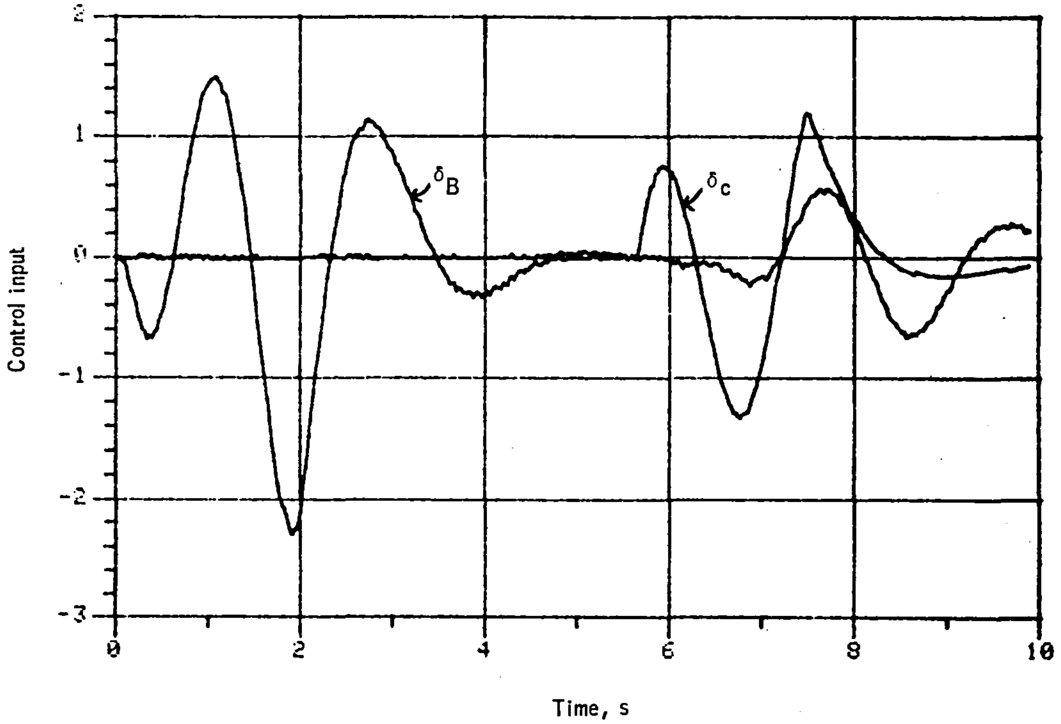

Figure 126. -Control input versus time -- maneuver no. 9.

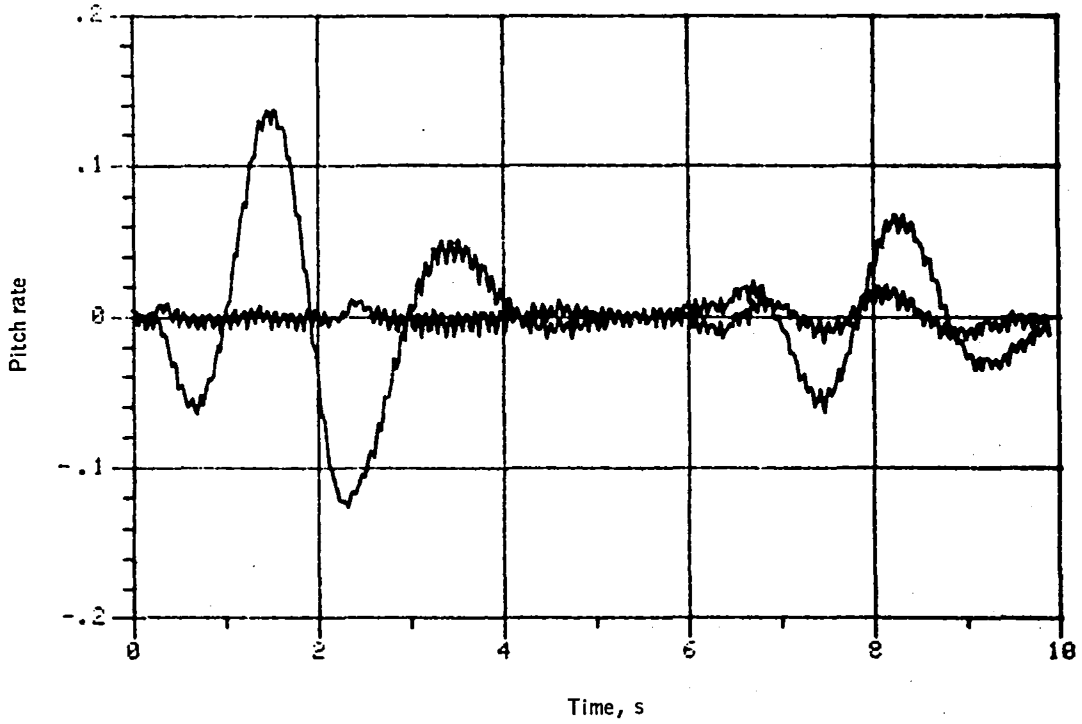

Figure 127. -Pitch rate versus time -- maneuver no. 9.

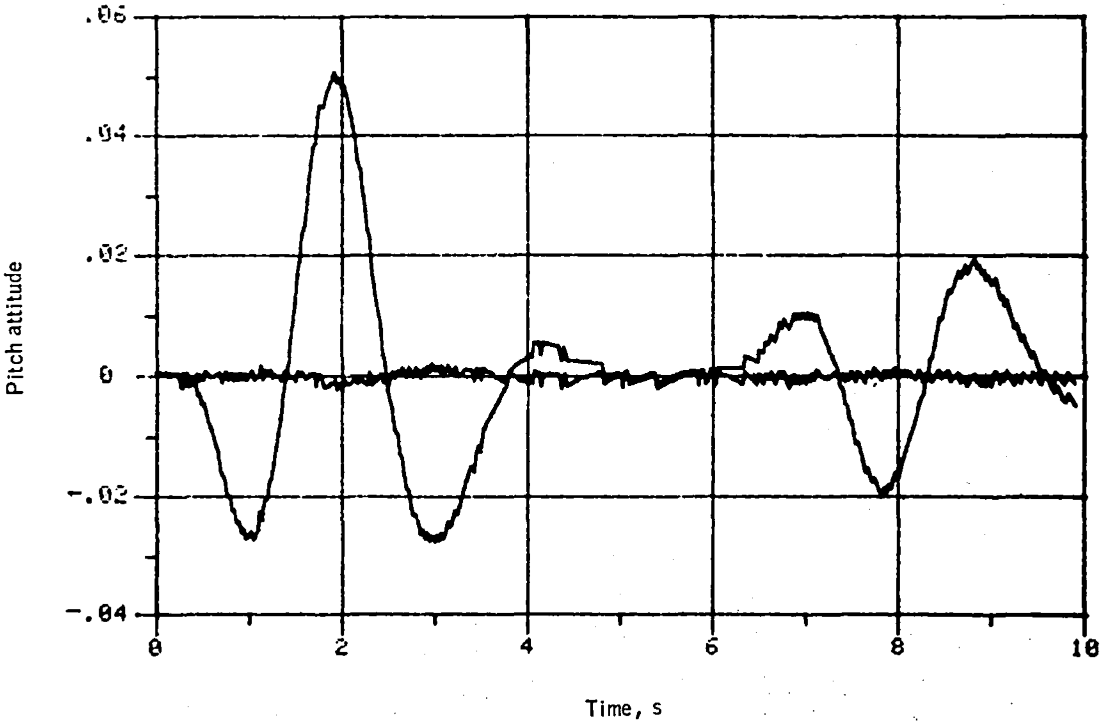

Figure 128. -Pitch attitude versus time -- maneuver no. 9.

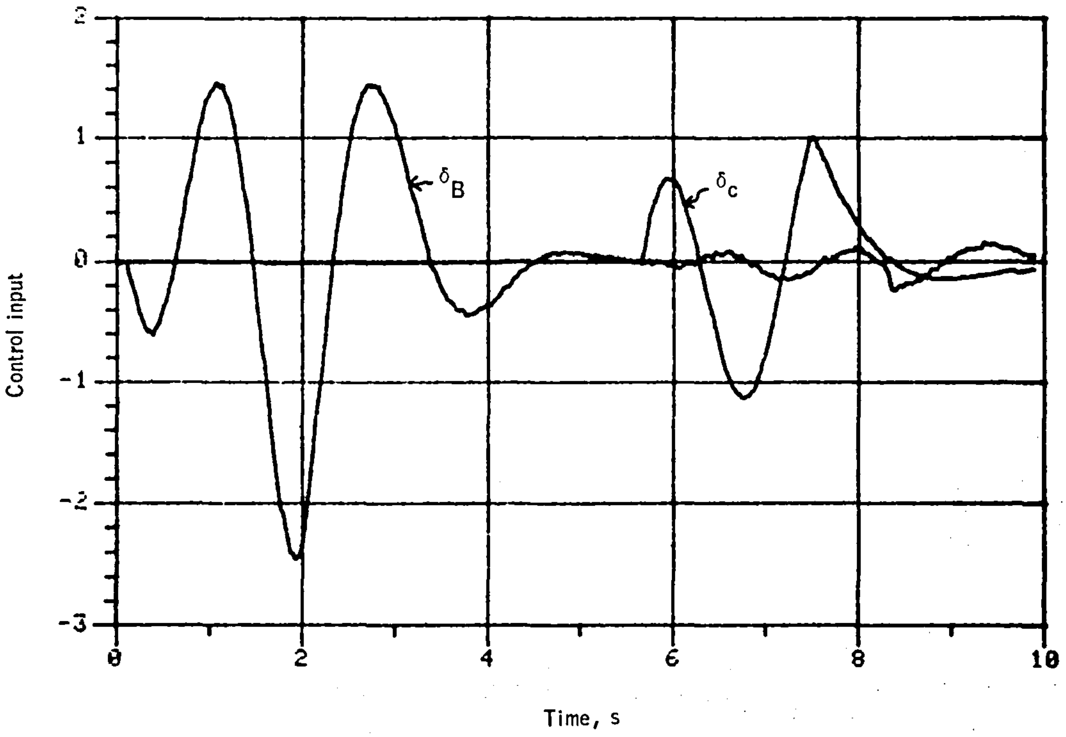

Figure 129. -Control input versus time -- maneuver no. 10.

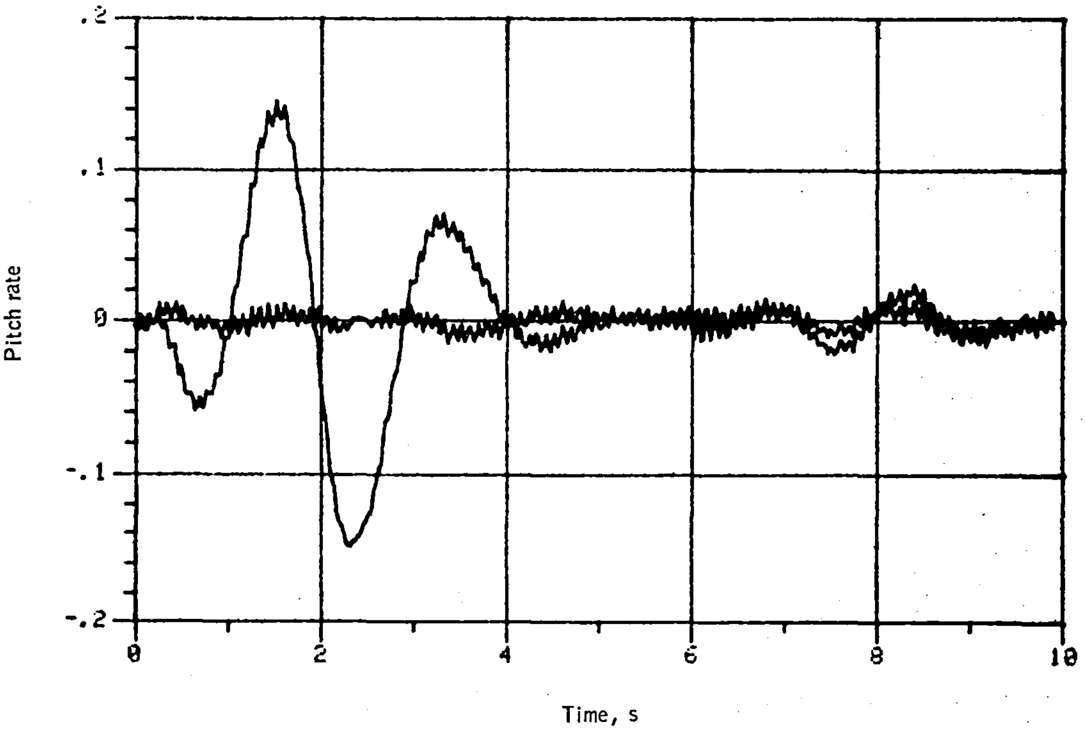

Figure 130. -Pitch rate versus time -- maneuver no. 10.

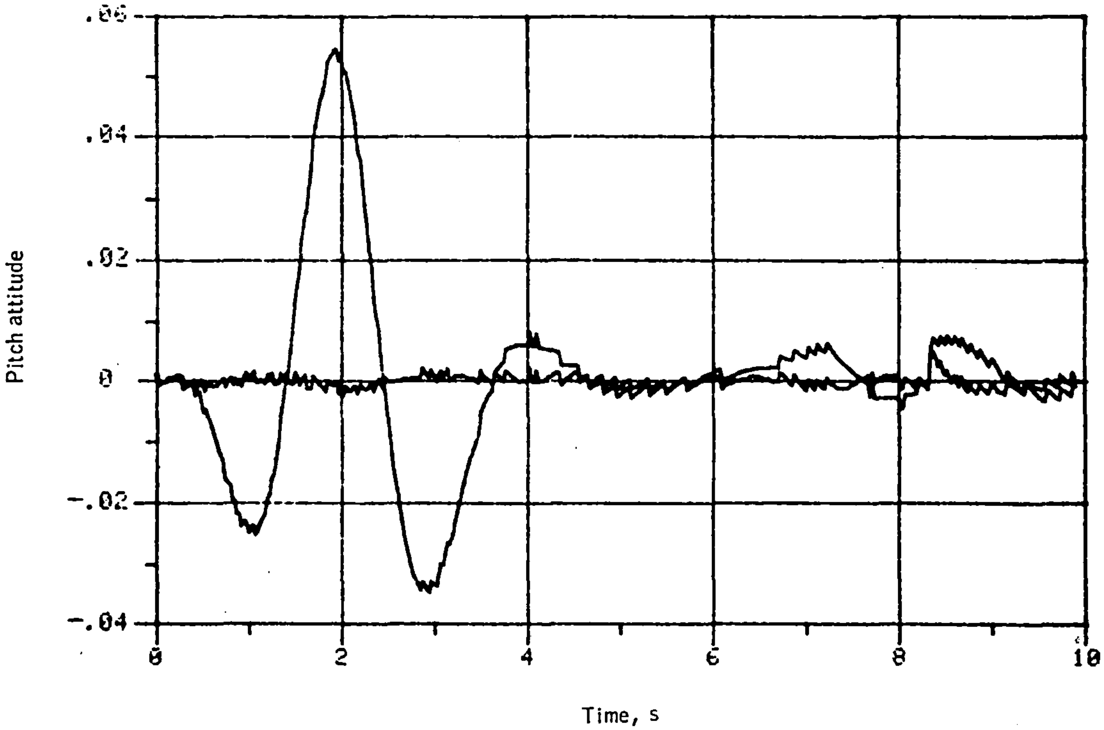

Figure 131. -Pitch attitude versus time -- maneuver no. 10.

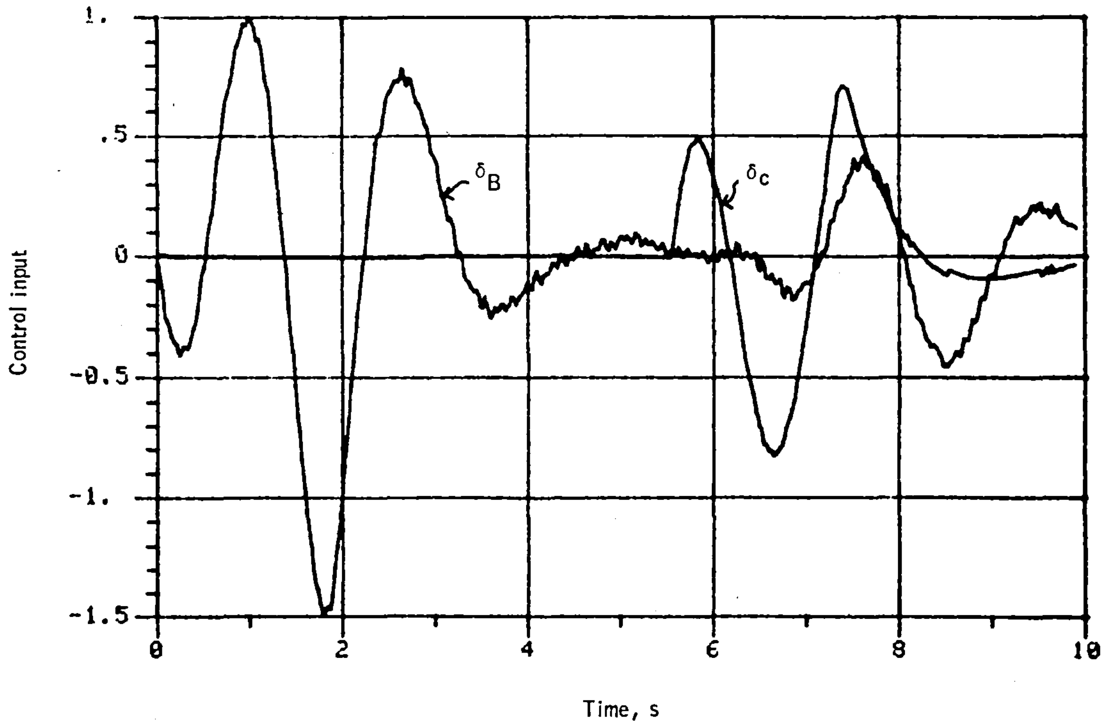

Figure 132. -Control input versus time -- maneuver no. 11.

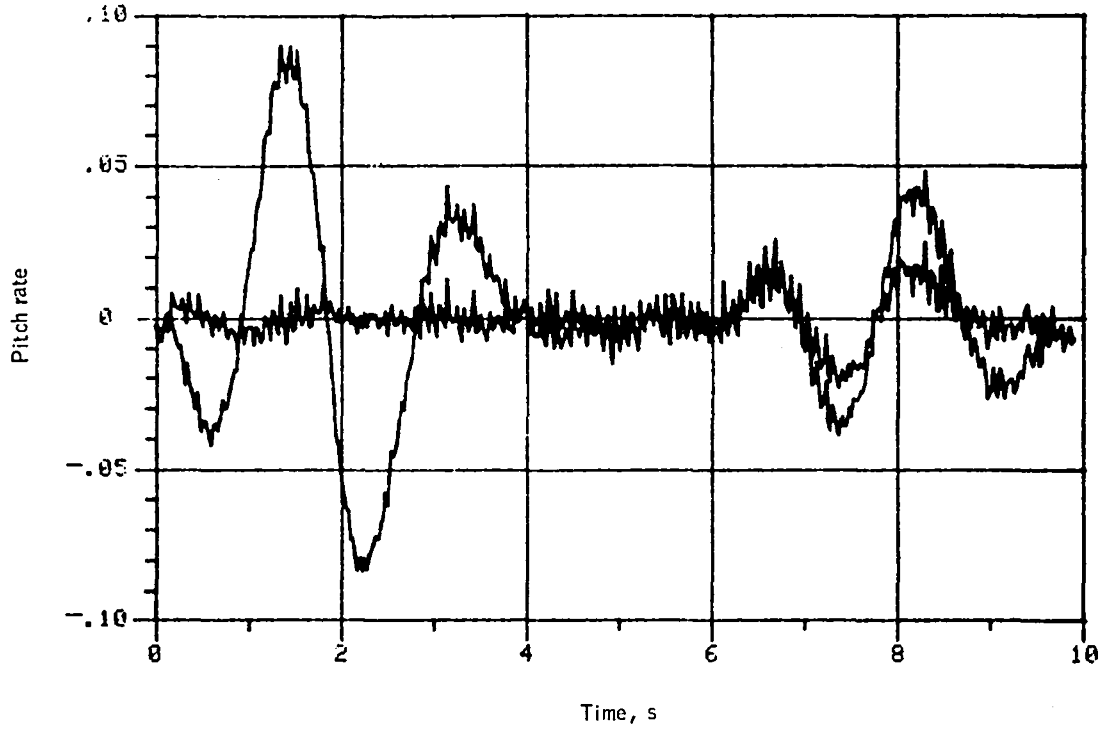

Figure 133. -Pitch rate versus time -- maneuver no. 11.

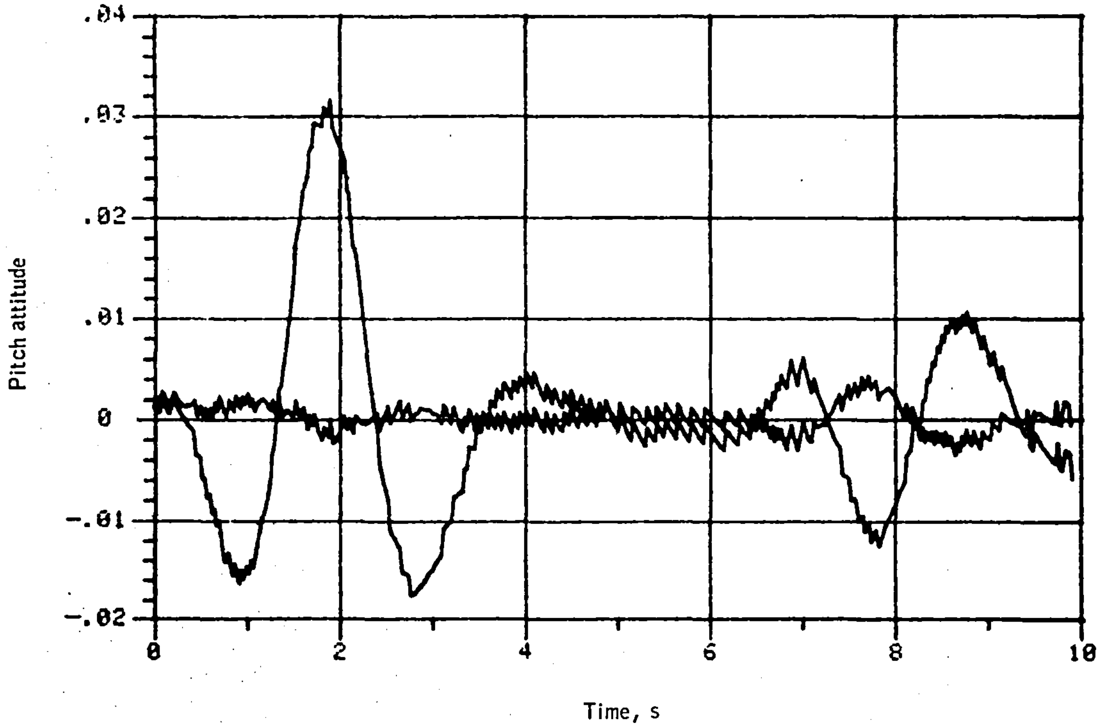

Figure 134. -Pitch attitude versus time -- maneuver no. 11.

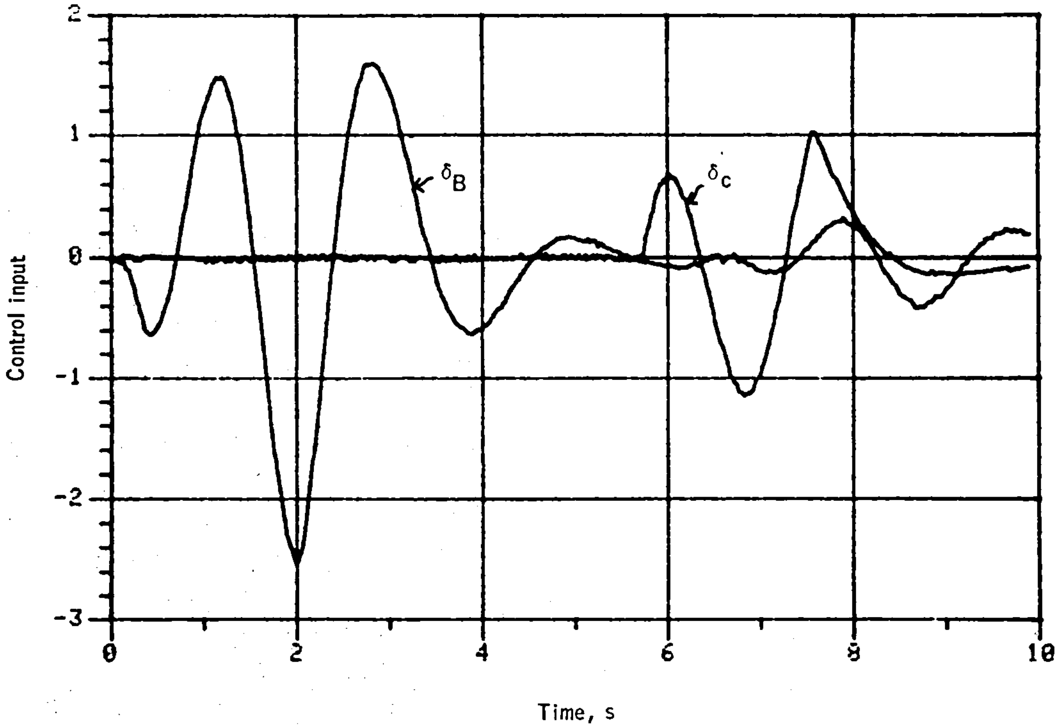

Figure 135. -Control input versus time -- maneuver no. 12.

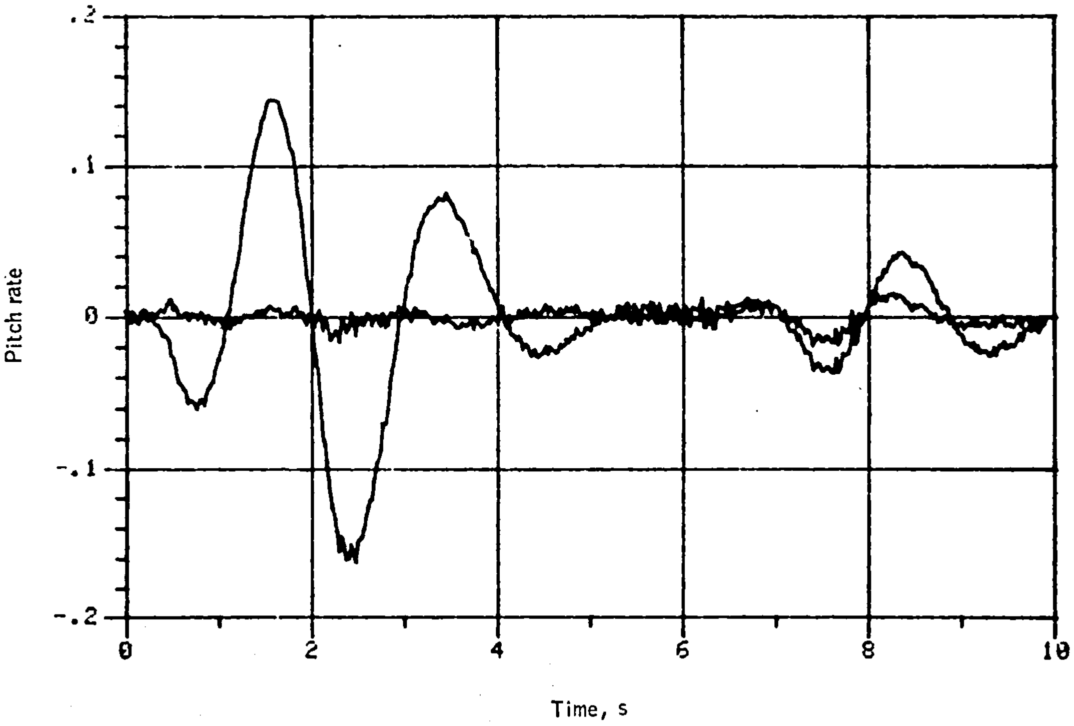

Figure 136. -Pitch rate versus time -- maneuver no. 12.

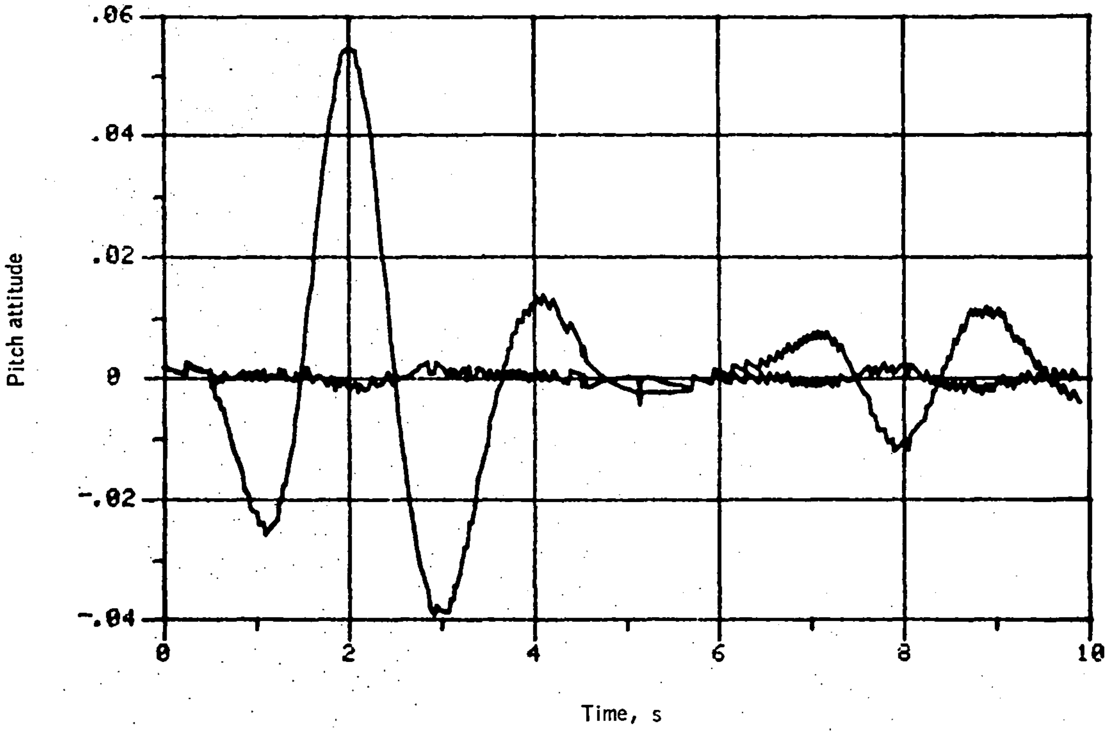

Figure 136. -Pitch attitude versus time -- maneuver no. 12.

REFERENCES

1. Anon., "Tactical Aircraft Guidance System Advanced Development Program Flight Test Phase Report," Vols. I and II, USAAMRDL TR-73-89A, B, Ft. Eustis, Virginia, April 1974.

2. Hartmann, G.L., et al., "F-8C Adaptive Flight Control Laws," NASA CR-2880, September 1977.

3. Landau, I.D., "A Survey of Model Reference Adaptive Techniques," Theory and Application Automatica, Vol. 10, p. 353, 1974.

4. Ostroff, A.J., Downing, D.R., and Root, W.J., "A Technique Using a Nonlinear Helicopter Model for Determining Trims and Derivatives," NASA TN D-8159, May 1976.

5. Gelb, et al., Applied Optical Estimation, The MIT Press, Cambridge, Mass., 1977.

6. Balakrishnan, A.V., "Identification and Adaptive Control: An Application to Flight Control Systems," Journal of Optimization Theory and Applications, Vol. 9, no. 3, March 1972.

7. Stein, G. and Saridis, G.N., "A Parameter Adaptive Control Technique," Automatica Vol. 5, pp. 731-739, 1969.

8. Lainiotis, D.G., "Optimal Adaptive Estimation: Structure and Parameter Adaptation," IEEE Trans. Auto Control, Vol. AC-14, no. 2, April 1969.

9. Tse, E., "Information Matrix and Local Identifiability of Parameters," JACC, Columbus, Ohio, 1973.